

ESR PLATEAU DATING OF FAULT ROCKS

by

Hee-Kwon Lee, B.Sc., MSc.

A Thesis

Submitted to the School of Graduate Studies

in Partial Fulfilment of the Requirements

for the Degree

Doctor of Philosophy

McMaster University

(c) Copyright by Hee-Kwon Lee, February 1995

**ESR PLATEAU DATING OF FAULT ROCKS**

DOCTOR OF PHILOSOPHY (1994)

(Geology)

McMASTER UNIVERSITY

Hamilton, Ontario

TITLE: ESR Plateau dating of fault rocks

AUTHOR: Hee-Kwon Lee

B. Sc. (Kongju National University, Korea)

M. Sc. (Seoul National University, Korea)

SUPERVISOR: Dr. Henry P. Schwarcz

NUMBER OF PAGES: xvii, 288

## **Abstract**

Past movement on faults can be dated by measurement of the intensity of ESR signals in quartz. These signals are reset by lattice deformation and heating on grain contacts during faulting. The ESR signals then grow back as a result of bombardment by ionizing radiation from surrounding rock. The age is obtained from the ratio of the equivalent dose,  $D_E$ , needed to produce the observed signal, to the dose rate. Fine grains are more completely reset during faulting, and a plot of age vs. grain size shows a plateau for grains with radius  $r < 75 \mu\text{m}$ ; these grains are presumed to have been completely zeroed by the last strain event, the age of which they record with a precision of 5-15 %.

Two major fault zones (San Gabriel and Santa Susana-Sierra Madre) and folds are developed in the Little Tujunga region, in southern California. The trace of thrust faults and folds of the Santa Susana-Sierra Madre fault zone are roughly parallel to the San Gabriel fault zone, indicating that the maximum horizontal stress was nearly perpendicular to the San Gabriel fault zone. Bends in the main strands of the San Gabriel fault zone yielded local transpressive regimes and changed the direction of maximum horizontal stress to a lower angle to the main strands, resulting in the development of subsidiary faults and folds oblique to the main trend of the fault. These structural features can be explained by the process of low drag-decoupled shear combined with transpression.

Type I and II fault zones in a single outcrop can give us the age of each stage of the evolution of fault rock zones. For Type III fault zone, we can determine only the age of last movement. The sequence of ESR plateau ages is consistent with the sequence of fault movement recognized by geological intersection relationship.

ESR ages from both the main strands and subsidiary faults range from 1170 to 40 ka. The ages show temporal clustering into active and inactive periods, analogous to that seen in historic and Holocene earthquake fault activity. Within a given active period, activity is spread out at a restraining bend in the San Gabriel fault zone. Historic earthquake faults similarly show that fault strain was prohibited in restraining bends and that fault activities spread out up to several km away from the main strand.

The San Gabriel fault zone was formerly considered to be an exhumed ancient fault of the San Andreas fault system. The results suggest that although much less active than the San Andreas fault zone (average recurrence interval in Pallett Creek: 132 a; Sieh et al., 1989), the long term (80-120 ka) cyclic fault activity of the San Gabriel fault zone continued during the Pleistocene.

I have studied the temporal distribution of paleoseismic records of earthquakes in several regions of California over time scales ranging from decades to several hundreds of thousands years, using dates obtained by ESR plateau dating of fault gouge,  $^{14}\text{C}$  dated sediments from fault zones and records of historic earthquakes. The historical record in the

San Andreas fault zone of central California, and the paleoseismic record of the San Gabriel fault zone both exhibit self similarity with a fractal dimension of 0.43-0.46. The fractal dimension of the San Andreas fault zone in Southern California both in historic and paleoseismic time scales is 0.67 indicating more evenly distributed fault movements than that of the central California. On time scales  $< 1$  y, the distribution is largely random.

Seven out of ten samples collected at the URL site of AECL, Pinawa, Manitoba were saturated. The three ESR plateau ages appear to lie in interglacials, which is consistent with a model in which movement on the thrust fault is triggered by melting of an ice sheet at the end of a glacial stage.

## **Acknowledgements**

I would first like to thank Dr. Henry P. Schwarcz for supervising this thesis and for providing help and encouragement throughout the course of the thesis. I also thank Dr. W.J. Rink for his advice and discussion about ESR dating of faults. Thanks are due to my supervisory committee, especially Dr. P.M. Clifford for his help with structural analysis. I also thank Dr. D. R. Eaton for his advice about ESR measurements.

I greatly appreciate the help of Dr. C. Scholz, Dr. R. Biegel and Dr. W. Wang for their assistance in the experiments at the Lamont Doherty Geological Observatory of Columbia University. I also thank to G. Holk and Dr. J.L. Kirschvink at California Institute of Technology, and X. Fan at McMaster University for their help during field work in California. I thank Dr. M. Gascoyne and Dr. A. Brown at AECL for guiding to the URL site and collecting samples.

Dr. R. Grün at Australian National University, Dr. G. Middleton at McMaster, W.M. Buhay at University of Waterloo, Dr. Kerry Sieh at California Institute of Technology, and Dr. T. Engelder at Pennsylvania State University are thanked for constructive comments which helped to improve the text.

I also thank all the members, old and new, of the MESRL research group. Dr. B. Blackwell taught me how to use the ESR spectrometer. Dr. N. Porat taught me sample

preparation and gamma ray irradiation and discussed the ESR spectra of quartz. I also thank K. Goodger for INAA analyses. Thanks must go to other members for their support and encouragement.

My thanks go to all of my friends here at McMaster; M. Zhai, J.H. Lee, A. Guo, M. Buck, W. Li, H. S. Williams, T. Schwartz and other classmates.

Finally I thank all of my family; my parents, my wife, Soon-Ae, my daughters, Heow-Won and Heow-Jin. They encouraged and waited for me to finish this research far away in Korea.



## Table of Contents

Chapter 1. Introduction	1
1-1. The background to fault dating	1
1-2. A review of ESR dating of fault movement	5
1-3. The project and its aims	8
Chapter 2. Electron spin resonance dating of fault rocks	12
2-1. Principles of electron spin resonance dating	12
2-2. Dating of fault movement by ESR method	14
2-2-1. Principles and assumptions of ESR dating of fault rocks	15
2-2-2. Appropriate geologic setting	19
2-2-3. ESR centers in quartz	20
2-2-3-1. Intrinsic defect ESR centers	23
2-2-3-1-1. E' type centers	23
2-2-3-1-2. Oxygen-hole center (OHC)	26
2-2-3-2. Extrinsic defect ESR centers	29
2-2-3-2-1. The Al center	29
2-2-3-2-2. The Ge center	32
2-2-3-2-3. The Ti center	33
2-2-3-3. Thermal stability of ESR signals	33
2-2-3-4. Irradiation sensitivity	36
2-2-3-5. Resetting of ESR signals	36
2-2-4. Time range of applicability	37
Chapter 3. Method of ESR dating of fault rocks	39
3-1. Field techniques and collection of samples	39
3-2. Sample preparation and measurement of ESR signals	44
3-3. Determination of equivalent dose ( $D_E$ )	46
3-3-1. Recognition of saturated samples	50
3-3-2. Unsaturated fault rock samples	57
3-4. Determination of dose rate	62
3-4-1. Measurement of gamma ray activity by gamma spectrometry	66
3-5. Determination of ESR ages	71

Chapter 4. Criteria of complete zeroing of ESR signals during fault movement	73
4-1. Introduction	73
4-2. Plateau method	75
4-3. Experimental studies of zeroing	77
4-3-1. A review of previous experimental studies	77
4-3-2. Experimental methods	79
4-3-3. Results of experimental studies	81
4-3-3-1. Mechanical properties and grain size distributions	81
4-3-3-2. Variation of ESR intensity of sheared quartz	81
4-3-3-3. Variation of radiation sensitivity of sheared quartz	83
4-3-3-4. Variation of ESR signals of sheared quartz	86
4-3-4. Conclusions from experiments	89
4-4. Field testing of plateau dating method	95
4-4-1. Results of ESR plateau dating	95
4-4-2. Discussion	107
4-4-2-1. Validity of the plateau method and resetting mechanism	107
4-4-2-2. Theoretical estimates of zeroing conditions	114
4-4-3. Conclusions for field testing of ESR plateau dating	120
4-5. Summary	121
Chapter 5. Geology of Little Tujung region	123
5-1. Stratigraphy	123
5-2. Structural Geology	124
5-3. The evolution of a fault zone in the brittle regime	133
5-3-1. Introduction	133
5-3-2. Structural features in the brittle fault rock zones	134
5-3-3. Fault rock zones developed in the Little Tujung region	137
5-3-3-1. Fault gouge zones bounded by fractured or intact host rocks	140
5-3-3-2. Fault gouge zones bounded by fault breccia	148
5-3-3-3. Fault gouge zone bounded by cataclasite	154
5-3-3-4. Fault gouge zone bounded by older gouge	167
5-3-4. The evolution of fault rock zones in the brittle deformation regime	172
5-4. Summary	178

Chapter 6. Chronology of movement on the San Gabriel fault zone	180
6-1. Fault movement history analysis using ESR plateau method	180
6-2. Fault movement history of the San Gabriel fault zone	183
6-2-1. Results of ESR dating of fault rocks	184
6-3-2. Temporal and spatial pattern of fault activity in the Little Tujunga region in the Pleistocene	190
6-3-3. Discussion	198
6-3. San Fernando Earthquake, California, 1971, $M_L=6.4$	202
6-4. Conclusions	203
Chapter 7. Structural evolution of the Little Tujunga region	205
7-1. Introduction	205
7-2. Structural evolution of the Little Tujunga region	207
7-3. Relation to regional tectonics	215
7-4. Conclusions	222
Chapter 8. Fractal clustering of fault activity in California	224
8-1. Introduction	224
8-2. Paleoearthquake and historic earthquake data	225
8-2-1. ESR dating of the San Gabriel fault zone in the Little Tujunga region	225
8-2-2. $^{14}\text{C}$ dating of paleoearthquakes at Pallett Creek, San Andreas fault zone	227
8-2-3. Historic record of earthquakes in California	227
8-2-4. Seismic records in southern California	228
8-3. Fractal clustering of fault activity	228
8-4. Discussion	231
8-5. Conclusions	235
Chapter 9. Underground Research Laboratory, Pinawa, Manitoba, Canada	238
9-1. Introduction	238
9-2. Analytical techniques	240
9-3. Results of ESR plateau dating	240
9-4. Possible mechanism of fault movement in URL site	252
9-5. Conclusions and recommendations for further research	256

Chapter 10. Conclusions	259
References	263

## List of Figures

2.1. Illustration of the trapping process	13
2.2. A history of ESR signals in quartz from fault rocks	16
2.3. Determination of $D_E$ by the additive dose method	17
2.4. Molecular models of the E' center	24
2.5. An example of typical ESR spectra of quartz measured at room temperature	27
2.6. Molecular models of OHC, Al, Ge, and Ti centers	28
2.7. Typical ESR spectra of quartz measured at low temperature	31
2.8. Thermal annealing of ESR centers in quartz	35
3.1. Procedures of ESR dating of fault rocks	40
3.2. Details of Al signal of quartz obtained at low temperature	47
3.3. ESR spectra for different measurement settings	49
3.4. Equivalent doses vs. modulation amplitude	51
3.5. An example of dose response curves of a saturated quartz (constant)	52
3.6. An example of dose response curves of a saturated quartz (increase)	53
3.7. An example of dose response curves of a saturated quartz (decrease)	55
3.8. An example of dose response curves of a saturated quartz (fluctuation)	56
3.9. Variation of intensity of Al signal with added dose for sample 91043	58
3.10. Growth curves of Ge signal for sample 91043	59
3.11. Growth curves of E' signal for sample 91043	61
3.12. Structural map in the Little Tujunga region showing the measurement sites of gamma ray activity	67
3.13. The distribution of gamma ray activity on the cross section of the Barrel Spring fault	69

3.14. The distribution of gamma ray activity on the cross section of the Bear Canyon fault	70
4.1. Growth of intensity in a sample which was partially zeroed by faulting	74
4.2. A hypothetical distribution of ESR ages in quartz as a function of particle size	76
4.3. Schematic diagram of shear apparatus	80
4.4. The relationship between intensity of E', shear strain, and grain size	82
4.5. The variations of ESR intensities as a function of shear strain	84
4.6. The relationship between $D_E$ , shear strain, and grain size	85
4.7. Growth curves of intensity of E' for sheared quartz	87
4.8. Variations of ESR spectra by heating, shearing, and irradiation of sheared quartz	88
4.9. The variation of intensities of the E' signal as a function of shear strain	90
4.10. The decrease of the intensities of the E' signal with shear strain	91
4.11. Complete resetting conditions determined by the shearing experiments	93
4.12. Complete resetting conditions for different grain size	94
4.13. Structural map of the Little Tujunga region, showing locations of sample sites analyzed in Chapter 4	96
4.14. An example of age vs. size diagram (91004)	98
4.15. An example of age vs. size diagram (91071)	99
4.16. Intersection relationships and age vs. size of Bear Divide fault	104
4.17. An example of age vs. size diagram (91030, 91031)	106
4.18. Schematic diagram of grain contacts deformation	110
4.19. Growth curves for the E' signal of sample 91004	113
4.20. Growth curves for the OHC and AI signals of sample 91071	115
5.1. Structural map of the Little Tujunga region	125
5.2. Map view of structures associated with a strike slip fault	127

5.3. The flower structure developed along the De Mille fault	129
5.4. Plot of poles to faults in Domains 3 and 4	130
5.5. Structural features developed in strike slip deformation regime	132
5.6. Schematic diagram of a shear zone	136
5.7. Schematic diagram of faulting mode; Type I, II, and III	139
5.8a. Anastomosing faults with narrow gouge zone in Domain 3	143
5.8b. Fault breccia zone bounded by fractured gneiss	143
5.9. Structural map showing locations of sample sites (Chapter 5)	144
5.10. Y-shear and $R_1$ -shear developed in the Barrel Spring fault	146
5.11a. Fault gouge zone of the San Gabriel fault near the Bear Divide	147
5.11b. Close up of the boundary in fig. 5.10a.	147
5.12a. The ramp segment of the Bear thrust fault	149
5.12b. Fault breccia developed in the hanging wall block of the Bear thrust fault	149
5.13a. Fault breccia zone bounding the gouge zone	150
5.13b. Close up of the breccia zone	150
5.14. Minor faults in the footwall block of the Bear thrust fault	152
5.15. Close up of the gouge zone	153
5.16. A fault rock zone showing various deformation along the dip direction	155
5.17a. A cataclasite zone bounded by less deformed cataclasite zone	156
5.17b. Close up of fig 5.17a.	156
5.17c. Transition zone from cataclasite to the narrow gouge zone	157
5.17d. Narrow gouge zone bounded by strongly deformed cataclasite	157
5.18. A strike slip fault with curved geometry	159
5.19a. A breccia patch with sharp boundary	160
5.19b. A breccia patch with irregular boundary	160
5.20a. An example of gouge zone bounded by cataclasite	162
5.20b. Close up of the left side of fig.5.20a.	162

5.20c. Close up of the right side of fig.5.20a.	163
5.20d. Cataclasite relics within the main gouge zone	163
5.21a. Microtexture of host granitic rock	164
5.21b. Microtexture of cataclasite	165
5.21c. Microtexture of gouge	165
5.22 An example of reactivated gouge zone bounded by older gouge zone	169
5.23a. Microtexture of primary or older gouge	170
5.23b. Microtexture of reactivated gouge (XZ plane)	171
5.23c. Microtexture of reactivated gouge (YZ plane)	171
5.24. Evolution of fault zones with fault rocks	173
5.25a. An example of Type I fault gouge zone	176
5.25b. Close up of the new gouge zone	176
5.26. An example of Type I mode of fault rock zone	177
6.1. Temporal variation of ESR intensity	181
6.2. Structural map showing locations of sample sites	185
6.3. Temporal pattern of fault activity of the San Gabriel fault zone	191
6.4. Spatial pattern of fault activity of the San Gabriel fault zone	194
6.5. Comparison of the fault activity pattern of the San Andreas fault and the San Gabriel fault	199
6.6. Examples of historic earthquake fault movement pattern	201
6.7. Vertical section, offset 80 km along the San Andreas fault, through the hypocenters of the 1952 Kern County and the 1971 San Fernando earthquakes	204
7.1. Structural evolution of the Little Tujunga region	208
7.2. Sequence of the development of the San Gabriel fault zone in the Little Tujunga region by the strike slip duplex process	210



7.3. The distribution of deformation	214
7.4. Tectonic evolution of the San Gabriel Mountain area	217
7.5. Transrotation model	220
8.1. Fault map of California showing the study area	226
8.2. Population curves for intervals of fault activities	230
8.3. Population curve for intervals of seismic events in Southern California (1981)	232
8.4. Fractal dimensions of fault activity in California	233
9.1. Generalized northwest-southeast section of the URL site	239
9.2. An example of dose response curves of a saturated sample	242
9.3. An example of dose response curves of an unsaturated sample	245
9.4. ESR spectra of quartz and gouge matrix	248
9.5. Growth curves for quartz and gouge matrix	249
9.6. Photograph of AECL 12 (thin gouge zone)	250
9.7. ESR age vs. size for samples from URL site	251
9.8a. A drill core sample of AECL3	253
9.8b. A drill core sample including fault breccia	253
9.8c. A fraction of thick fault gouge	253
9.9. Stable isotope stages and ESR plateau ages of fault rocks from URL site	254
9.10. Variation of stress field between glacial and interglacial period	257

## **List of Tables**

3.1. Data to be collected from a fault zone	42
3.2. Results of measurement of gamma ray activities in the Little Tujunga region	68
4.1. ESR analytical data and results for fault rocks from the San Gabriel fault zone	100
4.2. Examples of times of last movement on faults determined by ESR method	102
5.1. ESR analytical data and calculated ages for faults	141
5.2. Examples of times of last movement on distinct fault rock zones in a given fault zone determined by ESR method	142
6.1. ESR analytical data for fault rocks collected from the San Gabriel fault zone	186
6.2. Results of ESR age estimates	188
6.3. Recurrence intervals for the fault activity of the San Gabriel fault zone in the Little Tujunga region	193
9.1. Samples of fault rocks collected from drill cores in URL site	241
9.2. ESR analytical data and the minimum ages of fault movements for saturated samples	243
9.3. ESR analytical data and results for unsaturated samples from URL site	246

## **Chapter 1**

### **Introduction**

#### **1-1. The background to fault dating**

There are many disasters from earthquakes and volcanoes in the world. Fractures and faults play a predominant role in most rock engineering problems. The evaluation of active faults is important to select sites at which to construct structures such as nuclear reactors and dams. The times and frequencies of reactions of the earthquake fault zones are important for tracing the history of large earthquakes and predicting when and how often the fault will move. The long term history of earthquake fault movement cannot be defined reasonably using the limited instrumental or historical records. For example, some of the largest earthquakes have occurred along the segments of dormant faults that are now seismically very quiet. Therefore dating of prehistoric fault movements is a critical tool in the evaluation of active tectonism.

The two primary methods of dating of fault movement are the direct dating of movements and relative dating or correlation. In addition to conventional dating of stratigraphic units, materials found along the fault plane can be used to determine the fault

movement history. Relative dating methods provide approximate ages of fault movements. If the stratigraphic unit is disturbed, its age represents the maximum age of movement; and if it is undisturbed, it represents the minimum age for the last movement. Many geological phenomena yielded by earthquake faulting are preserved in the sedimentary record. These geological features include faults, folds, soft sediment deformation and sandblows. Relationship between these geological features and layers can be used to date prehistoric earthquakes and calculate average recurrence intervals (Sieh et al. 1989).

Dating techniques to determine the age of the layers or stratigraphic units include carbon-14, fission track, thermoluminescence (TL), optical stimulated luminescence (OSL), electron spin resonance (ESR) and K-Ar dating. Carbon-14 dating is generally the most precise and widely applicable numerical dating method in the late Quaternary and particularly in the Holocene. Sieh et al. (1989) used this method to date the earthquake ruptures of the San Andreas fault that are recorded in the sediments at Pallett Creek. They estimated an average recurrence interval of about 132 a from the latest 10 episodes of faulting. Recently, other researchers also used this technique to investigate the fault movement history on other fault systems in the world (Van Dissen et al., 1992; Vita-Finzi, 1992; Bartsch-Winkler and Schmoll, 1992; Wills and Borchardt, 1993).

Age determinations of sediments or volcanic rocks using radiation damage have been developed. These methods are based on one of two types of radiation damage: fission tracks and trapped charge techniques; these include luminescence and ESR dating methods. These methods are based on counting trapped electrons released from the atoms

by the external ionizing radiation. Forman et al. (1989) and McCalpin et al. (1994) applied thermoluminescence dating method to evaluate the paleoearthquakes on the Wasatch fault zone, Utah. The estimated ages by thermoluminescence show consistency with the ages obtained by the carbon-14 dating method. Application of optically stimulated luminescence (OSL) for dating of sediments was first demonstrated by Huntley et al. (1985). This technique has later been used to date minerals such as quartz, feldspars, and polymineral grains from unburnt sediment that was exposed to sunlight in the course of deposition (Smith et al., 1986, 1990; Aitken and Smith, 1988; Godfrey-Smith et al., 1988; Rhodes, 1988, 1990; Stokes, 1991, Wintle et al., 1994). This method has yet to be applied to a fault zone. The ESR dating method can be applied to materials found in the layers or stratigraphic units whose ages would relate to the timing of earthquakes. These include minerals from volcanic rocks (Buhay et al., 1992); teeth and bones from Pleistocene or Holocene sediments (Schwarcz and Grün, 1992); and possibly quartz grains from sediments, whose ESR signals were partially bleached by exposure to sunlight, and are then restored during subsequent burial (Tanaka et al., 1986).

Surface textures and weathering rinds of quartz grains, basaltic and andesitic stones have been used to determine the relative age (Kanaori et al., 1980, 1985; Colman and Pierce, 1981). These methods are based on the speed of creation of rinds or cavities; rind thickness or the amount of cavities increases with time. The surface texture groups of quartz extracted from fault gouge were correlated to the ESR ages of fault movements on the Atotsugawa fault in Japan (Kanaori et al., 1985).

Palaeomagnetic analysis of clay-rich fault gouge has been performed to date the last fault movement. Hailwood et al. (1992) suggest that the high-coercivity, reverse polarity component of magnetization of fault gouge collected from Porth-y-pistyll fault in Anglesey, North Wales was obtained by a chemical remanent magnetization. Since this chemical remanent magnetization was produced by a fluid activity within fault zone after last movement, the time of magnetization may be correlated to the time of last movement of the fault. However, these methods need calibration by numerical dating method.

The dating of materials collected on the fault zone can give us the direct time of earthquake. K-Ar and Rb-Sr isotopes of authigenic clay minerals can be used to date the clay mineralization in the fault zone after faulting (Kralik et al., 1987, 1992). Scholz et al. (1979) used K-Ar dating method of clay minerals based on the assumption that the Ar gas from the host rock is dispersed by frictional heating at the time of fault movements. The fission track dating method has been performed using epidote formed along the fault planes (Bar et al., 1974). Tagami et al. (1988) suggested that frictional heating anneals the fission tracks of the apatite at the time of fault movement.

Eyal et al. (1992) used uranium series dating of the uranium minerals, carnotite and tyuyamunite, found along a fault plane. This method is based on radioactive disequilibrium which utilize the time dependence of the radioactive equilibrium between parent and daughter isotopes.

## 1-2. A review of ESR dating of fault movement

Keya et al. (1982) showed that radiation-sensitive ESR signals in quartz from fault gouge exhibit equivalent doses ( $D_E$ ) which are much less than saturation or steady state doses observed in adjacent, unfaulted host rocks. Assuming that doses in the faulted materials have been partially or totally zeroed during movement along the fault, these authors suggested that the ratio of  $D_E$  to the environmental dose rate,  $d$ , would give an estimate of the time of last motion on the fault. They proposed that high shearing stress and frictional heating are responsible for the zeroing of ESR signals and that the precursors of ESR signals are created at the time of fault movements.

In using ESR to date the time of the last movement on a fault, it is essential to demonstrate that the ESR signal was fully zeroed at the time of faulting; if the signal was not completely reset, then the ESR age obtained will be too great. Therefore it was very important to develop some criteria to demonstrate that zeroing of ESR signals had occurred at the time of fault movement.

Various researchers have recognized from experimental tests of zeroing that complete resetting of ESR signals will only occur when the faulted material has been subjected to some normal stress at the time of faulting, and when there has been sufficient displacement (shear strain) during the fault event (Ariyama, 1985; Tanaka, 1990; Lee and Schwarcz, 1993). Schwarcz et al. (1987) suggested that the degree of zeroing of grains in fault gouge would increase with decreasing grain size, reaching a state of full zeroing

for grains below some critical size. Buhay et al. (1988) demonstrated that this method gave self-consistent ages for times of last movement on fault gouge from California, but they recognized some limitations in this method that needed further elaboration.

In contrast with above suggestions, Fukuchi (1989, 1992) has suggested that generation of frictional heat on the fault plane is the main mechanism for resetting of ESR signals. Fukuchi et al. (1986) suggested that complete resetting is indicated by convergent ages given by multiple centers with different zeroing sensitivities for thermal fading; complete zeroed centers yield a concordant age.

From detailed investigation of the age of known fault through stratigraphic relationship, Ito and Sawada (1985) suggested that samples should be collected from films of fault gouge about 2 mm thick from the principal fault plane. They also suggest that the faults must be buried at a minimum depth of 20 m for reverse faults, 70 m for strike-slip faults, and 100 m for normal faults in order to assure adequate normal stress for resetting at the time of faulting events.

Fukuchi (1992b) suggested that fault movement can be dated by the ESR method without zeroing of ESR signals from the fault gouge whose host rock do not have any ESR signals. Toyota (1992) also showed that the width of E' signal was increased by the distortion of lattice during crushing, and if we separate the distorted E' signal from normal E' signal, we can date the fault movement. These methods simply show that E' precursors were generated by faulting, but do not assure that the signal was zeroed in multi-cycle gouge.



Previous studies of ESR dating of fault movement have raised certain critical questions, some of which have been partially answered, but all of which require further study:

1. Zeroing of ESR signals: Has a given sample of fault rocks ever been completely zeroed during a faulting event? The dating method assumes that the ESR intensity was zero immediately after faulting, but there is no independent evidence from the ESR characteristics of a single sample to assure us that this was so.

2. Sensitization: The increase in radiation sensitivity of some ESR signals in strained quartz (Fukuchi, 1989) is believed to be due to the localization of charge traps on strain-induced defects in crystal lattice (e.g., dislocations or microcracks). This process has not been studied in detail, however.

3. Zeroing mechanism: Most ESR signals in quartz can be zeroed by shearing at room temperature (Tanaka, 1990), by mechanisms that have not been well-characterized. These signals can also be zeroed by heating and it is believed (Fukuchi, 1989, 1992b) that localized heating on the fault plane is responsible for the zeroing of ESR signals during earthquake faulting. This hypothesis is contradicted, however, by the variation in ESR age with particle size that Buhay et al. (1988) have described, since all particle sizes would be heated to the same extent.

4. Condition (stress/strain) of complete zeroing of ESR signals: In laboratory experiments, several researchers show that some normal stress and shear strain (displacement) was needed to permit complete zeroing.

### 1-3. The project and its aims

There are some critical questions described in a previous section that are still in need of definition if ESR analyses are to be made an effective tool in evaluating the pattern of paleoearthquake fault activity.

The principles and assumptions of ESR dating, ESR centers of quartz will be outlined in Chapter 2. The procedure of ESR dating of fault rocks will be discussed in Chapter 3.

One of the objectives of this study was to test the plateau method for recognition of complete zeroing, using both simulated gouge (experimentally sheared gouge) and fault rocks collected from the San Gabriel fault zone in the Little Tujunga region, in southern California (Chapter 4). I also investigated the grain size dependence of resetting and radiation sensitivity of ESR signals in quartz.

Most of the fault rocks collected in the Little Tujunga region appear to be reactivated or formed at high crustal levels and are classified by the proportion of matrix (breccia; < 50 %; cataclasite; 50-90 %; gouge; > 90 %). At several localities, fault gouge is bounded by fault breccia (or cataclasite) and fractured host rock. I also found several reactivated fault gouge zones, which generally are foliated and well defined within host fault rock zones. Another key aim of this study was to determine if ESR plateau ages of reactivated zones were younger than the ESR plateau ages of older host fault rocks (breccia, cataclasite, older gouge). This test verifies whether successive faulting events

had reset the date from the previous movement on that fault. Further, using data of measured stress field, uplift rate, and magnitude of earthquake (displacement), I attempted to investigate the deformation environment needed to reset ESR signals completely at the time of fault movement in the Little Tujunga region, and to define conditions need for the complete zeroing of ESR signals during fault movement (Chapter 4).

I tried to apply the ESR dating method to solve problems in the study of microtextures of fault rocks formed or modified in the shallow depth environment. The microtextures of fault rocks are overprinted by the successive faulting event. Thus, the microtextures on fault rocks represent the one modified in the last fault movement. The ESR ages also represent the time of the last fault movement at sampling locality. The relationship of the microtextures and structural features developed in fault rock zones and the ESR age estimates were used to study the evolution of fault rock zones in the shallow depth environment (Chapter 5).

In this study, the structural evolution in the Little Tujunga region was investigated. Curvatures along the major strand of the San Gabriel fault zone yielded local transpressive regimes. I divided the study area into several domains according to their structural characteristics. The high drag-distributed shear and low drag-decoupled shear models suggested by Mount and Suppe (1987) were tested to explain the geometrical characteristics of geological structures in the Little Tujunga region. The relationship between Quaternary or recent fault activities and the geometry of the fault zone is certainly a key to understanding many of the deformations of the past. By extrapolation

of the relation between Quaternary fault activity (ESR ages) and geometrical structural features, I investigated the structural evolution in the Little Tujunga region since the formation of the San Gabriel fault zone (Chapters 6 and 7).

Furthermore, I tried to study the relationship between the local structures in the Little Tujunga region and the evolution of the geological structures of the San Gabriel Mountains using grouping of different types of fault activities (Chapter 7). This model includes the transtension in the Ridge basin area, simple strike-slip faulting in the central segment of the fault zone (Little Tujunga region) and transpression in the southeast front of the San Gabriel Mountains along the San Gabriel fault zone. This model is based on the stratigraphic and structural data from the Ridge basin (May et al., 1993; Crowell, 1982; Link, 1982), palaeomagnetic data (Levi and Yeats, 1993, Terres and Luyendyk, 1985) and structural data from the Little Tujunga region and southeast front of the San Gabriel Mountains.

This work focuses on the application of ESR plateau dating in the evaluation of the pattern of fault activity. I have investigated temporal and spatial pattern of the Quaternary fault activity of the San Gabriel fault zone in the Little Tujunga region (Chapter 6). In particular, I tested spatial clustering of fault activity in the restraining bends as is also shown in historic earthquake faulting events on other fault systems. These characteristic relationships between structural features and fault activity can be used to analyze the dynamics and kinematics of paleoearthquake movements. I attempted to characterize certain aspects of the temporal pattern of fault activity. Specifically, I tried

to estimate the average recurrence interval of the paleoearthquake events. Using a fractal clustering approach (Turcotte, 1992), I attempted to derive the characteristics of temporal clustering of fault activity in California (Chapter 8). Such knowledge of the long term pattern of fault movement provides a better context to the evaluation of potential hazards from earthquakes.

In summary, I attempted to analyze the results of ESR plateau dating of quartz grains separated from fault rocks on different spatial scales: from quartz grain (plateau method); outcrop (cross-cutting relationship or evolution of fault rock zone); and local tectonics (tempo-spatial pattern of fault activity in the Little Tujunga region) up to regional scale (fractal clustering), in California.

Atomic Energy of Canada Limited (AECL) is constructing a test facility consisting of a cavity quarried out of the interior of a homogeneous granitic pluton. They will use various methods to test the stability of the site with respect to long-term migration of radionuclides. The site is cut by a number of shallow-dipping fault zones. I collected samples of fault rocks from drill-cores passing these fault zones. The goal of these studies is to test whether ESR can be used in general as a validation procedure in the construction of radwaste disposal sites (Chapter 9).

## **Chapter 2**

### **Electron spin resonance dating of fault rocks**

#### **2-1. Principles of electron spin resonance dating**

When an insulating crystal such as quartz is exposed to ionizing radiation from natural radioactivity, electronic charges are trapped in the crystal, at charge-trapping imperfections in the crystal (Fig.2.1). The number of such trapped charges (positive or negative) can be evaluated from the intensities of characteristic ESR signals produced by charges trapped at each type of site. In quartz, for example, more than 30 different such trap sites have been described (Weil, 1984). The number of trapped charges gradually increases until it reaches a saturation or steady-state value, determined by the environmental dose rate and the lifetime of the trapped charges (essentially, the temperature-dependent rate of spontaneous detrapping of charges). ESR signals have been widely used to date geological materials (Grün, 1989). The principle of ESR dating is that the ESR signal in a material must have been zeroed at the time of a geologic event; the age of the material can be subsequently determined by measuring the radiation sensitivity of the ESR signal and its height, giving the equivalent dose ( $D_E$ ). The dose rate at the site

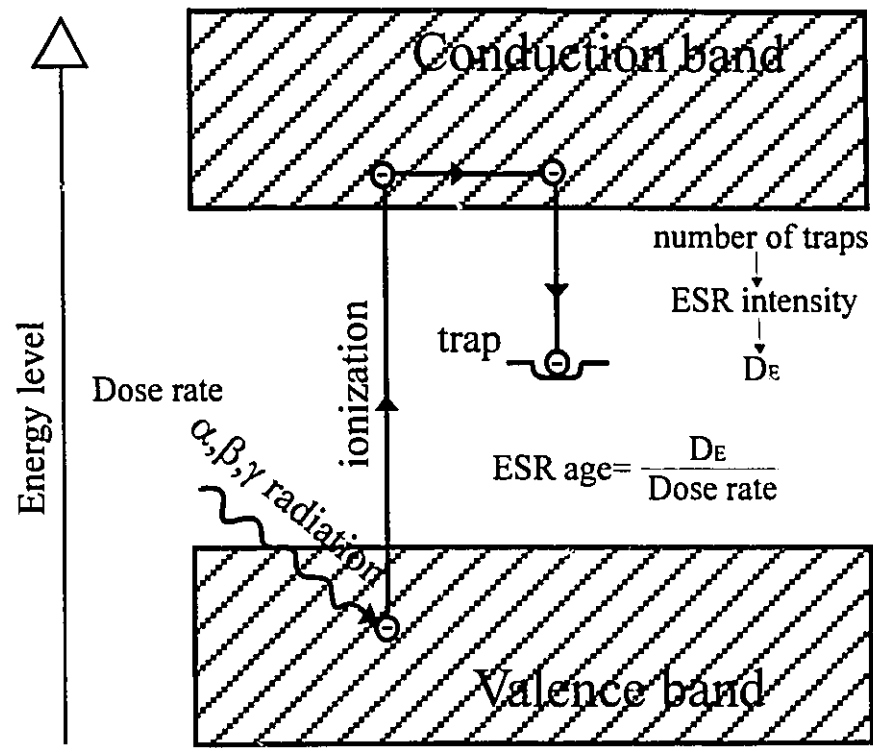


Figure 2.1. Illustration of the trapping scheme of electrons in minerals. The number of trapped electrons or holes at a given center can be detected by ESR spectrometer. Equivalent dose ( $D_E$ ) is estimated by the additive dose method. The dose rate is derived from the analysis of radioactive elements in the sample.

where the sample was stored is determined either by direct measurement or from the concentration of radioactive elements (U, Th and K) in the host matrix. Then the age is given by an equation of the form:

$$\text{Age (t)} = \text{equivalent dose (D}_E\text{)} / \text{dose rate (d)} \quad (2-1)$$

This method has been used effectively to date archaeological and paleontological sites up to 2 Ma in age (Grün, 1989).

## **2-2. Dating of fault movement by ESR method**

ESR dating of fault rocks has made use of quartz, because its ESR signals are well-characterized, and because of its relatively uniform chemical composition. ESR dating of fault gouge was first investigated by Ikeya et al. (1982) who showed that ESR signals in quartz from fault gouge had been at least partially zeroed by fault movement; experimentally, they showed that partial zeroing of E' signal occurred during simple crushing. Fukuchi (1992b) showed that unstrained igneous quartz did not exhibit the E' or OHC (oxygen-hole center) ESR signals, although the Al and Ti signals were present in some unstrained quartz. These four signals have been the most extensively investigated as indicators of fault movement.



### 2-2-1. Principles and assumptions of ESR dating of fault rocks

In host rocks, the number of trapped charges in quartz gradually increase until it reaches a saturation or steady-state value, determined by the environmental dose rate and the lifetime of the trapped charges. At the time of fault movement the ESR signals in quartz of fault rocks are zeroed by both cataclastic lattice deformation and local frictional heating on grain contacts. New paramagnetic centers are generated due to natural radiation and accumulated within quartz grains again after faulting (Fig. 2.2). The intensity ( $I$ ) of an ESR signal is proportional to the number of trapped electrons or holes, and is a function of the radiation dose rate and the elapsed time after faulting. An age of the last fault movement can be estimated by the age equation (2-1). It has been shown that the radiation response is independent of the dose rate of the artificial gamma irradiation (Grün et al., 1987). We therefore assume that we can determine the natural dose that the sample has received by giving the samples artificial doses of radiation to determine the form of the dose-response curve, and then, by backwards extrapolation, determining the intercept of the dose-response curve at  $I = 0$  (Fig. 2.3). This intercept value (with changed sign) is called the equivalent dose ( $D_E$ ), and represents the combined effects of  $\alpha$ ,  $\beta$ , and  $\gamma$  radiation and cosmic rays.

In most applications of ESR dating to fault movement, the ESR signal is supposed to have been set to zero by the earthquake event, that is, by work being done on the fault gouge. It is essential to demonstrate that the ESR signal was fully zeroed at the time of

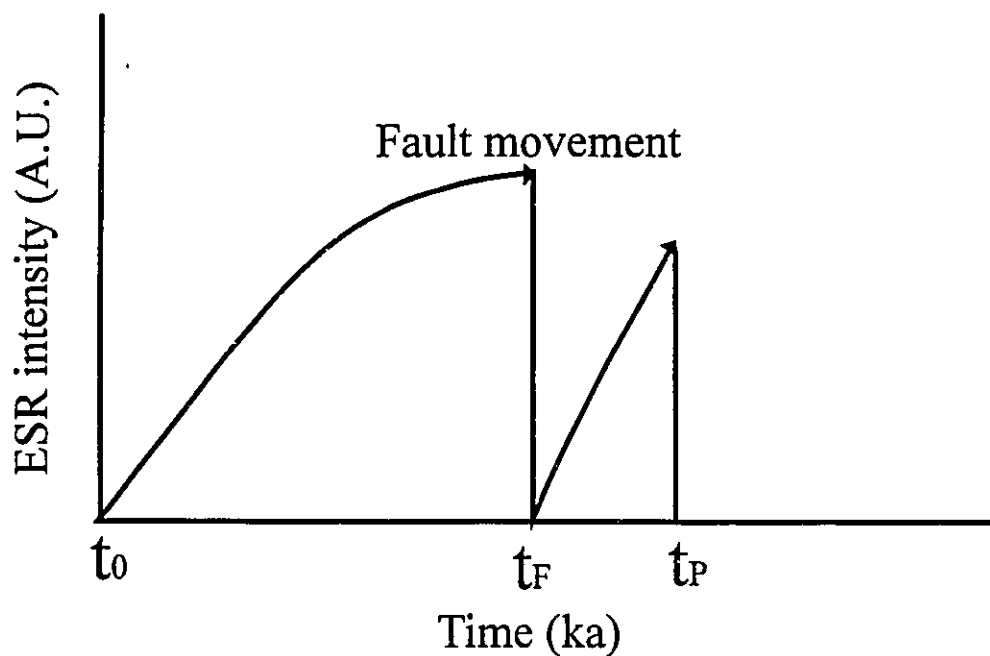


Figure 2.2. A history of ESR signals in quartz from fault rocks. Prior to faulting most of the traps are filled (saturated) due to the radiation dose received over geological time. At time  $t_F$  the ESR intensity is zeroed by shearing along a fault, and the radiation sensitivity is increased by creating precursors of ESR centers at the time of fault movement. Subsequently, the trap refills with electrons and signal intensity increases in proportion in the time since faulting ( $t_p$ ).

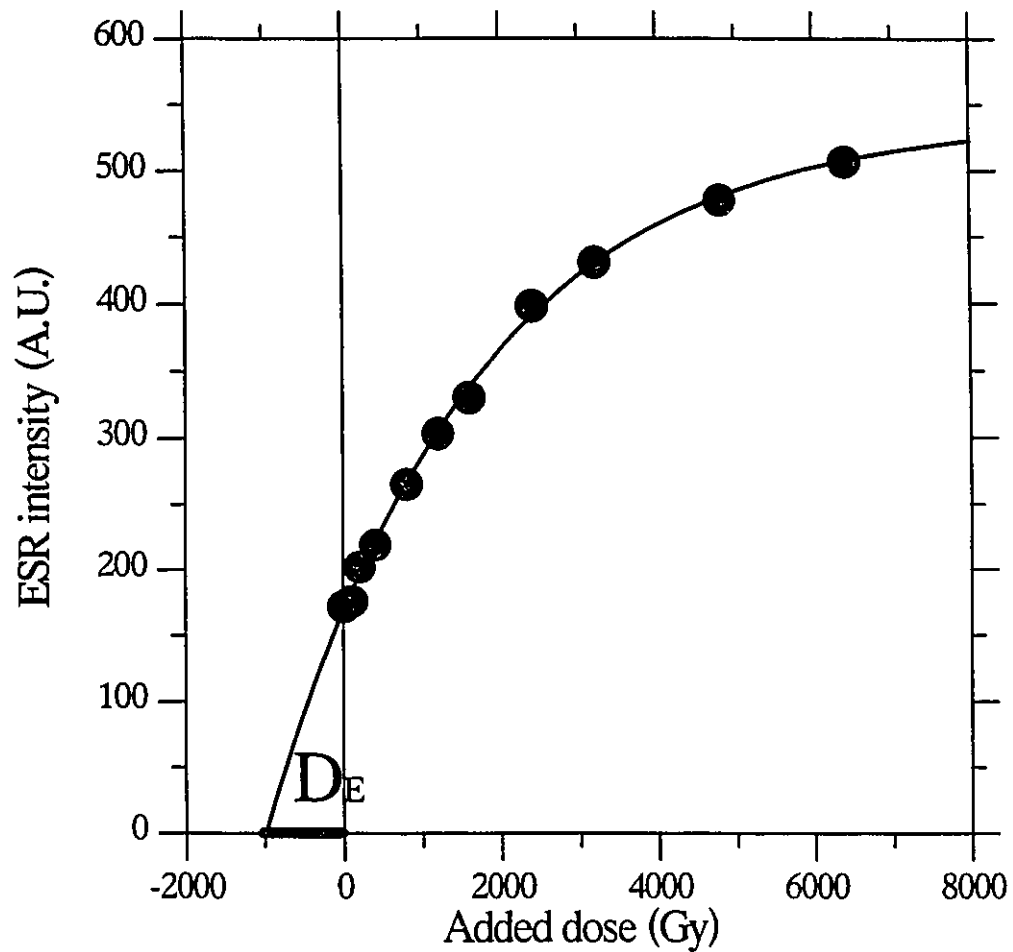


Figure 2.3. To determine the equivalent dose, we give the sample additional doses of artificial gamma radiation, and observe the rate of increase of the ESR intensity above the level of the natural signal. Back extrapolation to zero added dose gives the equivalent dose to which the natural signal would correspond.

faulting events. Two methods are now available to show completeness of zeroing:

(1) Multiple center method: We can determine an ESR age using  $D_E$  values from two or more ESR signals from the same mineral (e.g., OHC and E' in quartz). If the  $D_E$  values of these different signals agree then we suppose that each signal was fully zeroed and that the age obtained is the time of zeroing.

(2) The plateau method: A sample of quartz-bearing gouge typically contains a wide range of particle sizes. If we extract the quartz and sort it according to grain size, we find that the ESR ages of the quartz decrease systematically with decreasing grain size, reaching a minimum value (a plateau) for grains below a critical size  $r_c$ . We assume that, at the time of faulting, grains with radius  $r < r_c$  were completely zeroed, and that today their  $D_E$  values are equal to the dose rate multiplied by the time elapsed since faulting.

Ideally we can use both tests at the same time to show that multiple signals give the same plateau age. For further tests, we can use concordance of ESR plateau ages of several samples collected along/across a fault rock zone. If the dose rate is not the same in each sampling location, the concordance ages (the ratio of equivalent dose to local dose rate) can be explained if  $D_E$  of each sample was set to zero at the time of fault movement.

### 2-2-2. Appropriate geologic settings

ESR dating is applicable wherever there are exposures of fault rocks, including occurrences in faults which have not been active for up to several millions of years (the limiting age of the method). In many seismically active areas there may not be any appropriate exposures of gouge or other fault rocks associated with the faulting activity. Also, some fresh breaks tend to have fairly narrow zones of comminution, too thin to yield material for analysis. This problem can sometimes be remedied by sampling the fault at depth in drill cores, since the thickness of the gouge zones tends to increase with depth. The normal stress requirement for complete resetting of ESR signals suggests that the fault rock samples must have been at some depth ( $> 40$  m) during the last fault movement (Ariyama, 1985; Grün, 1992; Lee and Schwarcz, 1994b).

In areas of repetitive movements, well-developed zones of gouge are formed, which commonly display internal zones of reactivation. The reactivated zones are invariably found to yield younger ESR ages than their hosts. ESR analyses of such materials allow us to construct recurrence histories which are interesting for the prediction of future activity.

ESR studies of paleoseismology can be most conveniently done in tectonically active regions where there has been considerable uplift, and we would have access to exposures of fault gouge which were last reset when the material lay buried at depth  $> 40$  m. However, even where there has been little or no uplift associated with the faulting,

such as in zones of predominantly strike-slip motion, we can use drill-core to sample down to depths of 40 m or greater, in order to obtain samples whose loading was sufficient to zero ESR signals even in recent times.

### 2-2-3. ESR centers in quartz

Quartz is one of the most abundant minerals in the crust. It is found as porphyroclasts and matrix within fault rocks. There are many  $\text{SiO}_2$  polymorphs, each with a different temperature of stability. For ESR dating of fault rocks, we use alpha-quartz which is stable at atmospheric pressures and up to  $573^\circ\text{C}$ . The lattice structure of quartz is built from  $\text{SiO}_4$  tetrahedra which are linked by sharing each of their corners (O) with another tetrahedron. Alpha-quartz has trigonal symmetry and belongs to the enantiomorphic crystal class 32. The lattice structure of alpha-quartz can be defined on the basis of its space group symmetry. It belongs to the space group  $\text{P}3_121$  (right-handed) or  $\text{P}3_221$  (left-handed), depending on whether the crystal grew with a clockwise or counterclockwise sense about the screw triad axis (Gibbs, 1926). Each oxygen atom has two silicon neighbours with bond lengths of 0.1611 nm (long bonds) and 0.1607 nm (short bonds), and the Si-O-Si angle is  $143.65^\circ$  at room temperature.

There are always some local violations or defects in this perfect lattice arrangement in quartz occurring in nature. The importance of defects for ESR dating of fault rocks is that the stress is concentrated in defects in quartz during fault movement.

Stress concentration in defects cause to increase the amount of defects which act as precursors of ESR center, and to decrease the number of ESR centers, making it possible to date the last fault movement using the ESR method. For example, the theoretical strength of quartz (breaking of atomic bonds) is 5-10 Gpa, several orders of magnitude greater than the strength of real materials (Orowan, 1949). This discrepancy was explained by the stress concentration on defects which may propagate in response to an applied stresses much lower than the theoretical strength (Griffith, 1920, 1924). These defects tend to trap an electron or hole due to the charge deficit and become ESR centers by environmental irradiation. The quartz grains separated from fault rocks contain three types of defects; point, line and surface defects.

All materials contain some point defects at temperatures above absolute zero (Putnis, 1992). A Schottky defect is a point defect in which a vacant cation site (Si in quartz) in a lattice structure is balanced by a vacant anion site (O in quartz) to maintain electrical neutrality. A Frenkel defect is a point defect in which an atom moves from the site, leaving a vacancy, and is placed in an alternative interstitial site. These intrinsic defects can be created or destroyed by the displacement of atoms due to the concentration of stress in point defects in quartz during cataclastic flow. Several researchers showed that the precursors of E' or OHC in quartz were thus created, resulting in increase of radiation sensitivity (Ikeya et al., 1982; Fukuchi, 1989; Lee and Schwarcz, 1993, 1994b).

A dislocation is a line defect in which a plane of atoms stops within the crystal producing a line of dangling bonds. The line defects can be generated within quartz

grains during grain boundary frictional sliding at the time of fault movement. The movement of dislocation through a crystal generally takes place at high temperature in deep crustal levels. However, Evans (1988) observed that quartz porphyroclasts within the fault gouge show the undulose extinction and optical mismatches indicative of movement of dislocations (resetting of ESR signals) at brittle deformation environments. The formation of these line defects may increase the radiation sensitivity in quartz at the time of faulting.

Microcracks and grain surfaces are kinds of surface defects created by cataclastic deformation during fault movement. The density of microcracks of fault rocks is bigger than that of host rocks (Blenkinsop and Rutter, 1986). Although some E' centers located at the grain surfaces are not stable at room temperature (Arends et al., 1963), surface defects such as microcracks and grain surfaces can become the precursor of ESR centers. Lee and Schwarcz (1993) showed that shearing of thermally annealed Ottawa sand (no ESR signal) between Westerly granite planes create the precursors of E' centers. Because the stress is concentrated on grain contacts during grain boundary frictional sliding, the density of microcracks tends to be higher near the surface than the center of grains.

Many ESR signals (about 30) have been observed in quartz both at room temperature and at low temperature using liquid nitrogen (Weil, 1984). A few signals from them have been tested for their applicability to the ESR dating of quartz (Garrison et al., 1981, Imai and Shimokawa, 1989, Fukuchi et al., 1986, Buhay et al., 1988). To be useful for dating of fault movement, such a signal must have three important properties;



(1) it must be stable over a geological time scale; (2) it must be sensitive to radiation; and (3) it must be reset by fault movement. I will summarize data regarding those ESR centers which can be used for dating of fault movement in the next sections.

### **2-2-3-1. Intrinsic defect ESR centers**

#### **2-2-3-1-1. E' type centers**

The oxygen vacancy-related defects in  $\text{SiO}_2$  have been designated as E' centers, which include  $E'_1$ ,  $E'_2$ ,  $E'_4$ ,  $E''_1$ ,  $E''_2$  and  $E''_3$ . The single or double primes denote whether there is one or two unpaired electrons ( $S=1/2$  or  $S=1$ ) associated with the center and the subscripts distinguish between various centers having the same spin. The investigation of E' centers began in 1956 by Weeks (1956), who observed intrinsic ESR centers in both crystalline and amorphous neutron-irradiated  $\text{SiO}_2$ . The best known and simplest E' type defects is the  $E'_1$  center. Yip and Fowler (1975) suggested that the  $E'_1$  center is due to a vacancy defect by a O<sup>-</sup> ion missing from a normal bridging oxygen location with consequent relaxation (Fig. 2.4). In crystalline quartz the paramagnetic signal is generated by the trapped electron in the short bonded Si ion that has relaxed towards the oxygen vacancy. The other Si ion has relaxed away from the oxygen vacancy into the plane defined by its three remaining oxygen neighbours (Yip and Fowler, 1975).

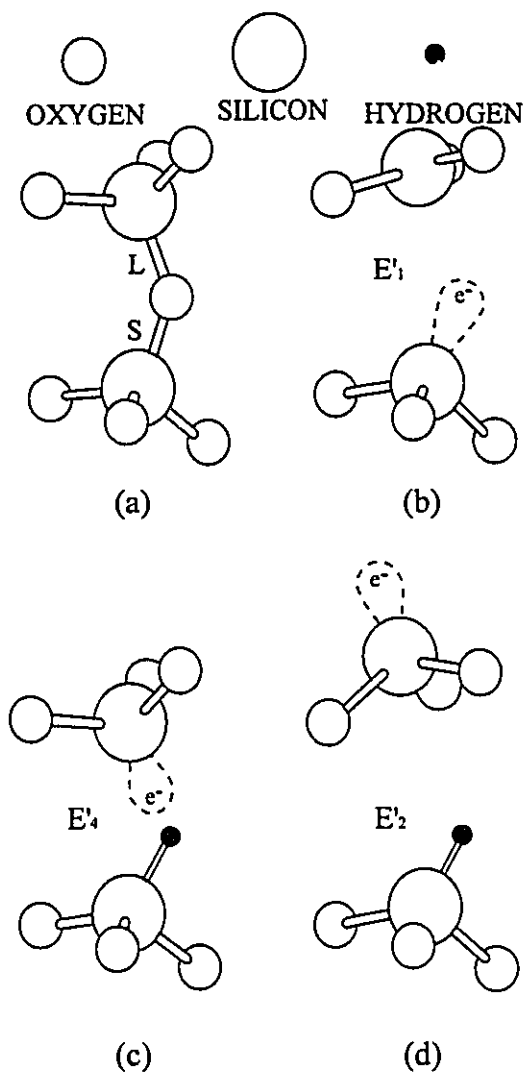


Figure 2.4. Molecular models of the E' center. (a) Fragment of perfect alpha quartz; "L" stands for long bond and "S" for short bond. (b) Model for the E'<sub>1</sub> center. (c) Model for the E'<sub>4</sub> center. (d) Model for the E'<sub>2</sub> center. In b-d. the unpaired electron is shown schematically as e<sup>-</sup> (after Rudra et al., 1985).

This center is created by fast neutron irradiation (Weeks, 1956; Garrison et al., 1981) as well as by electron irradiation (Halliburton, 1985) and gamma ray irradiation at a heavy dose followed by heating at 300 °C (Wieser and Regulla, 1989). The principal g-values measured at 300 °K are 2.00179, 2.00053, and 2.00030 (Jani et al., 1983).

The structure of E'<sub>2</sub> center is similar to the E'<sub>1</sub> center except that the spin has longer residence time on a long-bonded silicon (Rink, 1990). This center is created in the quartz lattice with hydrogen by strong ionizing radiation (Rudra et al., 1985). The observed g-values of E'<sub>2</sub> center measured at both 78 °K and 300 °K are  $g_{\parallel} = 2.0022$  and  $g_{\perp} = 2.0014$  (Weeks, 1963). Rudra et al. (1985) report a c-axis g-value of 2.0005 at 77 °K.

Isoya et al. (1981) shows that the E'<sub>4</sub> structure is a hydrogen ion trapped in an oxygen vacancy with an additional unpaired electron shared unequally by the two silicon ions (Fig. 2.4) neighbouring the vacancy. The E'<sub>4</sub> defects in alpha-quartz appear to be generated by hydrogen atoms diffusing to natural oxygen vacancies (Isoya et al., 1981). The E'<sub>3</sub> center has been observed in neutron-irradiated natural alpha-quartz that resembles the E'<sub>4</sub> center observed in synthetic alpha-quartz (Maschmeyer and Lehmann, 1984). The principal g-values of the E'<sub>4</sub> center observed at 40 °K are 2.00163, 2.00073 and 2.00053, while they are 2.00154, 2.00065 and 2.00060 when observed at 300 °K.

Three of E'' variants in alpha-quartz were first reported by Weeks and Abraham (1965) and later were briefly described by Solntsev et al. (1977). These E'' centers are easily bleached optically, and they become thermally unstable in the 30-100 °C range

(Halliburton, 1985).

For dating of fault rocks, we used the powder pattern spectra of quartz separated from fault rocks. These multi-cycle fault rocks include quartz grains from several types of host rocks with different thermal and deformation histories. Therefore, each quartz grain within fault rocks appears to have its own E' defects in its lattice structure. The typical E' center ( $g = 2.001$ ) in the powder pattern signal of quartz from fault rocks represent the unresolved sum of all of the E'-type centers in the sample. An example of typical E' signal of natural and gamma-ray irradiated quartz separated from fault rocks is shown in figure 2.5.

#### 2-2-3-1-2. Oxygen-hole center (OHC)

Although many researchers used a so-called OHC signal ( $g = 2.011$ ) to date fault movements and volcanic rocks, the configuration of this center is not well understood (Fukuchi et al., 1986; Shimokawa and Imai, 1987; Fukuchi, 1988, 1989; Buhay et al., 1988; Lee and Schwarcz, 1994a and b). Buhay (1986) and Fukuchi (1993) suggested that the OH-center is actually a trapped hole at a silicon vacancy site (Fig. 2.6a). However the interpretation of this signal was recently challenged by Rink and Odom (1991). Because the radiation sensitivity of some fault rocks is bigger than in quartz from the host rocks, the precursors of OHC appear to be created by cataclastic deformation in certain deformation environments at the time of fault movements (Lee and Schwarcz, 1994b).

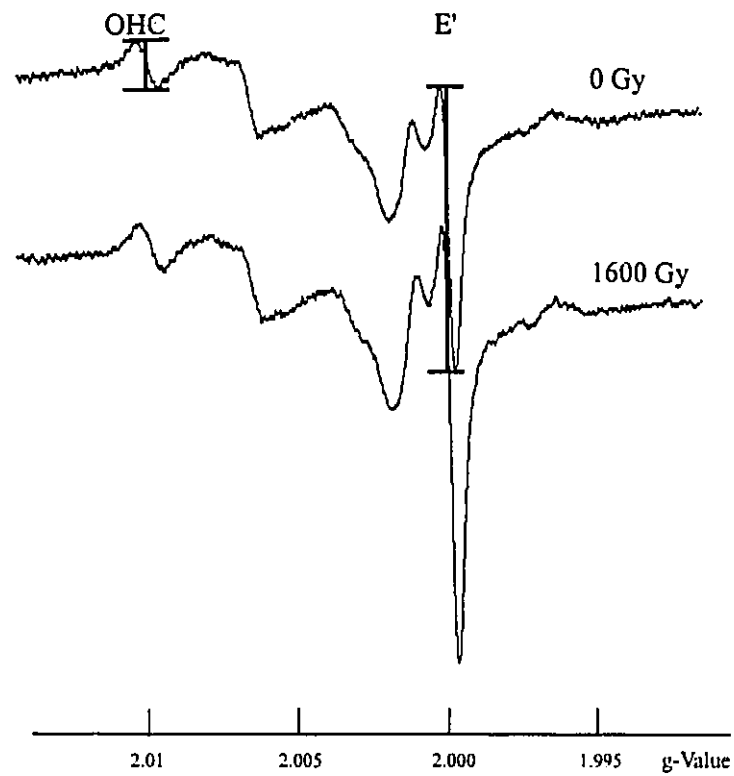


Figure 2.5. An example of typical ESR spectra measured at room temperature of natural and gamma-ray irradiated quartz separated from fault rocks. "I" shows the intensity measured for each ESR center.

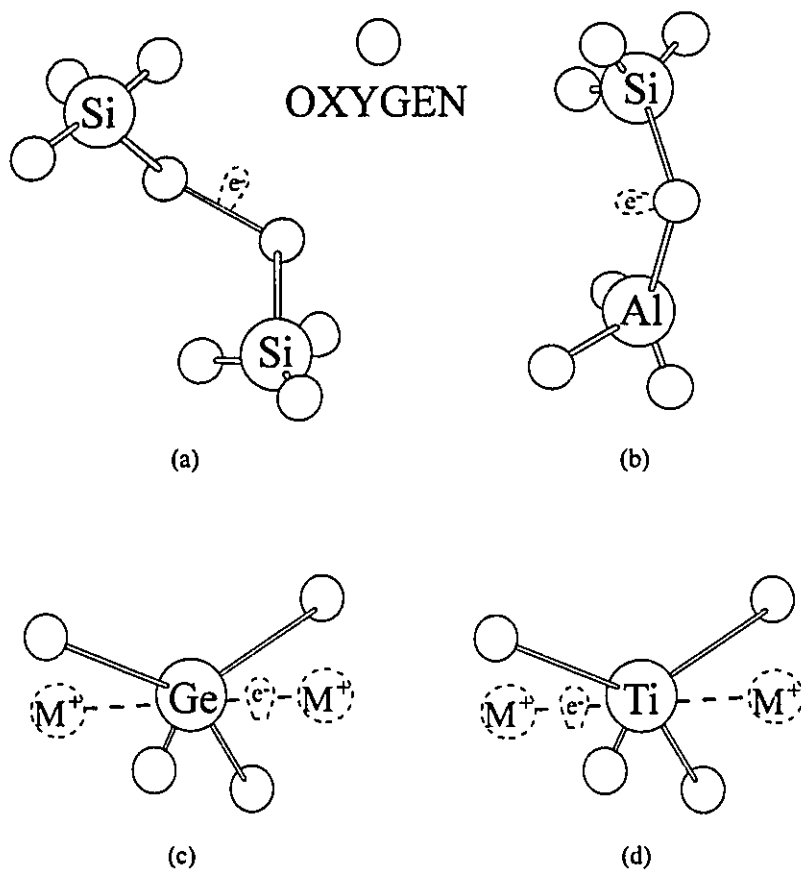


Figure 2.6. Molecular models of a) OHC , b) Al, c) Ge, and d) Ti centers (after Buhay, 1987).

There are some possibilities of conversion of precursors of vacancy type ESR centers by cataclastic lattice deformation of quartz grains during fault movement. An example of a typical OHC signal measured at room temperature is shown in figure 2.5.

### 2-2-3-2. Extrinsic defect (impurity) ESR centers

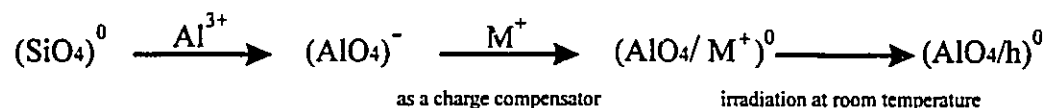
The extrinsic ESR centers of alpha quartz are formed by substitutional ions in silicon sites. The substitutional impurity ions in quartz include Al, Ge, Ti ions generating Al, Ge, and Ti centers.

#### 2-2-3-2-1. The Al center

Trivalent aluminum ions substituting at silicon sites generate the aluminum hole center (Fig 2.6b). Aluminum charge compensators ( $H^+$ ,  $Li^+$ ,  $Na^+$ ) are normally located within the large channels that extend along the c-axis direction and serve to provide overall neutrality at the nearby Al tetrahedral sites. These give rise to either  $[AlO_4/H^+]^0$ ,  $[AlO_4/Li^+]^0$  or  $[AlO_4/Na^+]^0$  centers (Halliburton, 1985).

Ionizing radiation removes one of the electrons in a non-bonding oxygen p orbital of  $[AlO_4/M^+]^0$ , where  $M^+$  represents either  $Li^+$  or  $Na^+$  ions and thus one of the oxygen anions becomes an atom with a hole in its valence shell. The aluminum charge compensators would then diffuse away leading to  $[AlO_4/h]^0$ , where h is a hole trapped in

a non-bonding 2p orbital of oxygen located adjacent to the substitutional aluminum (Hitt and Martin, 1983). This is schematically shown below:



The new defect,  $[\text{AlO}_4/\text{h}]^0$ , has an unpaired electron on the oxygen (Fig. 2.6), thus making the  $[\text{AlO}_4/\text{h}]^0$  center easily detected with ESR upon cooling of the sample to below 100 °K.

Typical ESR spectra of the Al center for quartz at 113 °K are shown in figure 2.7. Hyperfine structure is observed due to interaction of the hole with the  $^{27}\text{Al}$  nucleus ( $I=5/2$ , 100 % abundance) (Weil, 1984). The quartz grains separated from fault rocks show variations in the Al spectra, which appear to be caused by different source rocks and deformation environments such as composition of pore fluid, temperature, displacement rate and tectonic stress. During grain boundary frictional sliding, microcracks develop near the surface of quartz grains resulting in the generation of paths of diffusion of Al ions from the pore fluid into the quartz grains. Fracturing of grains can also increase the diffusion rate due to the greater grain surfaces. Local frictional heating at grain/grain contacts can also increase the diffusion rate. The diffusion of Al ions from pore fluid into the quartz grains appears to increase the number of the precursors of the Al center leading to the increase of radiation sensitivity with decreasing grain size, as for E' signals.



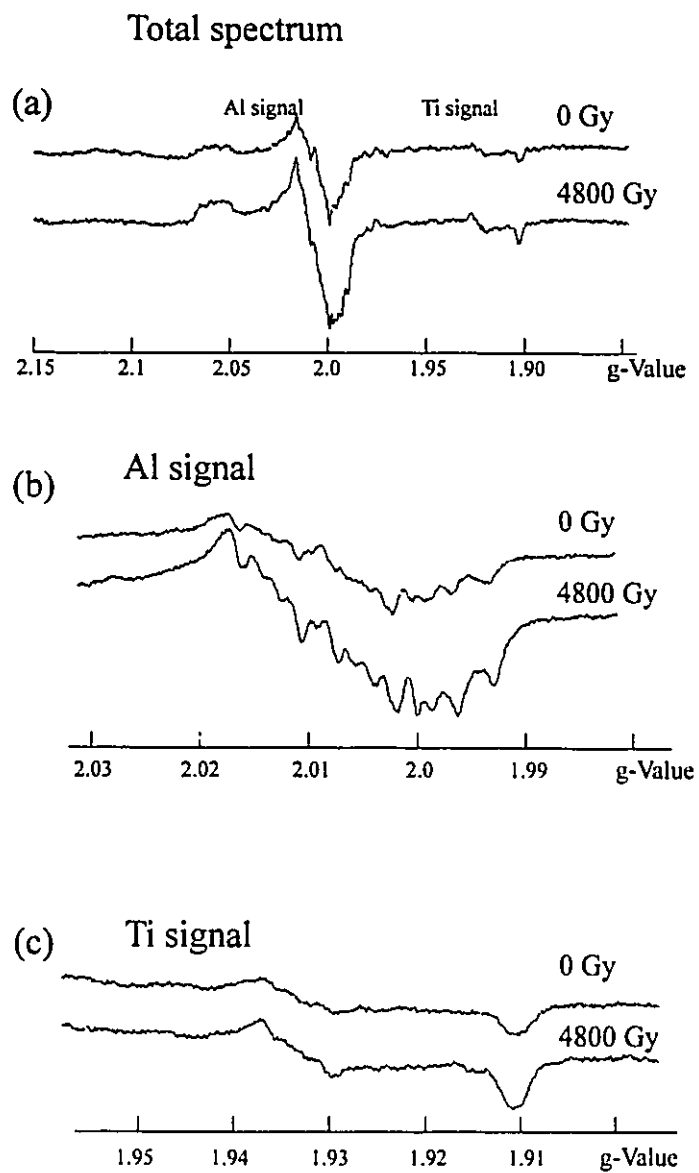
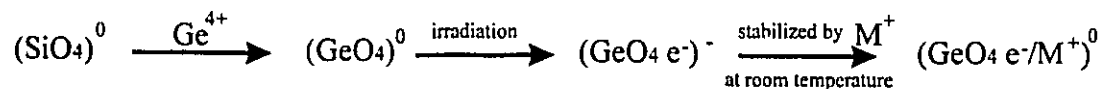


Figure 2.7. Typical ESR spectra measured at about 113 °K. (a) total spectra; (b) detail of Al peak, showing hyperfine splitting of peak; (c) detail of Ti signal.

### 2-2-3-2-2. The Ge centers

The Germanium electron centers are generated by the substitution of  $\text{Ge}^{4+}$  in the tetrahedral Si site (Fig 2.6c). The precursors of Ge centers are symbolized with the nomenclature  $[\text{GeO}_4]^0$  but electronic affinity (ionization potential) is considerably larger, resulting in trapping of an electron generated by ionizing irradiation to form  $[\text{GeO}_4 \text{e}^-]$  in the  $\text{SiO}_2$  lattice. These  $[\text{GeO}_4 \text{e}^-]$  centers are unstable at room temperature and become stable form  $[\text{GeO}_4 \text{e}^-/\text{M}^+]^0$  at room temperature by the charge compensators ( $\text{M}^+$ ) such as  $\text{H}^+$ ,  $\text{Li}^+$ , or  $\text{Na}^+$  (Anderson et al., 1974). The process is schematically shown below:



There have been many type of germanium centers reported (Weil, 1984). According to Rakov et al. (1986) the  $[\text{GeO}_4 \text{e}^-/\text{M}^+]^0$  centers accounts for 70-80% of the Ge center concentration.

Several researchers have been used Ge signal to date fault movement (Fukuchi et al, 1986; Ito and Sawada, 1985). Buhay (1986) showed that the intensity of Ge signal was decreased by UV-light and direct sunlight. In this study, because most of the fault rock samples are collected from outcrop surface in which the Ge signal was zeroed, I did not use the Ge signal to date fault movement.

### 2-2-3-2-3. The Ti centers

The Ti centers are formed by substitution of  $\text{Ti}^{4+}$  in the quartz lattice for  $\text{Si}^{4+}$  and the formation mechanism is the same as the Ge center (Fig 2.6d). The precursor state  $[\text{TiO}_4]^0$  captures an electron to form the paramagnetic Ti center  $[\text{TiO}_4]^-$ , which promptly decays at temperatures above  $20^\circ \text{K}$  (Isoya and Weil, 1979). Diffusion of charge compensator ions ( $\text{H}^+$ ,  $\text{Li}^+$ , or  $\text{Na}^+$ ) into interstitial sites makes stable paramagnetic centers,  $[\text{TiO}_4/\text{M}^+]^0$ . Because (1) during shearing experiment, the intensity is unchanged or actually increased (Lee and Schwarcz, 1993), (2) the Ti center underwent the least zeroing in the simple compression test (Buhay, 1987), (3) it showed no consistent trend in age with grain size for quartz separated from fault gouge (Buhay, 1987), (4) it has low closure temperature ( $31^\circ \text{C}$ ) leading to the lower ESR age limit (Toyoda and Ikeya, 1991), it appears that the Ti center is not suitable for ESR plateau dating of fault rocks. The Ti center, although present in some samples, was not used for  $D_E$  determination for the fault rocks in this study.

### 2-2-3-3. Thermal stability of ESR signals

Thermal stabilities of E', OHC, Ge, Al, and Ti centers have been studied by thermal annealing experiment (Shimokawa and Imai, 1986; Fukuchi et al., 1986; Toyoda and Ikeya, 1991). These authors have investigated the variations of ESR intensities as a

function of temperature. Up to 200 °C all signals remained unchanged, but at higher temperature, the intensities of the E' and Al centers was decreased much faster than those of OHC, Ge, and Ti centres. The Ge is the most stable center among these signals, followed by the OHC, Ti, Al, and E'centres (Fig. 2.8). The mean lifetimes of these centres have been obtained from isothermal annealing experiments using the Arrhenius plot (Shimokawa and Imai, 1986; Toyoda and Ikeya, 1991). The mean life at room temperature of the five centres in quartz grains are given below with their respective references:

Center	Mean-life (a)	Reference
Al	$2.4 \times 10^6$	Shimokawa and Imai (1987)
Ge	$3.1 \times 10^7$	Shimokawa and Imai (1987)
Ti	$8.0 \times 10^6$	Toyoda and Ikeya (1991)
E' <sub>1</sub>	$3.6 \times 10^{11}$	Toyoda and Ikeya (1991)
OH	$3.4 \times 10^9$	Shimokawa and Imai (1987)

Toyoda and Ikeya (1991) estimated closure temperatures of 91 °C, 78 °C, and 31 °C for E', Al and Ti centers respectively at a cooling rate of 10 °C/Ma. The closure temperature is defined here to be the temperature above which the ESR signals are quickly zeroed by the thermal release of ESR centers. Because the trapped electrons or holes are released at high temperatures leading to younger ages on old, deep fault rocks, we can not date the fault movement using ESR method.

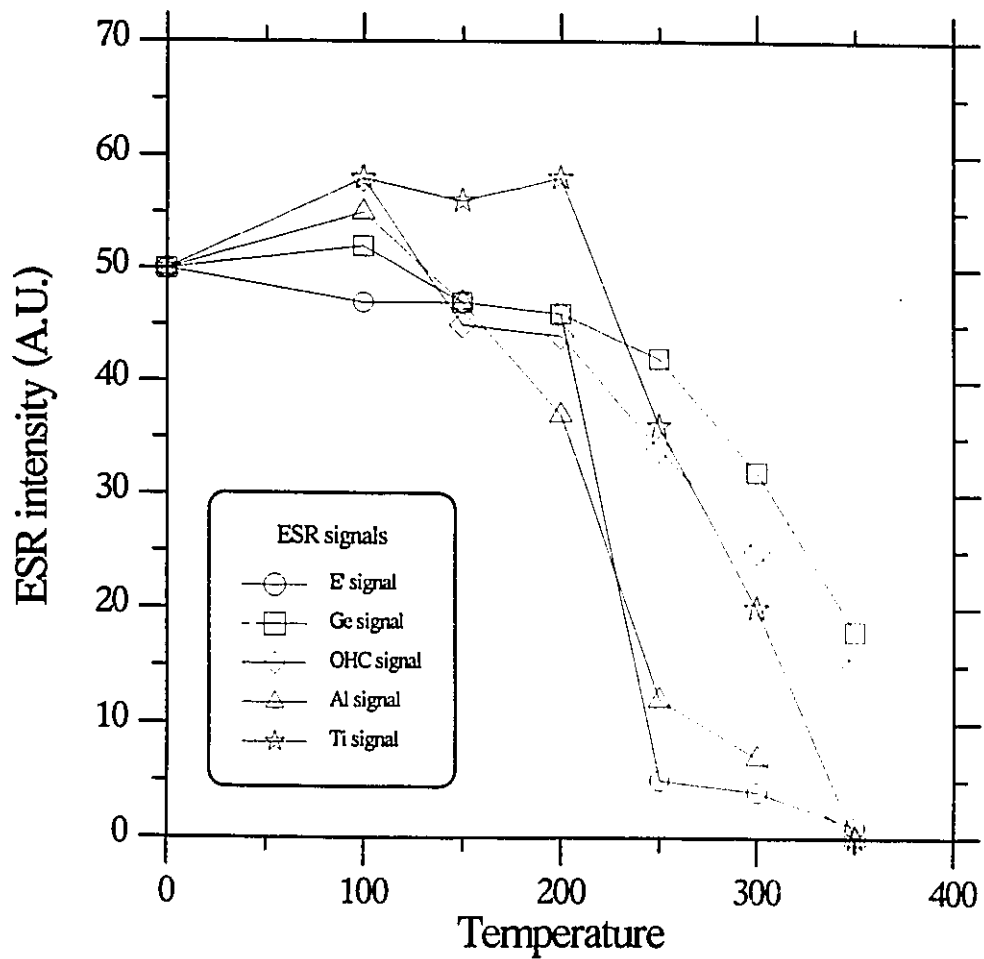


Figure 2.8. Thermal annealing of ESR centers in quartz. Data from Fukuchi et al. (1986) and Shimokawa et al. (1988).

#### **2-2-3-4. Irradiation sensitivity**

E', OHC, Ge centers observed at room temperature, and Al, Ti centres observed at low temperature all showed intensities which increased with irradiation by gamma-rays. The intensities of the peroxy centres were increased by the neutron bombardment while they did not change by gamma-ray irradiation (Odom and Rink, 1988). The radiation sensitivity of the E', OHC and Al centres are increased by fault movement due to generation of precursors of paramagnetic centres (Fukuchi, 1989, Lee and Schwarcz, 1994b). According to Odom and Rink (1988), Schottky-Frenkel defects are produced by elastic collisions initiated by the recoil of alpha-emitting nuclides. Using gamma-ray irradiation, the OHC, Ge, E', Ti, and Al centres can be used for ESR dating method. The peroxy centres can be used for dating on a  $10^8$  time scale by neutron irradiation or alpha-recoil, but are not useful for fault dating.

#### **2-2-3-5. Resetting of ESR signals**

As mentioned previous (2-2-3-3), all the signals are reset at high temperatures. Quartz from volcanic rocks would be formed in a completely zeroed state. Archaeological flint can be reset by heating by ancient peoples.

Some experiments on the effects of confining stress on ESR signals in quartz have been conducted. ESR signals did not reset completely by uniaxial compressive stress

(Buhay, 1987; Fukuchi, 1989). Meanwhile shearing experiments have shown that E', Ge, and Al centres can be reset completely at high shear strain at near-surface faulting condition (Ariyama, 1985). Some possible zeroing mechanisms of the ESR signals at the time of fault movement will be described in Chapter 4.

According to Buhay (1987), the Ge centre can be reset completely by sunlight exposure. Therefore the Ge centre can be used for the dating of sediment bleached by sunlight.

#### **2-2-4. Time range of applicability**

The total time range of the method is from a few hundred years to a few million years. The actual range (both upper and lower limits) depends on a number of factors:

a) ESR dating of a fault rock only shows the time of last movement in that rock. ESR signals stored after prior events are all erased by the most recent event. On faults with high recurrence rates signals are reset frequently and the probability of seeing very old events is small. However, we find that on major faults, different parts of the fault are reset at different times (due to uneven distribution of strain), and it is possible to recover dates back to > 1 Ma, and also to obtain samples which show faulting events over a wide time range. Also, due to transpression associated with the main fault, adjacent smaller faults share the activity history of the main fault. Therefore it is usually possible to construct a long-term history as long as more than one exposure or core can be sampled.

b) In areas of tectonic uplift, the minimum age obtainable from surface exposures of fault rocks is determined by the uplift rate; the faster the rate, the younger the events that can be determined; typically, the minimum determinable age would be 10-50 ka.

c) By use of drill core, it should be possible to obtain samples whose ESR signals were reset within the last decade or less. However, the minimum age in such samples is determined by the sensitivity of the ESR spectrometer (signal to noise ratio), and in effect by the rate of post-faulting growth of the ESR signal. This in turn depends on the radiation dose rate and the sensitivity of the ESR signal. Sensitivity increases with each successive cycle of faulting and zeroing, and is highest in re-activated parts of older fault zones. Using the E' signal at optimum sensitivity in an environment of normal radioactivity, we believe that we can record fault events a few hundred years in age, with a precision of about 10 %.

d) The upper limit of dating in areas of slow uplift is set by the rate of thermal annealing of ESR signals in samples which have been "stored" at higher temperatures deep in the earth. At  $T > 100$  °C, the lifetime of the main ESR signals is significantly decreased (Toyoda and Ikeya, 1991). The cutoff here depends on the uplift rate, the local temperature gradient, saturation dose and dose rate but in general would be several millions years.



## **Chapter 3**

### **Method of ESR dating of fault rocks**

The procedure of ESR dating of fault rocks is shown in figure 3.1. Basically, the procedure consists of three phases: a) collection of fault rock samples; b) determination of equivalent dose ( $D_E$ ) by the additive dose method; c) determination of the dose rate (d) by analysis of U, Th and K. The object of this chapter is to describe a method of ESR plateau dating which is efficient and reasonable.

#### **3-1. Field techniques and collection samples**

This section describes the field techniques and collection of fault rock samples from fault zones. It is essential to record all the information from observation and measurements of all structural elements. Since ESR dating method is based on the zeroing of ESR signals at certain deformation conditions (displacement and stress), the deducing of deformation environment at the time of fault movement is essential for ESR dating of fault movement.

The first step of field work in the fault zone is to recognize the fault surfaces or

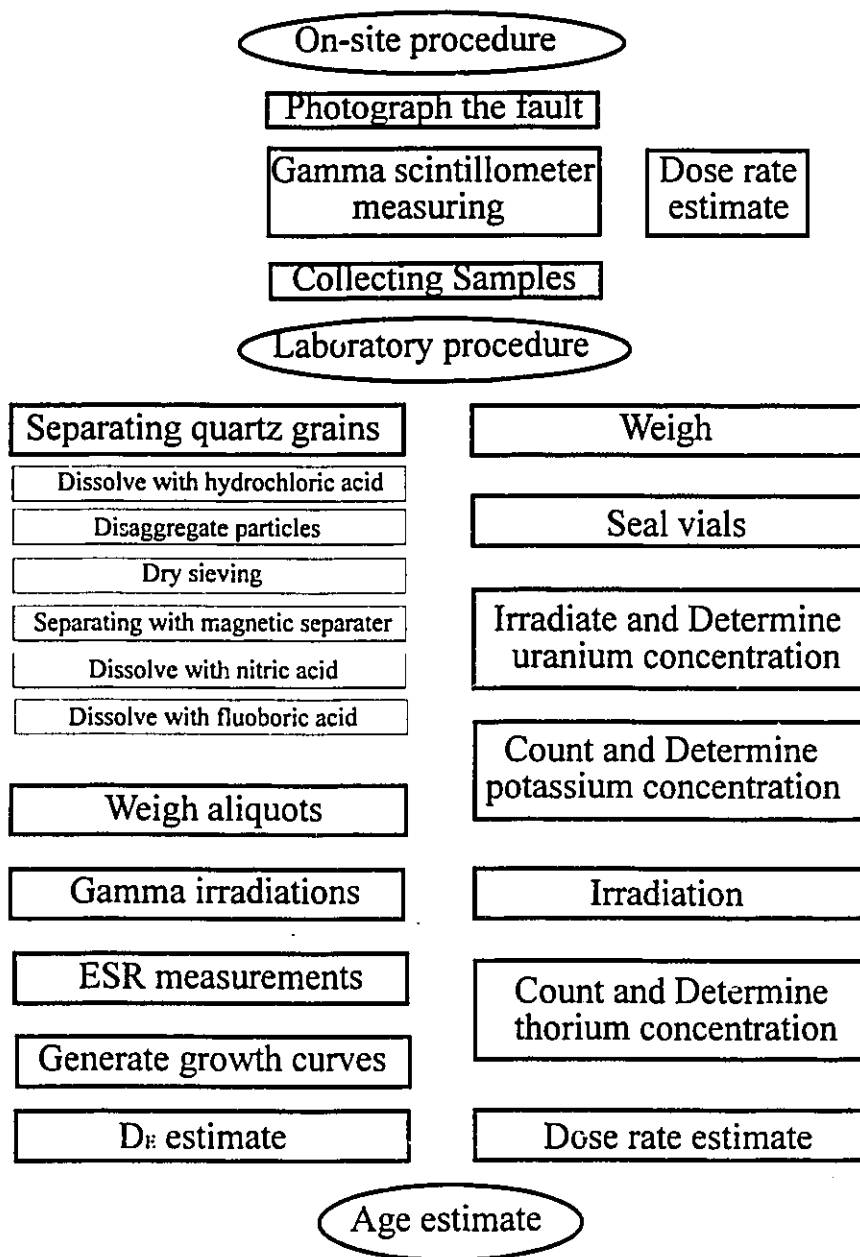


Figure 3.1. Procedures of ESR dating of fault rocks.

fault rock zones. The offset of planar structure such as bedding, foliation and unconformity surfaces simplifies the search for fault contacts. Sometimes fault rocks are developed between fault surfaces.

The faults are classified into three categories (normal, reverse or thrust, and strike-slip faults) based on the sense of movement and direction of slip across the fault plane. Since the normal stress on the fault plane is dependent on these fault types at a given stress field and is one of most important factors in resetting of ESR signals, it is important to recognize and describe the fault type in the field. Structural features developed on the fault plane or within the fault rock zones can be used to decide the sense and direction of movement. The methods to deduce of the sense of movement have been described by several reseachers on fault surfaces (Tjia, 1967; Fleuty, 1975; Means, 1987; Petit, 1987; Twiss and Gefell, 1990) and within fault rock zones (Simpson and Schmid, 1983; Rutter et al., 1986). The microtextures can also be used to determine the sense of movement.

The field relations of the fault zones should be studied carefully to determine the sequence of motions on each break, and to identify zones of reactivation and relationships between faults. Data to be collected from a fault zone are shown in table 3.1.

Before collecting the fault rocks, the sample site should be photographed with a scale, to give some indication as to the distance over which the radiation field was uniform. Because severe crushing can affect the ESR signals and also destroy the original grain size distribution, needed to determine the ESR plateau age, samples for ESR dating

Table 3.1. Data to be collected from a fault zone.

Structure	Measurement	Observation	Analysis
Fault Plane	Orientation of fault plane.	Nature of fault plane: curvature of fault plane.	Deformation process; extension or contraction.
	Lineations on fault plane: grooving, slickenlines etc.	Nature of lineations on fault plane. Movement sense.	Displacement direction.
Foot-wall and Hanging-wall	Orientation of displaced units on both sides of fault.	Cross-cutting relationships. Associated folding.	Amount of offset.
	Orientation data on subsidiary faults and fractures.	Cross-cutting relationships. Movement directions.	Fault sequences. Movement pattern. Fault system. Kinematic development.
Fault rock zone	Orientation data on structural elements developed within fault rock zone.	Types of fault rocks. Width of fault rock zone. Reactivated zone or new fault rock zone. Materials formed in the fault rock zone: quartz or calcite vein.	Movement pattern. Pattern of fault dynamics; strain softening or hardening. Fault movement history (ESR age).

should be collected from unindurated fault rock and weathered fault rocks or host rocks. Several subsamples along and across the fault rock zone have to be collected to check the consistency of the ESR plateau age. Each sample is placed in a labelled, water-tight sample container (e.g., zip-lock plastic bag additionally sealed with tape). The sample is protected from crushing, to preserve its internal water content, which will be determined in the laboratory. Ideally, samples containing 10 g or more of quartz are needed for the ESR analysis, although dates can be obtained on samples of quartz as small as 1 g. Whole-rock sample sizes should be adjusted accordingly, from knowledge of the source rock and its bulk quartz content.

The radiation dose rate will be determined from analyses of the wall rocks as well as the fault rock sample itself. Samples of 20-50 g of both adjacent wall-rocks are collected and also stored in water-tight containers. Where the ESR samples are taken from the centers of a very thick fault zone (>0.5 m thick) only samples of fault rock itself are needed, since the range of the most penetrating radiation (gamma rays) is < 30 cm.

Samples for analysis of microtextures have to be collected at fresh outcrops nearest to the sampling site for ESR dating. Friable samples should be put into a plastic bag with a small quantity of epoxy resin. For foliated fault rocks, oriented samples should be collected to study microstructures developed at the time of fault movement.

Care should be taken to prevent friable gouge samples from becoming disaggregated before arriving in the laboratory. Also, the water-tight seals on the sample bags should be guarded against leaks.

### 3-2. Sample preparation and measurement of ESR signals

In the laboratory, water content was determined as soon as possible (this influences dose rates). Very gentle disaggregation is required to prevent the generation of precursors of ESR centers and the change of the distribution of grain size which is related to the ESR plateau age. If the sample is very friable (weathered fault rocks), crushing is not needed. If the sample for estimation of dose rate is large and hard (host rocks), we first crush it with a hammer to reduce it to pieces 0.5 cm and smaller. For fault rock samples and weathered host rocks, gentle crushing is performed using mortar and pestle. After disaggregation of the sample, two subsamples are prepared for determination of equivalent dose and dose rate, respectively.

In order to determine the equivalent dose, disaggregated samples were washed in concentrated HCl (12 M) for two hours to dissolve any carbonate matrix. Then, the gouge samples were dry sieved to separate grains of  $< 425 \mu\text{m}$ . The non-magnetic fraction of the sample (quartz+feldspar) was separated using a Frantz isodynamic separator. Each grain size fraction was attacked with fluoboric acid ( $\text{HBF}_4$ , 1M) and  $\text{HNO}_3$  at room temperature for 1 hour each in order to dissolve feldspar and organic materials. All separations, particularly for grains smaller than  $75 \mu\text{m}$ , were repeated to improve the isolation of quartz grains from other materials.

Seven to twelve aliquots of 100 mg for each size fraction ( $<45$ , 45-75, 75-100, 100-150, 150-250, 250-425  $\mu\text{m}$ ) were weighed. Aliquots of each grain size (100 mg) were

irradiated with a  $^{60}\text{Co}$ -source in 4 mm outer diameter glass tubes with 0.9 mm thick walls. Aliquots were placed equidistant from the source and dose was controlled by exposure time. Dose received by the aliquots was determined by a portable dosimeter placed beside the samples during irradiation. The gamma dose rate was 0.23 Gy/s or 0.04 Gy/s.

The ESR spectra were measured on a Bruker ER100D ESR spectrometer with a TE4101 cavity. The quartz sample tube was placed in the NMR tube, beside a standard of  $\text{Mn}^{2+}$  dispersed in MgO powder. The spectra were recorded on a computer using EPR Data Acquisition System version 2.41 (Morse, 1987). In order to increase the signal-to-noise ratio, each aliquot was scanned 3-6 times and averaged automatically on a computer. The OHC and E' signals (at g value 2.011, 2.001, respectively) were obtained at room temperature. Instrumental settings for these centers were: microwave frequency = 9.436 GHz; microwave power = 0.3 mW; scan width = 4-6 mT; scan time = 50-100 s; modulation frequency = 100 kHz; modulation amplitude = 0.1-0.32 mT; and time constant = 0.05-0.2 s. The Al spectra can only be obtained at lower temperatures (here 113 °K) due to short spin relaxation times at room temperature. For the Al spectra, the microwave power = 2 mW, scan width = 10 mT, scan time = 100 s, modulation amplitude = 0.1-0.32 mT, time constant = 0.2 s, and the other settings were the same as the room temperature measurements. The ESR intensities were measured by the cursor on the data acquisition program (Fig. 2.5). For the Al signal, other researchers measured from the highest point on line 1 to the lowest point of line 14 (Buhay, 1987; Porat and Schwarcz 1991; Yokoyama, et al., 1985). Some samples have a very strong component

from line 6 to 9 (Fig. 3.2), and this component may overlap a peroxy signal (Lee and Schwarcz, 1993). Because this component would not grow by  $\gamma$ -ray irradiation, this would affect the determination of ESR intensity and  $D_E$ . In order to avoid this, I measured from the top point of line 1 to bottom point of line 4 (Fig. 3.2).

### 3-3. Determination of equivalent dose ( $D_E$ )

Because we can not determine the ESR age using the ESR intensity itself, it should be converted to the accumulated energy form (unit; Gy). The equivalent dose ( $D_E$ ) can be determined by the additive dose method in which the ESR intensity of a sample is measured in a number of sample aliquots irradiated progressively with gamma rays. The back-extrapolation to zero ESR intensity is the dose of radiation equivalent to that which the sample received as a result of environmental radiation since the sample was last zeroed (Fig. 2.3).

One factor relevant to the reliability of dates obtained is the precise estimation of equivalent dose. Several researchers showed that some instrumental settings affect the determination of  $D_E$ . For example, increase in microwave power tends to increase  $D_E$  values for coral and stalagmite samples (Renyou et al., 1989). They suggest that  $D_E$  values equivalent to 0 mW of microwave power is close to the true value, since the influence of microwave power to  $D_E$  increases with increasing microwave power. On the contrary, Lyons et al. (1988) suggest that  $D_E$  obtained on stalagmitic calcite using high



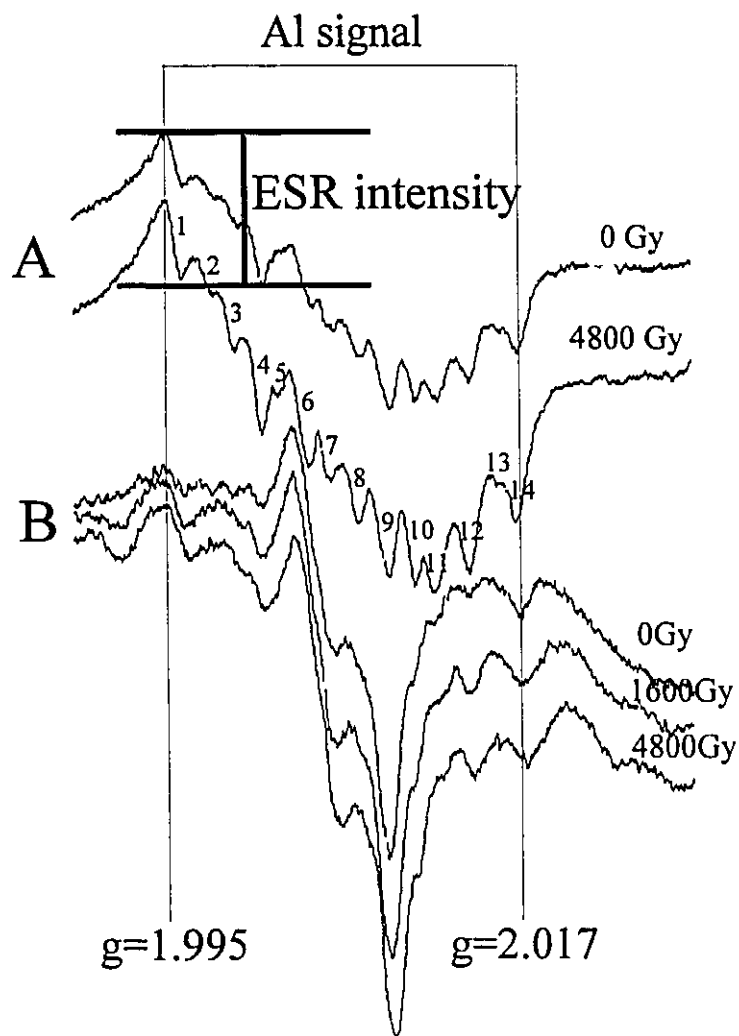


Figure 3.2. Details of Al signal spectra obtained at low temperature (here, 113 °K). The B spectra are amplified by a factor 1.6. Some quartz (B) shows strong component from line 6 to line 9. Sample A (91004) collected from the Limerock fault, and sample B (91071) collected from Santa Clara Divide fault.

microwave power is the best estimates of  $D_E$ , since interference by short-lived peaks is proportionate. Grün et al. (1987) tested the variations of  $D_E$  for tooth enamel with modulation amplitudes. They observed that the values of  $D_E$  were consistent in the range of 0.25-1 mT, but the  $D_E$  obtained by 0.01 mT of modulation amplitude was smaller due to low signal-to-noise ratio. They also tested the variation of  $D_E$  with dose rate of artificial gamma irradiation, grain size of sample, sample weight and microwave power and observed the independence of  $D_E$  for measurement settings and sample preparation of tooth enamel.

The intensity of E' signals for quartz increase with microwave power up to 0.01-0.1 mW and then decrease again with microwave power due to saturation effects (Toyoda, 1992). Measurement settings do not cause any variations in the estimated equivalent doses from quartz grains separated from fault rocks. The modulation amplitude is inversely related to the resolution of the spectra into its component. This is illustrated in figure 3.3. E' signals can be separated into  $g=2.0018$  and  $g=2.0005$  components with lower modulation amplitude (0.1 or 0.2 mT). I used the  $g=2.0005$  component to measure ESR intensities for lower modulation amplitude. For modulation amplitude of 0.32 mT, the combined E' signal ( $g=2.001$ ) was used to measure ESR intensities. For examples, the equivalent doses determined for AECL3E (0.045-0.075 mm) and AECL4F (< 0.045 mm) are shown in figure 3.4. There were no big differences in equivalent doses in both samples. The errors are smaller for larger modulation amplitude, probably, due to larger signal/noise ratio. However, the error can be decreased by measuring with smaller scan

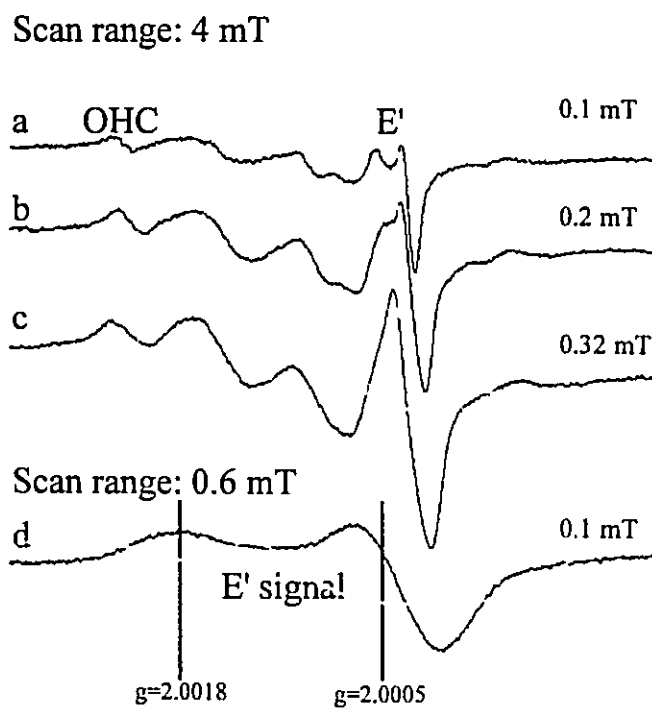


Figure 3.3. ESR spectra for different measurement settings.

a: measured at modulation amplitude of 0.1 mT and scan range of 4 mT.

b: measured at modulation amplitude of 0.2 mT and scan range of 4 mT.

c: measured at modulation amplitude of 0.32 mT and scan range of 4 mT.

d: measured at modulation amplitude of 0.1 mT and scan range of 0.6 mT.

range, because signal/noise ratio is increased by smoothing of the spectra in the range of signal (Fig. 3.3d and 3.4).

### 3-3-1. Recognition of saturated samples

Artificial gamma dose response of saturated quartz such as in host rocks or larger grain size fractions of gouge can be divided into four groups based on characteristic variation of intensities with added dose; a) consistent ESR intensity, b) increase of ESR intensity, c) decrease of ESR intensity, d) fluctuation of ESR intensity.

Quartz from the host rocks and saturated larger size fractions show generally constant ESR intensity with added dose, which was used to show the difference between host rocks and fault gouge in the early stage of ESR dating of fault rocks (Ikeya et al. 1982). Old fault gouges saturated by the natural environmental radiation show constant intensities with added dose even for the smallest size fraction (Fig. 3.5).

Some host rocks show consistent intensity for E' and OHC up to 400 Gy in which the intensity increase abruptly and then show consistent intensity repeatedly resulting in stepwise growth of ESR intensity (Fig. 3.6). Rink and Odom (1991) observed also the increase (1.9×) of intensity of E' signal of granitic rocks with 4400 Gy of gamma ray.

The intensity of E' and peroxy signals of granitic quartz show decreases with added dose up to 400 Gy, apparently indicating complete saturation of their respective paramagnetic states before irradiation (Rink and Odom, 1991). Quartz separated from

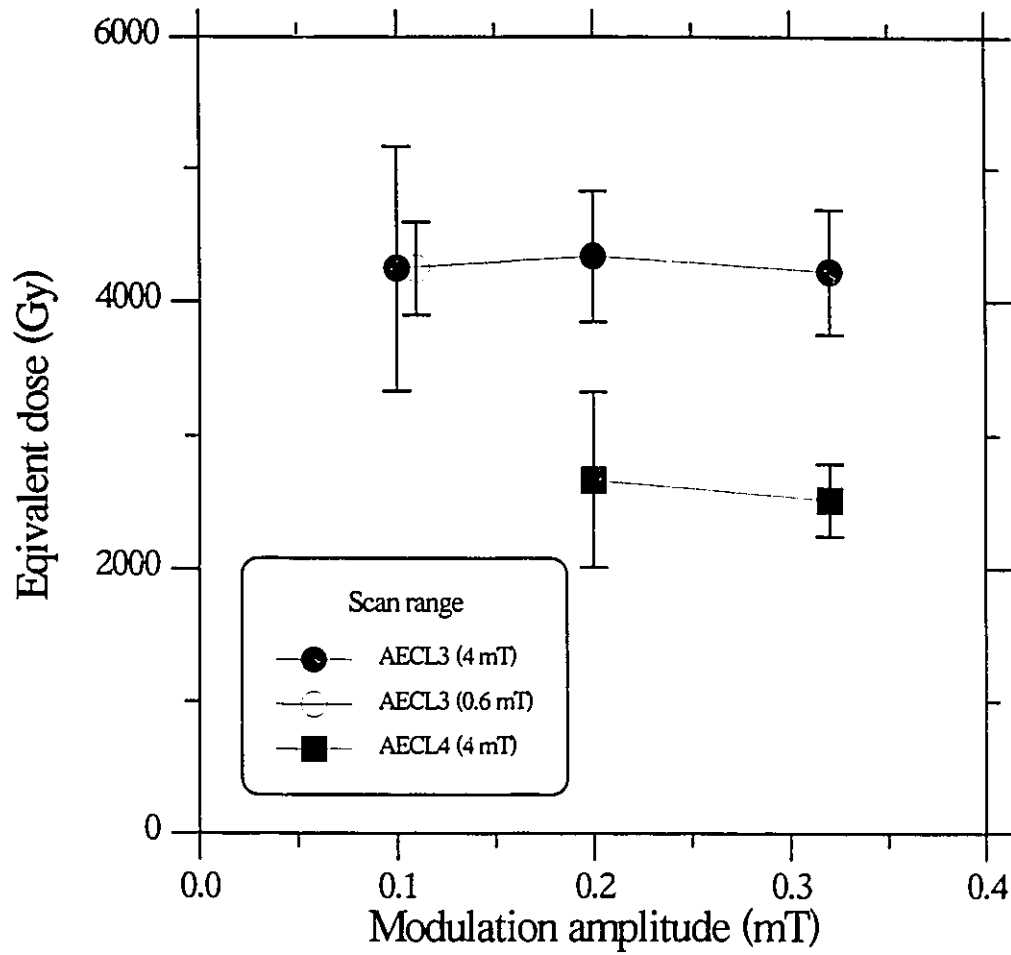


Figure 3.4. Equivalent doses vs. Modulation amplitude for AECL3 and AECL4.

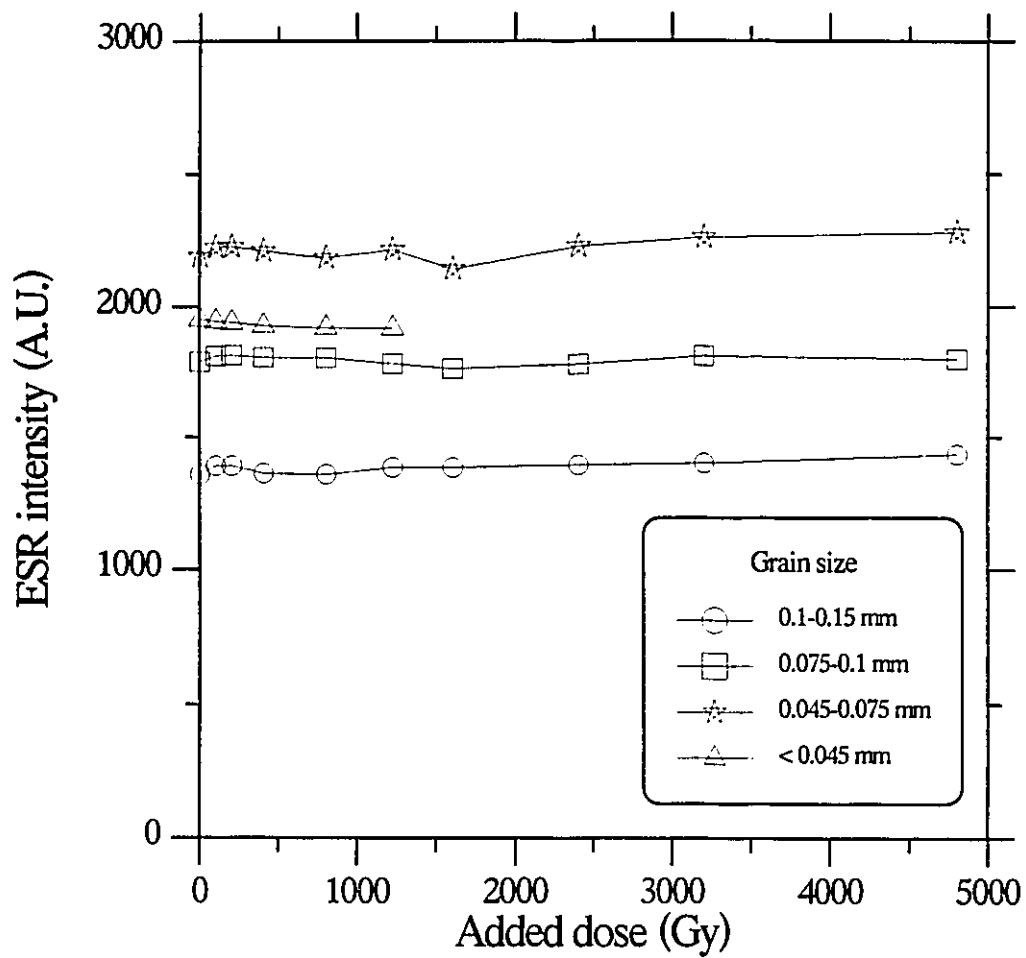


Figure 3.5. An example of dose response curves of a saturated sample. The intensities for E' signals of quartz from AECL2 are constant with added dose due to the saturation.

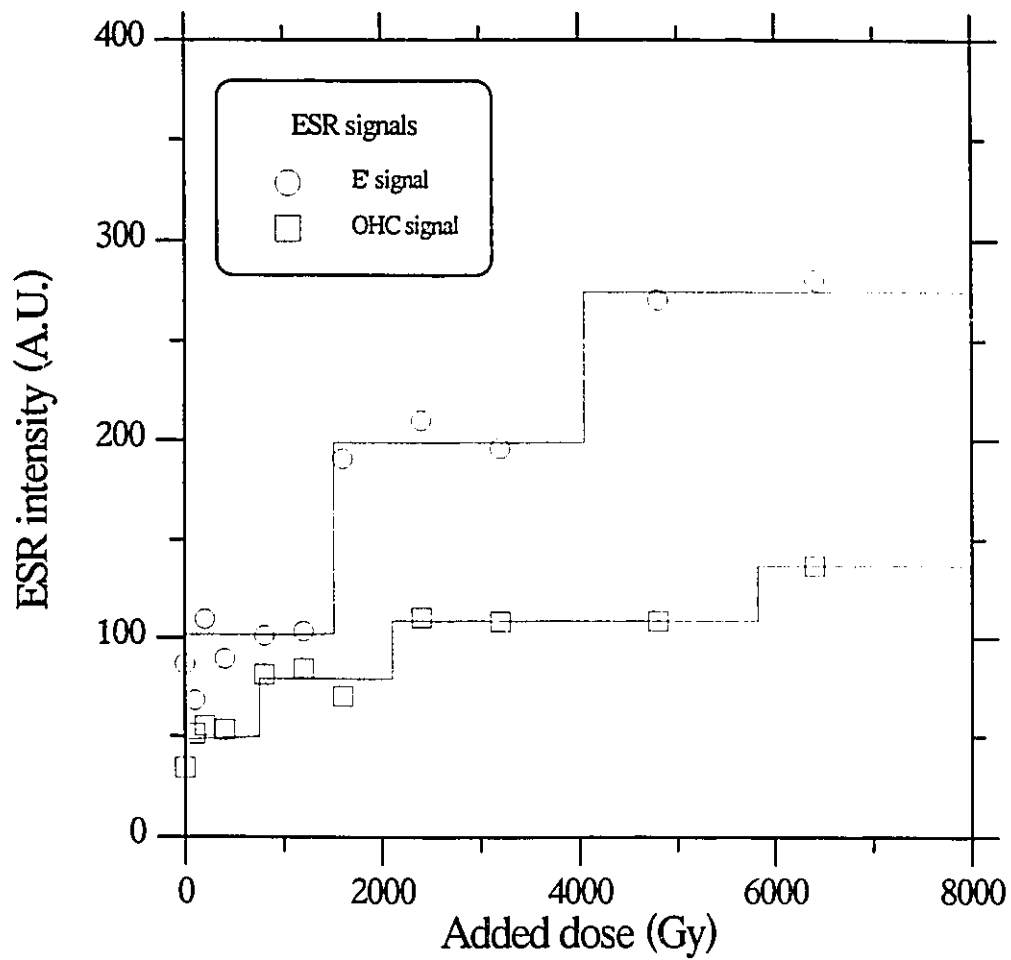


Figure 3.6. An example of dose response curves of a saturated sample. The intensities for both E' and OHC signals of quartz from gneiss (SG20) show stepwise increases in intensities with added dose.

saturated fault rocks also decrease up to 1200 Gy for all size fractions and then increase again slightly up to 4800 Gy (Fig.3.7).

Most of large size fractions of quartz which are supposed to be in saturation or steady state show fluctuation of ESR intensity with added dose (Fig. 3.8).

In summary, even though the intensities of saturated samples show various behaviors with added dose, they do not grow systematically along a single saturating exponential function curve with added dose (compare Fig. 3.5, 3.6, 3.7, and 3.8 with Fig. 2.3). These observations suggest that some ESR centers are not stable with respect to strong gamma ray irradiations and that some ESR centers are generated after saturation of given empty centers (precursors) by strong gamma ray irradiation. Before saturation, gamma-ray irradiation is mostly used to increase the number of certain ESR centers. On the other hand, after saturation, gamma ray appears to ionize the ESR centers themselves, that is, electrons or holes are detrapped from ESR centers. Another possibility is that the rate of increase of the number of ESR centers is much higher than the rate of detrapping of electrons or holes by gamma ray irradiation before saturation. These variations of behavior of ESR signals with artificial added dose appear to be caused by the different number of precursors of ESR centers generated during various thermal, metamorphic and deformation history of host rocks. Rink et al. (1993) showed also variations in thermoluminescence spectra for different types of geological quartz.

In a natural environment, since the dose rate is much lower, and detrapping of electrons and holes occur by thermal release, most host rocks or old fault rocks appear



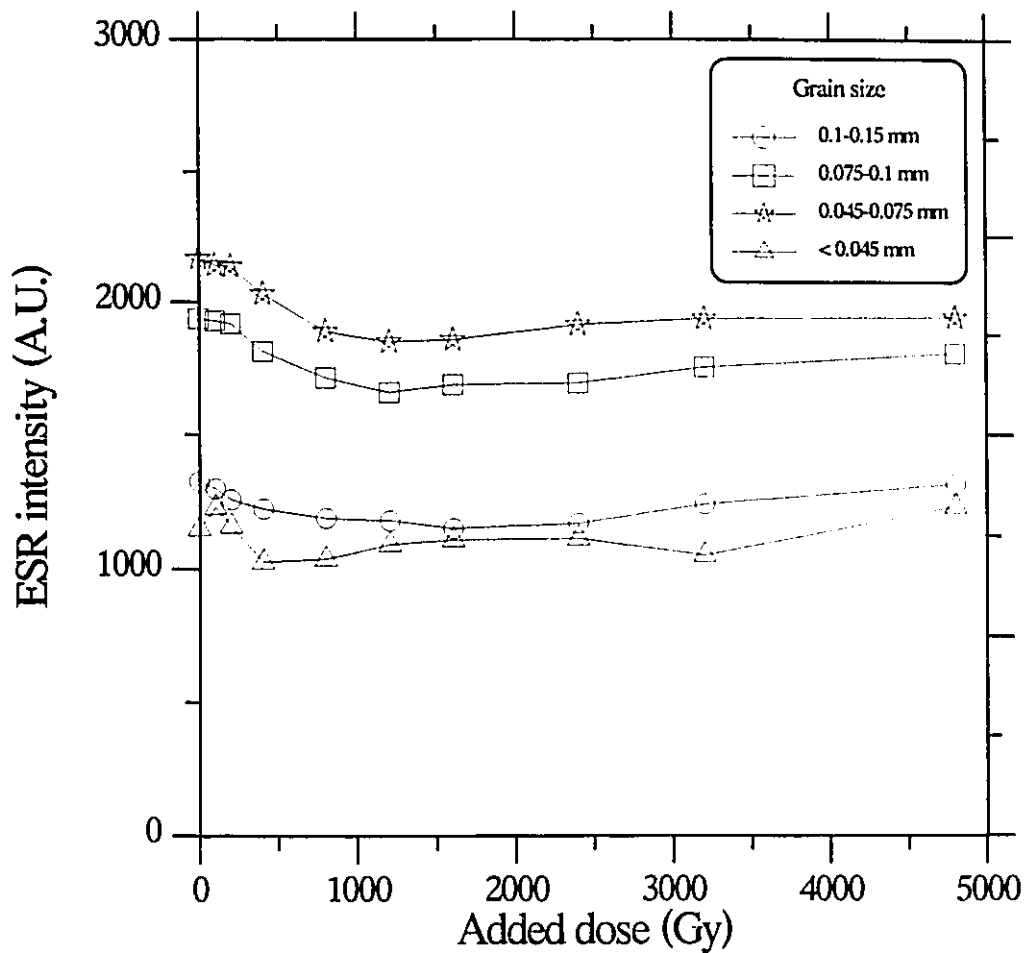


Figure 3.7. An example of dose response curves of a saturated sample. The intensities for E' signals of quartz from fault gouge (AECL7) decrease with added dose up to 1200 Gy and then increase slightly again.

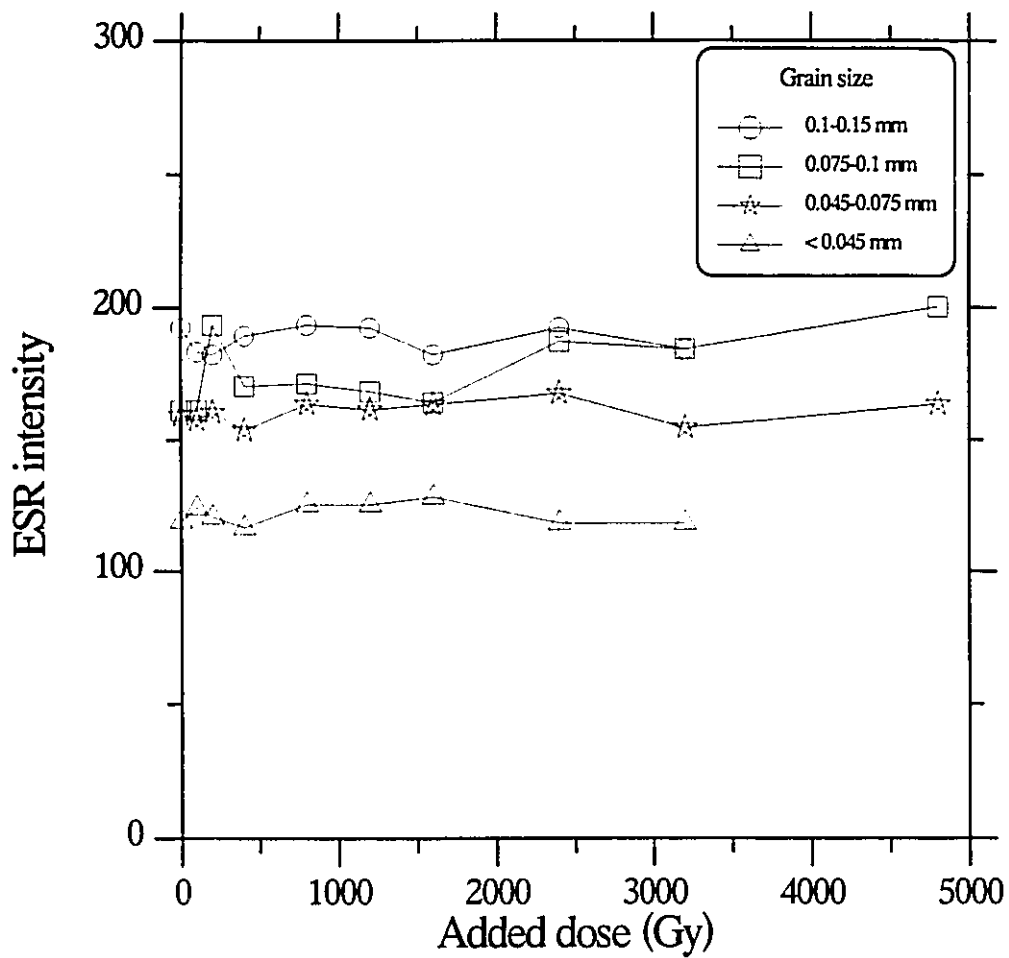


Figure 3.8. An example of dose response curves of a saturated sample. The intensities for OHC signals of quartz from fault gouge (AECL5) show fluctuation with added dose.

to be in saturation or in steady state, in which the rate of production of ESR centers and recombination (decrease of ESR centers) are equal.

### 3-3-2. Unsaturated fault rock samples

Since the last fault movement (If sufficiently recent) has zeroed the ESR centers and created the precursors of ESR centers, quartz grains separated from fault rocks have abundant empty ESR centers. Therefore they generally show systematic growth of ESR intensity with artificial added dose, which is the characteristic behavior of unsaturated samples (Fig. 2.3). The possible zeroing mechanism of ESR signals at the time of fault movement will be discussed in Chapter 4.

Various types of behavior with added dose were observed between grain size fractions and for different centers. For example, in sample 91043 collected from the Kagel fault, the Al center was saturated for all grain size fractions; the intensities show fluctuation with added dose (Fig. 3.9). The Ge center is not suitable for ESR dating of fault rocks due to resetting of ESR signal by solar bleaching on the outcrop surface (Buhay, 1987). For comparison, I tested the behaviour of this center. For grain size of 75-100  $\mu\text{m}$ , the intensity grows systematically along a single saturating exponential function curve. On the other hand, for grain sizes of 100-150  $\mu\text{m}$ , the intensity grows systematically up to saturation level (2400 Gy), and then shows fluctuation (Fig. 3.10).

As for the E' signal, the larger grains (>100  $\mu\text{m}$ ) show fluctuation in intensity

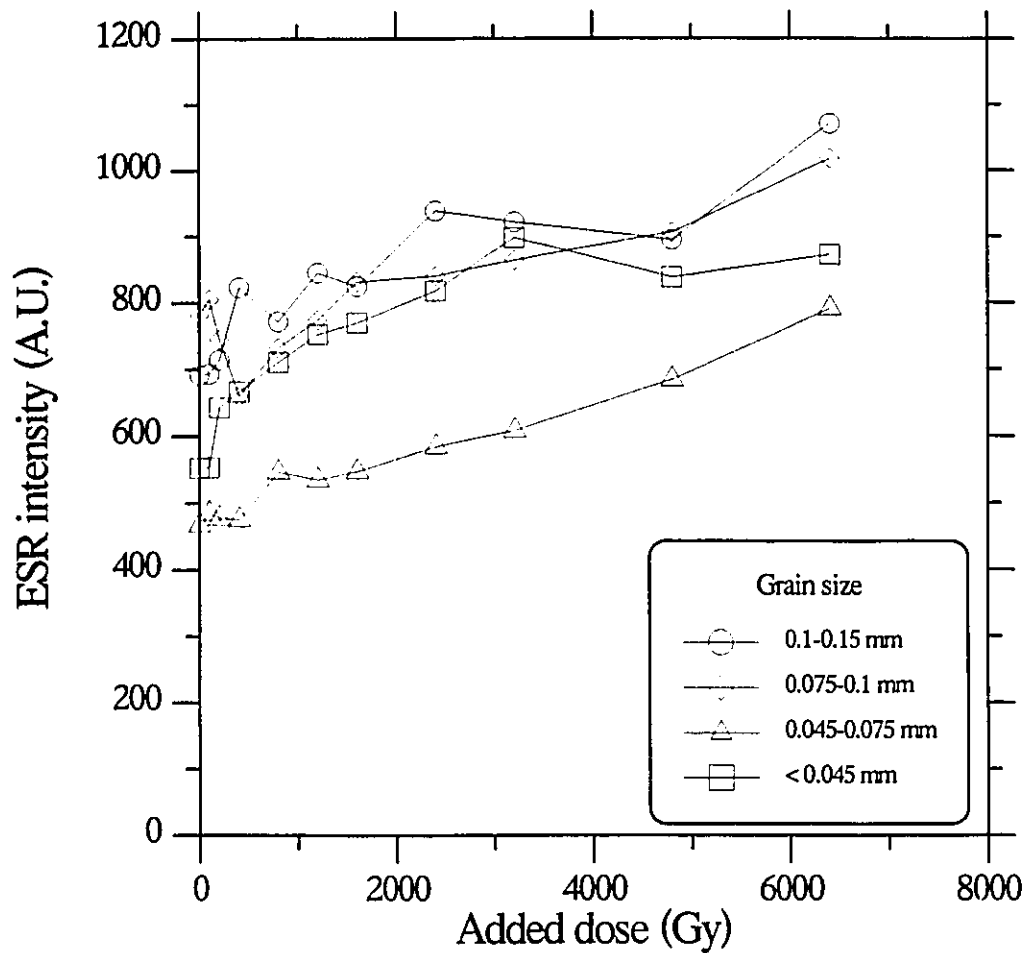


Figure 3.9. Variations of ESR intensity (AI) with added dose for sample 91043 collected from Kagel fault. ESR intensity shows fluctuation with added dose for all grain size, which appears to be characteristic of grains in ESR saturation.

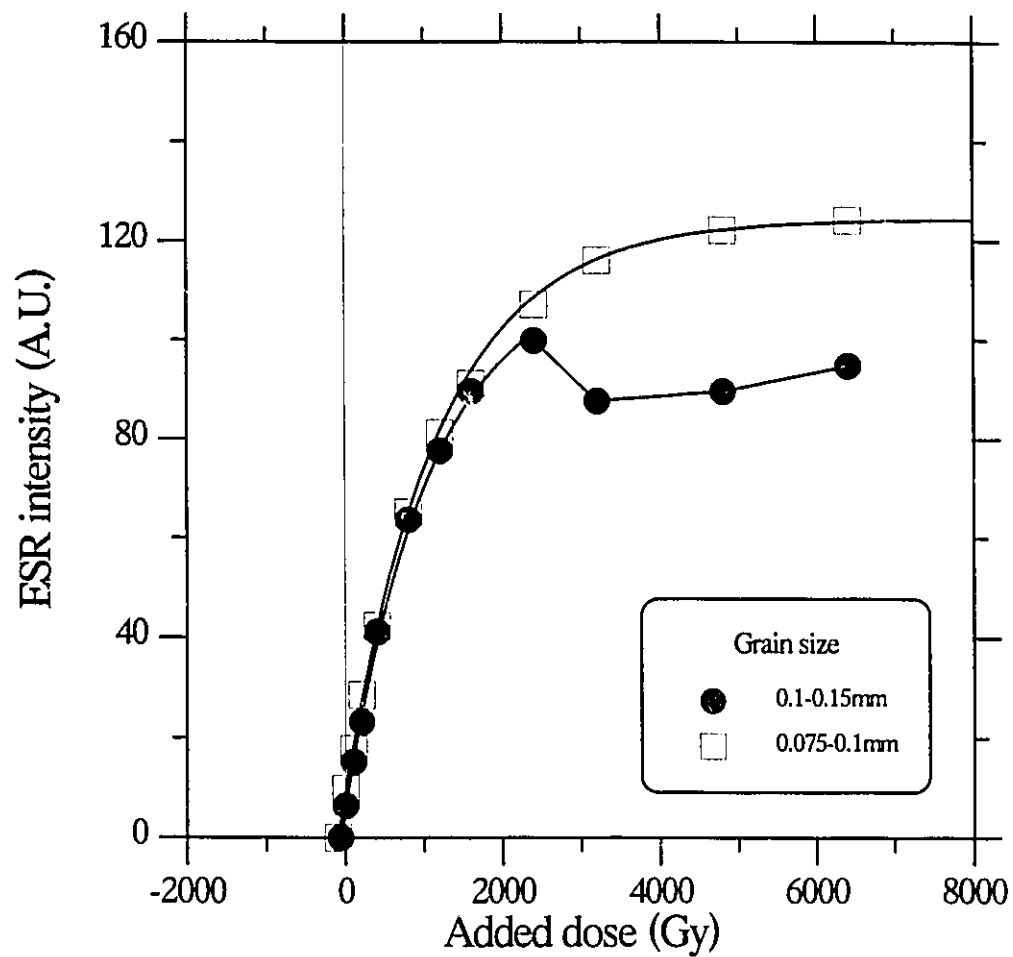


Figure 3.10. Growth curves of Ge signal for sample 91043 collected from Kagel fault. The Ge signal appear to be bleached almost completely on the outcrop surface by the solar energy. The larger grains shows fluctuation in intensity after saturation.

which appears to be characteristic of grains in ESR saturation. The smaller grain size fractions extracted from this sample are fitted to single saturating exponential function curves leading to the same  $D_E$  (Fig. 3.11). OHC signals on this sample are fitted to single saturating exponential function curves for all grain size. In particular, for grains smaller than 75  $\mu\text{m}$ , this growth curve converges to the same  $D_E$  value determined for the E' signal indicating complete resetting during the last fault movement. The above observations suggest that (1) the AI signal for all grain size fractions and the E' signal for the larger grains ( $> 75 \mu\text{m}$ ) were reset partially at the time of fault movement and then saturated by natural irradiation since last faulting event, (2) the OHC and E' signals for grains smaller than 75  $\mu\text{m}$  were reset completely at the time of the last fault movement leading to a plateau age, (3) the OHC signals for larger grains were partially reset, but do not reach a saturation state at present.

In general, after saturation by artificial irradiation, these signals will show the various behaviours in ESR intensity described in the previous section (3-3-1). In this study, the equivalent dose was determined by the growth curve limit up to the saturation dose since the errors of  $D_E$  are increased by the outliers after saturation. For samples which saturated with lower dose (about 400-800 Gy), it is very difficult to distinguish saturated from steady state samples in nature, since ESR intensity grows systematically up to saturation level and then decreases or increases leading to fluctuation in ESR intensity. It is impossible to date fault movement using these kinds of fault rock samples. Fortunately, most fault rock samples have very large saturation doses (or saturation ESR

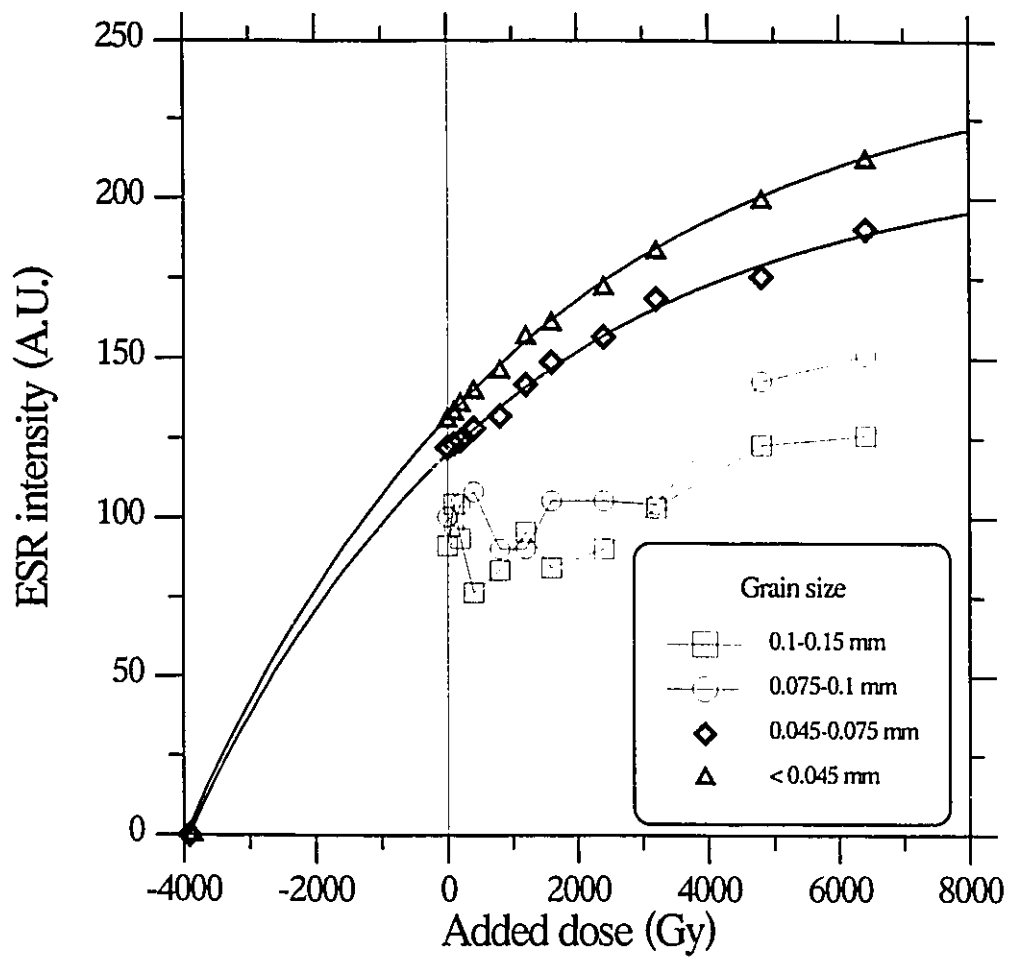


Figure 3.11. Growth curves of E' signal for sample 91043 collected from Kagel fault. The grains larger than 75  $\mu\text{m}$  were partially zeroed at the time of fault movement, and then saturated after faulting event.

intensity) due to creation of precursors of ESR centers during fault movement.

Different curve fitting methods and their strength and weakness were described in detail in Lyon's Ph.D. thesis (1989). In the present study,  $D_E$  was determined by the additive dose method using Grün's Fit-Sim program. I fitted a single saturating exponential function (Grün, 1989), and the  $D_E$  and error were determined by equal weight method.

### 3-4. Determination of dose rate

The dose rate is a measure of the environmental radioactivity caused by the U, Th and K in the samples and host rocks. It can be calculated from the concentrations of radioactive elements in the samples and surrounding host rocks. The gamma dose rate components can be estimated by direct measurement using TL phosphors which were buried in the sampling sites for up to a year, or with a portable gamma spectrometer. To determine the dose rate, several parameters such as water content, attenuation factor,  $\alpha$ -efficiency etc. should be estimated and incorporated in the dose rate equation shown below:

$$d = C_U (k W_\alpha G_{U-\alpha} D_\alpha + W_\beta G_{U-\beta} D_\beta + W_\gamma D_\gamma) + C_{Th} (k W_\alpha G_{Th-\alpha} D_\alpha + W_\beta G_{Th-\beta} D_\beta + W_\gamma D_\gamma) + C_K (k W_\alpha G_{K-\alpha} D_\alpha + W_\gamma D_\gamma) + G_{cos} D_{cos} \quad (3-1)$$

where  $C_{U,Th,K}$  = concentration of radioactive elements present



$k$  =  $\alpha$ -efficiency

$W_{\alpha,\beta,\gamma}$  = water correction factors for  $\alpha$ ,  $\beta$ , and  $\gamma$

$G_{\alpha,\beta,\gamma,\text{cos}}$  = attenuation factors for  $\alpha$ ,  $\beta$ ,  $\gamma$  and cosmic rays

$D_{\alpha,\beta,\gamma}$  = dose rate per unit concentration

$D_{\text{cos}}$  = cosmic dose rate

U is assumed to be secular equilibrium with its daughters. Although several extensive reviews of the estimation of dose rate for TL and ESR dating have been published (e.g., Aitken, 1985; Grün, 1989), the dating of fault rocks presents some special problems, which have not yet been presented together. Therefore I will describe how each of these parameters must be evaluated.

The concentration of radioelements, U, Th and K in the samples can be obtained from neutron-activation analyses. The concentration of U, Th, and K may be significantly inhomogeneous within the range of gamma rays (about 30 cm). To avoid problems from inhomogeneous distribution of radioelements, homogenization of the samples is essential for the determination of U, Th and K contents. Fault rock samples appear to be mixtures of materials from both wall rocks. After disaggregating the fault rock, it is mixed and split into subsamples until we obtain a sample of about 1 g for NAA analysis.

Alpha particles are less efficient at depositing energy in minerals than  $\beta$  or  $\gamma$  rays, and a correction factor ( $k$ , about 0.1 - 0.2) is used to adjust the dose from  $\alpha$  particles. At present, as the  $\alpha$ -correction factor of quartz for ESR has not been determined, I used a value ( $k=0.1\pm 0.02$ ) experimentally determined for TL (Zimmerman, 1971, 1972). If I

use Bell's (1980)  $k$  value of 0.07, the dose rates decrease leading to ESR age estimates which are generally higher by 1-5 %, depending on the proportion of Th and U.

Variation of water content of some fault zones through time will have a corresponding effect on the dose rate. Pore fluid pressure of the fault zone shows cyclic variation. During fault movements, the porosity and permeability in fault rock zones are increased and therefore the pore-fluid pressure increased. On the contrary, the porosity, permeability and pore-fluid pressure are decreased after fault movement and then are relatively constant during the dormant period (Sibson, 1992; Chester et al., 1993). Therefore, I assumed that the water content remained relatively constant since the last fault movement and that we can use the present water content to estimate the dose rate. All dose rates are corrected for attenuation of radiation by the water content of the rock. The estimated water content of fault rocks (5 samples) from minor faults of the San Andreas fault zone was  $7.1 \pm 2.6$  %. I used this value for estimating dose rate because most of fault rock samples for this study were dried out on the outcrop surface.

The radioactive elements surrounding the quartz grains in the matrix of fault rocks emit alpha, beta particles and gamma rays. Alpha particles have a penetration range of about 20  $\mu\text{m}$  in a matrix with a density of 2.5  $\text{g}/\text{cm}^3$ . This low penetration range means that alpha particles can increase the ESR intensity only at the outer surface of quartz grains. Beta particles are energetic electrons with an average penetration range of about 2 mm in a density of 2.5  $\text{g}/\text{cm}^3$ . Since we used quartz grains smaller than 2 mm for dating of fault rocks, we have to consider attenuation factors for both alpha and beta

particles in the calculation of the dose rate. On the other hand, the gamma ray has a long penetration range of 30 cm in a medium with a density of 2.5 g/cm<sup>3</sup>. Therefore, it is not significantly attenuated in the quartz samples separated from fault rocks. Since the dose rates for quartz separated from fault rocks are different with grain size due to the attenuation of the radiation, a narrow range of size is desirable for fault dating.

The sample's dose rate includes short-range alpha and beta doses, while the gamma component is based on the dose rate from the surrounding rock. The isotopic concentrations were converted into dose rates from published tables (Nambi and Aitken, 1986), assuming the <sup>238</sup>U decay series to be in secular equilibrium.

Cosmic rays, for the most part, penetrate only a few meters of sediment. Since the fault rocks in this study area were probably located much deeper than this during most of their history, cosmic-ray input to  $D_E$  is probably negligible. Loss of <sup>222</sup>Rn from the gouge zone and incorporation of <sup>222</sup>Rn into the gouge zone from surrounding rocks should be relatively steady state at deep fault zone.

The internal concentration of radioactive elements within quartz grains was too low to be determined by NAA; I therefore assumed 0.05 ppm of U, and 0.1 ppm of Th (W. J. Rink, personal communication).

### 3-4-1. Measurement of gamma ray activity by gamma spectrometer

A test of determination of the gamma ray component from dose rate using a portable gamma ray spectrometer was performed in some outcrops (Fig 3.12). In general, the measured values are consistent (within about 30 %) with the estimated gamma ray component by NAA analysis. However, the gamma-ray radioactivity showed inhomogeneous distribution over about a 30 cm distance and too high a measured value (6 times higher than estimation by NAA) in some outcrops. The measurement results are summarised in Table 3.2. Note that samples for NAA analysis were collected on the outcrop surface near (30-100 cm) the holes 35-40 cm deep used for measurement of gamma-ray activity.

For examples, gamma ray activities were measured at six holes 35 cm deep separated by 50-130 cm horizontally in the Barrel Spring fault. The dose rates from gamma rays are generally homogeneous within gouge zone. The dose rate estimated by NAA for the samples collected on the surface are similar with the measured values (Fig. 3.13).

Six holes in gouge and breccia zone were measured for gamma ray activity in the Bear Canyon fault. The measured values show inhomogeneous distribution ranging over one order of magnitude in radioactivity (Fig 3.14). There is some possibility that even small amounts of radioactive minerals near the gamma ray spectrometer can yield high value of radioactivity. It is very difficult to determine the component of gamma ray

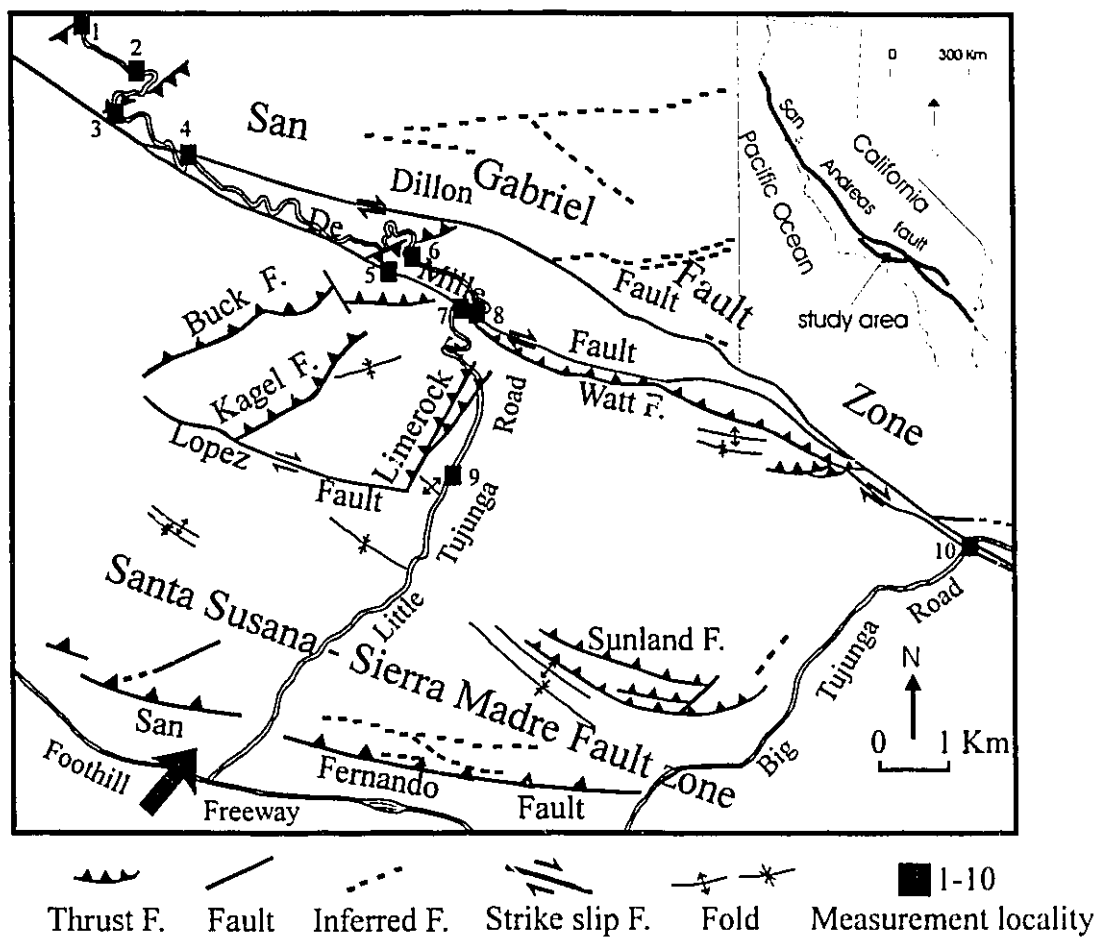


Figure 3.12. Structural map in the Little Tujunga region showing sites for measuring the gamma ray activities.

Table 3.2. Results of measurement of  $\gamma$ - ray activities in the Little Tujunga region.

Fault	Hole	Rock type	Measure dose rate ( $\mu\text{Gy/a}$ )	* Dose rate determined by NAA ( $\mu\text{Gy/a}$ )	Site
Bear	1	breccia	2250	398	3
	2	gouge	3389	1097	3
	3	gouge	2670	1097	3
San Gabriel	1	gouge	778	1324	10
	2	reactivated	641	661	10
De Mille		gouge	1290	1117	5
San Gabriel		gouge	468	462	4
Santa Clara		gouge	567	731	2
Dillon Divide		gouge	1102	681	6
Spring		gouge	907	1142	7
Barrel Spring	1	gneiss	1014		8
	2	gouge	1306		8
	3	gouge	1020		8
	4	gouge	1015	947	8
	5	gouge	769	1120	8
	6	conglomerate	685		8
Bear canyon	1	breccia	2213		1
	2	gouge	1229		1
	3	gouge	7628		1
	4	gouge	901		1
	5	breccia	4976		1
	6	gouge	785		1
Lovell	1	sandstone	704		9
	2	gouge	705		9

\* Even though the samples were collected on the same site as the holes for gamma ray activities, the positions of samples were separated at least 40 cm from measuring points of gamma ray activities.

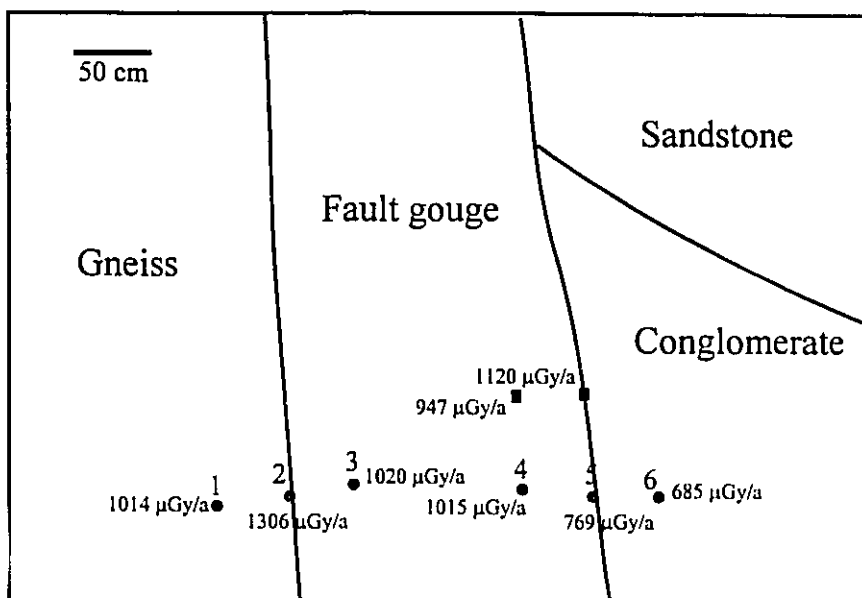


Figure 3.13. The distribution of gamma ray activities on the cross section of the Barrel Spring fault. Filled circle; measured value; Filled square; the value determined by NAA analysis.

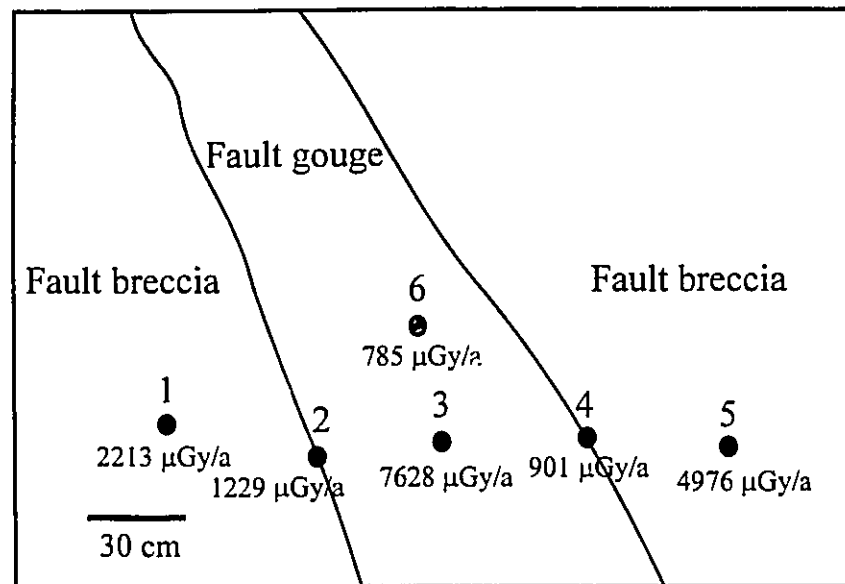


Figure 3.14. The distribution of gamma ray activities on the cross section of the Bear Canyon fault.



activity for the homogenized host rocks or fault rocks for radioactive minerals with a gamma ray spectrometer. Therefore, in this study the dose rate determination by NAA analysis using homogenized samples as described above was preferred for dating of fault rocks.

### 3-5. Determination of ESR ages

Ages were calculated using a program (ESR-DATA) that takes into account attenuation of  $\alpha$ - and  $\beta$ -particles in the quartz grains (as a function of their size) as well as  $\alpha$ -efficiency, energies of  $\alpha$  and  $\beta$  particles in the U, Th, and K decays, and  $\gamma$ -doses from the surrounding rocks.

The error in  $D_E$  was estimated by Grün's Fit-Sim program, and was generally 5-20 %. The errors in dose rate arise from many sources. A relatively large error ( $7.1 \pm 2.6$  % by weight) in the water content was assumed. The errors in the concentrations of radioactive elements determined by NAA range from 1 to 10 %. The total uncertainty in dose rate was 5-10 %. The total error of age for each size fraction ranges from 5 to 20 %.

Weighted means were calculated for all ages and for data from convergent centers which lay on a single plateau. The weighted mean age for more than two size fractions and convergent ages for two different ESR signals is given by:

$$Y = (Y_1 / S_1^2 + Y_2 / S_2^2 + \dots) / (1 / S_1^2 + 1 / S_2^2 + \dots) \quad (3-2)$$

and the error limits on the weighted mean are given by:

$$S = \{1 / (1/S_1^2 + 1/S_2^2 + \dots)\}^{1/2} \quad (3-3)$$

where  $Y_1, Y_2, Y_3 \dots$  etc. are the individual ages of different size fractions or ESR signals, and  $S_1, S_2, S_3 \dots$  etc. are the individual quoted error limits (Aitken, 1990). The final errors of the weighted mean were generally 5-15 %.

## Chapter 4

### Criteria of complete zeroing of ESR signals during fault movement

#### 4-1. Introduction

The ESR dating method is based on the premise that the ESR signals of quartz grains are reset by frictional heating and cataclastic deformation during fault movement. In using ESR to date the time of last movement on a fault, it is essential to demonstrate that the signal was fully zeroed at the time of fault movement. This is a very difficult problem; if the signal was not completely zeroed, then the age obtained will be too great. We can see the nature of this problem in figure 4.1. Let us assume that a sample was only partially zeroed, leaving intensity  $I_p$ . ESR researchers determine the value of  $D_E$  by the method of additive dose, in which they submit the sample to additional doses,  $D_a$ , and determine a growth curve,  $I(D_a)$ , which is generally a saturating exponential (Grün, 1989). Then  $D_E$  is determined by back extrapolation to  $I = 0$  (Fig. 4.1). We can then use equation (2-1) to determine  $t$ . This assumes, however, that at  $t = 0$ ,  $I = 0$ . If  $I = I_p > 0$  at  $t = 0$ , then we will obtain a value  $D_E'$  which leads to an apparent age  $t' > t$ . Simple analysis of quartz extracted from a sample of gouge does not inform us whether or not the quartz was fully zeroed by the last fault event. Therefore it is very important to

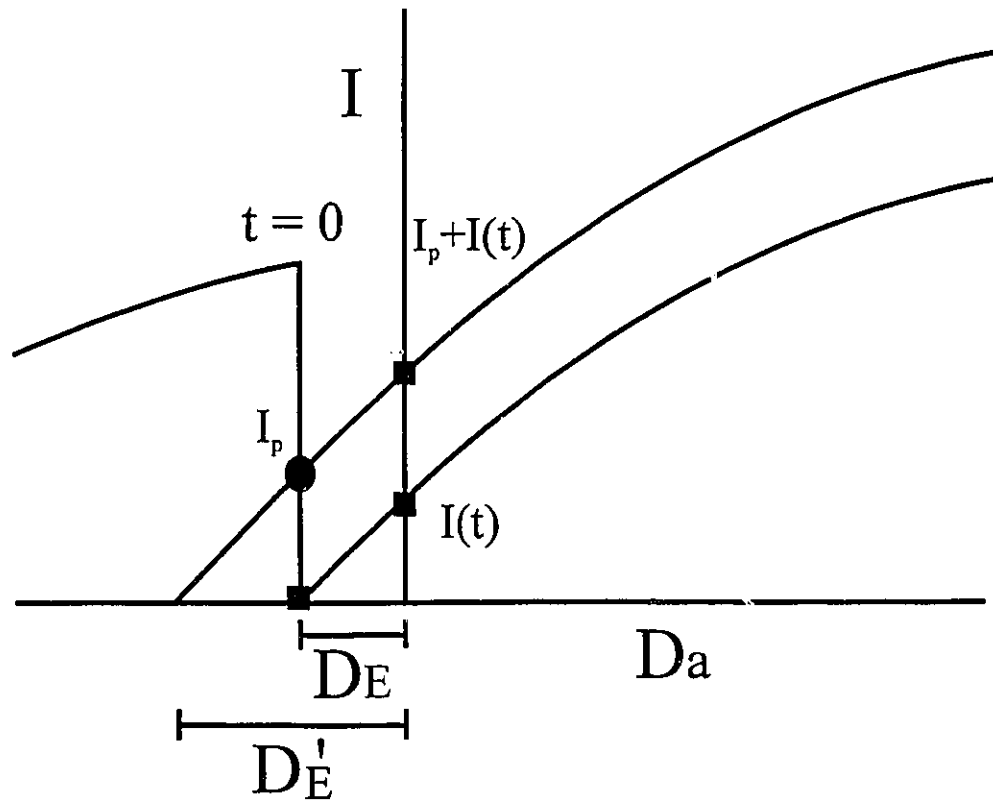


Figure 4.1. Growth of intensity in a sample which was not fully zeroed by faulting:  $I(t)$  = ESR intensity in a sample which had been fully zeroed at time,  $t$ , of faulting, and had then regrown due to environmental radiation (dose rate =  $d$ ) without further zeroing;  $I_p$  = hypothetical residual intensity in a sample not fully zeroed at  $t$ ;  $D_E$  = equivalent dose for fully zeroed sample;  $D_E'$  = equivalent dose for partially zeroed sample;  $D_a$  = additional gamma doses administered to sample in additive dose method (Grün, 1989); curves show saturating exponential growth of  $I$ , typical of ESR signals.

develop some criterion to demonstrate that zeroing had occurred.

#### **4-2. Plateau method**

The basic assumption for the plateau method is that the smaller grains were more completely zeroed than the larger grains. In grains smaller than some critical radius, some ESR signals would be totally reset at the time of fault movement whereas the larger grains and the more stable ESR centers would have been only partially reset. Immediately after fault movement, the curves in the age versus grain size diagram would look like the curves A and B of figure 4.2. After fault movement, the number of paramagnetic centers increases again with the passage of time by irradiation from the environment. Thus, in a graph of age versus grain size, we would expect to find a plateau of constant age for grains below some critical size (curve C in Fig. 4.2). The estimated age of smallest grains from two or more stable centers for zeroing of ESR signals should yield the same age (curves C and D in Fig. 4.2). Note that other researchers did not measure quartz particles of varying grain size, but merely analysed one size fraction (Ikeya et al., 1982: 74-250  $\mu\text{m}$ ; Fukuchi et al., 1986 :105-250  $\mu\text{m}$ ). In next sections, I will describe the validity of this plateau method by experimental (shearing experiment) and field (San Gabriel fault zone) studies.

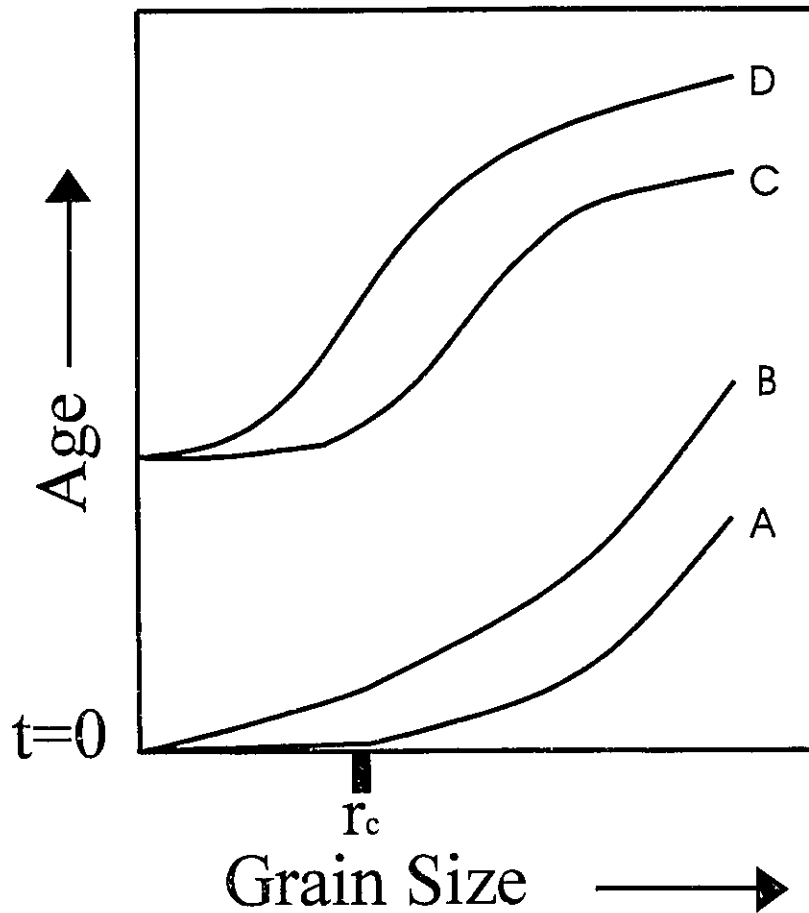


Figure 4.2. A hypothetical distribution of ESR ages in quartz as a function of particle size. Immediately after faulting, apparent ESR ages recorded by two centers (A; less stable and B; more stable) decrease from saturation or steady state value to zero, for particles below some critical radius ( $r_c$ ). Larger particles are only partially zeroed. After some time has elapsed, the apparent ESR ages of all particles increase (C, D) preserving the plateau of constant age for  $r < r_c$ . Doses of the largest grains approach saturation or steady state, leading to flattening of the curve of age vs. size.

### 4-3. Experimental studies of zeroing

#### 4-3-1. A review of previous experimental studies

Several researchers (Ikeya et al., 1982; Buhay, 1987) showed that simple crushing in uniaxial compressive experiments decreases the intensities of ESR signals. The smaller size fractions were more reset than the larger ones. Tanaka and Shidahara (1985) carried out triaxial compressive experiments and found out that higher differential stress ( $\sigma_1 - \sigma_2$ ) was more effective in zeroing of ESR signals.

Experiments to determine the normal stress and displacement (shear strain) needed to achieve zeroing of ESR signals have been carried out by Tanaka and Shidahara (1985), Ariyama (1985), and Tanaka (1990). Tanaka and Shidahara (1985) ground pegmatitic quartz in an agate mortar. The intensities of ESR signals were decreased with grinding time (shear strain) and smaller grains were more effectively zeroed (see Fig. 8. of their paper; the slopes are approximately inversely proportional to the grinding time and the slope for smaller particles is steeper than those for the larger ones). Ariyama (1985) sheared an 0.5 mm layer of a mixture of quartz (74-250  $\mu\text{m}$ ) and kaolinite using a shearing apparatus and found that the minimum necessary condition for complete resetting of ESR signals is 50 cm displacement (shear strain=1000) under a normal stress of 2 Mpa. Tanaka (1990) sheared a 1 mm layer of quartz sands (420-840  $\mu\text{m}$ ) between ring shaped shearing surfaces (metal) at a controlled normal stress. After sieving (74-250  $\mu\text{m}$ ,

250-420  $\mu\text{m}$ , 420-840  $\mu\text{m}$ ), he analyzed ESR signals and found out that the annealing of the E' signal is consistently more effective in smaller grain sizes and higher normal stresses. However, Hataya and Tanaka (1993) seemed to retract part of Tanaka's experimental data. They washed the completely zeroed quartz with water and HCl and found out that the E' and peroxy signals were completely recovered. They concluded that zeroing of ESR signals resulted from disturbance by the powdered metal which was produced during shearing.

Hataya and Tanaka (1993) did not, however, measure the size-sorted samples and did not show any experimental conditions (normal stress and strain). Also it seems strange that they find no zeroing of ESR signals in samples which were ground in their apparatus, since all other investigators have found at least partial reduction in ESR intensity by grinding. I would assume that in experimentally sheared samples, just as in nature, there would be a grain size effect. Therefore, only the grains with  $r < r_c$  would reach zero intensity. Tanaka (1990) also partially dissolved sheared quartz (grain size; 74-250  $\mu\text{m}$ ; normal stress; about 1 Mpa; displacement; 84 cm; slip rate; 4.7 cm/s; intensity of the E' signal; 30 % of unsheared sample) with 10 % HF. He found that after removing up to 10  $\mu\text{m}$  from the surface, up to 80 % of the intensity of the E' signal was restored. This fact suggest that the zeroing zone of ESR signals is distributed near the surface of quartz grains and that zeroing of ESR intensity (30 % of that in unsheared quartz) was a real result of shearing, and not the disturbance of powdered metal. Therefore, I believe that the shearing experimental data in Tanaka's thesis (1990) can be used to compare with



other researcher's data.

In shearing experiments, zeroing of ESR signals is due to both lattice deformation and frictional heating on the shearing planes. Fukuchi (1989, 1992) interpreted that zeroing of ESR signals in shearing experiments is due to only cataclastic deformation, whereas zeroing during actual fault movements is due only to heating (Fukuchi, 1989, 1992). He misunderstood that shearing in nature yields heating but shearing using shear apparatus does not yield heating. The degree of zeroing of ESR signals, by lattice deformation, frictional heating from shear plane, and frictional heating on grain/grain contact, is dependent on experimental conditions.

In order to define the conditions for complete zeroing of ESR signals, and to study the effect of shearing of quartz at conditions of stress and strain rate, I have carried out extensive experiments.

#### **4-3-2. Experimental methods**

I used Ottawa sand, consisting of 100 % quartz in the form of fine, well rounded grains. The sand was dry sieved, retaining the > 250  $\mu\text{m}$  fraction. Layers of these subsamples, 5 mm thick, were sheared between Westerly Granite surfaces in a servo controlled rotary shear apparatus (Fig. 4.3). The normal stress was kept constant (5 Mpa, 10 Mpa) by a servo-controlled system. The slip rates were 50  $\mu\text{m/s}$  and 500  $\mu\text{m/s}$ . The resulting simulated fault gouge was dry sieved, to determine the grain size distribution

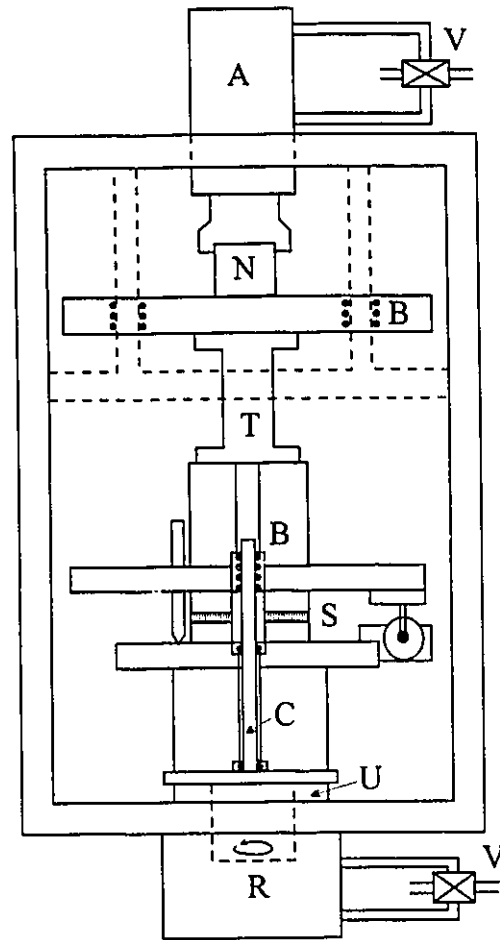


Figure 4.3. Schematic diagram of shear apparatus: A, axial actuator; B, linear bearing; C, central rod; N, axial load cell; R, rotary actuator; S, sample assemblage; T, torque cell; U, thrust bearing; V, servovalve.

(weight percent basis) corresponding to different levels of shear strain. ESR signals were then measured on 100 mg aliquots representing different grain size and shear strain. The packing density in the ESR sample tubes was assumed to be constant, since the grain shapes are approximately uniform in each size fraction. A second suite of 100 mg aliquots separated by grain size and shear strain was irradiated step by step, using a  $^{60}\text{Co}$  source, over the range of 100-800 Gy, to construct dose response curves.

#### **4-3-3. Results of experimental studies**

##### **4-3-3-1. Mechanical properties and grain size distributions**

During shearing, the sample exhibits a rapid increase of shear strength up to the frictional yield point, after which it slides at a roughly constant shear stress regardless of slip rate. At low shear strains fracturing and crushing predominate. Large increases of shear strain do not change grain size distribution markedly. A normal stress of 10 Mpa decreases grain size more rapidly than 5 Mpa. The steady state of grain size distribution is reached more rapidly at the higher slip rate.

##### **4-3-3-2. Variation of ESR intensity of sheared quartz**

ESR intensities of the E' signal are shown in figure 4.4. In general, there is a

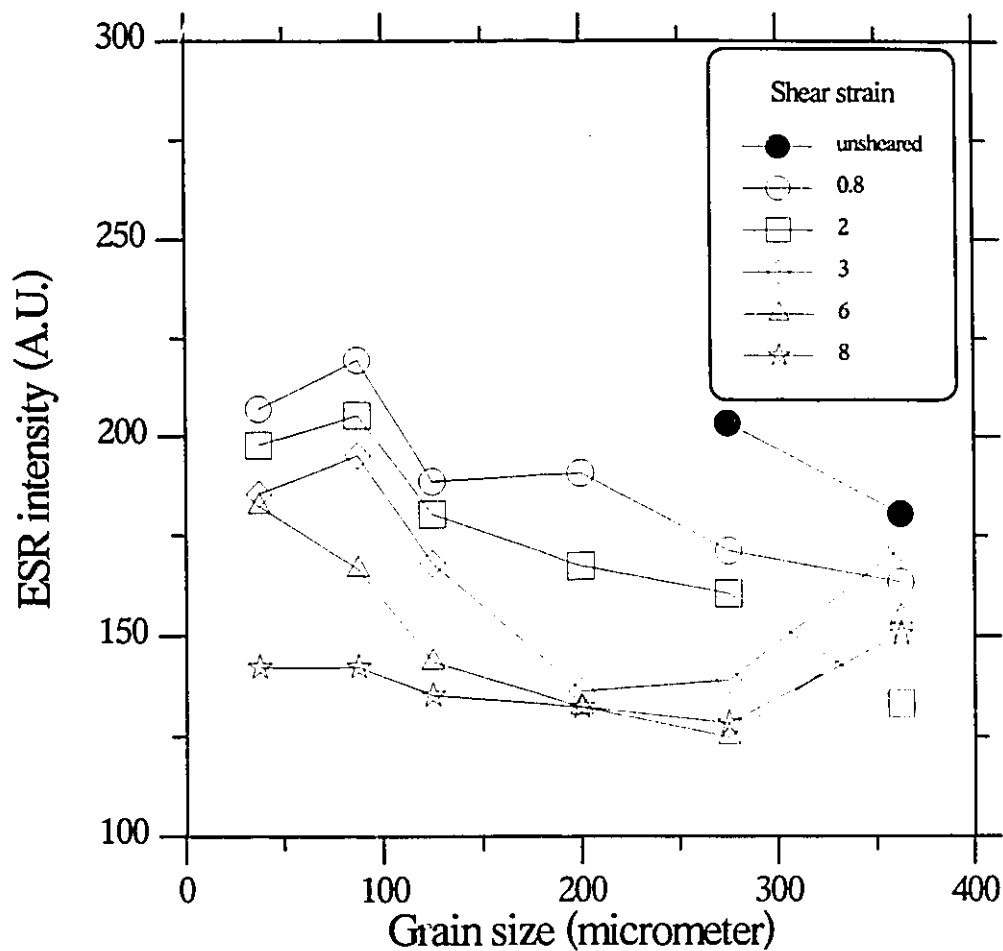


Figure 4.4. The relationship between ESR intensities ( $E'$ ), shear strain, and grain size. At lower shear strain, the smaller grains have larger ESR intensities. With the increase of shear strain, both ESR intensities and the differences of ESR intensities between grain size are decreased. Note decrease in intensity relative to unsheared sand. (normal stress = 10 Mpa; slip rate = 0.05 mm/s).

decrease in intensity for particles of a given grain size with increasing shear strain. However, there is also an increase in intensity with decreasing grain size, for grains below 200  $\mu\text{m}$ , to values even exceeding that of the unsheared sand. The largest fractions give relatively higher intensities, possibly due to the admixture of totally unsheared grains from the original sand. The degree of resetting was proportional to normal stress applied. At the highest strain values, there is essentially no variation in  $E'$  intensity with grain size, although the signal has not been totally zeroed. As we shall see, however, the same is not true of  $D_E$  values. Figure 4.5 shows the variation in intensity with shear strain (= displacement/thickness) for three ESR signals; the  $E'$  intensity drops more rapidly with increasing strain, while  $T_i$  is unchanged or actually increases. Note that the so-called OHC signal shown by Buhay et al. (1988) ( $g=2.011$ ) was not seen in any of our runs or in the natural Ottawa sand.

#### 4-3-3-3. Variation of radiation sensitivity of sheared quartz

Unsheared quartz sand exhibited saturation in  $D_E$ : showing fluctuation of ESR intensity with added dose.

Figure 4.6 shows the relationship of  $D_E$  to grain size for two shear strain values. At low shear strain, there is almost no difference in  $D_E$  estimated by  $E'$  between larger grain size fractions, but  $D_E$  decreases in the finest grain size fractions. At high strain, there is a decrease in  $E'$  with decreasing grain size;  $A_1$  shows no consistent trend in  $D_E$ 's

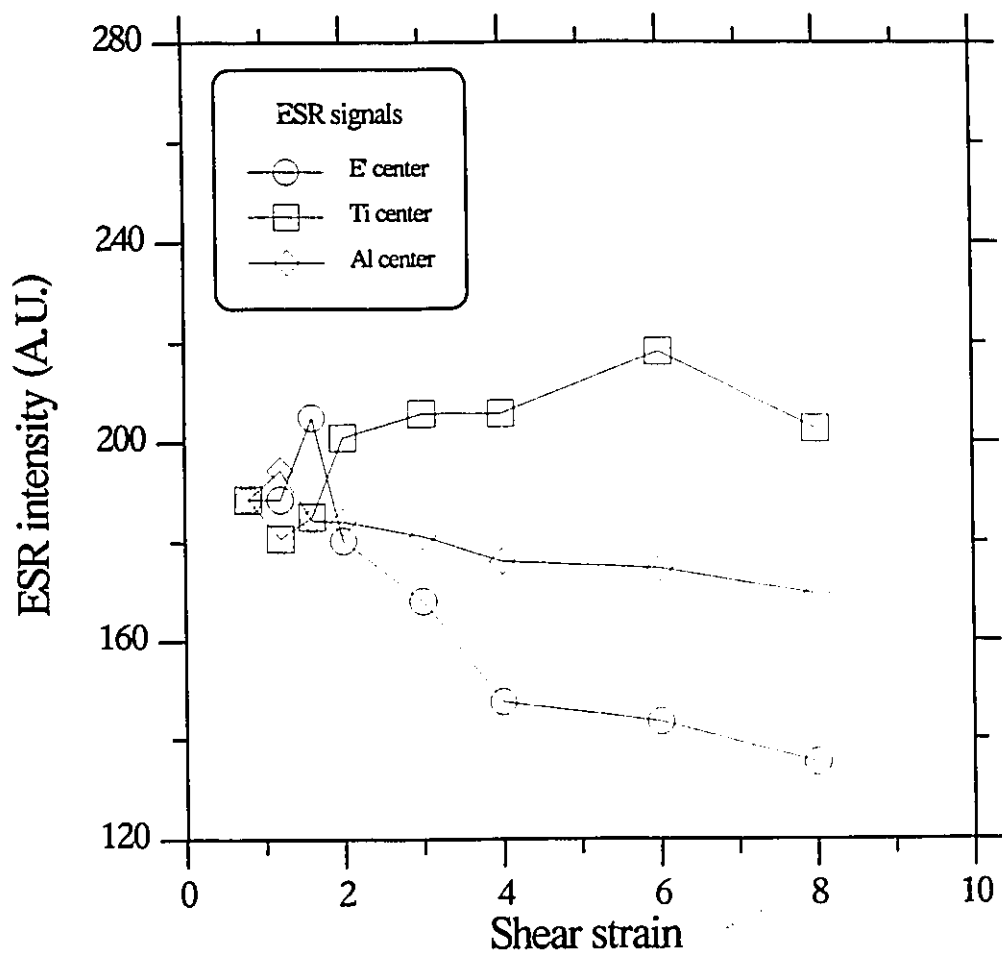


Figure 4.5. The variations of ESR intensities as a function of shear strain. The E' signal is most reset, followed Al. The intensity of Ti centre is not decreased as a function of shear strain. (normal stress = 10 Mpa; slip rate = 0.05 mm/s; grain size = 0.1-0.15 mm).

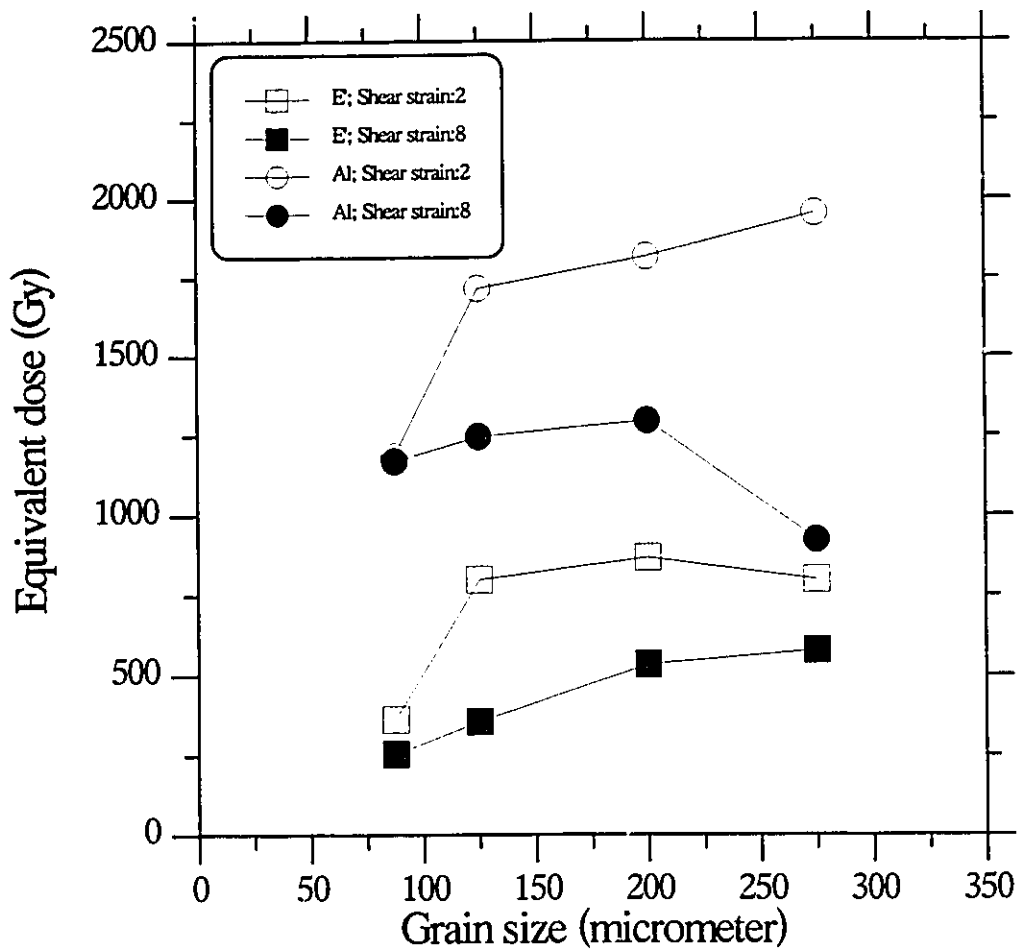


Figure 4.6. The relationship between  $D_E$ , shear strain and grain size (normal stress = 10 Mpa) for unannealed quartz sand.

with grain size. Thus, whereas intensity of E' shows no change with grain size (Fig. 4.4),  $D_E$  decreases in the finer grains. This corresponds to a difference in radiation sensitivity between size fractions, as can be seen in figure 4.7. As a result, the apparent  $D_E$  can decrease even though intensity does not vary or even increases with decreasing grain size. I presume that this increase in sensitivity is a result of the finer grains having experienced greater internal strain, resulting in the formation of defects capable of generating E' centres upon irradiation.

#### 4-3-3-4. Variation of ESR signals of sheared quartz

A suite of samples was annealed at 550 °C for 24 hours. This material showed only a weak peroxy signal. This annealed sample was then artificially irradiated with 500 Gy of gamma rays using a  $^{60}\text{Co}$  source.

Figure 4.8 shows the variation in the ESR signals with heating, gamma irradiation, and shearing. In the natural Ottawa sand we observe E', peroxy, Al and Ti signals; the Al signal (at 115 °K) may overlap a peroxy signal, which survives the annealing episode. The Ge, Al and Ti signals are regenerated by irradiation, while E' is not. However, after shearing, the E' can be regenerated by irradiation; shearing alone does not produce the E' signal. The high-g part of the peroxy signal is permanently lost by annealing, while the lower-g component is unaffected significantly by either shearing or irradiation. The behaviour of the E' signal suggests that during shearing defects are produced which



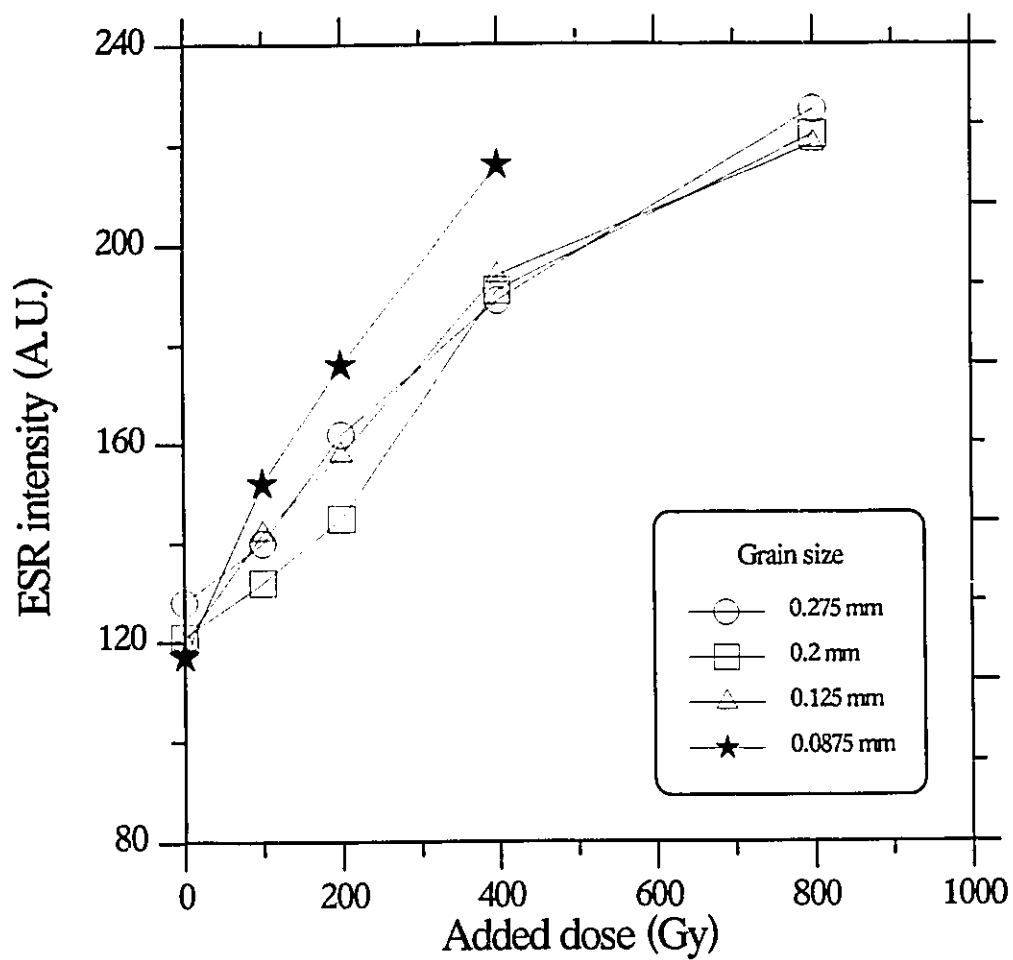


Figure 4.7. Growth curve of ESR intensities for E' signal as a function of artificial gamma irradiation. The slope of particles less than 100  $\mu\text{m}$  is much steeper than the others. (normal stress = 10 Mpa; shear strain = 8).

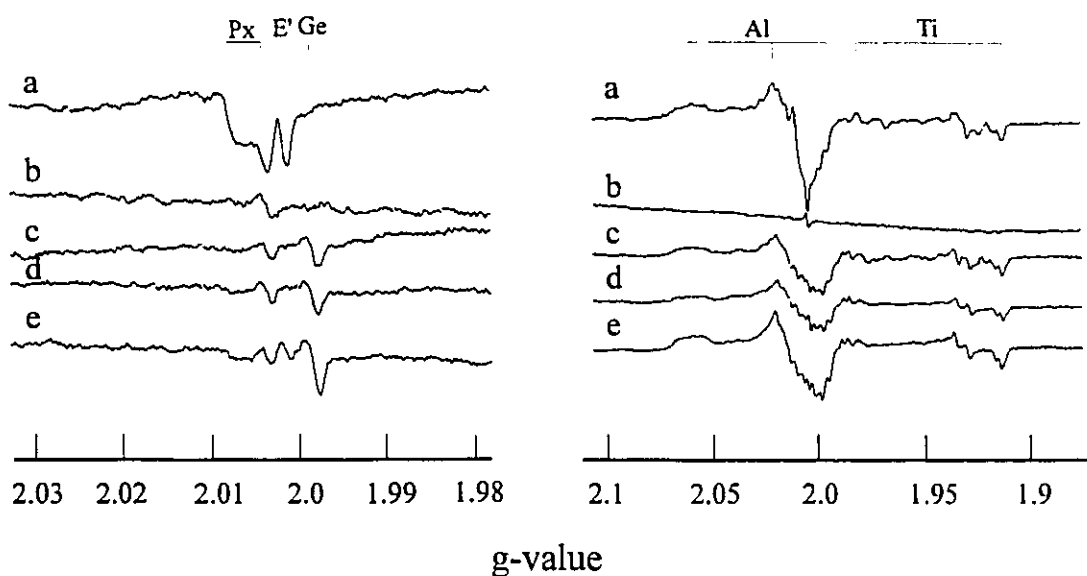


Figure 4.8. Variations of ESR spectra by heating, shearing, and gamma ray irradiation for simulated fault gouge. right: measured at 115 °K; left: measured at room temperature.

a: natural Ottawa sand (grain size: 250-810  $\mu\text{m}$ )

b: annealed for 24 hours at 550 °C (annealing)

c: gamma ray irradiation (500 Gy) to the annealed sand (annealing + irradiation)

d: shearing (shear strain: 8; normal stress: 5 Mpa) of the irradiated sand (annealing + irradiation + shearing).

e: gamma ray irradiation of the sheared quartz (annealing + irradiation (500 Gy) + shearing + irradiation (800 Gy). Note appearance of E' signal.

Al: Al signal ( $g=1.995-2.06$ ); Ti: Ti signal ( $g=1.979-1.913$ ); Px: peroxy signal ( $g=2.003, 2.007$ ); E': E' signal ( $g=2.001$ ); Ge: Ge signal ( $g=1.998$ ).

act as precursors for the E'. This is consistent with Fukuchi's (1989) observation that E' develops in fault gouge of rocks whose (unsheared) quartz does not display an E'; he attributes this to increase of sensitivity during shearing.

#### 4-3-4. Conclusions from experiments

The intensities of ESR signals decrease as a function of shear strain. Higher normal stress is more effective for zeroing of ESR signals (Fig. 4.9). At an early stage of shearing, the ESR intensity is increased by fracturing, and then decreases gradually by grain boundary frictional sliding and rotation of grains with shear strain (Fig. 4.9). The smaller size fractions are more reset than larger ones as shown in figure 4.10. This result explain the plateau model: using these data as an example, we see that if the displacement were increased to 26 cm, the smaller size fractions (0.075-1 mm, 0.1-0.15 mm) would be zeroed completely, but the larger ones would be only partially zeroed, leading to the formation of a plateau (Fig. 4.10 and curve A in Fig. 4.2).

$D_E$  values using the E' signal decrease with decreasing grain size, and also with increasing shear strain (Fig. 4.6). Part of this decrease is due to increase in radiation sensitivity of the quartz as a result of shearing. I attribute this increased sensitivity to increase in the concentration of defects (precursors of ESR center) in the quartz. As long as the ESR signal is completely zeroed, the  $D_E$  value will become zero regardless of the radiation sensitivity.

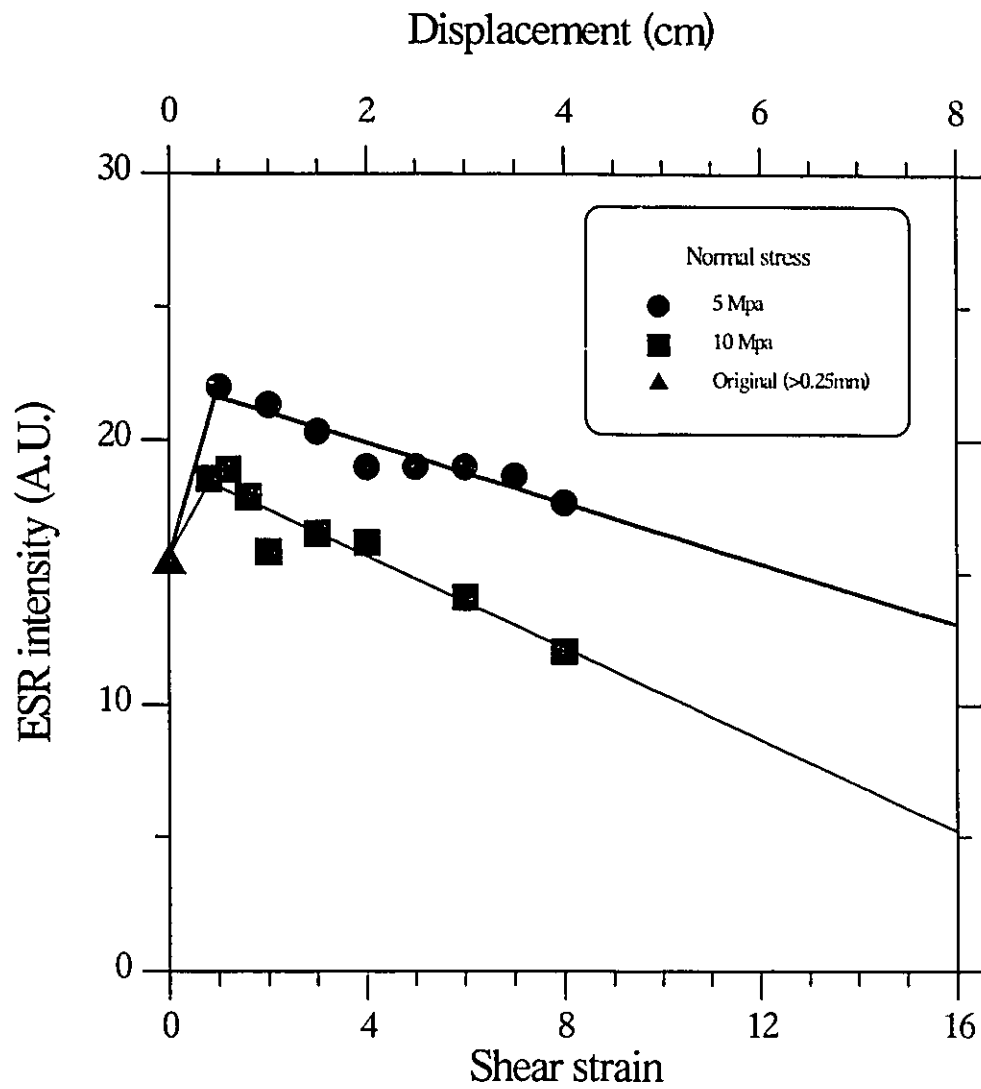


Figure 4.9. The variation of intensities of the E' signal as a function of shear strain. Higher normal stress is more effective for zeroing of E' signal. (slip rate = 0.05 mm/s; grain size = 0.075-0.1 mm).

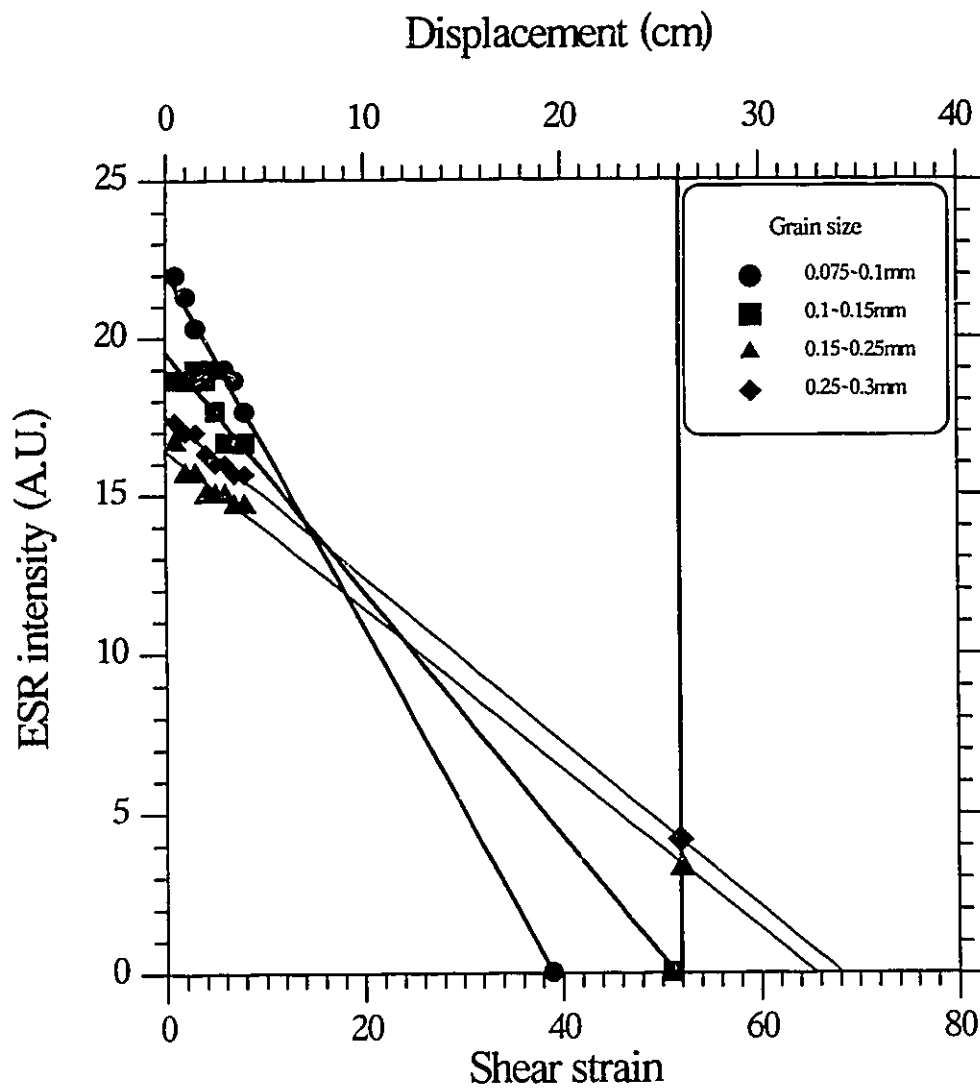


Figure 4.10. The decrease of the intensities of the E' signal with shear strain. Displacement represents the shearing of 5 mm layer of quartz grains. (normal stress = 5 Mpa; slip rate = 0.05 mm/s)

Figure 4.11 shows the conditions of displacement and normal stress for complete resetting of the  $E'$  signal (74-250  $\mu\text{m}$ ). Because different researchers sheared different layer thicknesses of quartz, I use the shear strain (displacement / thickness) instead of displacement to compare their data. Displacement in figure 4.11 represents the shearing of 1 mm layers of material. Even though, Tanaka's data appear to have some problems mentioned in the previous section (4-3-1), I plotted his data in figure 4.11 to compare with other researcher's data. This figure indicates that at higher normal stress ( $> 4$  Mpa), shear strain needed for resetting does not depend on normal stress. However resetting is dependent on shear strain at stresses lower than 4 Mpa. Figure 4.12 (lower shear strain part of figure 4.11) shows conditions of complete resetting (displacement and stress) for different grain sizes, showing how smaller grains need smaller normal stress and shear strain for resetting of  $E'$  signals than larger grains. Assuming shearing of 5 cm at normal stress of 5 Mpa, grains smaller than 0.1 mm will be reset completely (plotted as "complete reset" area for smaller grains in Fig. 4.12) and larger grains will be reset partially (plotted as "partial reset area" for larger grains in Fig. 4.12). These relationships lead to the gradient and plateau in the age versus grain size diagram (Curve A in Fig. 4.2). The shearing experiments thus support the plateau method in which grains smaller than some critical size are believed to have been reset completely at certain conditions (displacement and normal stress to the fault plane).

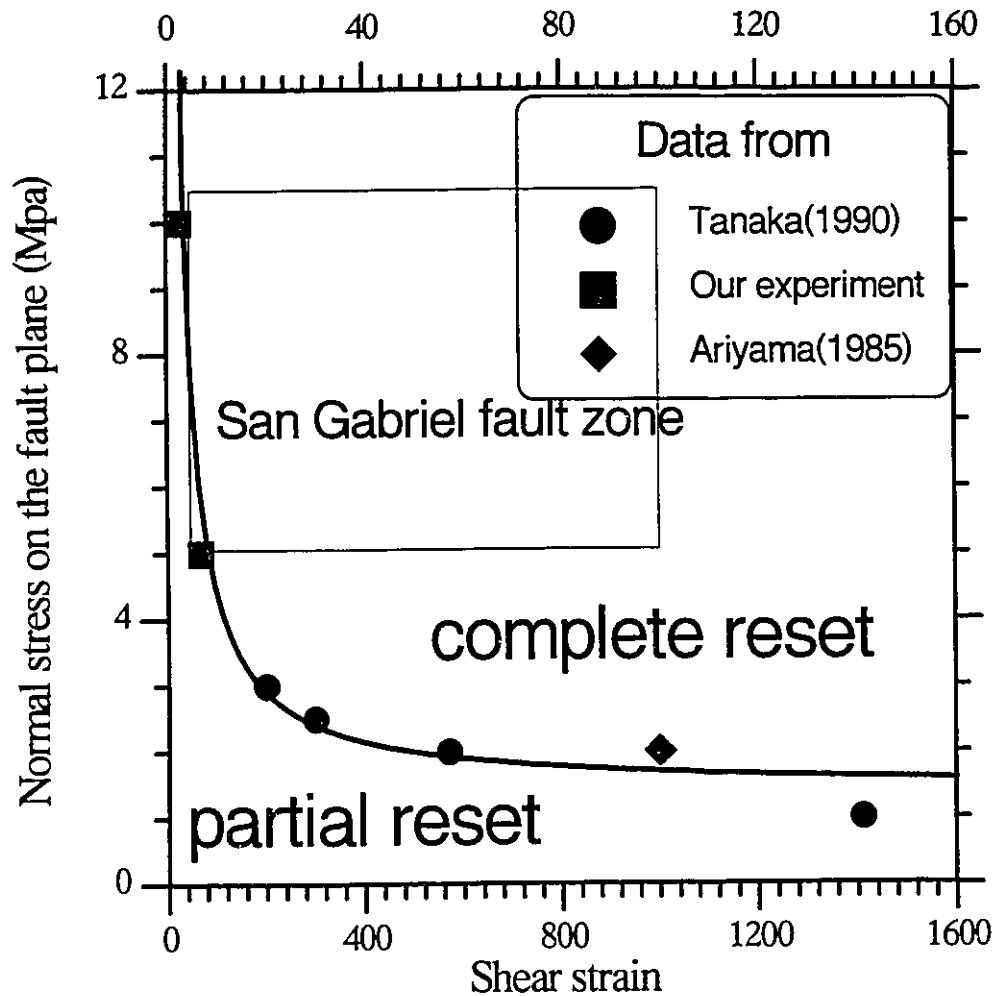


Figure 4.11. Complete resetting conditions for  $E'$  signals as determined by the shearing experiments, in which normal stress and displacement was controlled (grain size; 75-250  $\mu\text{m}$ ). Stress conditions in the San Gabriel fault zone are estimated from the measured stress in Southern California by several researchers (McGarr et al., 1982; Stock and Healy, 1988; Hickman et al., 1988). The mean slip calculated from elastic dislocation theory ranges from 4 cm (M 4) to 1 m (M 7).

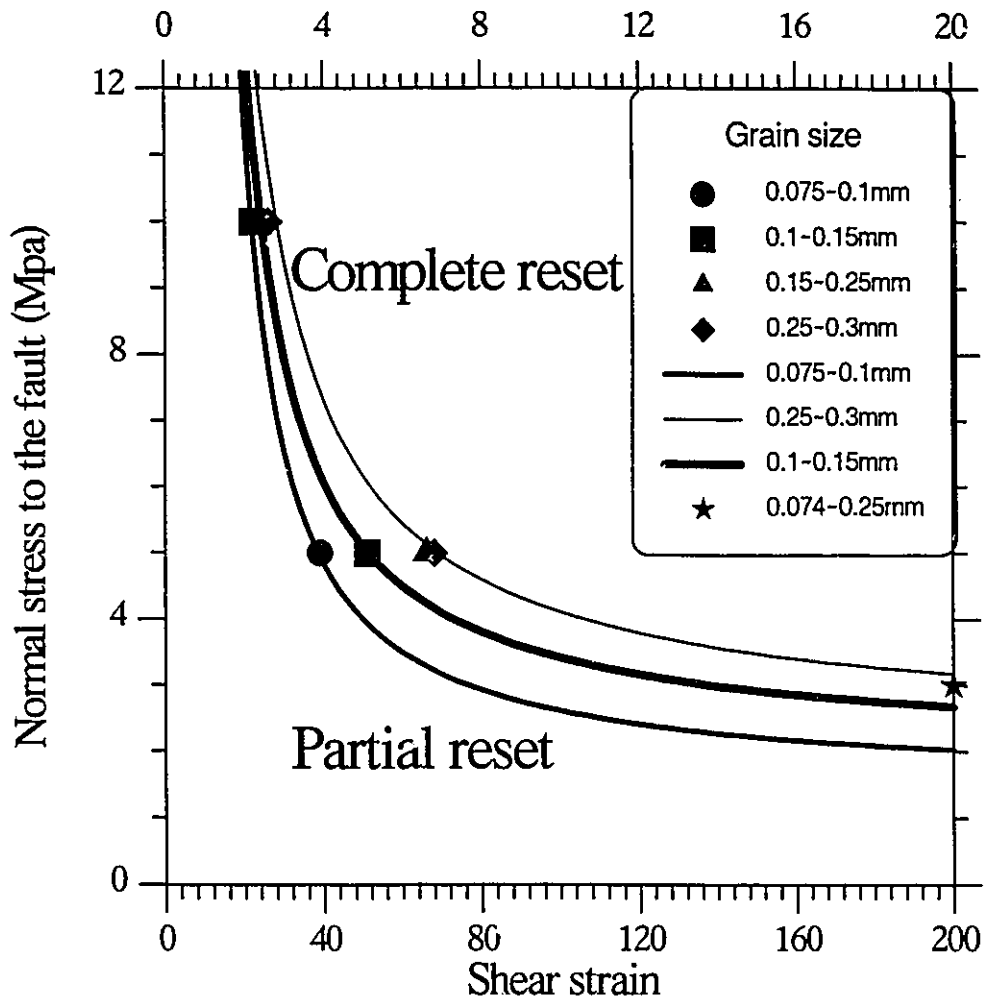


Figure 4.12. Complete resetting conditions for different grain sizes (lower shear strain part of figure 4.11). The value represented by the star symbol is from Tanaka's (1990) shearing experiment and the others are from my experiments. Different grain size fractions show different resetting conditions; smaller grains need smaller normal stress and shear strain for complete resetting of the E' signal.



#### **4-4. Field testing of plateau dating method**

In this section, I will test the ESR data, using analysis of fault rocks collected from the San Gabriel fault zone, to compare with plateau model.

Buhay et al. (1988) presented preliminary data for the San Gabriel and San Jacinto faults, demonstrating the plateau pattern in the age vs. grain size. Here, I present further confirmation of the plateau-like behavior of ages in sized fractions of quartz from fault rocks collected along the San Gabriel fault zone near Los Angeles, in California (Fig 4.13).

The San Gabriel fault zone is a dominantly strike-slip fault zone that was formerly the main trace of the San Andreas fault, and that has been intermittently active through the Pleistocene. It traverses the San Gabriel Mountains near Los Angeles, in California. The San Gabriel Mountains have been uplifted at a rate of about 0.3 cm/a through the Holocene and 0.03 cm/a through the Pleistocene (Menges et al., 1979), and therefore we now have access to exposures of gouge which were buried at depths of up to several tens of meters over the past  $10^6$  a. This is critical in assuring that normal stress on the fault plane was sufficient to permit zeroing (see section 4-3-4).

##### **4-4-1. Results of ESR plateau dating**

As described in Chapter 3, size fractions of quartz were prepared from samples

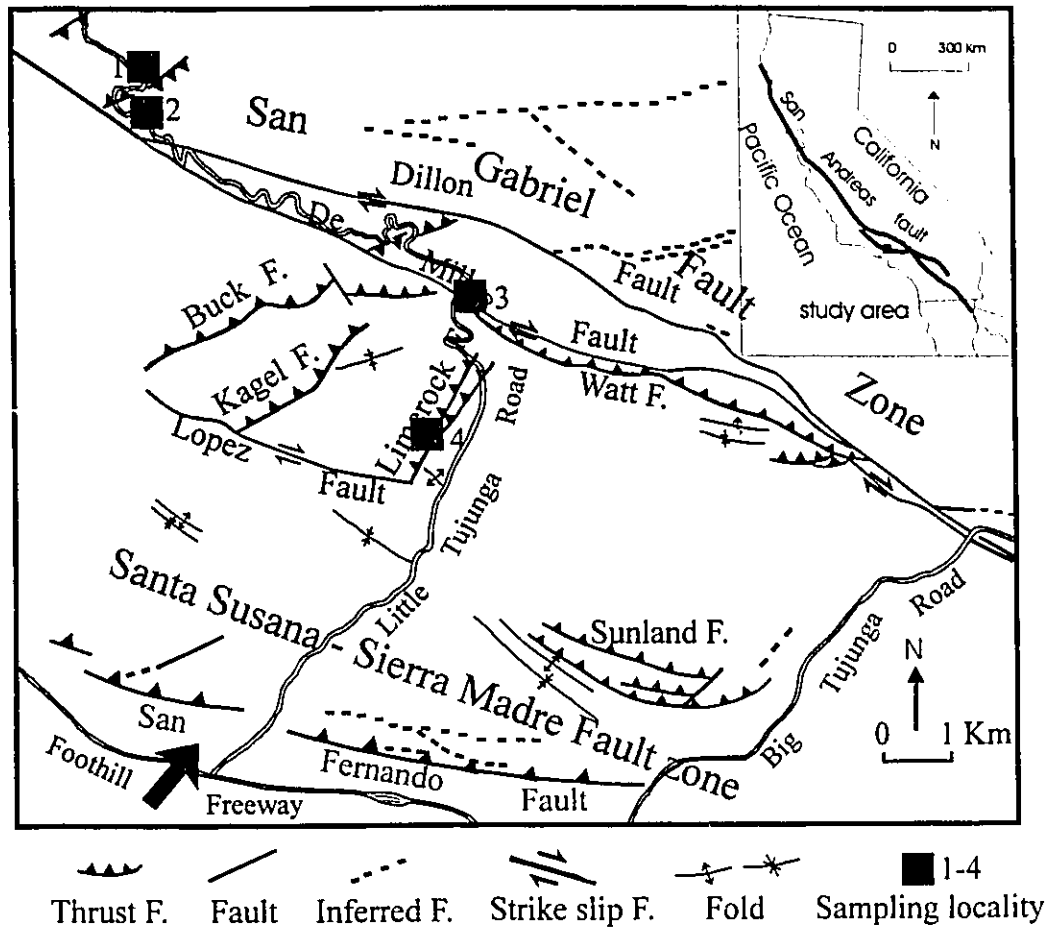


Figure 4.13. Structural map of the Little Tujunga region, showing locations of sample sites; locality 1, Santa Clara Divide fault; locality 2, Bear Divide fault; locality 3, Barrel Spring fault; locality 4, Limerock fault.

collected at localities on figure 4.13. Typical examples of ages calculated from the ESR spectra of size-fractions of quartz are shown in figures 4.14 and 4.15. The ESR data and calculated ages for individual size fractions are presented in Table 4.1 and the weighted mean ages and their error limits are presented in Table 4.2. As expected, the estimated ages for both E' and OHC signals in all fault rock samples analyzed decrease with grain size down to a plateau value for particles smaller than critical grain size. In some cases, the Al signal in the smallest grains yields the same age as the plateau age of either the E' or OHC signal. The estimated ages of smaller grains lying on the plateau would be the true ages of the last fault movement, whereas the ages of larger grains are the apparent ages due to partial resetting of ESR signals at the time of fault movement. Other researchers (e.g. Fukuchi et al., 1986; Fukuchi, 1988) usually used larger grains (105-250  $\mu\text{m}$ ), but my data suggest that larger grains would in most cases give older ages due to incomplete resetting of the ESR signals at the time of fault movement. In the next two chapters, I will discuss the ages obtained in more detail and relate them to the structural history of the region.

The Limerock fault thrusts crystalline rocks over the Pleistocene Saugus formation (Fig. 4.13; locality 4), and is marked by a 1 m wide zone of dark grey gouge. Very well foliated, schist-like gouge (4 cm in width; sample 91004) occurs at the boundary with very coarse sandstone. This gouge yields a plateau of constant E' ages for grains of  $< 75 \mu\text{m}$ . The ages from the Al signal converge to the plateau value for the smallest grain size, and a weighted mean of the E' and Al ages is  $346 \pm 23 \text{ ka}$  (Fig. 4.14).

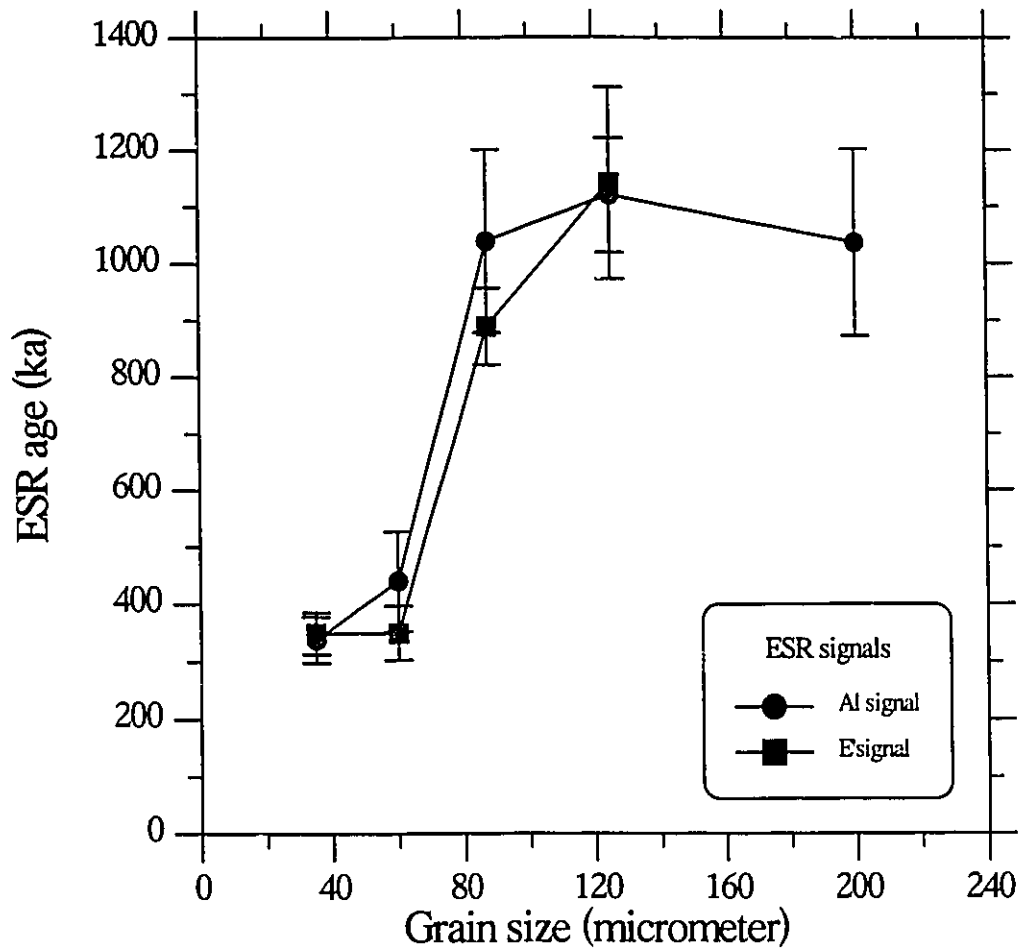


Figure 4.14. Age versus grain size for the E' and Al signals of sample 91004 collected from the Limerock fault (locality 4).

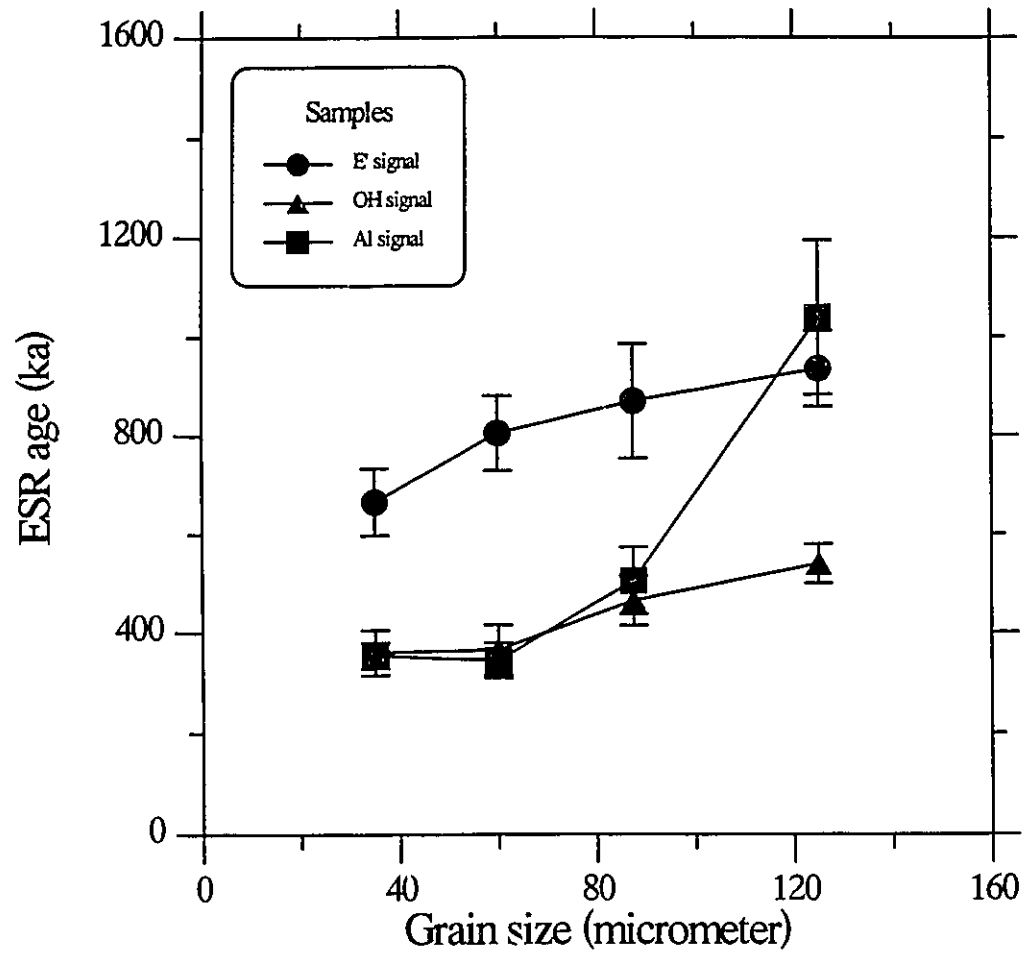


Figure 4.15. Age versus grain size for the E', OHC, and Al signals of sample 91071 collected at the Santa Clara Divide fault (locality 1). The ages estimated for OHC and Al for sample 91071 show the concordant plateau value.

Table 4.1. ESR analytical data and results for fault rocks from the San Gabriel fault zone.

Fault	Sample	Grain size ( $\mu\text{m}$ )	Center	$D_E$ (Gy)	U (ppm)	Th (ppm)	K (%)	*Dose rate ( $\mu\text{Gy/a}$ )	ESR age (ka)	Figure
Limerock	91004B	150-250	AI	2537 $\pm$ 386	1.81	4.58 $\pm$ 0.11	1.78 $\pm$ 0.09	2447 $\pm$ 118	1037 $\pm$ 165	fig.4.14
Limerock	91004C	100-150	E'	2907 $\pm$ 407	1.81	4.58 $\pm$ 0.11	1.78 $\pm$ 0.09	2545 $\pm$ 124	1142 $\pm$ 169	fig.4.14
Limerock	91004C	100-150	AI	2852 $\pm$ 215	1.81	4.58 $\pm$ 0.11	1.78 $\pm$ 0.09	2545 $\pm$ 124	1121 $\pm$ 101	fig.4.14
Limerock	91004D	75-100	E'	2336 $\pm$ 136	1.81	4.58 $\pm$ 0.11	1.78 $\pm$ 0.09	2626 $\pm$ 130	889 $\pm$ 68	fig.4.14
Limerock	91004D	75-100	AI	2728 $\pm$ 402	1.81	4.58 $\pm$ 0.11	1.78 $\pm$ 0.09	2626 $\pm$ 130	1039 $\pm$ 161	fig.4.14
Limerock	91004E	45- 75	E'	954 $\pm$ 119	1.81	4.58 $\pm$ 0.11	1.78 $\pm$ 0.09	2727 $\pm$ 139	350 $\pm$ 47	fig.4.14
Limerock	91004E	45- 75	AI	1199 $\pm$ 228	1.81	4.58 $\pm$ 0.11	1.78 $\pm$ 0.09	2727 $\pm$ 139	440 $\pm$ 87	fig.4.14
Limerock	91004F	<45	E'	1018 $\pm$ 88	1.81	4.58 $\pm$ 0.11	1.78 $\pm$ 0.09	2905 $\pm$ 160	350 $\pm$ 36	fig.4.14
Limerock	91004F	<45	AI	986 $\pm$ 102	1.81	4.58 $\pm$ 0.11	1.78 $\pm$ 0.09	2905 $\pm$ 160	339 $\pm$ 40	fig.4.14
Barrel Spring	91030C	100-150	OHC	2786 $\pm$ 113	1.86	6.45 $\pm$ 0.15	1.99 $\pm$ 0.10	2910 $\pm$ 140	958 $\pm$ 60	fig.4.17
Barrel Spring	91030D	75-100	OHC	2755 $\pm$ 151	1.86	6.45 $\pm$ 0.15	1.99 $\pm$ 0.10	3005 $\pm$ 147	917 $\pm$ 67	fig.4.17
Barrel Spring	91030D	75-100	E'	2370 $\pm$ 281	1.86	6.45 $\pm$ 0.15	1.99 $\pm$ 0.10	3005 $\pm$ 147	789 $\pm$ 101	fig.4.17
Barrel Spring	91030E	45- 75	OHC	2456 $\pm$ 218	1.86	6.45 $\pm$ 0.15	1.99 $\pm$ 0.10	3125 $\pm$ 159	786 $\pm$ 80	fig.4.17
Barrel Spring	91030E	45- 75	E'	716 $\pm$ 56	1.86	6.45 $\pm$ 0.15	1.99 $\pm$ 0.10	3125 $\pm$ 159	229 $\pm$ 21	fig.4.17
Barrel Spring	91030F	<45	OHC	1605 $\pm$ 162	1.86	6.45 $\pm$ 0.15	1.99 $\pm$ 0.10	3337 $\pm$ 184	481 $\pm$ 55	fig.4.17
Barrel Spring	91030F	<45	E'	796 $\pm$ 38	1.86	6.45 $\pm$ 0.15	1.99 $\pm$ 0.10	3337 $\pm$ 184	238 $\pm$ 17	fig.4.17
Barrel Spring	91031C	100-150	OHC	5943 $\pm$ 761	1.87	9.17 $\pm$ 0.19	2.18 $\pm$ 0.11	3316 $\pm$ 158	1792 $\pm$ 245	fig.4.17
Barrel Spring	91031C	100-150	E'	786 $\pm$ 88	1.87	9.17 $\pm$ 0.19	2.18 $\pm$ 0.11	3316 $\pm$ 158	237 $\pm$ 29	fig.4.17
Barrel Spring	91031D	75-100	OHC	2242 $\pm$ 251	1.87	9.17 $\pm$ 0.19	2.18 $\pm$ 0.11	3431 $\pm$ 167	653 $\pm$ 80	fig.4.17
Barrel Spring	91031D	75-100	E'	789 $\pm$ 78	1.87	9.17 $\pm$ 0.19	2.18 $\pm$ 0.11	3431 $\pm$ 167	230 $\pm$ 25	fig.4.17
Barrel Spring	91031E	45- 75	OHC	2185 $\pm$ 246	1.87	9.17 $\pm$ 0.19	2.18 $\pm$ 0.11	3576 $\pm$ 182	611 $\pm$ 76	fig.4.17
Barrel Spring	91031E	45- 75	E'	836 $\pm$ 41	1.87	9.17 $\pm$ 0.19	2.18 $\pm$ 0.11	3576 $\pm$ 182	234 $\pm$ 17	fig.4.17
Barrel Spring	91031F	<45	OHC	1465 $\pm$ 223	1.87	9.17 $\pm$ 0.19	2.18 $\pm$ 0.11	3832 $\pm$ 214	382 $\pm$ 62	fig.4.17
Barrel Spring	91031F	<45	E'	877 $\pm$ 47	1.87	9.17 $\pm$ 0.19	2.18 $\pm$ 0.11	3832 $\pm$ 214	229 $\pm$ 18	fig.4.17
Santa Clara	91071C	100-150	OHC	1367 $\pm$ 74	1.29	2.82 $\pm$ 0.13	2.07 $\pm$ 0.10	2530 $\pm$ 128	540 $\pm$ 40	fig. 4.15
Santa Clara	91071C	100-150	E'	2367 $\pm$ 154	1.29	2.82 $\pm$ 0.13	2.07 $\pm$ 0.10	2530 $\pm$ 128	936 $\pm$ 77	fig.4.15
Santa Clara	91071C	100-150	AI	2628 $\pm$ 372	1.29	2.82 $\pm$ 0.13	2.07 $\pm$ 0.10	2530 $\pm$ 128	1039 $\pm$ 156	fig.4.15
Santa Clara	91071D	75-100	OHC	1202 $\pm$ 115	1.29	2.82 $\pm$ 0.13	2.07 $\pm$ 0.10	2592 $\pm$ 132	464 $\pm$ 50	fig.4.15
Santa Clara	91071D	75-100	E'	2255 $\pm$ 277	1.29	2.82 $\pm$ 0.13	2.07 $\pm$ 0.10	2592 $\pm$ 132	870 $\pm$ 116	fig.4.15
Santa Clara	91071D	75-100	AI	1309 $\pm$ 162	1.29	2.82 $\pm$ 0.13	2.07 $\pm$ 0.10	2592 $\pm$ 132	505 $\pm$ 68	fig.4.15
Santa Clara	91071E	45- 75	OHC	974 $\pm$ 123	1.29	2.82 $\pm$ 0.13	2.07 $\pm$ 0.10	2665 $\pm$ 137	365 $\pm$ 50	fig.4.15
Santa Clara	91071E	45- 75	E'	2145 $\pm$ 170	1.29	2.82 $\pm$ 0.13	2.07 $\pm$ 0.10	2665 $\pm$ 137	805 $\pm$ 76	fig.4.15
Santa Clara	91071E	45- 75	AI	918 $\pm$ 79	1.29	2.82 $\pm$ 0.13	2.07 $\pm$ 0.10	2665 $\pm$ 137	344 $\pm$ 35	fig.4.15
Santa Clara	91071F	<45	OHC	1004 $\pm$ 114	1.29	2.82 $\pm$ 0.13	2.07 $\pm$ 0.10	2789 $\pm$ 149	360 $\pm$ 45	fig.4.15

Santa Clara	91071F	<45	E'	1857±160	1.29	2.82±0.13	2.07±0.10	2789±149	666± 68	fig.4.15
Santa Clara	91071F	<45	AI	988± 52	1.29	2.82±0.13	2.07±0.10	2789±149	354± 27	fig.4.15
Bear Divide	SG40C	100-150	OHC	1047±132	0.54	0.68±0.12	1.03±0.17	1181±164	887±166	fig.4.16
Bear Divide	SG40C	100-150	E'	2155±194	0.54	0.68±0.12	1.03±0.17	1181±164	1826±302	fig.4.16
Bear Divide	SG40D	75-100	OHC	1033±161	0.54	0.68±0.12	1.03±0.17	1204±166	858±178	fig.4.16
Bear Divide	SG40D	75-100	E'	1670±198	0.54	0.68±0.12	1.03±0.17	1204±166	1387±252	fig.4.16
Bear Divide	SG40E	45- 75	OHC	1017± 65	0.54	0.68±0.12	1.03±0.17	1230±168	826±125	fig.4.16
Bear Divide	SG40E	45- 75	E'	1210±108	0.54	0.68±0.12	1.03±0.17	1230±168	984±160	fig.4.16
Bear Divide	SG40F	<45	OHC	1056± 69	0.54	0.68±0.12	1.03±0.17	1273±170	830±123	fig.4.16
Bear Divide	SG40F	<45	E'	1013±140	0.54	0.68±0.12	1.03±0.17	1273±170	796±153	fig.4.16
Bear Divide	SG41C	100-150	OHC	943±130	0.54	0.44±0.13	1.98±0.16	2047±165	461± 74	fig.4.16
Bear Divide	SG41C	100-150	E'	1932±234	0.54	0.44±0.13	1.98±0.16	2047±165	944±137	fig.4.16
Bear Divide	SG41D	75-100	OHC	943± 89	0.54	0.44±0.13	1.98±0.16	2078±167	454± 56	fig.4.16
Bear Divide	SG41D	75-100	E'	1524±280	0.54	0.44±0.13	1.98±0.16	2078±167	734±147	fig.4.16
Bear Divide	SG41E	45- 75	OHC	767± 45	0.54	0.44±0.13	1.98±0.16	2109±169	363± 36	fig.4.16
Bear Divide	SG41E	45- 75	E'	1351±172	0.54	0.44±0.13	1.98±0.16	2109±169	640± 96	fig.4.16
Bear Divide	SG41F	<45	OHC	759± 21	0.54	0.44±0.13	1.98±0.16	2154±171	352± 30	fig.4.16
Bear Divide	SG41F	<45	E'	773± 31	0.54	0.44±0.13	1.98±0.16	2154±171	359± 32	fig.4.16
Bear Divide	SG44C	100-150	E'	2850±209	0.54	0.68±0.12	1.03±0.17	1181±164	2414±379	fig.4.16
Bear Divide	SG44D	75-100	E'	2315±130	0.54	0.68±0.12	1.03±0.17	1204±166	1923±286	fig.4.16
Bear Divide	SG44E	45- 75	E'	1518±183	0.54	0.68±0.12	1.03±0.17	1230±168	1234±225	fig.4.16
Bear Divide	SG44F	<45	E'	1457± 58	0.54	0.68±0.12	1.03±0.17	1273±170	1145±160	fig.4.16

\* Note that dose rate varies because of varying  $\alpha$  and  $\beta$  doses as function of grain size.

Table 4.2. Examples of times of last movement on faults determined by the ESR dating method; dates are given only for samples lying on plateaus.

Fault	Sample	Grain size ( $\mu\text{m}$ )	ESR signal	ESR age (ka)	#Weighted mean (ka)
Limerock	91004E	45-75	E'	350 $\pm$ 47	
Limerock	91004F	<45	E'	350 $\pm$ 36	346 $\pm$ 23
Limerock	91004F	<45	AI	339 $\pm$ 40	
<sup>1</sup> Barrel Spring	91030E	45-75	E'	225 $\pm$ 21	234 $\pm$ 13
Barrel Spring	91030F	<45	E'	238 $\pm$ 17	
Barrel Spring	91031C	100-150	E'	237 $\pm$ 29	
Barrel Spring	91031D	75-100	E'	230 $\pm$ 25	241 $\pm$ 10
Barrel Spring	91031E	45-75	E'	234 $\pm$ 17	
Barrel Spring	91031F	<45	E'	229 $\pm$ 19	*(238 $\pm$ 8)
Santa Clara	91071E	45-75	OHC	365 $\pm$ 50	
Santa Clara	91071E	45-75	AI	344 $\pm$ 35	354 $\pm$ 18
Santa Clara	91071F	<45	OHC	360 $\pm$ 45	
Santa Clara	91071F	<45	AI	354 $\pm$ 26	
<sup>2</sup> Bear Divide	SG40D	75-100	OHC	858 $\pm$ 178	
Bear Divide	SG40E	45-75	OHC	826 $\pm$ 125	824 $\pm$ 70
Bear Divide	SG40F	<45	OHC	830 $\pm$ 123	
Bear Divide	SG40F	<45	E'	796 $\pm$ 153	
Bear Divide	SG41E	45-75	OHC	363 $\pm$ 36	
Bear Divide	SG41F	<45	OHC	352 $\pm$ 30	357 $\pm$ 19
Bear Divide	SG41F	<45	E'	359 $\pm$ 32	
Bear Divide	SG44E	45-75	E'	1234 $\pm$ 225	1173 $\pm$ 130
Bear Divide	SG44F	<45	E'	1145 $\pm$ 160	

# The weighted mean is given by :  $\bar{Y} = (Y_1 / S_1^2 + Y_2 / S_2^2 + \dots) / (1 / S_1^2 + 1 / S_2^2 + \dots)$ , and the error limits on the weighted mean are given by:  $\bar{S} = \{1 / (1/S_1^2 + 1/S_2^2 + \dots)\}^{1/2}$  where  $Y_1, Y_2, Y_3 \dots$  etc. are the individual ages of different size fraction or ESR signals, and  $S_1, S_2, S_3 \dots$  etc. are the individual quoted error limits.

\* The weighted mean age (6 fractions) of two subsamples from the Barrel Spring fault.

1. Two subsamples (50cm apart) were collected from the Barrel Spring fault.
2. The fault breccia (SG44) zone was cut by a fault gouge zone (SG40) which was reactivated (SG41) in the central part (see Fig.4.16).



The Santa Clara Divide fault developed in the Mendenhall gneiss in Domain 4 (Fig. 4.13; locality 1). The gouge zones branched and recombined on a scale of a few meters; some were later reactivated. The older gouge is massive, but the reactivated gouge is well foliated indicating severe cataclastic flow during the last fault movement near the surface. Sample 91071 is from a reactivated well-foliated fault gouge zone on the footwall side of the main gouge zone. Both the OHC and Al centers for sample 91071 show the same age plateau (Fig. 4.15), but E' does not converge with this plateau value. The weighted mean of four ages for 91071 lying on the plateau is  $354 \pm 18$  ka.

A critical test of this dating method is to show that the sequence of ages obtained by ESR analysis agrees with the sequence indicated by geological relationships. A good example is that shown in figure 4.16. Here granitic gneiss has been brecciated in a zone 10-15 cm wide. This zone was later cut by a fault, producing a gouge zone. The central part of that gouge can be seen to have been later reactivated. Finally, there was renewed movement along one of the faults bounding the breccia zone. Samples of the breccia, the primary gouge zone, and the reactivated central part of the latter give ages of  $1173 \pm 130$ ,  $824 \pm 70$  and  $357 \pm 19$  ka, respectively (Fig. 4.16; note that the zone of last motion along the breccia zone was too thin to sample). The two youngest dates are confirmed by convergence of OHC and E' ages with decreasing grain size. Thus we see that the sequence of ESR ages agrees with the geologically determined sequence, and indicates the relatively long intervals between each of these events.

I also find that two subsamples collected from a single fault gouge zone show

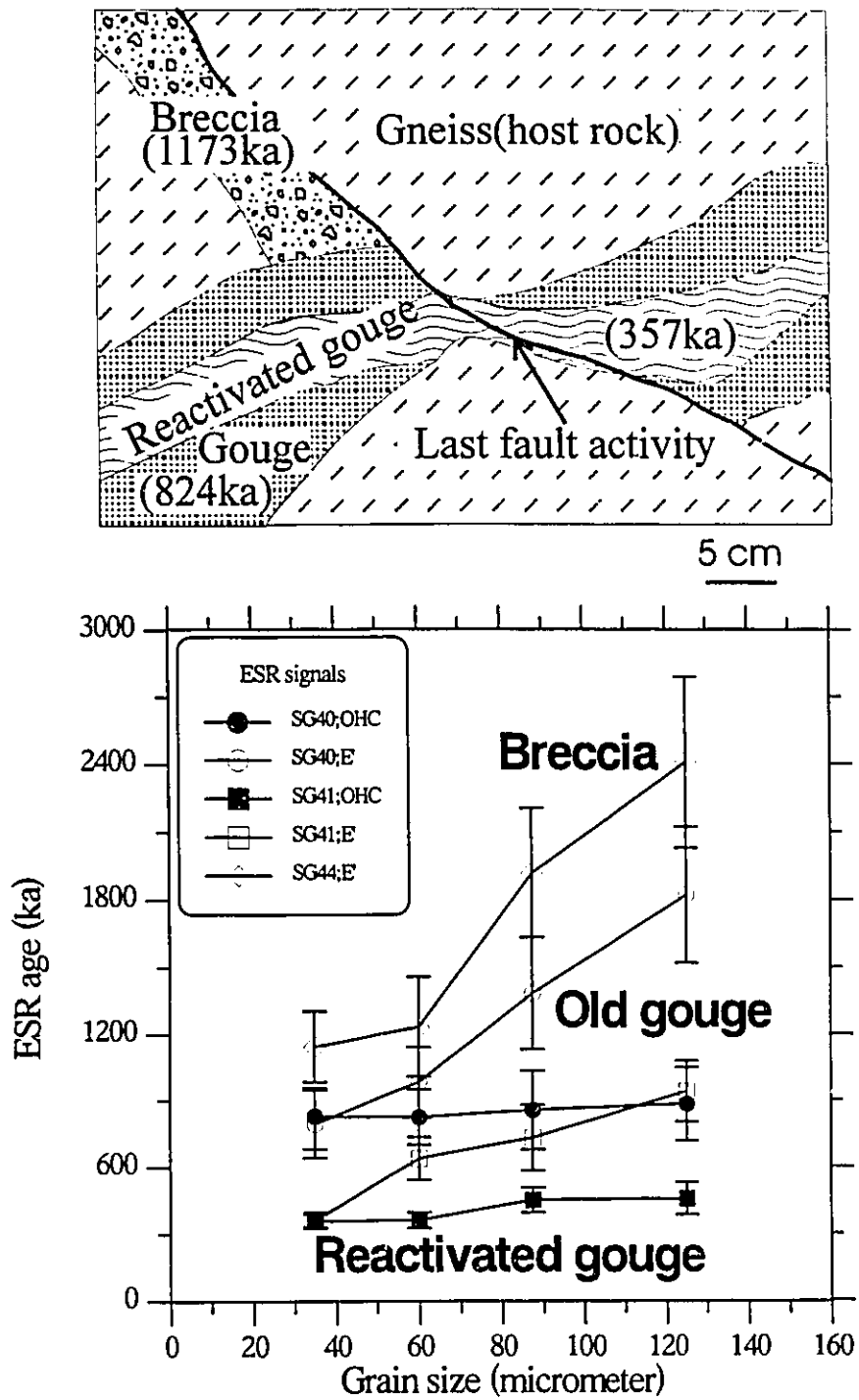


Figure 4.16. Intersection relationships and age versus grain size of the Bear Divide fault (locality 2).

consistent ESR age estimates. A good example is the data set of samples 91030 and 91031 collected from Barrel Spring fault in Domain 3 (Fig 4.13; locality 3). A gouge zone about 2.5 m wide is developed here between fractured gneiss and Quaternary terrace deposits. Sample 91031 was collected from the boundary between gouge and sedimentary rocks and 91030 was collected from 50 cm towards the center from this boundary. The E' signal of larger grains ( $>100\ \mu\text{m}$ ) of sample 91030 is too small to measure, whereas those of smaller grains are big enough to measure. This indicates that the precursors of E' signal were created by comminution during fault movement (Fukuchi,1989, Lee and Schwarcz, 1993). The lowest ages were found for the E' center of both samples (Fig. 4.17) and this age was the same in both samples. Furthermore, these ages were uniform in all particle sizes for sample 91031. This suggests that deformation was stronger in the boundary than inside the fault gouge zone; in effect,  $r_c$  was larger in the more intensely sheared sample. The ages of OHC for both samples decrease with decreasing grain sizes, but do not converge to a plateau, showing only partial resetting at the time of fault movement. These data show that, even though the ESR spectra from subsamples taken at different positions in the same gouge zone are different, the estimated ages are consistent. The varying ESR age vs. grain size data indicate inhomogeneous strain distribution within gouge zone. This also confirms that resetting occurred uniformly below some critical grain size through a large volume of fault gouge, and not just along a narrow zone of sliding. The weighted mean of ages of these samples is  $238 \pm 8$  ka.

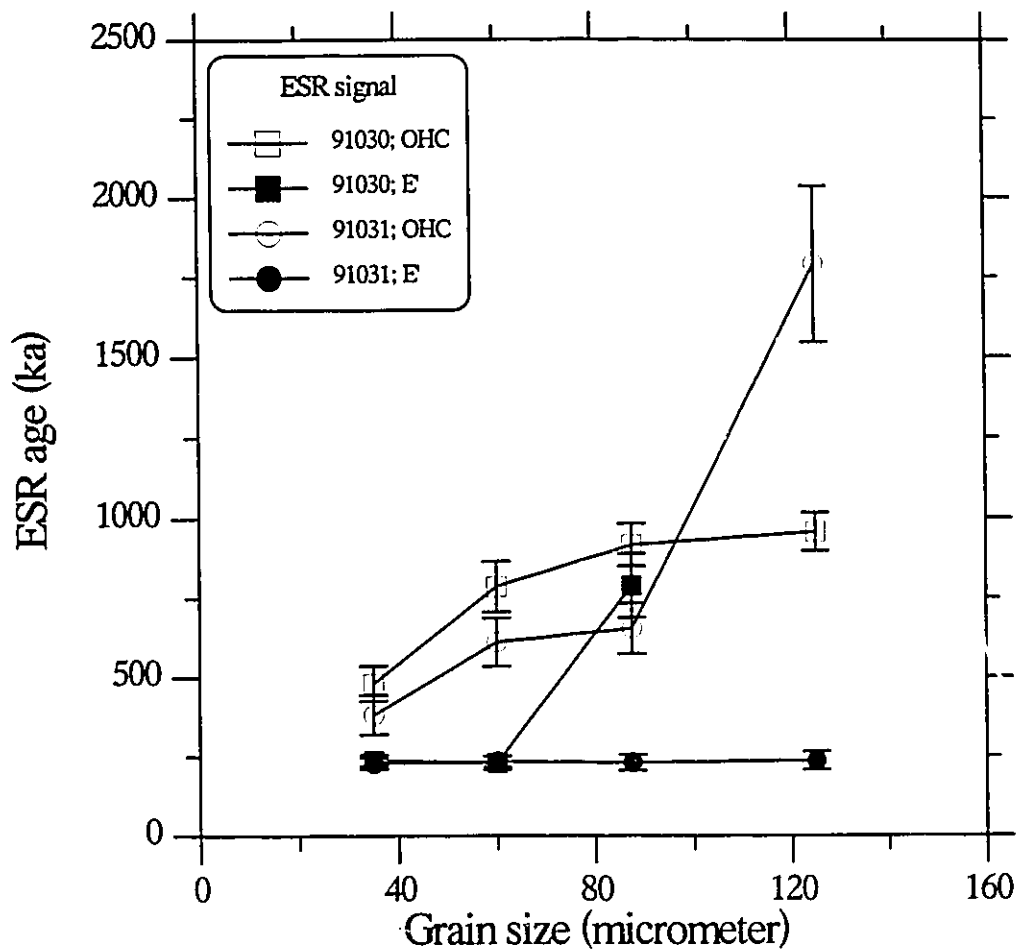


Figure 4.17. Age versus grain size for E' and OHC signals of samples 91030 and 91031 collected at the Barrel Spring fault (locality 3). Two subsamples from the same fault show a concordant plateau for the E' signal.

#### **4-4-2. Discussion**

##### **4-4-2-1. Validity of the plateau method and the resetting mechanism**

The ESR data presented here for fault gouge from the San Gabriel fault zone consistently demonstrate that finer grains exhibit lower ESR ages than coarser grains, and that there is a convergence to a plateau for some signals, and a general convergence of all ESR dates to the plateau age. These data are consistent with the results of experimental studies of the resetting of ESR signals, which showed that finer grains are more reset than larger ones during shearing (Ikeya et al., 1982; Fukuchi et al., 1986; Lee and Schwarcz, 1993). Both the field-based and experimental studies suggest that shear strain alone can zero the ESR signals in quartz, but the exact mechanism by which this occurs is as yet unclear.

I now envision that at least two mechanisms may play a part: release of trapped charges during deformation of the quartz crystals; and local heating at grain/grain contacts.

First, let us consider the direct effects of shearing on the quartz grains that might be the cause of ESR signal zeroing. Experimental studies have shown that the number of E' centers near the surface of quartz grains increase as a result of crushing (Walters and Estle, 1961; Arends et al., 1963; Hochstrasser and Antonini, 1972). This process alone would tend to have the reverse effect to that which we observe. My shearing experiments

(Fig. 4.4) also showed that smaller fragments of quartz have larger ESR intensity than the unsheared quartz, but with further shearing the intensity decreases.

The increase in zeroing with decreasing grain size could not be due to zeroing by fracturing alone, because the amount of fracturing experienced by a grain actually decrease as a function of grain size. Therefore, there must be some process acting on already-fractured grains which leads to zeroing. As the grains are loaded during shearing events, stress tends to be concentrated around defects within each grain, resulting in development of distributed microcracks. These then coalesce to form intra- and inter-grain fractures (Scholz, 1990). E' and OHC centers can form at vacancies located at such defects: points, lines (dislocations), or surfaces (microcracks or grain surfaces).

A possible resetting mechanism for ESR centers found at such defects is as follows. During grain boundary frictional sliding, the above mechanism of stress concentration leads to bond breaking. Therefore, pre-existing vacancies (unsatisfied bonds) which were decorated with E' or OHC centers tend to be displaced, allowing charges trapped at these sites to recombine. Similarly, impurity sites (Al, Ti) can migrate during this deformation, and trapped charges associated with them can be released to recombine with holes. Essentially, the effect of stress is to produce localized, atomic-scale diffusion of oxygen and impurity atoms just far enough to permit delocalization of associated trapped charges.

These effects will tend to be strongest at points of grain impingement where stress concentration is highest (Kranz, 1983). Therefore, the volume fraction of the grain that

is affected by these processes increases with decreasing grain size. We can envision a quasi-spherical zone or radius  $R$  around each point of impingement in which the stress-concentration is high enough to zero the ESR signal (Fig. 4.18); for grains smaller than some critical radius  $r_c \approx 2R$ , the entire grain will be zeroed. Thus, the zeroing, by this mechanism is essentially due to breaking of Si-O bonds in the path of microcracks (see Lloyd and Knipe, 1992). Blenkinsop and Rutter (1986) found that the density of microcracks was much higher in quartz grains from fault rocks than in adjacent quartzite host rock. Note that the same process can develop precursors of E' signals (Fukuchi, 1989; Buhay, 1991; Fukuchi, 1992a).

Studies of simulated fault gouge by Marone and Scholz (1989) showed that shearing within a layer of gouge is inhomogeneous, and is concentrated at minor shear bands. The same fine-scale shear bands are seen to be developed in natural fault gouge (Chester and Logan, 1987) and strain is concentrated on these shear bands in the matrix of a fault gouge zone, during the later stages of shearing. As a result, small grains (which are dominantly found in these shear zones) have more chance to be sheared than larger ones. During this stage of shearing, frictional grain-boundary sliding and rotation of fragments predominates over fracturing.

Now, let us consider possible zeroing by frictional heating. Localized heating can also account for the grain-size dependence of the ESR ages. This model of zeroing should, however, be clearly distinguished from the mechanism of zeroing by heating as proposed, for example, by Fukuchi (1989, 1992b). In that model, the temperature of the

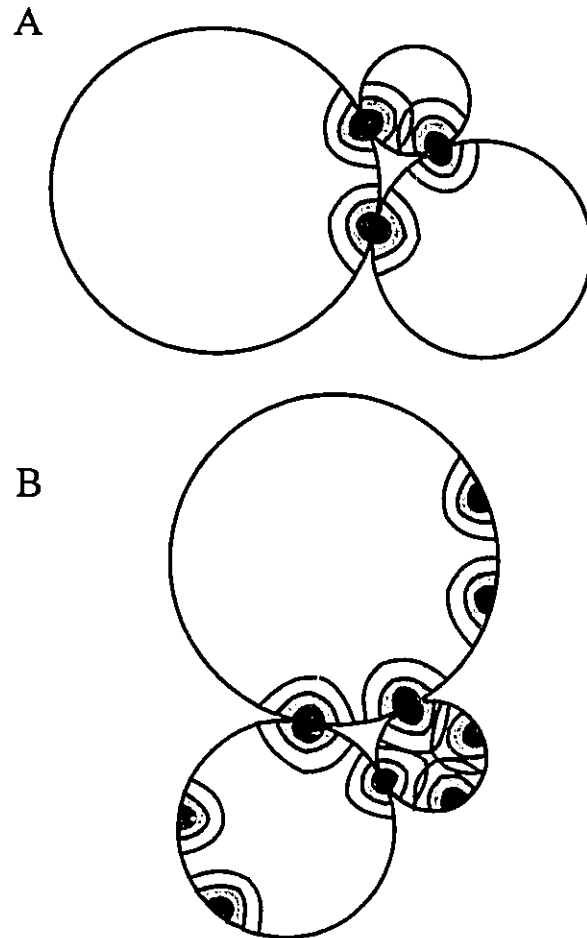


Figure 4.18. Schematic diagram of grain contacts deformation. Contours represent the degree of deformation, local frictional heating, and zeroing of ESR signals on the grain contacts, increasing with the shading density. The gradient of zeroing of ESR signals is dependent on deformation factors such as temperature, pressure, pore fluid, strain rate, composition of gouge, grain size distribution, and history of deformation of quartz grains. Note that contours are not dependent on the grain size; the proportion of resetting of ESR signals increase with decreasing grain size and displacement. A; an early stage of shearing; B; by repetition of shearing and reorientation process, resetting of ESR signals is increased at the later stages of shearing.



entire mass of fault-gouge is raised by generation of frictional heat on the fault plane. There are several problems with this model of zeroing by bulk heating of the gouge.

First, we would expect that the main heating would only occur within a few mm of the fault boundary, since this is the zone of most intense heat-generation. I have shown in this study, however, that gouge samples collected within the interior of broad zones of fault gouge (10 to 200 cm wide) have all been zeroed at the same time. Because of the low thermal conductivity of fault gouge (Scholz, 1990), frictional heat generated at the fault plane cannot have been efficiently transported to the interior of the zones of fault gouge to an extent sufficient for resetting of ESR signals. Some estimate of the actual temperatures experienced by cataclasite (gouge) is seen in the work of Anderson et al. (1983), who studied the mineral assemblages in cataclasite of the San Gabriel fault. They assigned it to the laumontite-chlorite zone of the zeolite facies, corresponding to a temperature of 200 °C, but at a depth of 2 to 5 km. By contrast, I find that the depth of burial gouge of the San Gabriel fault zone at the time of resetting of ESR signals was between 40 and 360 m. there is no evidence of high-temperature, low-pressure metamorphism in the fault gouge as would be expected in a model of resetting by heating  $T \gg 200 \text{ }^\circ\text{C}$  (Fukuchi, 1989, 1992b).

This model of zeroing of ESR signals by heating of the bulk fault gouge (rather than just the finest grains) encounters another problem, when we consider the plateau data themselves. Diffusion of heat through the entire mass of the fault gouge would result in zeroing of all grains to the same extent, regardless of their size. This is contrary to our

observation that the equivalent doses (and thus, the ages) of grains decreases with decreasing grain size. Therefore, it is hard to see how frictional heat diffusing from the fault plane can be responsible for zeroing.

Now consider frictional heating at grain/grain contact. As strain energy is dissipated during a deformation event, it will inevitably result in some temperature rise. This will take place to the greatest extent at the points of maximum deformation, that is, the points of impingement and stress concentration on the grain surfaces. Just as in the previous model where localized volumes of material are zeroed by lattice deformation, we can likewise envision that the zone of most intense heating will be a hemisphere of radius  $R$  centered about a grain/grain contact. During the shear event, heat dissipation from shear strain in this volume leads to a rise of temperature above some critical temperature  $T_c$  at which ESR signals are totally zeroed. As with strain-induced zeroing, the volume fraction of each grain that is zeroed in this way is greater for smaller grains. Grains with radius  $r_c < 2R$  will be totally zeroed.

The model of localized frictional heating which I have proposed also has some problems, especially in accounting for the increase in sensitivity of the  $E'$  center during shearing, as is observed in natural and artificially sheared samples of fault gouge. This can, on the other hand, be explained by the model of deformation-induced zeroing, which produces both reduction of ESR age, and increase in at least  $E'$  sensitivity with decreasing grain size. I see this effect in my data, for example, in figure 4.19 which shows that, for  $E'$  signals of sample 91004, the smaller grain sizes show increasing radiation sensitivities

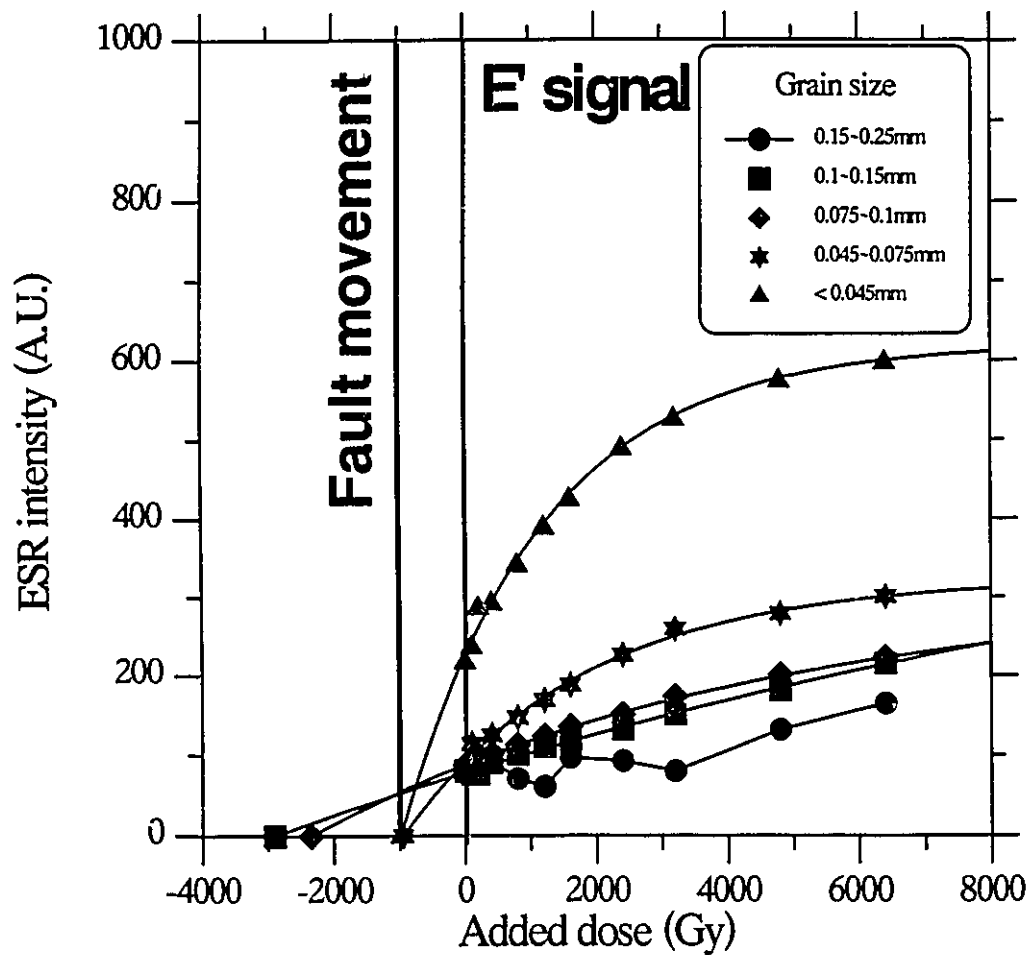


Figure 4.19. Growth curves for the E' signal of sample 91004 collected at the Limerock fault (locality 4) where very coarse sandstone was converted to well foliated fault gouge. The largest grain size fractions show fluctuations with added dose due to the saturation.

with decreasing grain size. Nevertheless, the two finest fractions (< 44  $\mu\text{m}$  and 45-74  $\mu\text{m}$ ) converge to the same  $D_E$  indicating complete resetting during the last fault movement. The largest grains (150-250  $\mu\text{m}$ ) show fluctuation in intensity which appears to be characteristic of grains in ESR saturation.

In general, I believe that the self-consistency of the dating by multiple centers confirms the validity of the plateau method. For example, figure 4.20 shows the growth curves for OHC and Al signals of sample 91071 in the plateau range of the age versus grain size diagram. Even though they have different radiation sensitivities, all of these growth curves converge to the same  $D_E$  value. This also suggests complete resetting of these signals during fault movement. Alternatively, partial resetting of these fractions could coincidentally also lead to the same  $D_E$  value. However, I judge this to be far less likely than complete resetting, since similar convergence is seen in many samples (Table 4.1), for a comparable range of grain sizes.

#### 4-4-2-2. Theoretical estimates of zeroing conditions

Brittle shear failure of intact rock or reactivation of existing faults is described by the Mohr-Coulomb criterion, modified to take account of fluid pressure (Sibson, 1992). This criterion is stated as an equation:

$$\tau = C_0 + (\sigma_n - P_f) \tan \phi \quad (4-1)$$

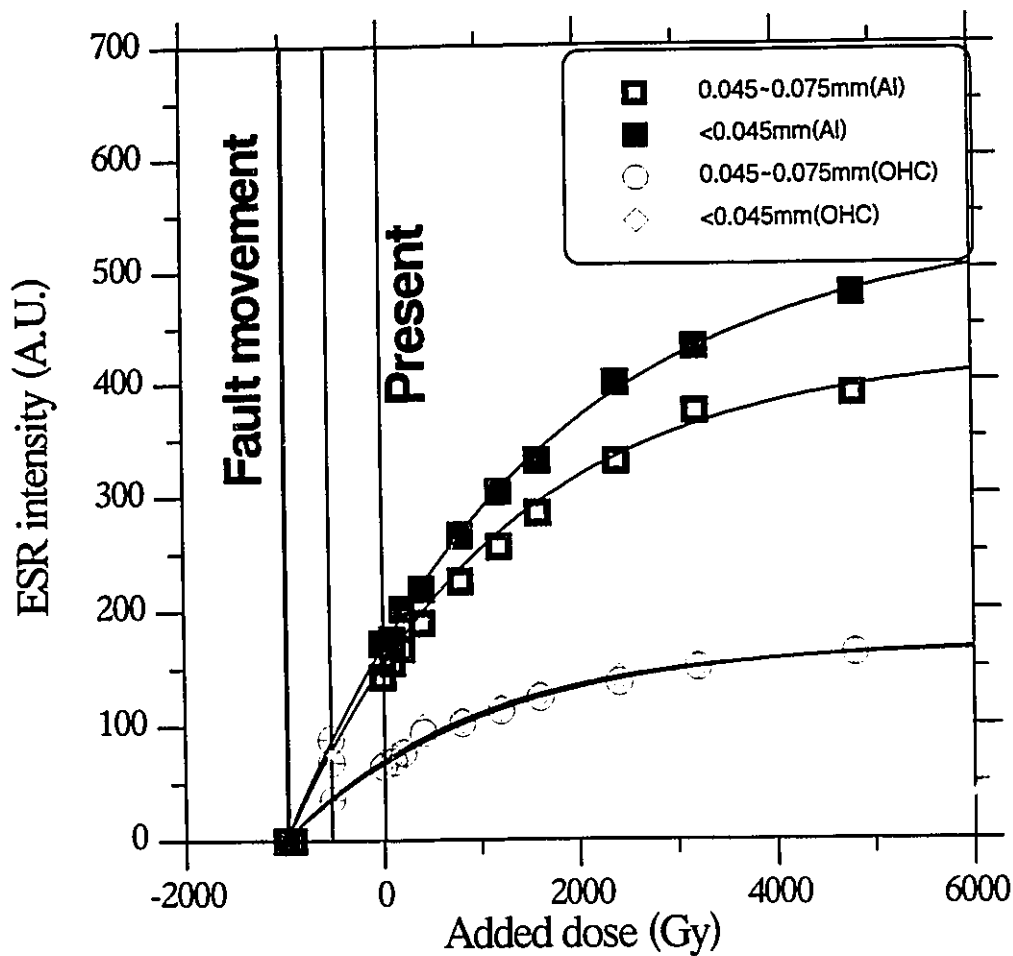


Figure 4.20. Growth curves for the OHC and Al signals of the grains lying on the plateau of age vs. size (sample 91071; locality 1). The growth curves for OHC signals show no differences between grain sizes but the radiation sensitivity of Al is higher than OHC. All curves converge to the same  $D_E$  value indicating complete resetting at the time of fault movement. Alternatively, partial resetting (points  $\oplus$  in the figure) of these fractions could also lead to the same  $D_E$  value. However, I judge this to be far less likely than complete resetting.

where  $\tau$  is the shear stress,  $C_0$  is cohesive strength,  $\sigma_n$  is the normal stress on the eventual fault,  $P_f$  is the fluid pressure and  $\phi$  is the angle of internal friction. The relationship between the angle of friction and the coefficient of static friction ( $\mu_s$ ) is given by:

$$\mu_s = \tan \phi \quad (4-2)$$

so that the shear failure criterion may be written as:

$$\tau = C_0 + (\sigma_n - P_f) \mu_s \quad (4-3)$$

Byerlee (1978) suggested that the surface of the Earth is at zero shear stress, that one of the three principal compressive stresses ( $\sigma_1 > \sigma_2 > \sigma_3$ ) is vertical and that the magnitudes of the horizontal stresses, relative to that of the vertical geostatic stress induced at some depth by gravitational loading, could change. Because the intermediate axis ( $\sigma_2$ ) is contained within the plane of the faults and has, in theory, no influence upon the failure, equation (4-1) may be rewritten :

$$(\sigma'_1 - \sigma'_3) \sin 2\theta = \mu_s [(\sigma'_1 + \sigma'_3) - (\sigma'_1 - \sigma'_3) \cos 2\theta] \quad (4-4)$$

where,  $\sigma'_1 = (\sigma_1 - P_f) > \sigma'_2 = (\sigma_2 - P_f) > \sigma'_3 = (\sigma_3 - P_f)$  are the effective principal stresses and  $\theta$  is the angle between the fault plane and the direction of greatest principal stress.

Therefore, the two-dimensional equations for shear and normal stress on a fault plane are then:

$$\tau = 1/2 (\sigma'_1 - \sigma'_3) \sin 2\theta = 1/2 (\sigma_1 - \sigma_3) \sin 2\theta \quad (4-5)$$

$$\begin{aligned} \sigma_n &= 1/2 [(\sigma'_1 + \sigma'_3) - (\sigma'_1 - \sigma'_3) \cos 2\theta] \\ &= [1/2 \{(\sigma_1 + \sigma_3) - (\sigma_1 - \sigma_3) \cos 2\theta\}] - P_f \end{aligned} \quad (4-6)$$

At a depth,  $h$ , in the crust the effective vertical stress is usually given by

$$\sigma'_v = \sigma_v - P_f = \rho gh (1 - \lambda_v) \quad (4-7)$$

where  $\rho$  is the mean crustal density,  $g$  is the acceleration due to gravity, and the pore fluid factor

$$\lambda_v = P_f / \rho gh \quad (4-8)$$

If we assume that  $\rho = 2.6 \text{ g/cm}^3$  and  $h = 40 \text{ m}$  (see below), and  $\lambda_v = 0.35$  (Sibson, 1992),  $\sigma'_v$  becomes about 0.7 Mpa. In contrast to vertical stress it is not possible to make any a priori estimate of the magnitude of horizontal stresses at depth. However, in situ absolute stress measurements provide some information on the magnitude of horizontal stresses acting in uppermost crust. The increase of horizontal stresses with depth is less than the increase in vertical stress near the surface. The state of horizontal deviatoric stress can

be characterized in terms of two parameters: the maximum horizontal shear stress given by:

$$\tau_m = 1/2 (\sigma_H - \sigma_h) \quad (4-9)$$

and the angle  $\theta$  between the fault plane and the direction of  $\sigma_H$  where,  $\sigma_H$  is the maximum horizontal stress and  $\sigma_h$  is the minimum horizontal stress. Lachenbruch and McGarr (1990) give a summary of measured stress data in the San Andreas fault zone. The data show that the magnitudes of deviatoric stresses are not affected by proximity to the main fault or by their position along the strike of the San Andreas fault. Shear stress in crystalline rocks of the San Andreas fault zone was found to vary with depth according to the equation:

$$\tau_m \text{ (Mpa)} = 1.58 + 7.51 h \text{ (km)} \quad (4-10)$$

If we assume a depth,  $h = 0.04$  km (see below) for the fault rocks at the time of movement in the San Gabriel fault zone,  $\tau_m$  is about 1.9 Mpa;  $\sigma_H$  must be larger than this value (see equation 4-9).

Most large earthquake ruptures ( $M > 6$ ) tend to nucleate in the transition zone from unstable frictional faulting to quasi-plastic shearing flow (10-15km), rupturing upwards and outwards. Because displacement is different spatially in each earthquake fault event,



it is difficult to estimate the amount of displacement at the sampling site during the paleoearthquake. Sibson (1989) calculated that the mean slip can range between 1 mm (Magnitude 1) and 4 m (Magnitude 8). Since displacement increases with depth, the normal stress requirement for complete resetting of ESR signals suggests that the fault rock samples must have been at some depth during the last fault movement.

Rates of late Quaternary uplift were estimated near the mouth of Little Tujunga Canyon by physiographic position,  $^{14}\text{C}$  dating methods, and soil maturity (Menges et al, 1979). They obtained uplift rates of about 0.3 cm/yr for the Holocene and about 0.03 cm/yr for the late Pleistocene. The depth of fault rocks during the last fault movement can thus be estimated from uplift rate and the ESR ages. The youngest fault movement which has been measured was at 40 ka (Buhay et al., 1988). The depth of the fault rock at this time would have been in about 40 m. The faults analysed in this study were oblique reverse faults, thrust faults, and strike slip faults. The maximum horizontal stress at these depth in southern California measured by several researchers range between 5 Mpa and 10 Mpa (McGarr et al., 1982; Hickman et al., 1988; Stock and Healey, 1988). Mount and Suppe (1987) concluded that the vertical principal stress is less than the horizontal such that

$$\sigma_1 \text{ (NE - SW)} > \sigma_2 \text{ (NW- SE)} > \sigma_3 \text{ (vertical)} \quad (4-11)$$

regionally near the San Andreas fault in southern California. At a depth of 70 m, the

calculated vertical stress ( $\sigma'_v = \sigma'_3$ ) is 0.7 Mpa and measured maximum horizontal stress ( $\sigma_H = \sigma'_1$ ) is about 5 Mpa. The angle ( $\theta$ ) between the strike of the San Gabriel fault and the direction of maximum horizontal stress is about  $85^\circ$  (Fig. 4.9). Substituting the above values to the equations of (4-3) and (4-4), the shear stress ( $\tau$ ) on the fault is about 0.67 Mpa and the normal stress ( $\sigma_n$ ) to the fault is about 5 Mpa. If we assume a mean displacement of between 4 cm (M4) and 1 m (M7), then these depths were sufficient to reset ESR signals in quartz below critical grain sizes at the time of fault activity (Fig. 4.11).

#### **4-4-3. Conclusions for field testing of ESR plateau dating method**

I have found that the plateau ages of reactivated younger gouges are indeed smaller than those of older fault host rocks. I conclude that the development of an age plateau for a critical grain size for an ESR signal is an adequate criterion for determination of total resetting. Two or more ESR signals with different zeroing sensitivities show the same age plateau, enhancing the likelihood that resetting was complete, and that the plateau age represents the time of last fault movement. Subsamples collected across and along a fault gouge zone can be used to check the complete zeroing of ESR signals during the last faulting. The plateau ages from individual subsamples would agree only if the resetting had been complete. Theoretically, stresses and shear strains in the Little Tujunga region (at depths of 40 m) were sufficient for complete

zeroing of ESR signals at the time of last recorded movement on the San Gabriel fault zone.

#### **4-5. Summary**

Shearing experiments showed that the intensities of ESR signals decrease as a function of shear strain and normal stress on the shearing plane. It also showed that the smaller size fractions are more efficient in zeroing of ESR signals leading to the plateau in intensity versus size diagram on certain deformation conditions (stress/strain).

Experimental studies showed that the radiation sensitivity of quartz increases with decreasing grain size, as observed in natural gouge. Indeed, the E' signal is absent in unsheared quartz but can be generated by irradiation of sheared quartz.

ESR data from the San Gabriel fault zone showed consistently that the estimated ages decrease with decreasing grain size leading to an age plateau. The plateau ages of reactivated gouges were younger than those of primary fault rocks. The sequence of plateau ages agrees with the sequence of fault movements determined by cross-cutting relationship.

When quartz grains are sheared, the stress will tend to concentrate at vacancies and other lattice imperfections, which may also be the sites of charge trapping. Therefore it seems possible that shearing is capable of zeroing the ESR signals, and to an increasing degree in smaller, more highly strained grains. ESR signals also appear to be reset by

heating on grain contacts during faulting. Therefore, the proportion of resetting of ESR signals increases with decreasing grain size leading to the plateau in age versus size diagram.

Due to the uplift of the San Gabriel Mountains, we have access today to exposures of fault gouge which were buried at the time of their last displacement, at depths of > 40 m. They would therefore have been subjected to sufficient normal stress to permit complete zeroing of ESR signals in the finest quartz grains, during earthquakes of  $M > 4$ . Earthquakes which occurred after this date would not be recorded. In general, this principle limits the minimum age of faulting that we can observe by analysis of surficial exposures of fault gouge and this age will depend on uplift rate.

I conclude that ESR plateau dating method can be used as a criterion of complete zeroing of ESR signals during faulting, based on the results from both experimental and field studies. I also conclude that some normal stress and strain (displacement) are needed in order for zeroing to occur. In order to observe zeroing due to recent movements on faults, it would be necessary to use artificially deepened exposures such as quarries, tunnels, or drill core (Grün, 1992).

## **Chapter 5**

### **Geology of Little Tujunga region**

#### **5-1. Stratigraphy**

The basement rocks in the Little Tujunga region consist of Precambrian Mendenhall gneiss and an anorthosite-gabbro suite of rocks, pre-Cretaceous diorite gneiss and lower Cretaceous granodiorite. The marine Martinez formation (Palaeocene) occurs in a few wedges within the San Gabriel fault zone. It consists of conglomerate, black shale, grey to tan siltstone and sandstone. The marine Modelo formation (Miocene) is exposed continuously in an east-west belt across the southern part of area. It is composed of a siliceous shale, with interbedded sandstone and conglomerates. The marine Pico formation (Pliocene) was unconformably deposited over the Modelo formation. The lower part of this formation is mainly conglomerate containing rounded boulders of igneous and metamorphic rocks. The upper part of this formation consists primarily of grey, yellowish or tan arkosic sandstone. The Saugus formation is a terrestrial deposit of probable lower Pleistocene age lying with slight unconformity on the Pico formation. Reddish-brown, coarse pebbly sandstone beds are common, particularly in the lower part of the formation.

Individual beds are lenticular and many are cross-laminated. Reddish brown fine sandstone and siltstone are interbedded in the upper part of this formation. Deposits of mid to upper Pleistocene alluvium are uplifted and eroded to form terraces widely distributed in this area (Howell, 1949; Oakeshott, 1958).

## 5-2. Structural Geology

The San Gabriel fault zone was formed as a result of jumping of the southern triple junction to the southeast (Sedlock and Hamilton, 1991). A minimum upper age limit of 14 to 12 Ma for movement on the San Gabriel fault is indicated by the displacement of the lower part of the Mint Canyon Formation in the Ridge basin area (Crowell, 1982). On the basis of fossil and magnetostratigraphic evidence, this fault shows about 60 km of right lateral slip from about 12 to 5 Ma; parts of it were later reactivated (Crowell, 1982). Weber (1986, 1988) suggested however that the fault has much smaller right lateral displacement than that proposed by Crowell (1962, 1982, 1986), and argued that activity along the San Gabriel fault zone continued into the Quaternary.

Structure of the San Gabriel fault zone is dominated by strike slip faults (Dillon, De Mille and Lopez faults), thrust faults (Buck, Kagel, Limerock and Watt faults) and en echelon folds in the Little Tujunga region (Fig. 5.1a, b). To the southwest, there occur the Sunland and San Fernando thrust faults belonging to the Santa Susana-Sierra Madre fault zone.

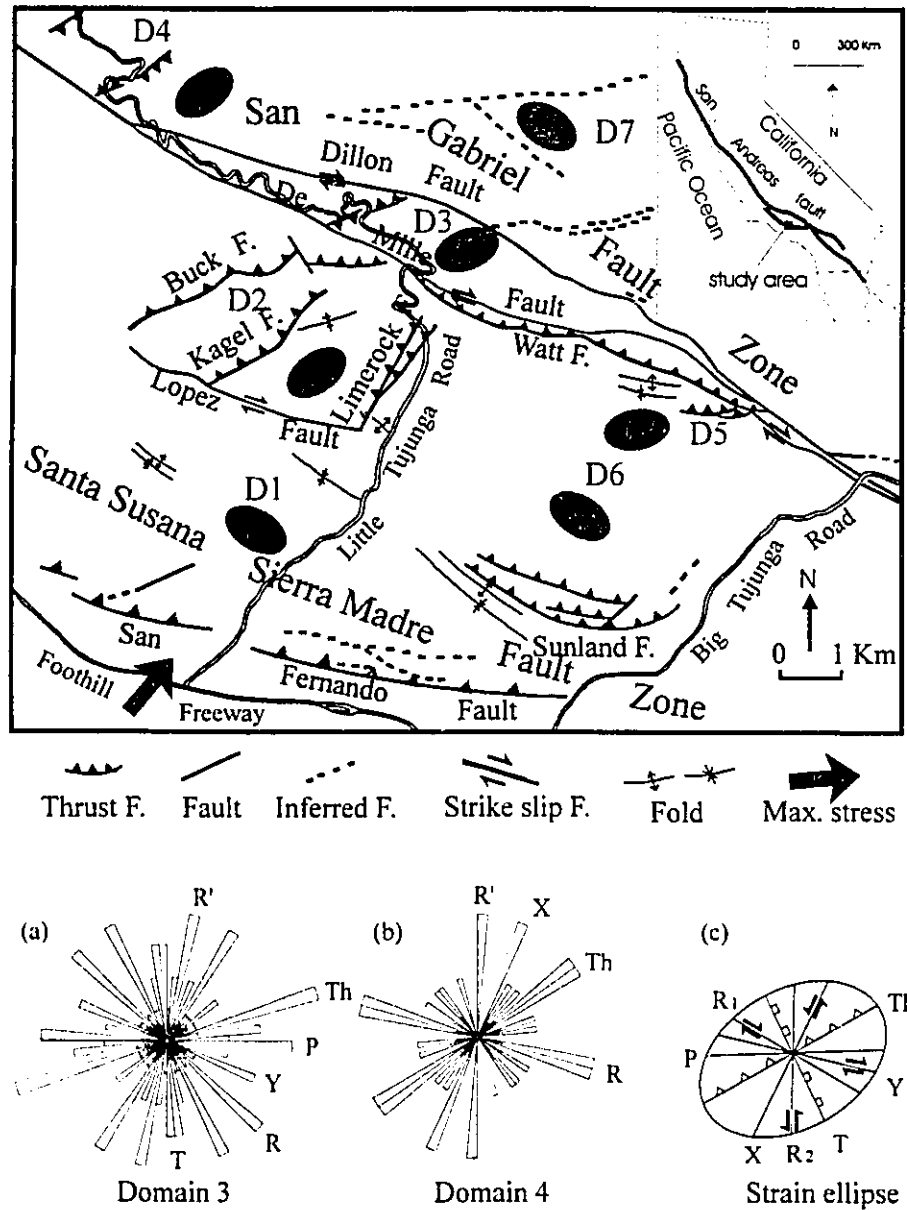


Figure 5.1. Structural map of the Little Tujunga region. (a) Rose diagram of the faults in the Domain 3. (b) Rose diagram of the faults in the Domain 4. (c) Structural pattern developed in each domain. Symbols: D1 etc., Domain 1; Th, thrust fault or reverse fault; Y, Y shear; T, extension fault or fracture; X, X shear; P, P shear; R<sub>1</sub>, Riedel shear; R<sub>2</sub>, antithetic Riedel shear.

Present-day regional stress direction estimated from well bore breakouts and earthquake focal mechanism indicates that the direction of maximum horizontal stress ( $S_{H1}$ ) is oriented NE-SW at a high angle ( $70^{\circ}$ - $90^{\circ}$ ) to the San Andreas fault system (Mount and Suppe, 1987, 1992, Zoback et al., 1987).

The geometry of possible structures associated with strike-slip faults depends on the form, scale, time and environment in which specific structures develop (Fig. 5.2). Strike-slip movements on a major fault that exhibits bends or en-echelon segmentation creates spatial compatibility problems (Sylvester, 1988). In a restraining bend, the local shear displacement along the fault must be accompanied by a component of horizontal shortening across the strike-slip fault and a local transpression is generated. This transpression is generally relieved by vertical uplift and contraction associated with folds, reverse faults and subsidiary oblique strike-slip faults. Folds and thrusts initiated in a transpression regime are developed oblique to the main shear direction at an angle lower than  $45^{\circ}$  (Fig. 5.2). Conversely, releasing bends provide for transtension accompanied by stretching, crustal extension, and pull-apart basins. The orientation of normal faults initiated in this transtension regime is generally lower than  $45^{\circ}$  to the main shear direction (Fig. 5.2).

Curvatures along the main San Gabriel fault yielded local transpressive regimes and changed the direction of maximum horizontal stress to a lower angle ( $30^{\circ}$ - $40^{\circ}$ ) to the main fault in the Little Tujunga region (Fig. 5.1). I divided the study area into several domains according to the structural characteristics (Fig. 5.1). In Domain 1, folds and



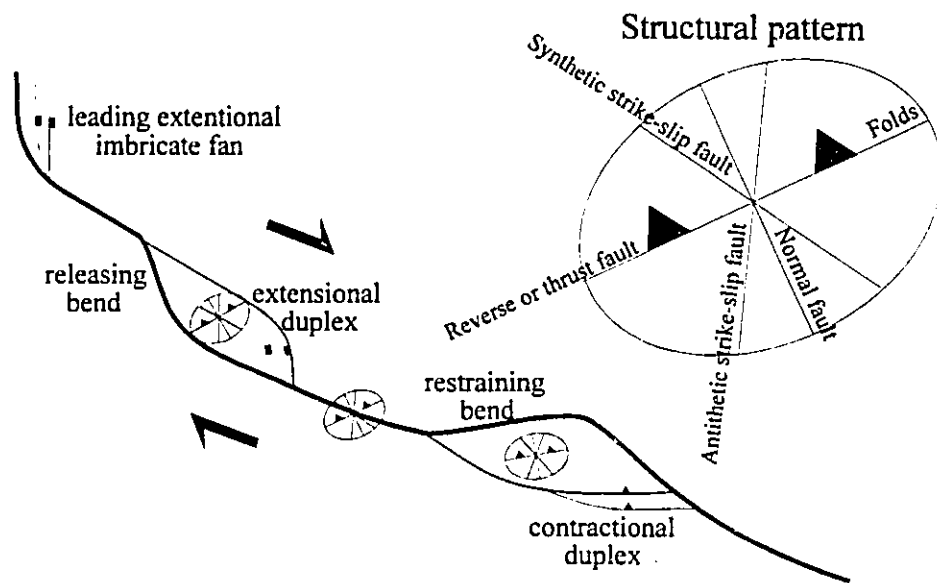


Figure 5.2. Map view of structures associated with a dextral strike-slip fault.

thrust faults roughly parallel to the San Gabriel fault are developed in the Tertiary sedimentary rocks of the Santa Susana-Sierra Madre fault zone. This direction indicates that the maximum horizontal stress was oriented at a high angle to the San Gabriel fault and are consistent with the regional stress system in southern California (Mount and Suppe, 1987, 1992, Zoback et al., 1987). In Domain 2, crystalline rocks are thrust over the Pleistocene Saugus formation. Basement rocks were severely fractured and faulted, while, the strain was also accommodated by folding in the Saugus formation. In Domain 3, the basement rocks was uplifted between the Dillon and De Mille faults by transpression. A flower structure developed along the De Mille fault; in which the fault plane is vertical at depth but flattens to horizontal at the surface (Fig. 5.3). The basement rocks in this domain were severely fractured and faulted. Figures 5.1a and 5.4a show the rose diagram and equal area projection of poles to faults measured on outcrops. In Domain 4, subsidiary faults with fault gouge up to 3 m wide developed in the local transpressive regime. In some areas, broad fault breccia zones up to a few hundred meters wide were developed in the severely fractured basement rocks. Figures 5.1b and 5.4b show the rose diagram and equal area projection of poles to faults measured on outcrops in this Domain. In Domain 5, thrust faults and open folds subparallel to the main fault developed in the sedimentary rocks. In Domain 6, conjugate fractures (airphoto scale) are well developed in the basement rocks. In Domain 7, faults and joints developed in the basement rocks; the density of fractures is lower than the other domains.

Mount and Suppe (1987) suggested models for the San Andreas fault of high



Figure 5.3. The flower structure developed along the De Mille fault. The left side block of photograph is uplifted.

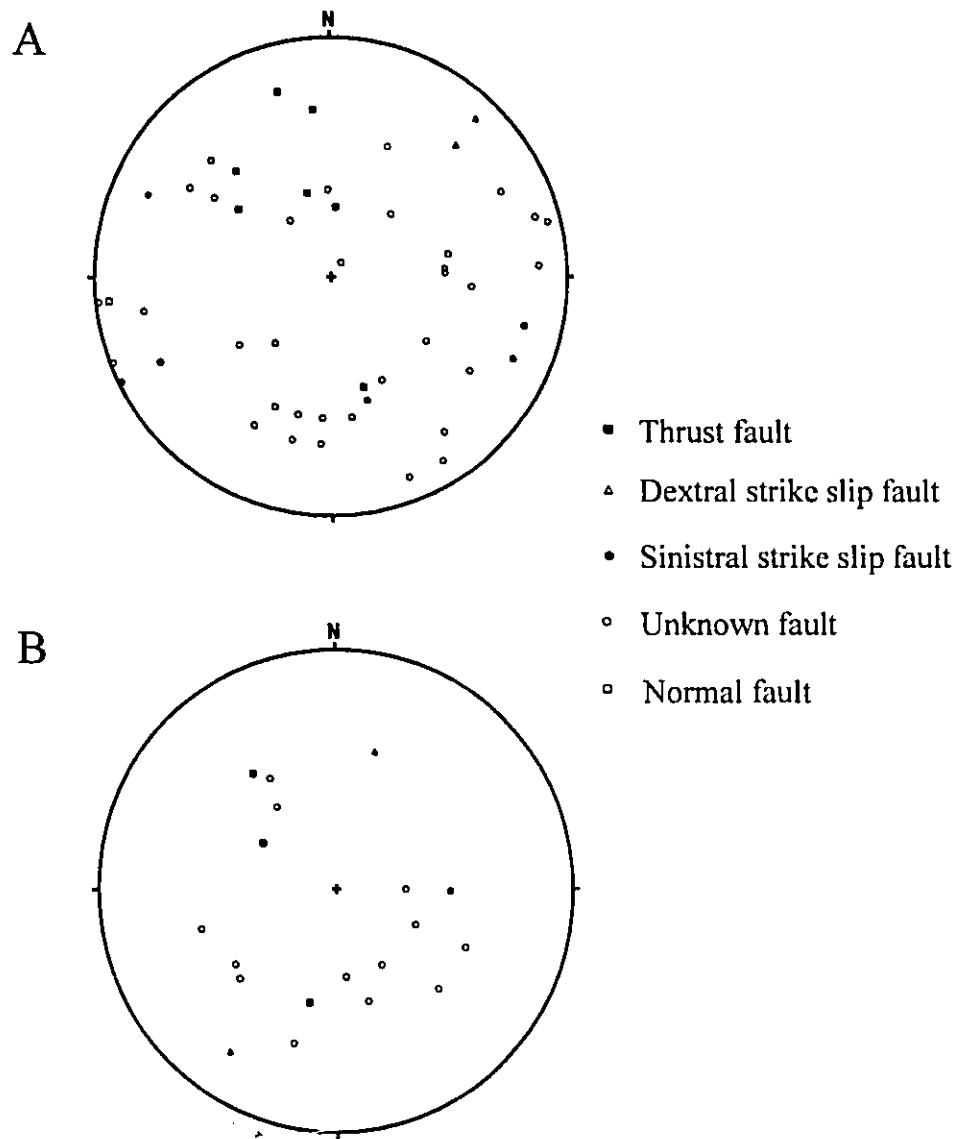


Figure 5.4. Plot of poles to faults in Domain 3 (A) and Domain 4 (B) of the Little Tujunga region. Schmidt equal-area projection, lower hemisphere.

drag-distributed shear and low drag-decoupled shear (Fig. 5.5). The former is derived from the model of wrench tectonics suggested by Wilcox et al. (1973), characterized by en echelon folds, Riedel shear, and extension fractures. Mount and Suppe (1987) investigated the direction of regional maximum horizontal stress in the San Andreas fault system in central California using borehole elongation or breakouts. The deduced direction of maximum horizontal stresses was nearly perpendicular to the San Andreas fault system and to the axes of young thrust-related anticlines. They could not explain these observations using the basic wrench tectonics, so that they suggest the thrust structures are largely decoupled from the strike-slip fault (Fig. 5.5B).

Although the scale is different, the Little Tujunga region can be explained by a combination of Mount and Suppe's low drag-decoupled model and transpression (Fig. 5.5C). The folds (Little Tujunga syncline and anticline) and thrust faults (Sunland and San Fernando faults) in the Santa Susana-Sierra Madre fault zone subparallel to the San Gabriel fault were formed by NE-SW oriented compressional stress ( $S_H$ ) in Domain 1. The San Fernando (1971) and Northridge (1994) earthquakes in the San Fernando valley had been occurred by this compressional stress. Note during these earthquakes, any faults related with the San Gabriel fault zone were not active (Crowell, 1986b). When strike-slip deformation along the San Gabriel fault zone was strong, the local bends of the San Gabriel fault changed the direction of maximum horizontal stress to a state of high drag-distributed shear temporarily (Fig. 5.5C). Folds and thrust faults (Limerock, Kagel and Buck faults) oblique to the San Gabriel ault were developed in Domains 2 and 4 by

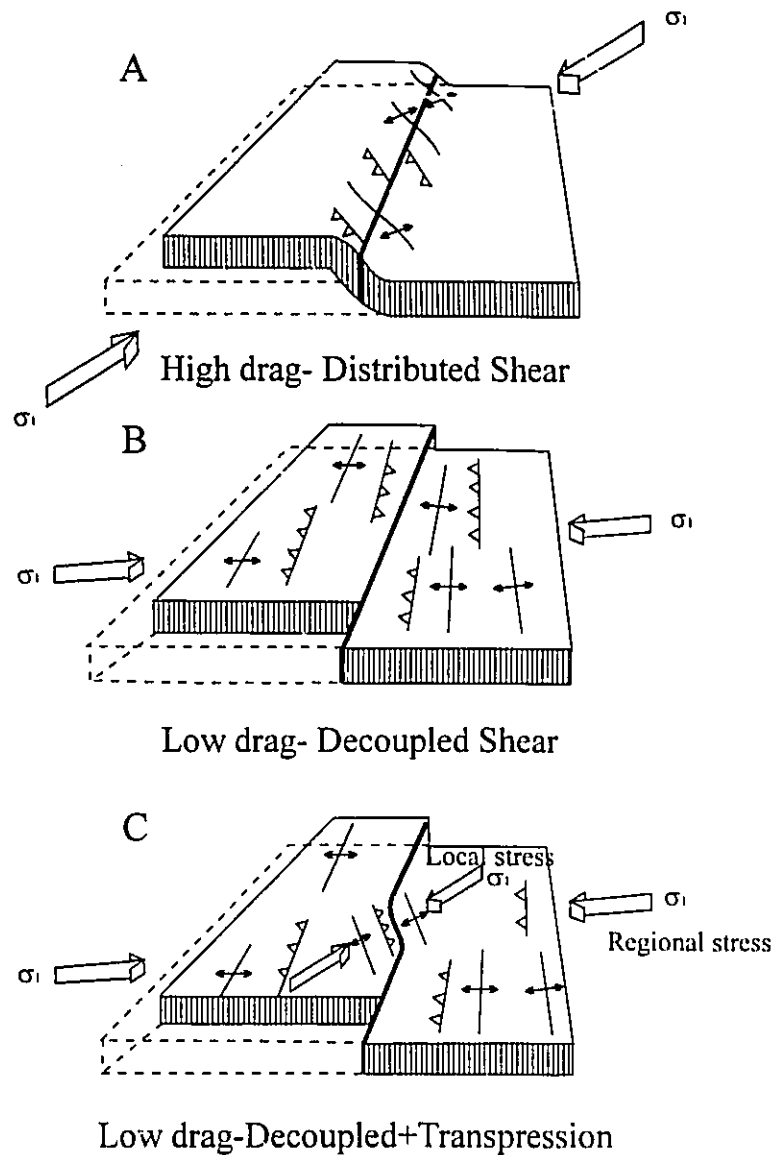


Figure 5.5. A: Structural features predicted by the high drag-distributed shear concept of wrench fault tectonics. B: Structural features predicted by the low drag-decoupled shear concept of wrench fault tectonics. C: Structural features by the low drag-decoupled shear combined by transpression due to the bend of the main fault trace. (A,B; after Mount and Suppe, 1987).

transpression (Fig. 5.1 and 5.5C).

### **5-3. The evolution of fault zone in the brittle regime**

#### **5-3-1. Introduction**

Quartzofeldspathic basement rocks largely determine the behaviour of continental crust in large-scale tectonic processes. The deformation of basement rocks is very inhomogeneous in the crust; being distributed or being concentrated in ductile shear zones or brittle fault zones (Mitra, 1992). One of the results of the shear deformation in the brittle regime is the production of fault rocks in the brittle fault zones. Several studies of fault zones showed that a continuous gouge layer was bounded by zones of extensively fractured host rocks or fault breccia (Flinn, 1977, House and Gray, 1982, Chester and Logan, 1986, Wojtal and Mitra, 1986). Subsidiary faults are developed in the fractured zone, particularly in transtension/transpression regimes. Approaching the main gouge zone, the cataclasis is increased (Chester and Logan, 1986; Chester et al., 1993; Lee and Schwarcz, 1994b).

It is very difficult to distinguish reactivated fault rocks from primary fault rocks in the brittle regime. For example, Chester et al. (1993) collected the reactivated fault gouge from the San Gabriel fault zone and observed that the microtexture of mother or grandmother gouge is similar with the grandson's microtexture.

In this study, I investigated the evolution of fault zones with fault rocks developed by successive reactivation at shallow depth. At several locations in the Little Tujunga region, the fault gouge (or reactivated gouge) was bounded by cataclasite, fault breccia and older gouge. Some of cataclasite and gouge was foliated by reactivation of fault rock zones at a shallower crustal level. I collected fault rock samples from distinctive bands (breccia, cataclasite, gouge, reactivated gouge) which appeared to be developed by sequential fault movements. Applying the ESR plateau dating of fault rocks, I determined the times of the last fault movements at sampling locations (distinctive fault rock bands). The relationships between ESR ages and the meso- and micro-scale structures within the fault rock zones were used to evaluate the evolution of fault rock zones in the brittle regime.

### **5-3-2. Structural features in the brittle fault rock zones**

The progressive evolution of brittle fault zones is characterized by the localization of shear strain. These localized zones of shear deformation show characteristic geometric features related to slip sense and orientation of the main fault rock zone. The structural features developed in brittle and ductile shear zones have been used to deduce the movement directions (Simpson and Schmid, 1983; White et al., 1986; Rutter et al., 1986; Hanmer and Passchier, 1991). In this section, the structural features developed in the brittle fault rock zones will be outlined, and in the successive sections, the relationships



between these structural features and the stage of evolution of fault rock zones will be given. I will use the directional nomenclatures of structural features following the terminology (Fig 5.6) of Logan et al. (1979).

Intensely deformed bands or preferred alignment of platy minerals produce a foliation with an orientation between  $135^\circ$  and  $180^\circ$  to the direction of fault zone wall. These foliations are referred to as the S foliation by Berthe et al. (1979) and as the P orientation on the structures produced in the laboratory by Logan et al. (1979). Sometimes, these intensely deformed bands were developed in braided or anastomosing networks producing lens-shaped domains of low strain. In clay rich gouge, pervasive smooth foliation was developed by the preferred alignment of clay minerals. Sometimes, calcite crystals precipitated within fault gouge zone were fractured or flattened and arrayed along the foliation during successive reactivation of fault gouge zone. This indicates that P orientation represents the extension direction within gouge zone and that it forms initially at a high angle ( $\sim 135^\circ$ ) to the shear direction and may be rotated to a lower angle ( $\sim 180^\circ$ ) with progressive shearing of fault gouge zone (Ramsay and Huber, 1983).

$R_1$  and  $R_2$  Reidel shears often cut the P-foliations.  $R_1$  shears with the same sense as the shear of fault rock zone itself are more common than  $R_2$  shears with the opposite sense of shear of fault zone itself (antithetic shears). The amount of displacement on these shears is necessarily quite limited by their geometry (Marone and Scholz, 1989). These Reidel shears are well developed both in simulated gouge (Marone and Scholz, 1989) and

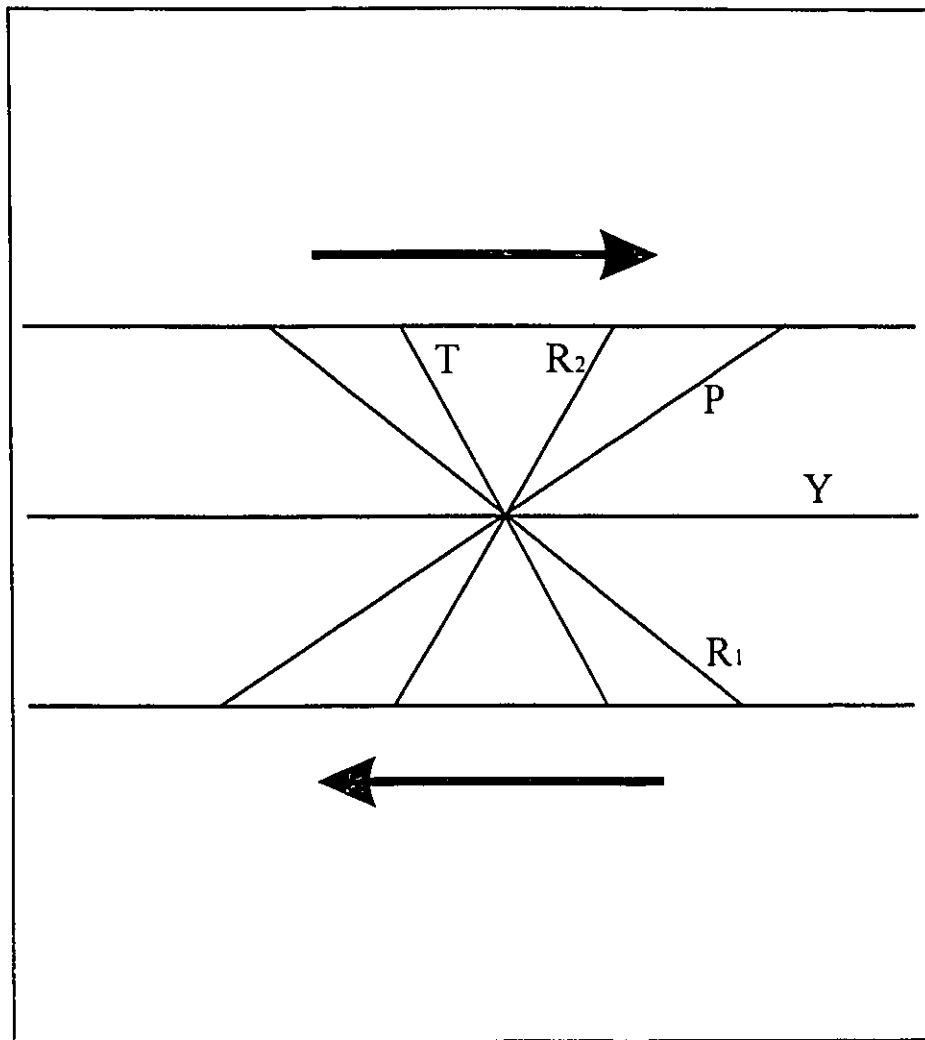


Figure 5.6. Schematic diagram of a shear zone, showing the geometrical relationships of the main structural elements.

natural fault gouge zone (Rutter et al., 1986; Chester and Logan, 1987).

Localized shear bands which are subparallel to the fault rock zone itself are well developed. These are called C-surfaces in ductile shear zones and Y-shear surfaces in brittle fault rock zones. The Y-surfaces in fault gouge zones can accommodate large finite displacement (Rutter et al., 1986; Chester and Logan, 1986). Boundary shear zones or principal slip surfaces in Y-shear direction are well developed at the fault rock-host rock interface. These principal slip surfaces have the highest shear strain within the fault rock zone (Sibson, 1986). The presence of a principal slip surface is noted for the simulated fault gouge (Marone and Scholz, 1989; Biegel et al., 1989) and natural fault gouge zones (Anderson et al., 1983).

Sometimes tensile fracture arrays are developed in the brittle fault rock zones. Some other small-scale features such as trails and kink bands are commonly found in both simulated and natural fault rock zones (Rutter et al., 1986).

### **5-3-3. Fault rock zones developed in the Little Tujunga region**

There are many subsidiary faults developed in local transpressive regimes of the Little Tujunga region. These include oblique-strike slip faults, thrust or high angle reverse faults and though much less common, normal faults. The widths of the fault rock zones of these subsidiary faults range from a few mm to 2-3 m, even wider than the main strands of the San Gabriel fault zone. Structures developed in the fault rock zones of the

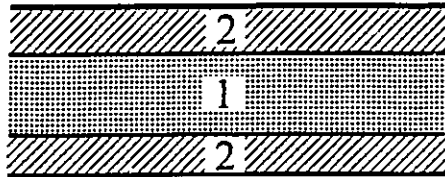
Little Tujunga region define complex deformation patterns. They show much variation along the fault rock zones, even in outcrop scale.

Some of them appear to be developed by multi-cyclic deformation. Means (1984) and Mitra (1992) divide fault zones into Type I, II and III modes based on the behaviour of strain hardening and strain softening (Fig 5.7). A Type I fault zone is characterized by strain hardening deformation, whose margins are active but whose center is effectively dead. Type II fault zones are developed by strain softening deformation, where successive deformation is confined or concentrated in a narrow part or parts of the original fault rock zone. On the other hand, the entire fault rock zone is active in Type III shear zone, whose margins are growing (Mitra, 1992). The structural features of Type III shear zone are overprinted across the whole zone leading to difficulty in recognizing reactivation. Some fault rock zones in the Little Tujunga region show distinct bands of fault rocks which appear to be developed sequentially by strain softening or strain hardening process; Type I or Type II fault zones.

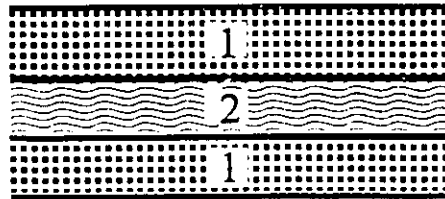
I divided fault rock zones in the study area into four groups based on characteristic development of fault rocks by sequential reactivation: (1) fault rock zone bounded by fractured or intact host rocks, (2) fault gouge zone bounded by fault breccia, (3) fault gouge zone bounded by cataclasite and (4) reactivated gouge zone bounded by primary or older gouge zone.

In this section, special attention has been given to the evolution of fault zones with equivalent fault rocks at each outcrop scale in the brittle regime by the analysis of the

## Type I faulting mode



## Type II faulting mode



## Type III faulting mode

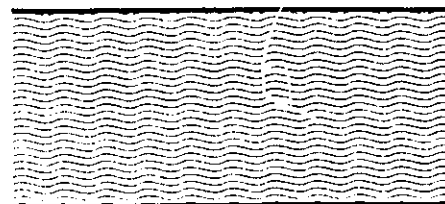


Figure 5.7. Schematic diagram of faulting mode; Type I, II, and III.

structural features, microtextures and ESR data of the fault rocks (Table 5.1 and 5.2) developed by the multiple cyclic reactivation.

#### **5-3-3-1. Fault gouge zones bounded by fractured or intact host rocks**

There are many faults with a sharp fault plane or narrow fault gouge zone (a few mm wide) in the sedimentary and basement rocks in the Little Tujunga region (Fig. 5.8a). Discrete sliding surfaces are characterized by slickenside with striations. These small displacement faults appear to accommodate internal deformation in each block bounded by major fault rock zones. Some of the subsidiary faults show wider fault rock zones 2-300 cm wide, which appear to accommodate large displacement (Fig. 5.8b).

Where later reactivation has obliterated the earlier ESR record (Type III mode), we can determine only the time of last movement of a fault rock zone using the ESR dating method. For example, a gouge zone about 2.5 m wide is developed in the Barrel Spring fault between fractured gneiss and a Quaternary terrace deposit in Domain 3 (Fig. 5.9; locality 1). Strongly deformed subzones about 0.5-5 mm wide formed the P-foliations or Y-shears which are subparallel ( $180^\circ$ ) to the shear direction of fault in both boundary. Some of them (subzones) in the central part of gouge zone are oriented to the  $R_1$  Reidel shear direction ( $40^\circ$  to the shear direction of fault) and are connected to the P-foliations resulting in irregular pattern. Fractures 5-20 cm long occur within gouge zone, which are oriented in  $R_2$  Reidel shear orientation. White gouge 1-3 cm wide is developed to the Y-

Table 5.1. ESR analytical data and calculated ages for faults presented in this chapter.

Fault	Sample	Grain size ( $\mu\text{m}$ )	Center	$D_g$ (Gy)	U (ppm)	Th (ppm)	K (%)	Dose rate ( $\mu\text{Gy/a}$ )	ESR age (ka)	Locality
San Gabriel	91075C	100-150	OHC	1024 $\pm$ 57	4.25	8.57 $\pm$ 0.18	2.34 $\pm$ 0.12	4052 $\pm$ 187	253 $\pm$ 18	2
San Gabriel	91075C	100-150	E'	901 $\pm$ 64	4.25	8.57 $\pm$ 0.18	2.34 $\pm$ 0.12	4052 $\pm$ 187	222 $\pm$ 19	2
San Gabriel	91075D	75-100	OHC	1030 $\pm$ 64	4.25	8.57 $\pm$ 0.18	2.34 $\pm$ 0.12	4213 $\pm$ 202	245 $\pm$ 19	2
San Gabriel	91075D	75-100	E'	806 $\pm$ 38	4.25	8.57 $\pm$ 0.18	2.34 $\pm$ 0.12	4213 $\pm$ 202	191 $\pm$ 13	2
San Gabriel	91075E	45-75	OHC	782 $\pm$ 72	4.25	8.57 $\pm$ 0.18	2.34 $\pm$ 0.12	4422 $\pm$ 225	177 $\pm$ 19	2
San Gabriel	91075E	45-75	E'	748 $\pm$ 59	4.25	8.57 $\pm$ 0.18	2.34 $\pm$ 0.12	4422 $\pm$ 225	169 $\pm$ 16	2
San Gabriel	91075F	<45	OHC	802 $\pm$ 31	4.25	8.57 $\pm$ 0.18	2.34 $\pm$ 0.12	4801 $\pm$ 279	167 $\pm$ 12	2
San Gabriel	91075F	<45	E'	806 $\pm$ 143	4.25	8.57 $\pm$ 0.18	2.34 $\pm$ 0.12	4801 $\pm$ 279	168 $\pm$ 31	2
San Gabriel	91076D	75-100	E'	917 $\pm$ 90	9.46	3.41 $\pm$ 0.12	1.66 $\pm$ 0.08	4611 $\pm$ 218	199 $\pm$ 22	2
San Gabriel	91076E	45-75	E'	785 $\pm$ 34	9.46	3.41 $\pm$ 0.12	1.66 $\pm$ 0.08	4920 $\pm$ 262	160 $\pm$ 11	2
San Gabriel	91076F	<45	E'	823 $\pm$ 130	9.46	3.41 $\pm$ 0.12	1.66 $\pm$ 0.08	5500 $\pm$ 359	150 $\pm$ 26	2
San Gabriel	91077E	45-75	E'	572 $\pm$ 71	1.01	0.98 $\pm$ 0.11	1.32 $\pm$ 0.07	1684 $\pm$ 92	340 $\pm$ 46	2
San Gabriel	91077F	<45	E'	613 $\pm$ 63	1.01	0.98 $\pm$ 0.11	1.32 $\pm$ 0.07	1759 $\pm$ 98	348 $\pm$ 41	2
Dillon Divide	91091D	75-100	E'	3467 $\pm$ 248	4.07	4.62 $\pm$ 0.19	0.15 $\pm$ 0.01	1741 $\pm$ 93	1829 $\pm$ 175	4
Dillon Divide	91091E	45-75	E'	1466 $\pm$ 114	4.07	4.62 $\pm$ 0.19	0.15 $\pm$ 0.01	1895 $\pm$ 120	773 $\pm$ 76	4
Dillon Divide	91091F	<45	E'	1689 $\pm$ 78	4.07	4.62 $\pm$ 0.19	0.15 $\pm$ 0.01	2188 $\pm$ 173	772 $\pm$ 71	4
Dillon Divide	91092E	45-75	E'	1933 $\pm$ 225	1.84	10.14 $\pm$ 0.22	0.31 $\pm$ 0.02	1883 $\pm$ 113	1026 $\pm$ 135	4
Dillon Divide	91091F	<45	E'	2223 $\pm$ 142	1.84	10.14 $\pm$ 0.22	0.31 $\pm$ 0.02	2140 $\pm$ 159	1039 $\pm$ 102	4

Table 5.2. Examples of times of last movement on distinct fault rock zones in a given fault zone determined by the ESR dating method.

Fault	Sample	Grain size ( $\mu\text{m}$ )	ESR	ESR age (ka)	Weighted mean (ka)
San Gabriel	91075E	45-75	E'	169 $\pm$ 16	
San Gabriel	91075E	45-75	OHC	177 $\pm$ 19	169 $\pm$ 8
San Gabriel	91075F	< 45	E'	168 $\pm$ 31	
San Gabriel	91075F	< 45	OHC	167 $\pm$ 12	
San Gabriel	91076E	45-75	E'	160 $\pm$ 11	
San Gabriel	91076F	< 45	E'	150 $\pm$ 26	158 $\pm$ 10
San Gabriel	91077E	45-75	E'	337 $\pm$ 47	
San Gabriel	91077F	< 45	E'	346 $\pm$ 43	342 $\pm$ 32
Dillon Divide	91091E	45-75	E'	773 $\pm$ 78	
Dillon Divide	91091F	< 45	E'	772 $\pm$ 71	773 $\pm$ 53
Dillon Divide	91092E	45-75	E'	1026 $\pm$ 135	
Dillon Divide	91092F	< 45	E'	1039 $\pm$ 102	1034 $\pm$ 81



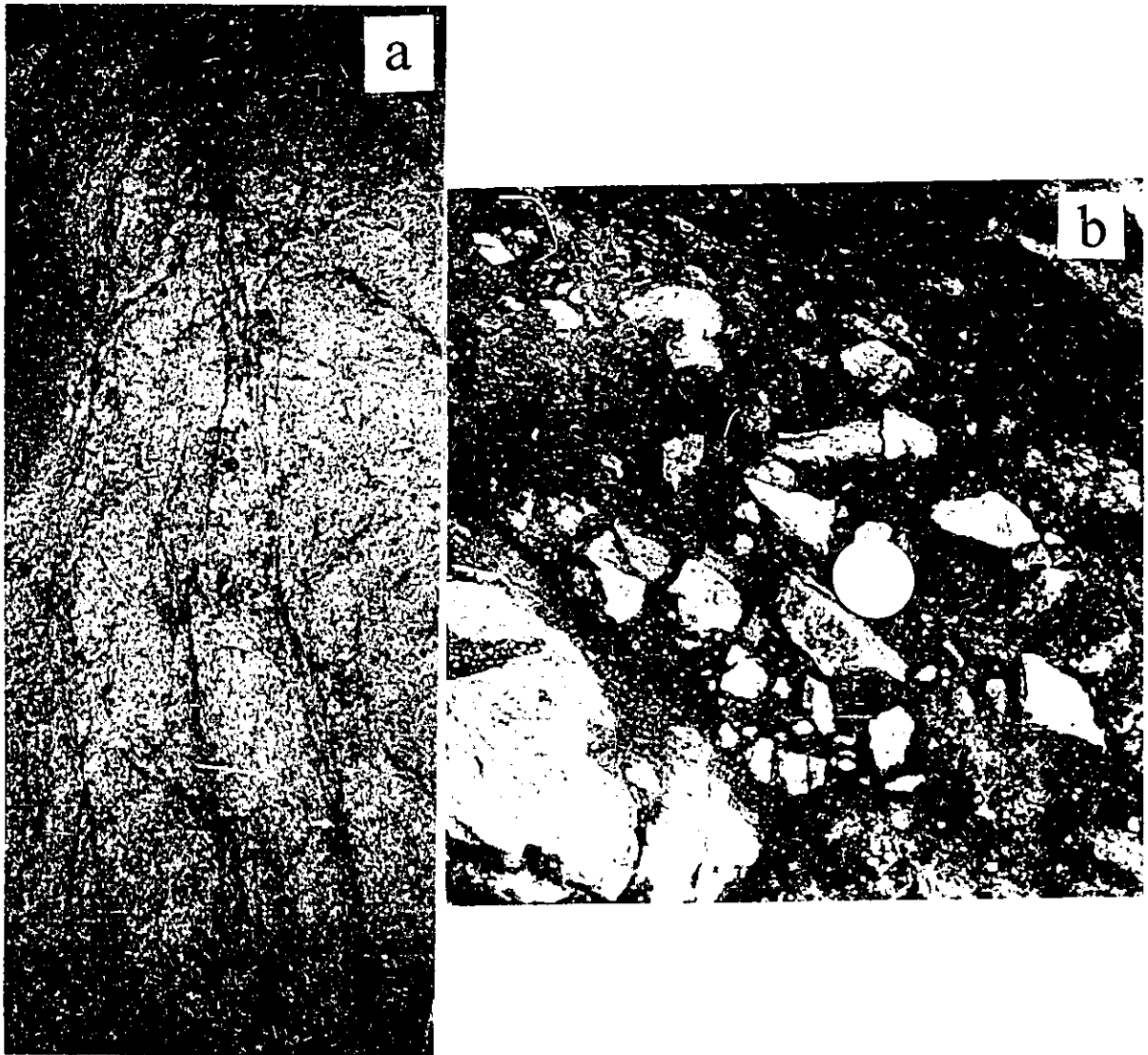


Figure 5.8. (a) Anastomosing faults with narrow gouge zone developed in Domain 3. Scale; coin on the center of photograph. (b) Fault breccia zone bounded by fractured gneiss. scale; coin on the center of photograph.

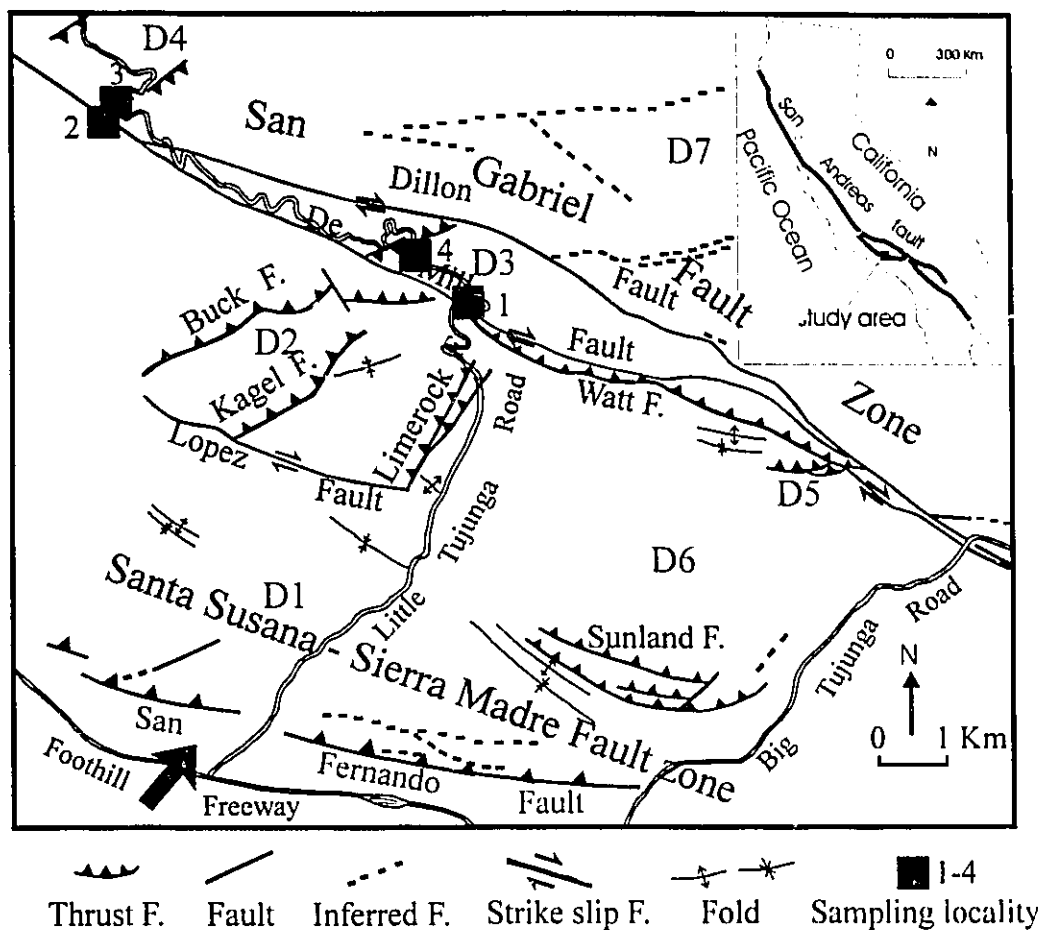


Figure 5.9. Structural map of the Little Tujunga region, showing locations of sample sites discussed in this chapter.

shear direction between gouges derived from gneiss and terrace deposit (Fig. 5.10). The above observations indicate strike slip motion combined with reverse dip-slip fault movement.

The result of ESR analysis in this site was described in the earlier chapter (4-4-1 and Fig. 4.17). It showed that complete resetting of ESR signals had occurred below some critical grain size within the whole gouge zone, even though the shear strain was heterogeneous.

At Bear Divide (Fig. 5.9; locality 2), the main San Gabriel fault, separating leucocratic granodiorite from Paleocene Martinez formation, is marked by well-foliated brown gouge (91076) about 2 m thick containing relics of cataclasite (91077); dark grey compact gouge (91075) about 2-3 cm wide separates the granodiorite and the main brown gouge zone (Fig 5.11a). Minor shear bands subparallel with the main fault plane occur in the cataclasite. Using the E' signal of grains  $< 75 \mu\text{m}$ , an estimated age ( $342 \pm 32 \text{ ka}$ ) for this component of the cataclasite is obtained. The dark grey compact gouge (91075) shows plateau for both E' and OHC, and its estimated age is  $169 \pm 8 \text{ ka}$ , indistinguishable from the E' age of the well-foliated brown gouge:  $158 \pm 10 \text{ ka}$  (Table 5.1 and 5.2). This sequence of ESR age is consistent with the geologically determined sequence: two of the faulting episodes were too closely-spaced in time to be distinguished by the ESR dating method (Fig.5.11).



Figure 5.10. Y-shear and  $R_1$ -Reidel shear (direction of pencil) developed in the central portion of the Barrel Spring fault.

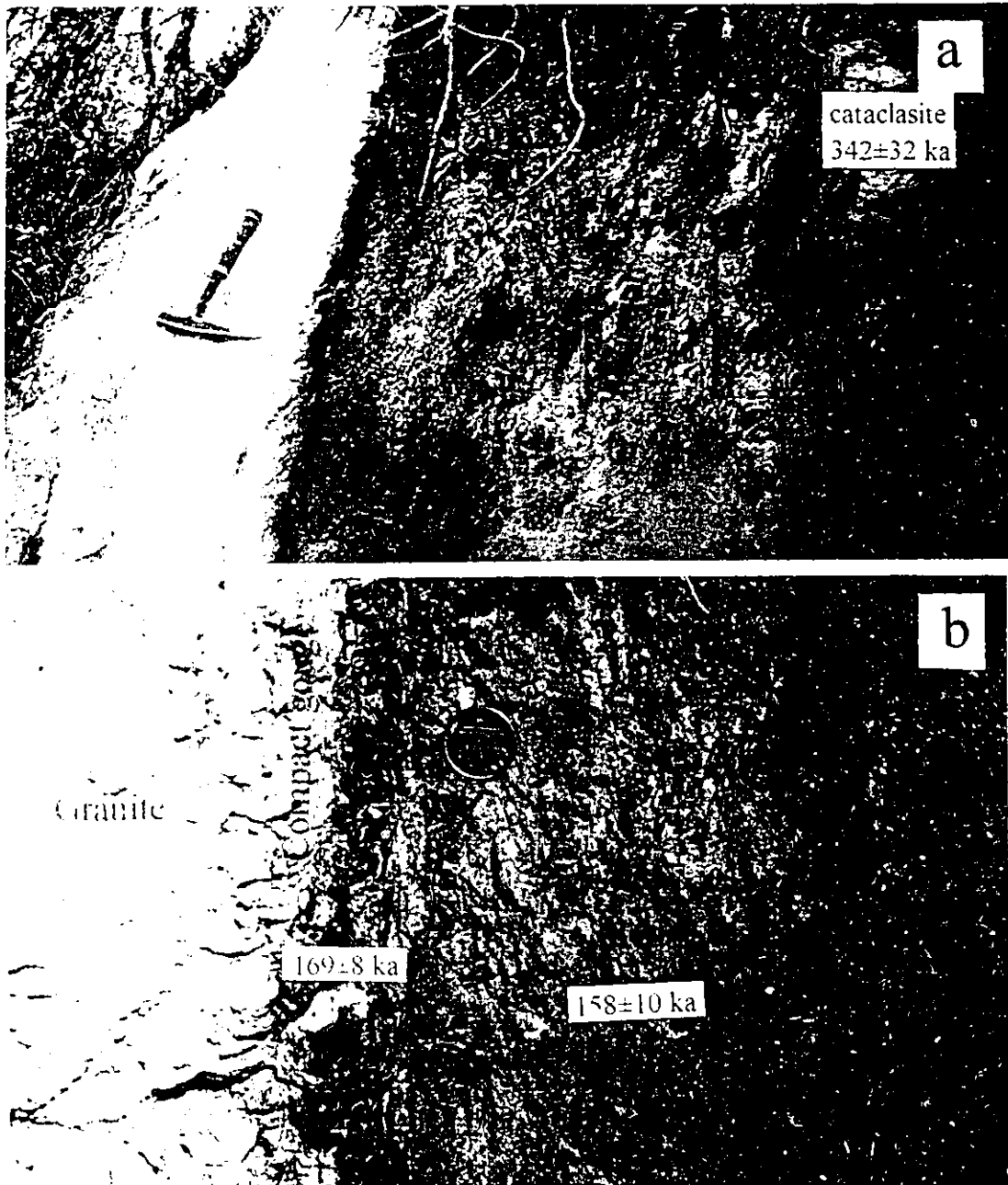


Fig 5.11. (a) Fault gouge zone of the main strand of the San Gabriel fault zone near the Bear Divide. (b) Close up of the boundary between granite, dark gray compact gouge and well-foliated brown gouge.

### 5-3-3-2. Fault gouge zones bounded by fault breccia

The best exposures of reactivated fault rock zones bounded by fault breccia are found in Domains 3 and 4. The Bear thrust fault is developed in the Mendenhall gneiss near Bear Divide (Fig. 5.9, locality 3). The hanging wall block was displaced along the fault gouge zone showing flat and ramp geometry, in typical thrust geometry (Fig 5.12a). This thrust fault is bounded by fractured host rock and fault breccia; the intensity of fracturing increases towards the main gouge zone. The fault breccia is developed partly in the hanging wall block. Foliation of the Mendenhall gneiss in this fault breccia was not severely disturbed indicating weak rotation and displacement of fragments (Fig. 5.12b). These observations suggest that this fault breccia was formed by the distributed crush brecciation, shearing displacement of which is likely to be minute in comparison with slip on the main fault gouge zone (Sibson, 1986a). It indicates that the ESR intensities of the matrix of these fault breccia may be partially zeroed due to low shear strain. In some part of the boundary between the gouge and fractured gneiss, the breccia is well developed and has a very sharp contact with the fractured Mendenhall gneiss, while displaying an irregular contact with the gouge zone (Fig 5.13a). The subangular to subrounded fragments of Mendenhall gneiss are situated in a medium- to coarse-grained matrix of gneiss fragments, quartz, feldspar or other minerals. The foliations developed within gneiss fragments were rotated and severely disturbed, indicating that shear displacement of this breccia zone is much larger than that of breccia partly developed

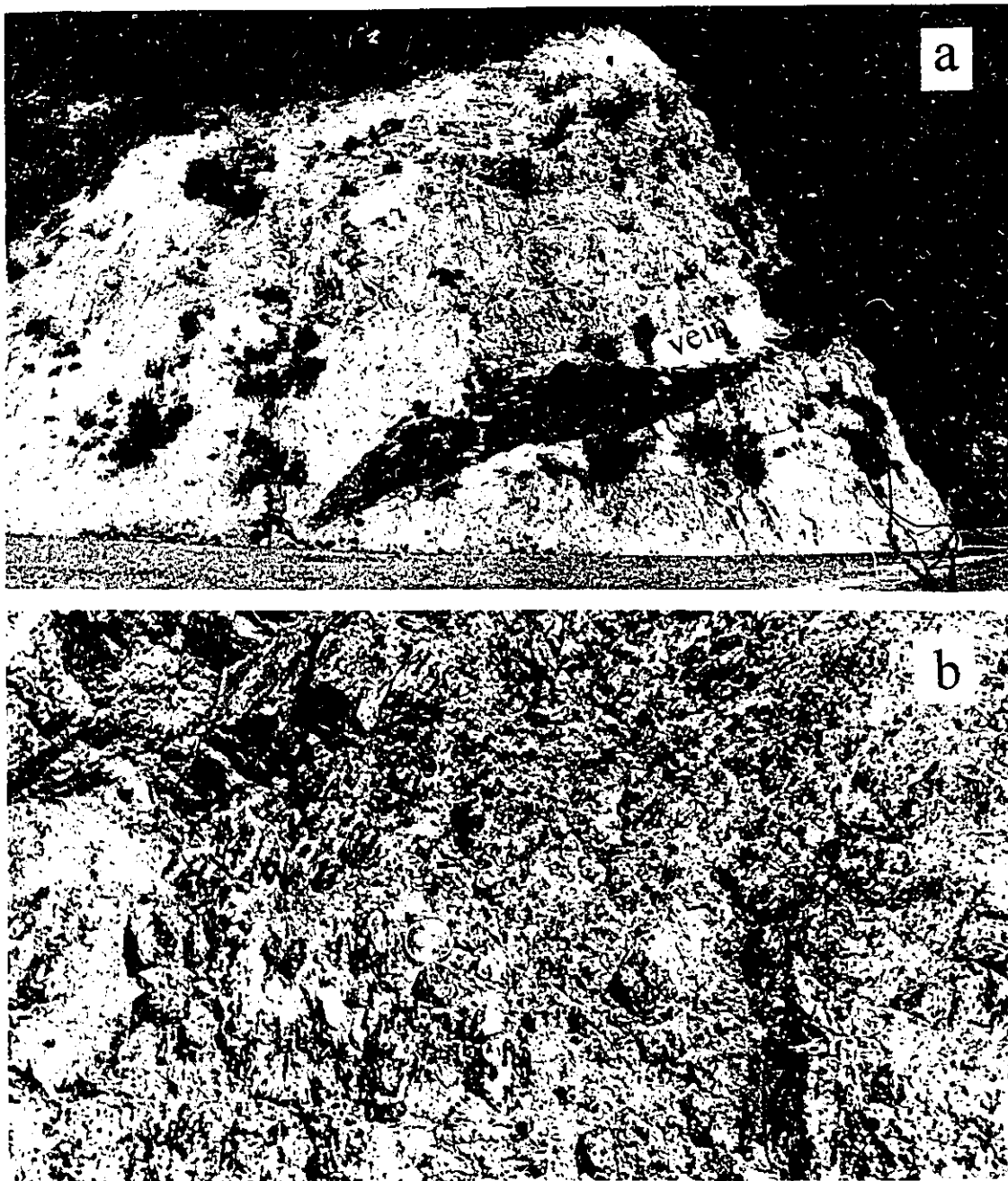


Figure 5.12. (a) The ramp segment of the Bear thrust fault. The flat segment is subparallel to the road (not shown in this photograph). (b) Fault breccia developed in the hanging wall block of the Bear thrust fault.

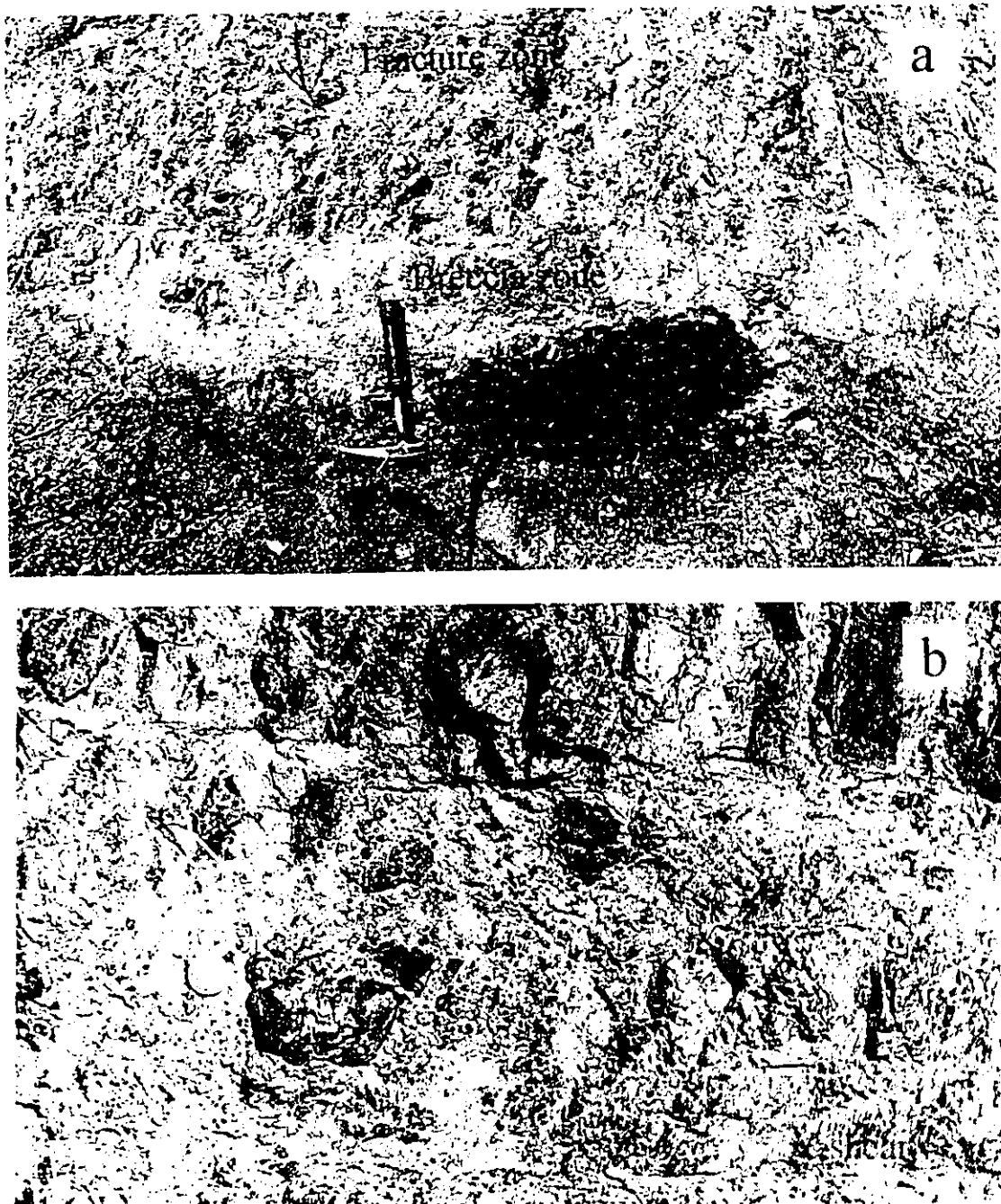


Fig 5.13. (a) Fault breccia zone bounding the gouge zone. (b) Close up of the breccia zone.



within fractured Mendenhall gneiss in the hanging wall block. Y-shears subparallel to the principal fault plane are developed in the breccia zone (Fig 5.13b). Quartz veins are injected along the thrust plane on the hanging wall side and into fractures in the hanging wall block, while in the footwall block there were no quartz veins (Fig 5.12a). This suggests that the fault gouge zone acted as an impermeable barrier to flow of the hydrothermal fluid to the footwall block (Suppe, 1985, Ramsay and Huber, 1987). There was no indication of effects of these hydrothermal fluid on the fault gouge in the outcrop scale. Shear joints or minor faults developed within quartz veins indicate that main fault gouge zone appears to have been reactivated several times after formation of the quartz veins.

There are many minor faults in the footwall block. Some of them show more than 90 cm of separation of the basic dyke intruded vertically before faulting (Fig. 5.14). There was no way to tell whether these displacements had occurred during more than one fault movement.

The main gouge zone has 50-300 cm of thickness, N4°E/28°NW trend and olive grey colour. The foliations subparallel to the gouge zone wall are very well developed. Where the boundary between the gouge and breccia zone is curved locally, these foliations follow the contact. The gouge is injected partly into the breccia (Fig. 5.15, point A) and shows sidewall cracking and plucking (Fig. 5.15, point B). It suggests that the gouge formed by attrition brecciation at a later stage of development of the gouge zone (Sibson, 1986a).



Figure 5.14. Minor faults developed in the footwall block of the Bear thrust fault.



Figure 5.15. Gouge injected into the breccia zone (point A) and shows cracking and plucking (point B) by which the thickness of gouge zone is expended.

### 5-3-3-3. Fault gouge zone bounded by cataclasite

Several typical examples of fault gouge zones bounded by cataclasite are developed near Dillon Divide in the central block between the Dillon and De Mille faults (Domain 3). The host granitic rocks are severely fractured on both mesoscopic and microscopic scales. Mesoscopic deformational features in the cataclasite zone include anastomosing minor gouge zones, foliations defined by the elongated felsic mineral aggregates and dark greenish gray gouge matrix, disrupted mineral aggregates and minor fractures crosscutting the foliations. These structural features indicate that multiple cyclic cataclastic deformation has been occurred in the transpressive regime associated with main strands of the San Gabriel fault zone during its long movement history. The widths of cataclasite zones are variable in outcrop scale, averaging about 20-40 cm. The contacts with fractured granitic rocks are irregular and gradational; qualitatively, the density of minor gouge zones 0.2-2 mm wide and a few cm long increases toward the main gouge zone.

In some outcrops, fault rock zones show various deformation pattern along the dip direction (Fig. 5.9, locality 4). A good example is shown in figure 5.16. Pervasive P foliations defined by strongly comminuted matrix and felsic mineral aggregates are developed in an orientation between  $130^{\circ}$  and  $170^{\circ}$  to the shear direction within cataclasite zone about 10 cm wide (Fig 5.17a and b). Riedel shears, which are curved or bifurcated sharp shear planes without gouge materials, are discretely developed at an angle of  $50^{\circ}$

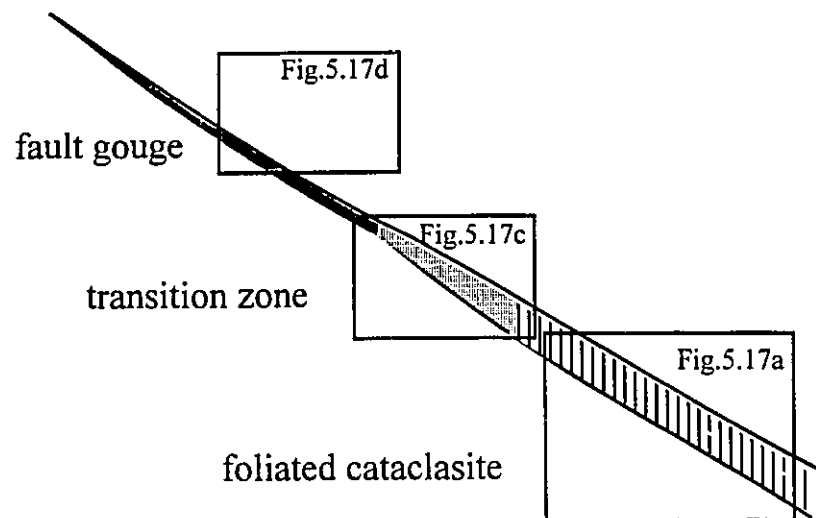


Figure 5.16. A fault rock zone showing various deformation along the dip direction.

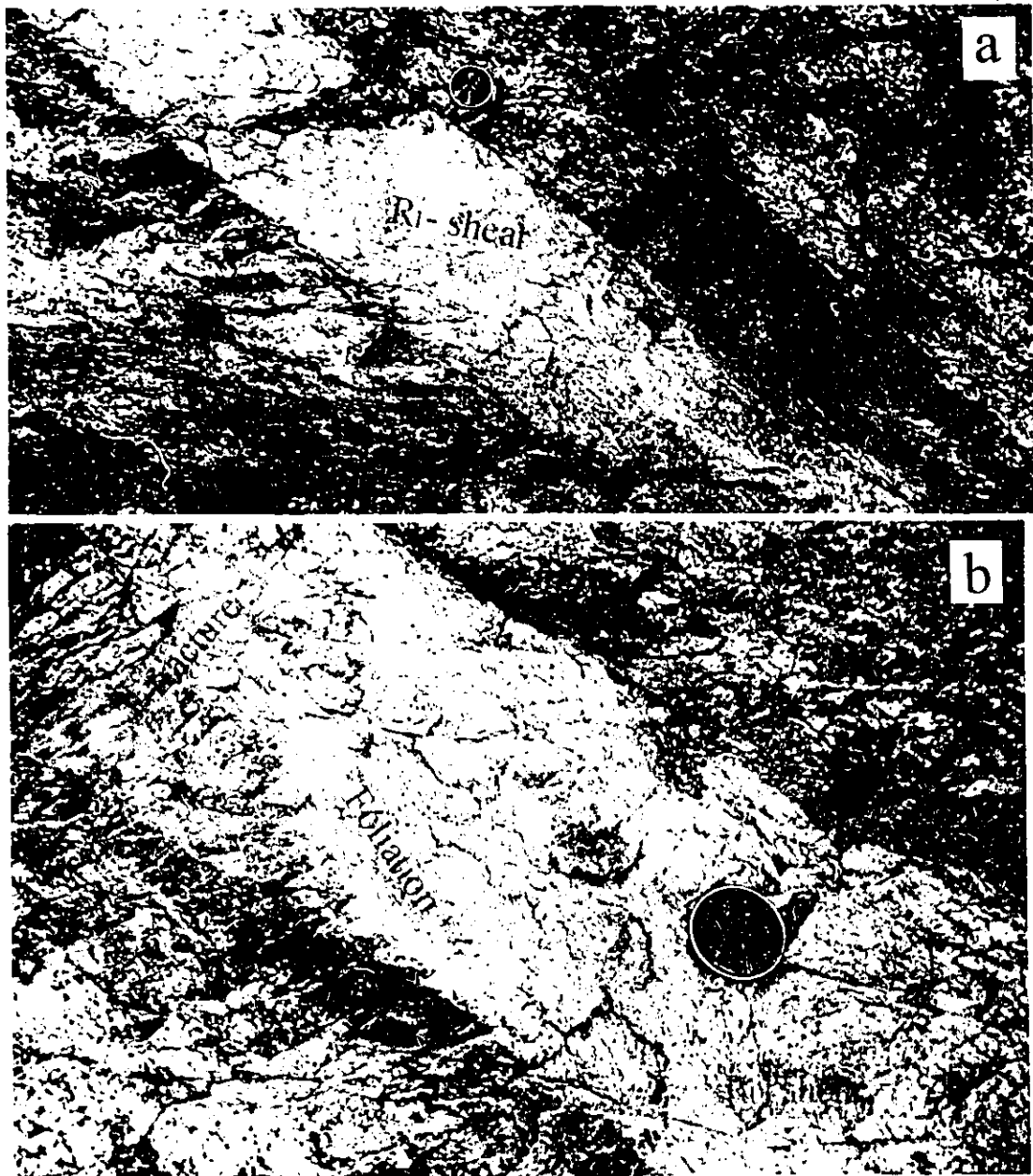


Figure 5.17. (a) A strongly deformed cataclasite zone bounded by less deformed cataclasite. Sharp fault planes are developed in both sides (b) Close up of Fig 5.17a. P-foliations are developed within cataclasite zone. Extension fractures roughly perpendicular to the P-foliations are developed in the upper left corner of photograph. Curved  $R_1$ -Reidel shear is developed in the lower right corner of the photograph.

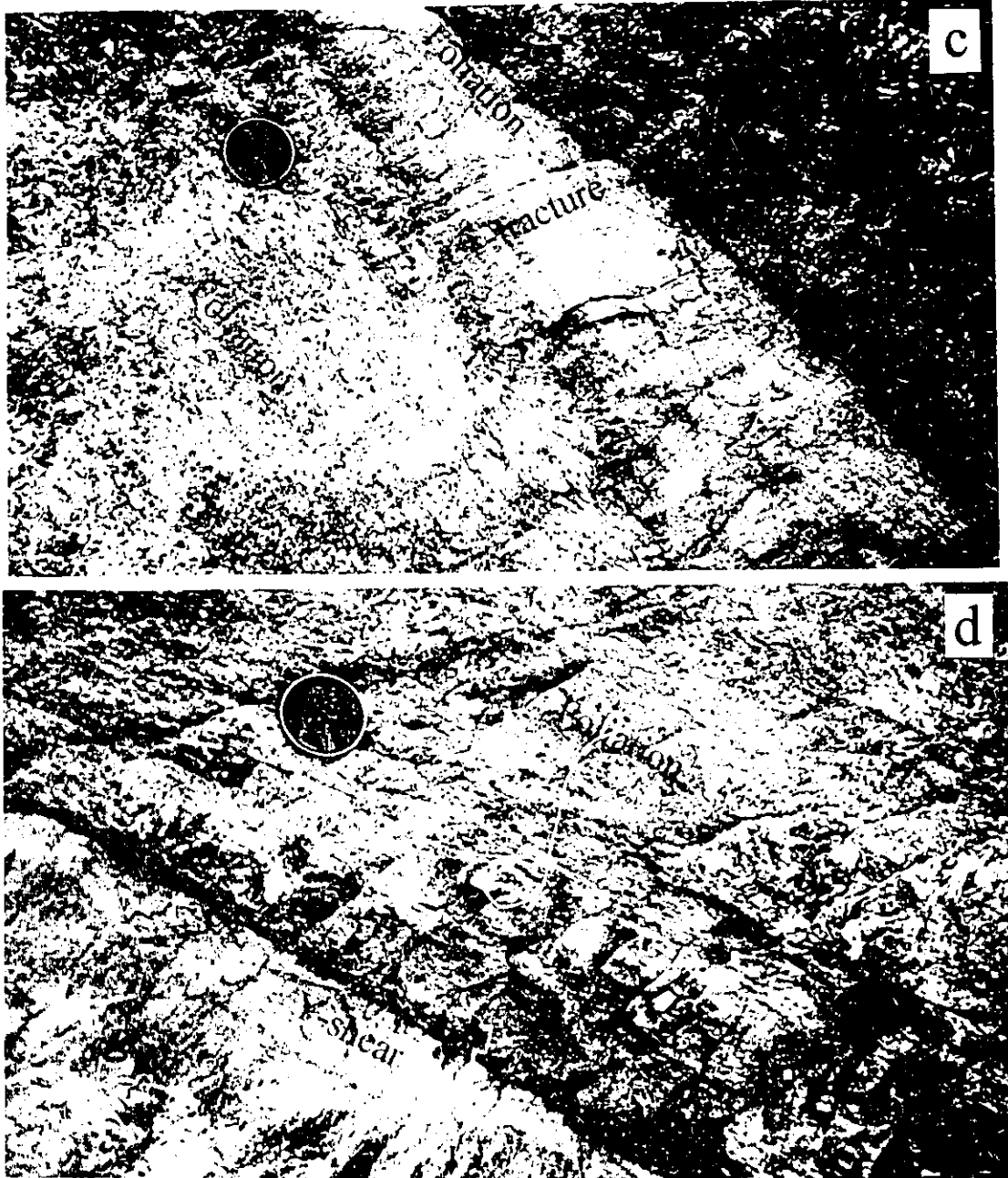


Figure 5.17. (c) Transition zone from cataclasite (Fig. 5.17b) to the narrow gouge zone (Fig. 5.17d) along the fault rock zone. Extension fractures roughly perpendicular to the P-foliations are developed. (d) Narrow gouge zone bounded by strongly deformed cataclasite.

from the principal fault plane (Fig 5.17b). The principal fault planes separating this cataclasite zone are extremely sharp and Y-shears subparallel to these fault planes are developed partially near the wall of cataclasite zone (Fig 5.17a). This cataclasite zone is gradational into the massive fault gouge in a zone 1-7 cm wide along the dip direction of the fault rock zone (Fig. 5.16 and 5.17c, d). One of the sharp fault planes bounding the cataclasite zone continues into the fault gouge zone and the other disappears in the fault gouge zone resulting in undulose contact with less deformed cataclasite zone bounding the gouge zone (Fig 5.17c). Extension fractures roughly perpendicular to the P-foliation are developed in transition zone from cataclasite to gouge zone along the fault (Fig 5.17b, c). Where the gouge zone become narrower, the deformation of cataclasite zone bounding the gouge zone become stronger (compare Fig. 5.17c with 5.17d). The above observations suggest that the distribution of cataclastic deformation was not uniform along the fault zone during long history of movement. These structural features developed within a fault rock zone suggest sinistral movement combined with a reverse dip-slip component.

A strike slip fault with gouge zone bounded by cataclasite zone 10-50 cm wide (Fig. 5.9., locality 4) shows curved geometry leading to a change of dip angle and directions in roughly vertical outcrop section (Fig. 5.18). The width of the fault rock zone is narrower in the segment with steeper dip angle (N10°W/70°NE) than those of the segment with lower dip angle (N36°W/30°NW). The granitic host rocks in both side are severely fractured and faulted. Some breccia patches (20-50 cm) with sharp (Fig. 5.19a) or irregular (Fig. 5.19b) boundary are developed in the hanging wall block. In the



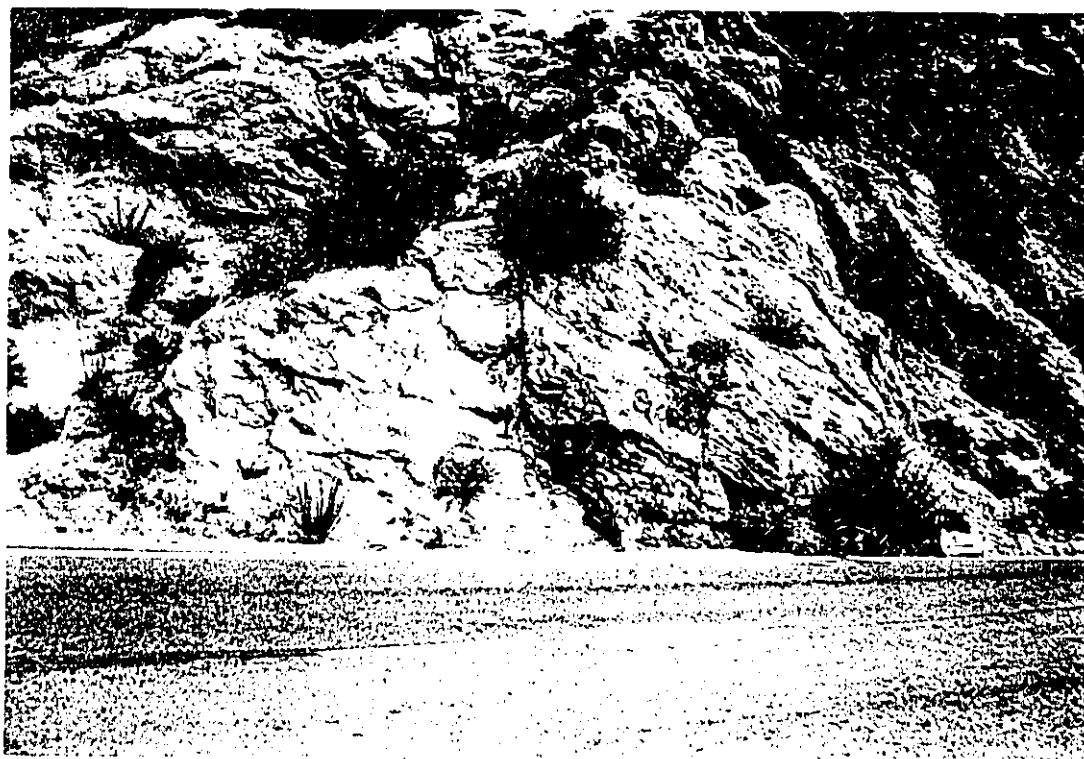


Figure 5.18. A dextral strike-slip fault with curved geometry of fault rock zone in roughly vertical section.

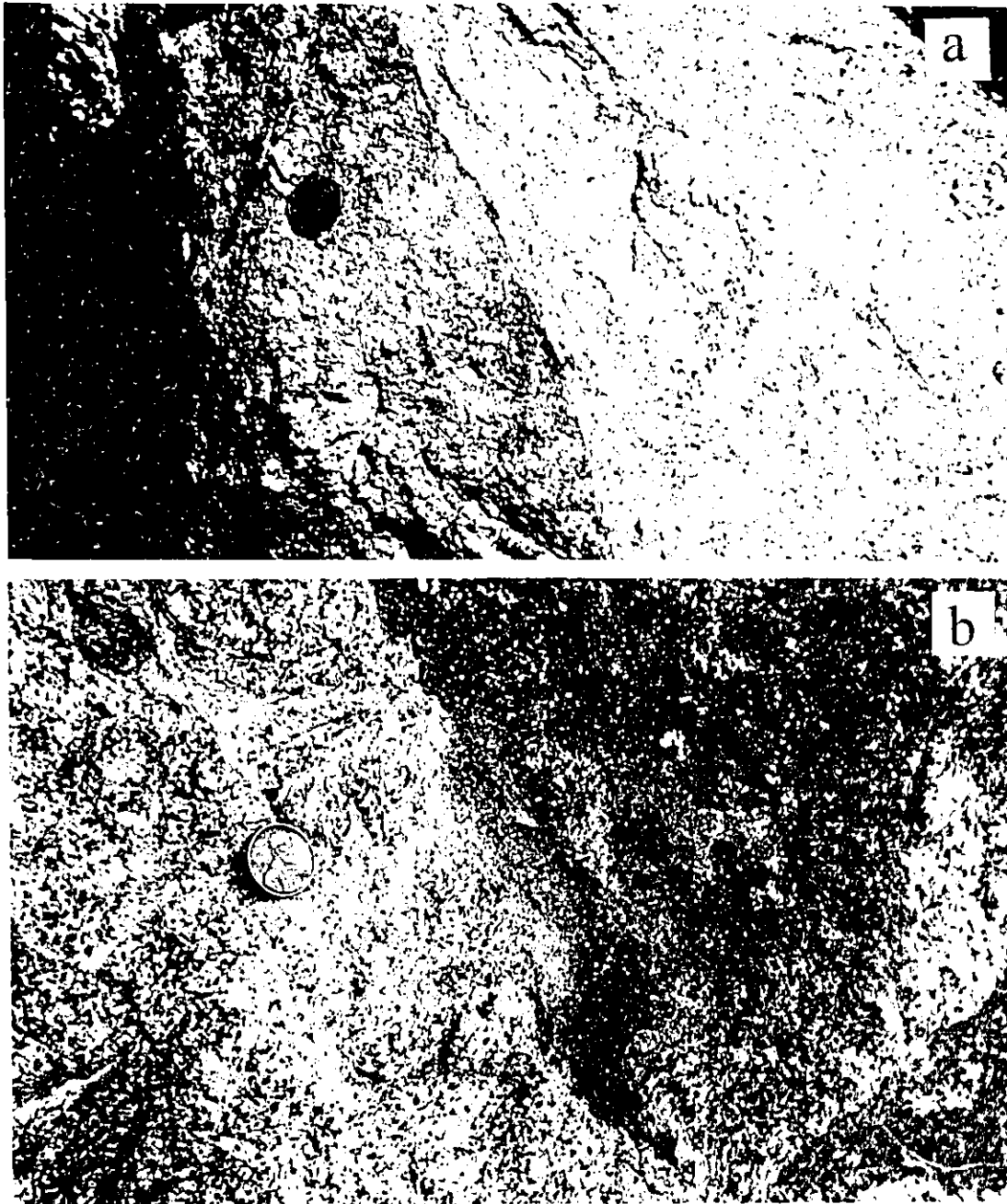


Figure 5.19. A breccia patch with sharp boundary (a) and with irregular boundary (b) developed in the hanging wall block.

cataclasite zone of footwall side, the irregular gouge zones are developed at the direction of  $R_1$ -Reidel shear and Y-shear direction. Minor gouge zones of  $R_1$ -shear direction merge into the main gouge zone (Fig. 5.20a, b). The contact between gouge and cataclasite zone in the footwall side is irregular (Fig. 5.20b); on the contrary, it is relatively sharp in the hanging wall side (Fig. 5.20c). Lens-shaped cataclasite fragments are observed in the main gouge zone, which are produced by concentration of cataclastic flow in the anastomosing arrangement of highly sheared gouge zone (Fig. 5.20d). This suggests that this fault rock zone was evolved by strain softening deformation into a typical Type II shear zone (Means, 1984), in which its deformation is concentrated into a fine grained zone within the primary fault rock zone, so that the cataclasite zone bounding the main gouge zone is inactive in the later stages of deformation (Fig. 5.7). The pervasive P-foliations defined by slip surfaces with slickensides are developed in the main gouge zone. The foliations defined by anastomosing highly deformed matrix and lenticular mineral aggregates are developed in the cataclasite zones of both side.

The host granitic rocks in the fractured zone contain quartz, plagioclase, K-feldspar and biotite. Stable and unstable fractures are developed in quartz and feldspar grains, which show little or no internal deformation (e.g., undulose extinction) indicating that the fractures are cleavage 1-type cracks (Mitra, 1984). The biotite grains are kinked and fractured. Stable fractures are developed in smaller grains in microbreccia zones crosscutting the entire thin sections (Fig. 5.21a). The grains within the microbreccia zone show little or no internal lattice deformation (e.g., undulose extinction, deformation band

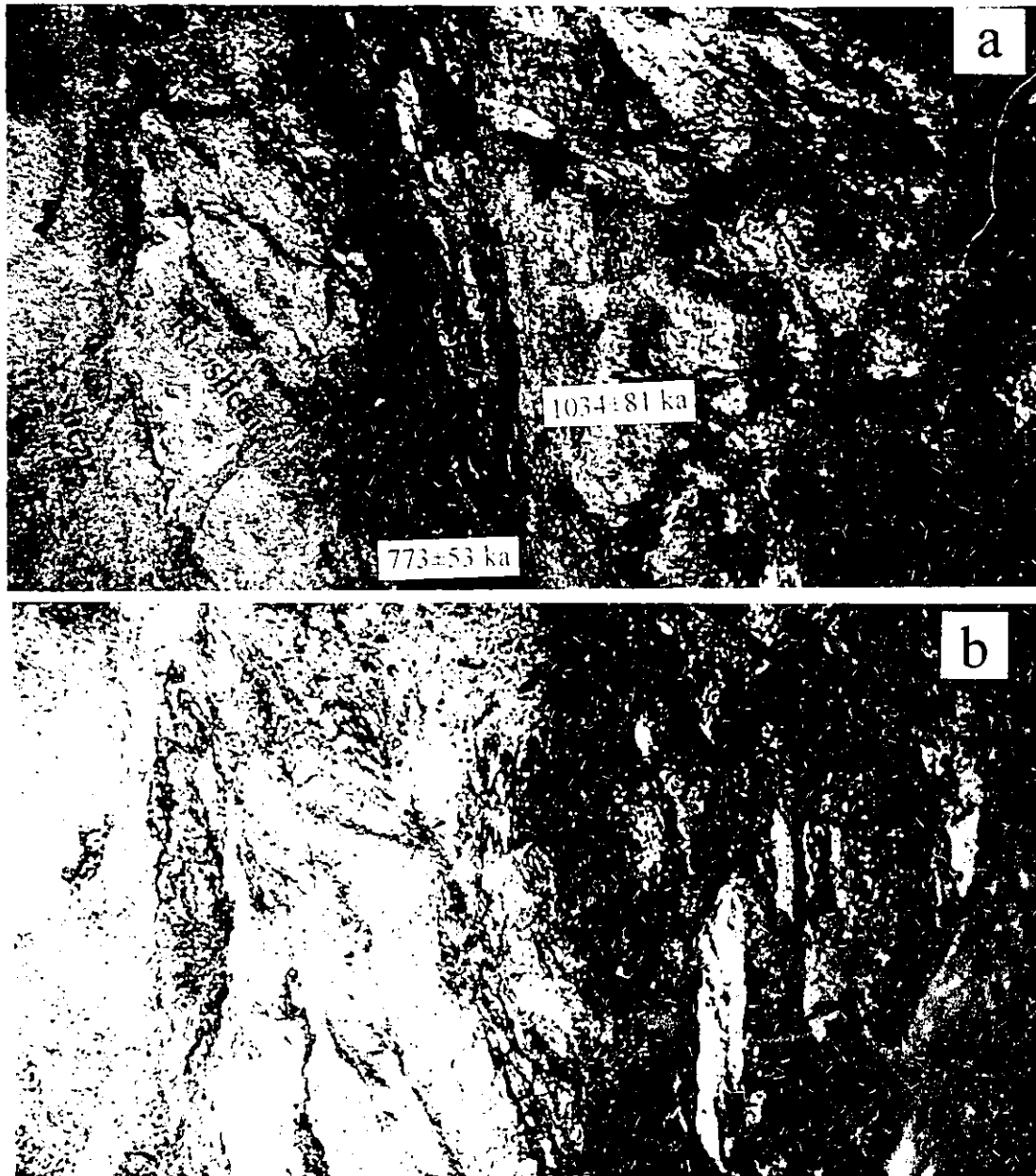


Figure 5.20. (a) Minor shear zones are developed at the direction of  $R_1$ -shear and Y-shear direction. The contact between gouge and cataclasite zone in the left side of this photograph is irregular and the one in the right side is relatively sharp. (b) Close up of the left side of Figure 5.20a. The displacements are concentrated minor shear zones in the cataclasite zone; the cataclasite between shear zones are less deformed than that of the right side of the main gouge zone (compare with figure 5.20c).

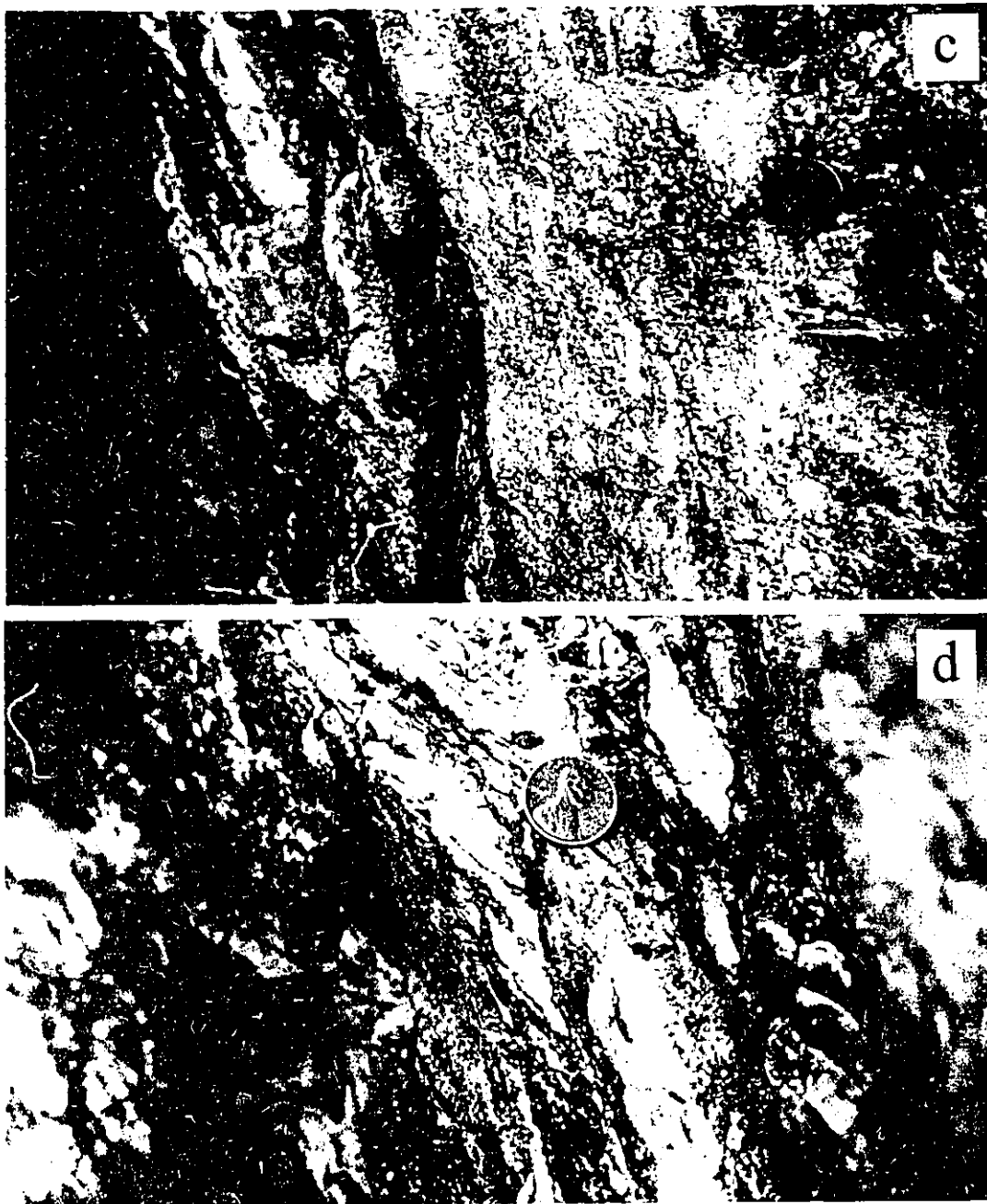


Figure 5.20. (c) Close up of the right side of figure 5.20a. The cataclasite are pervasively foliated by micro shear zone and lense shaped felsic mineral aggregates. The displacements are accomodated by uniformly distributed micro shear zones leading to disjunctive foliations. (d) Cataclasite relicts within the main gouge zone.

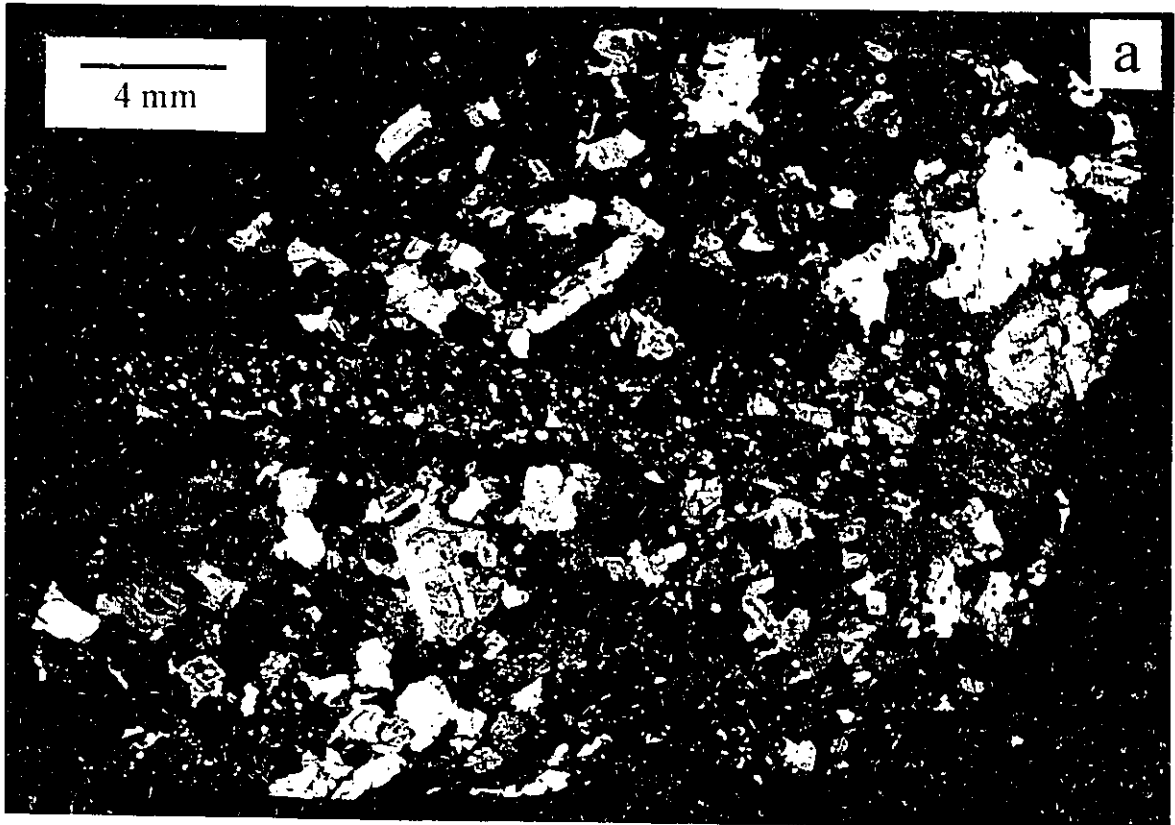


Figure 5.21. (a) Microtexture of host granitic rock. Microfractures are developed within each grain of quartz and feldspar. Note a microbreccia zone developed in the host rock.

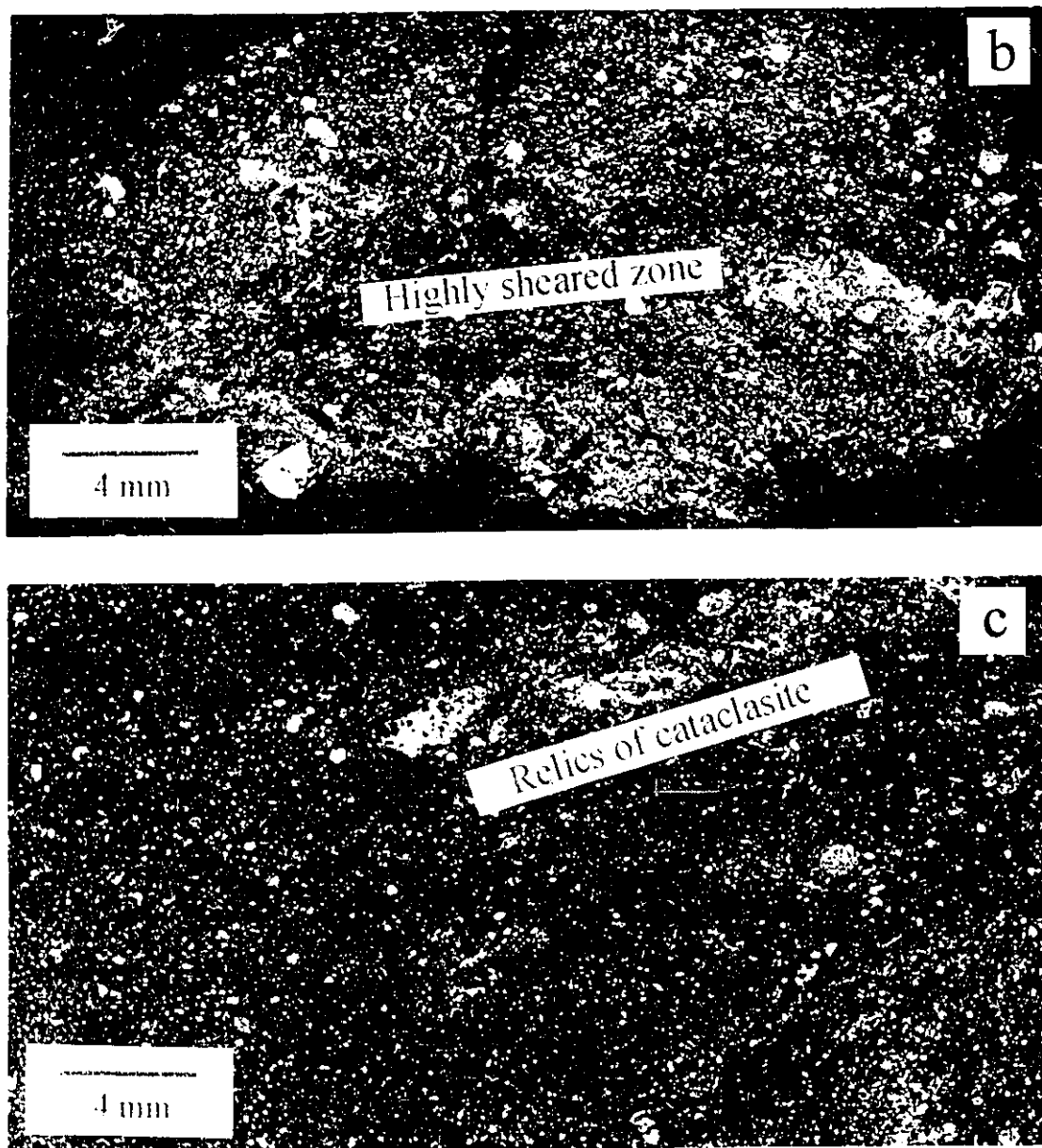


Figure 5.21. (b) Microtexture of cataclasite zone. Severely comminuted layering in the central part of this photograph define the foliation in hand specimen scale. (c) Microtexture of gouge zone. Relics of cataclasite fragments in the upper right of the photograph define the foliation in hand specimen scale.

and subgrains etc.), indicating that reduction of grain size are taken place by comminution of grains. The boundary between microbreccia zone and fractured host minerals is relatively sharp. The width of microbreccia zone appear to be increased by frictional wear in the sidewalls during movements, that is, they belong to a Type III fault rock zone (Fig 5.7) in which the entire zone is active and the width is increased with progressive displacement (Mitra, 1992).

The deformation in the cataclasite zone is inhomogeneous in both mesoscopic- and microscopic-scales. Strongly comminuted zones define the weak foliation or layering in the foliated cataclasite zone in microscopic textures (Fig. 5.21b). In some cases, preferred alignment of deformed biotite form fluxion structures. Porphyroclasts of quartz, feldspar and older cataclasite fragments float in a fine grained matrix. The amount of porphyroclasts in the less deformed domains is larger than that of the strongly sheared domains. The most obvious feature is the fracturing of feldspar grains with intragranular tensile fractures and alteration along the fractures. Quartz grains exhibit mild undulose extinction and widely spaced intragranular fractures. The rounded host rock fragments are surrounded with some fine grained mineral fragments leading to a mantle and core structure, which indicates localized fracturing in the boundary of rock fragments during grain boundary frictional sliding and rotation of fragments.

Pervasive slickensides are developed in the gouge zone. The microtextures are similar to those of the cataclasite zone without the smaller size and amount of porphyroclasts; the amount of matrix is increased (Fig. 5.21c). The microfractures in the



porphyroclasts are less developed than those in the cataclasite zone. This fact suggests that grain boundary frictional sliding has predominated over fracturing in the late stage of the evolution of the fault rock zones.

Both cataclasite and gouge samples show ESR age plateaus for grain size  $< 75 \mu\text{m}$ . The estimated ESR ages for gouge (91091) and cataclasite (91092) are  $773 \pm 53$  ka and  $1034 \pm 81$  ka, respectively (Fig.5.20a).

The evolution of the fault zone at this site (Fig 5.20) can be summarised as follows: fractures and minor faults were formed during main active period (12-5 Ma) of the San Gabriel fault zone (Fig. 5.8). The localization of shear strain had occurred resulting in the development of a cataclasite zone about 1 m wide during rapid uplift of the Little Tujunga region (1030 ka). The gouge zone had formed in the direction of Y-shear (boundary shear zone) and  $R_1$ -shear direction within cataclasite zone by strain softening process (Fig 5.20a, b). One of the boundary gouge zones was reactivated in about 770 ka ago resulting in increasing the thickness of the boundary gouge zone (Fig 5.20a).

#### **5-3-3-4. A fault gouge zone bounded by older gouge**

Several fault gouge zones developed in the Little Tujunga region show a reactivated fault gouge zone bounded by older gouge zone. In general, the older gouge is massive, but the reactivated gouge is foliated with preferred orientation of chlorite

minerals (Fig. 5.22).

A good example is developed near the Bear Divide. The Bear Divide thrust fault with a gouge zone 4 m wide is bounded by fractured gneiss 5 m wide in the hanging wall block and 2.5 m wide in the footwall block (Fig. 5.9, locality 3). Roughly half of the gouge zone of the footwall side is well foliated with chlorites oriented by reactivation. Lens shaped quartz veins are developed subparallel with the foliation only in the reactivated gouge zone. Slickensides are developed both in the interior and boundary of quartz veins indicating the reactivation of the fault after formation of the quartz veins.

Fractured feldspar and quartz grains occur as porphyroclasts in a matrix of very fine grained plagioclase and phyllosilicates in the massive older gouge (Fig 5.23a). The chlorite minerals appear to be developed by alteration of feldspar after faulting events. They do not show any preferred orientation (Fig. 5.23a). Coarse grained calcite veins are undeformed and show an anastomosing distribution.

The foliations are developed by the preferred orientation of chlorite minerals in the reactivated gouge zone. The calcite veins are also foliated by preferred arrangement of elongated calcite crystals (Fig. 5.23b). The quartz porphyroclasts are floating in the matrix of fine grained chlorite and other minerals. The preferred orientation of chlorite minerals appears to be formed by mechanical rotation during reactivation of fault gouge zone. The calcite minerals in veins show elongated shape in the XZ plane and do not show any elongation or weakly elongate shape in the YZ plane indicating deformation of the prolate ellipsoidal type (Fig. 5.23b and c).



Figure 5.22. An example of fault gouge zone developed in the Mendenhall gneiss. Note well foliated reactivated gouge zone in the footwall side.

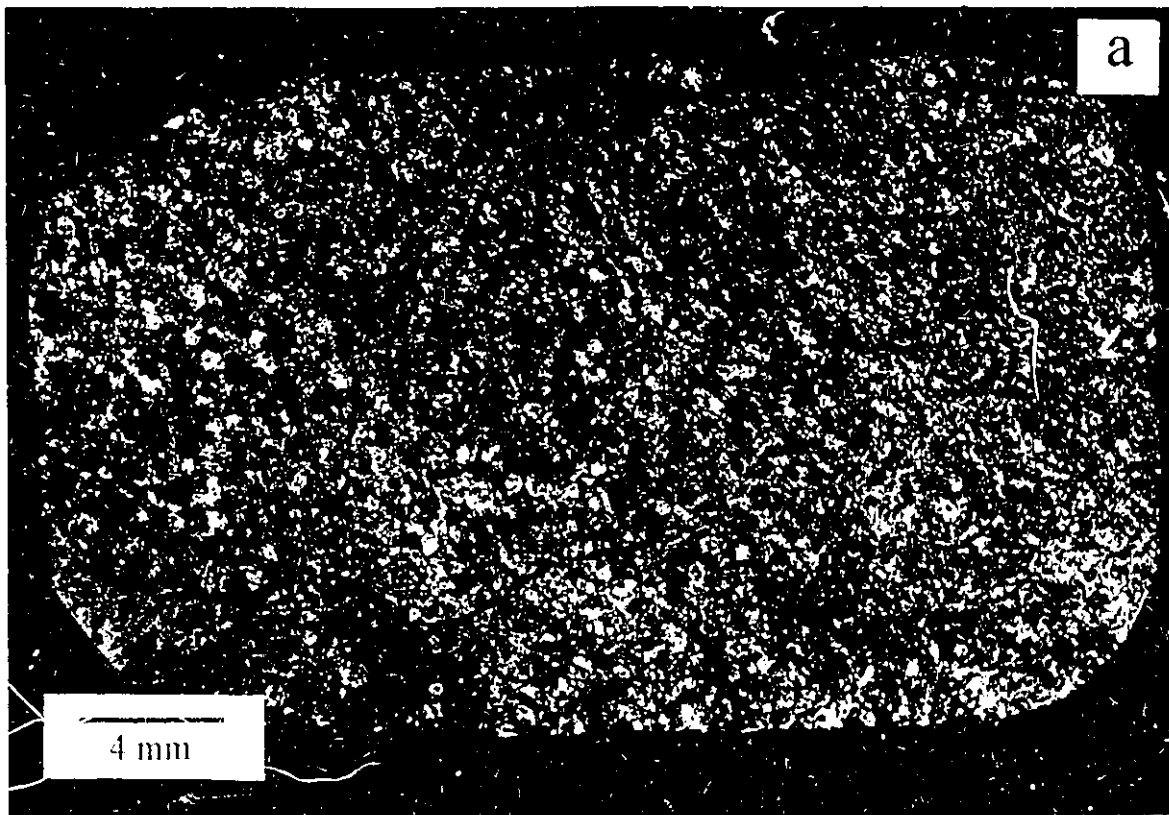


Figure 5.23. (a) Microtexture of primary or older gouge zone. Feldspar and quartz porphyroclasts are surrounded by matrix of chlorite and mineral fragments. Calcite veins are developed irregularly.

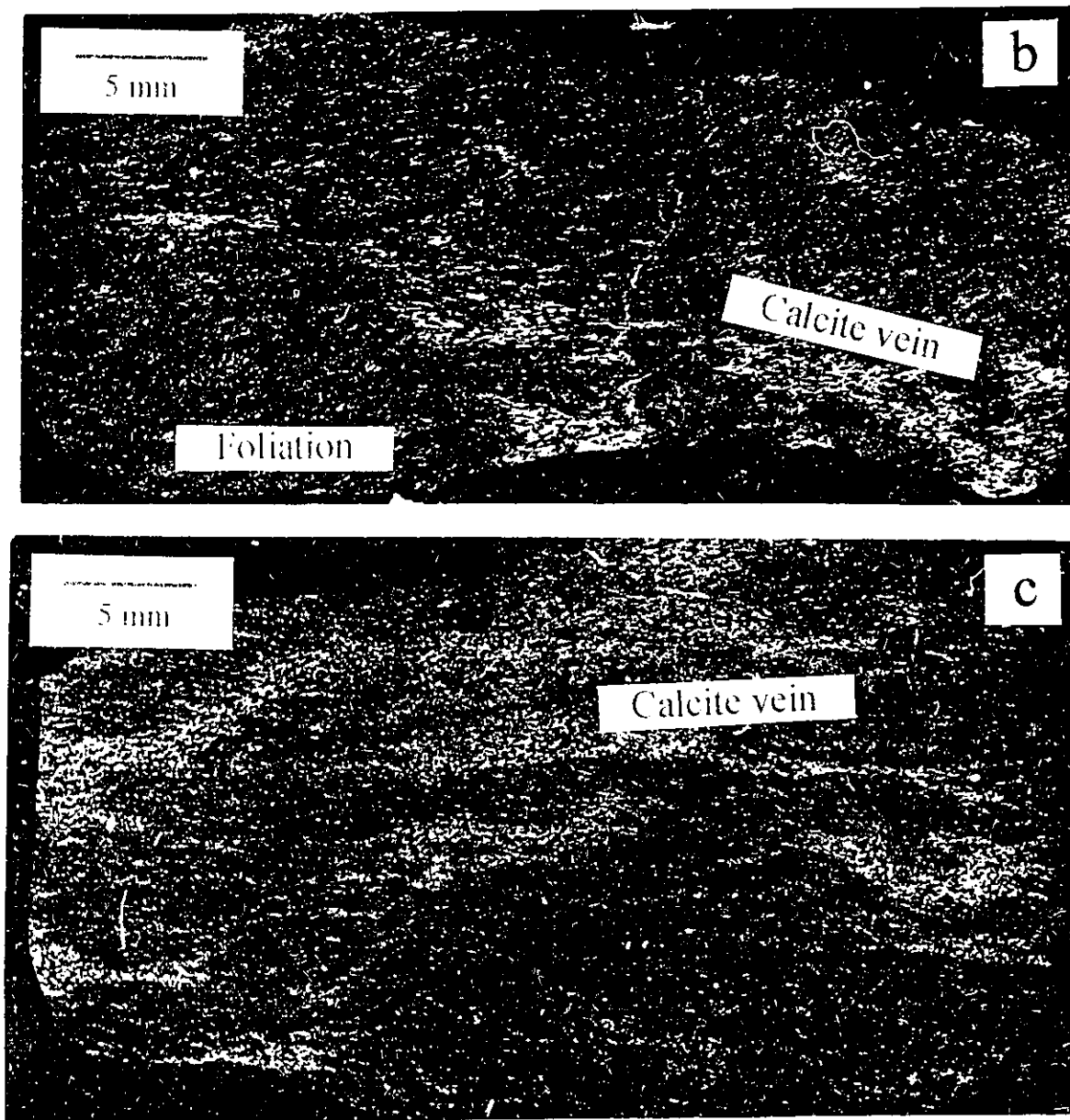


Figure 5.23. (b) Microtexture of reactivated gouge zone (XZ plane). Preferred arrangement of chlorite minerals define the foliations. Note elongated calcite minerals in the vein (white part of photograph). (c) Microtexture of reactivated gouge (YZ plane). Calcite minerals in the vein (white part of photograph) were not elongated (compare with Fig. 5.23b).

#### **5-3-4. The evolution of fault rock zones in the brittle deformation regime**

The observations and analysis in the above sections suggest that the generation and development of fault zones and equivalent fault rocks is considered progressive and sequential (Fig. 5.24). The sequential development of Type II fault zones can be explained as follows; at the first stage, there occur fracturing of host rocks or movement of preexisting fractures (Fig 5.8 a). At the second stage, the strain is localized and shear zones develop with fault breccia or cataclasite with increasing shear strain (Fig 5.8b and 5.17). This shear zone with fault breccia or cataclasite is localized to the centre of the fractured zone or at one margin of it, or it may be in several discrete bands woven throughout the zone (Fig 5.8b and 5.20a). At the third stage, the fault gouge is formed by extensive cataclasis, frictional grain boundary sliding and rotation of particles in the highly deformed zone within primary fault rock zone (Fig. 5.17c, d, 5.20a, and 5.22). At the fourth stage, with the increase of shear strain within localized fault gouge zone, progressive grain size diminution ceases. Several studies of simulated fault gouge and natural fault gouge show that the gouge has constant grain size distribution (Wojtal and Mitra, 1986, Biegel and Sammis, 1989, Marone and Scholz, 1989). Sliding on grain boundaries and rotation of particles are the main deformation mechanisms in the later stage of the development of fault gouge (Fig 5.21c, and 5.23b, c). Further deformation becomes localized in principal slip surface (boundary shear zone), Riedel shear or Y-shear in the main gouge zone. Progressive wear in the gouge and rock interface increases the

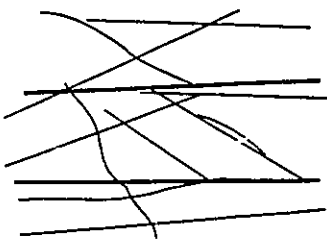
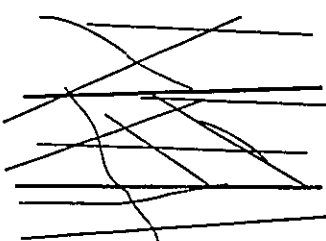
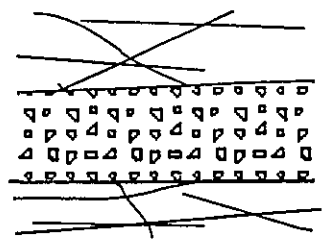
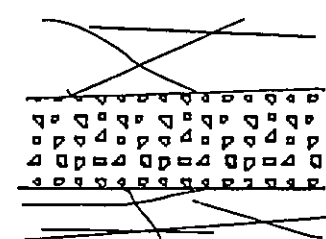
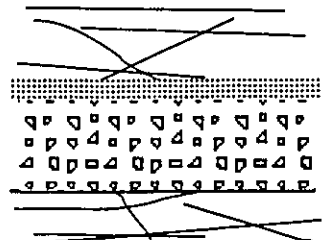
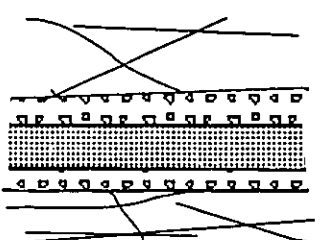
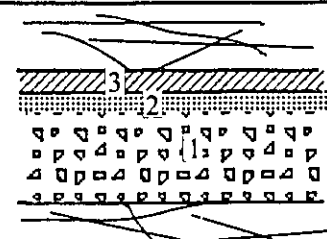
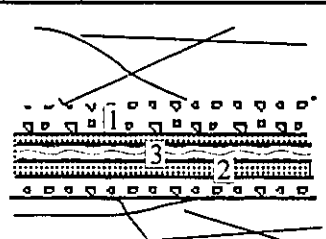
Faulting Mode	Type I	Type II
Stage 1		
Stage 2		
Stage 3		
Stage 4		
	Strain hardening	Strain softening

Figure 5.24. Evolution of fault zones with fault rocks.

amount of fault gouge and expands the thickness of the main gouge zone (Fig. 5.15).

For a Type I fault zone, the thickness of fault breccia or cataclasite zones is increased and fracturing of the host rocks continues with shear strain. In some stages, the new fault rock zone is added to an inactive fault rock zone resulting in increase of the thickness of gouge zone.

This deformation sequence may be stopped at some stage; it may also become reactivated by conversion from strain softening to strain hardening or vice versa. The reactivation of a whole fault rock zone overprints the structural elements within the gouge zones for Type III fault zone.

For Type I and II fault zones, ESR plateau dating method can determine the time of activity in each subzones (for example, breccia, cataclasite, gouge). Therefore, we sometimes are able to identify not only the most recent displacement of a fault, but also two or more older ones. Some good examples of Type II fault zones were described with their ESR ages in the former section (Fig 5.13a, 5.15, 5.17, 5.20, 5.22). Distinct fault rock units represent distinct faulting events, whose last times of motion may be separated in time by up to several hundred thousand years, but also be so close in time to be irresolvable by ESR dating method. Generally, for Type II modes of faulting in the Little Tujunga region, the footwall side of thrust fault rock zone were reactivated in a later stage (Fig 5.22).

On the other hand, for the Type I mode of thrust fault zone in the Little Tujunga region, the hanging wall side was reactivated. Some good examples were developed in



Domain 3. A thrust fault gouge zone 80 cm wide is bounded by broad fault breccia zone (~ 500 m) indicating strain softening deformation in some stage of the development of fault zone (Fig. 5.25a). In the hanging wall side of this gouge zone (1 in Fig 5.25a), a new gouge zone 20 cm wide (2 in Fig.5.25a) was developed and then a gouge zone 10 cm wide (3 in Fig. 5.25a) was added but less deformed than the main gouge zone. During this adding of new gouge zones, the main gouge zone was inactive (Type I fault zone). The margins of the new gouge zone are strongly deformed (Y-shear zone) and P-foliation and  $R_1$ -shears are developed (Fig. 5.25b).

Another example is the thrust cataclasite zone in Domain 3. A cataclasite zone about 10 cm wide developed in the Mendenhall gneiss and minor gouge zones a few mm wide are developed in Y-shear direction within cataclasite zone. In the footwall side, a gouge zone several mm wide is developed and P-foliations subparallel with the fault boundary are developed within cataclasite. On the hanging wall side, two gouge zones a few mm wide are separated about 0.8 cm and between them P-foliations are developed in the cataclasite at a higher angle (about  $30^\circ$ ) to the fault boundary (Fig. 5.26). This new cataclasite zone is less deformed than the main cataclasite zone indicating that the main cataclasite zone was reactivated several times during its movements history. This suggest that this thrust fault rock zone was developed by cyclic alternation of strain hardening and strain softening. Thrust fault rock zones alternated between Type I and Type II mode in successive sheet motions were also reported in Appalachian thrusts (Wojtal and Mitra, 1986,1988; Mitra, 1992).

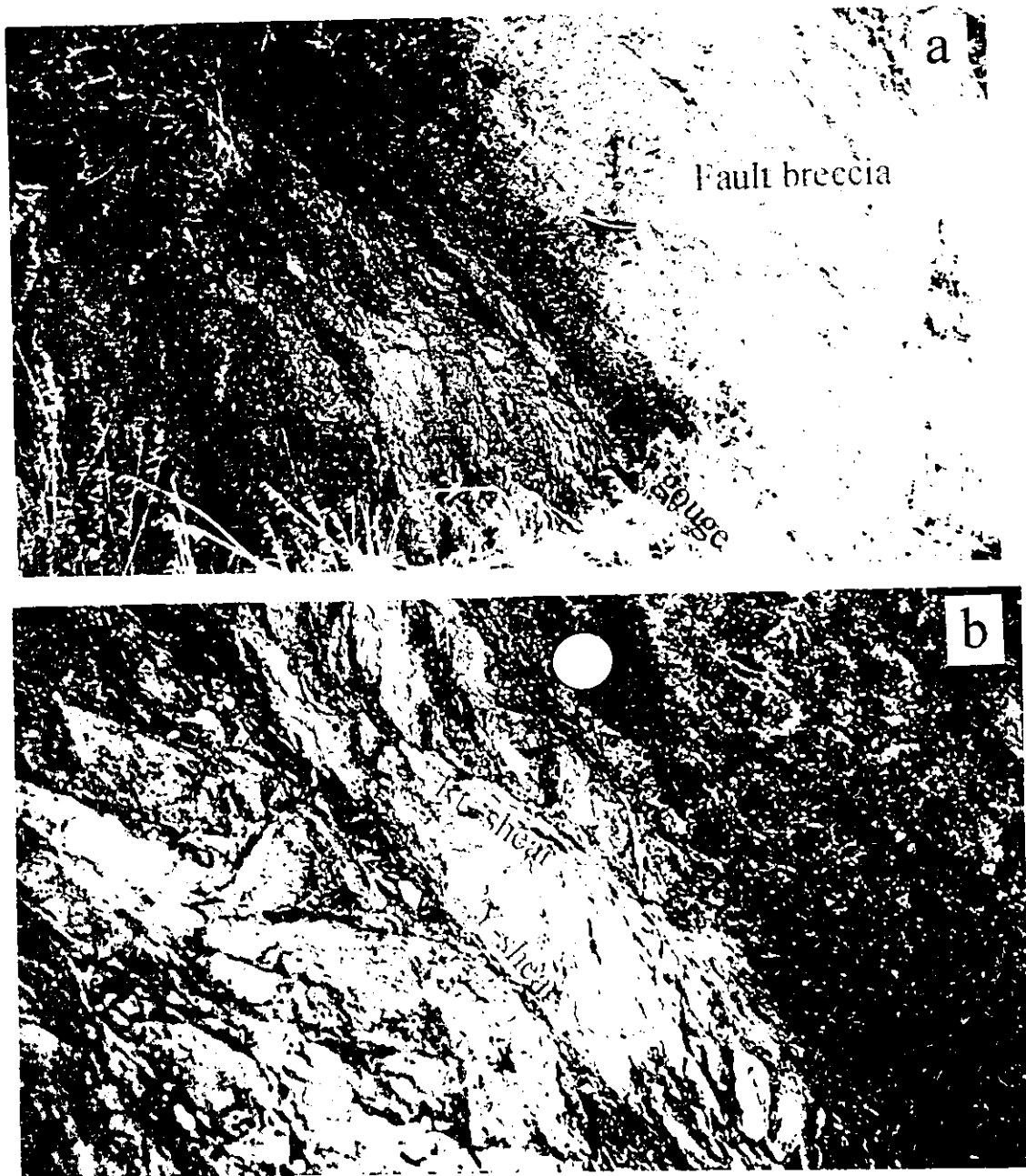


Figure 5.25. (a) An example of Type I fault gouge zone. (b) Close up of the new gouge zone.

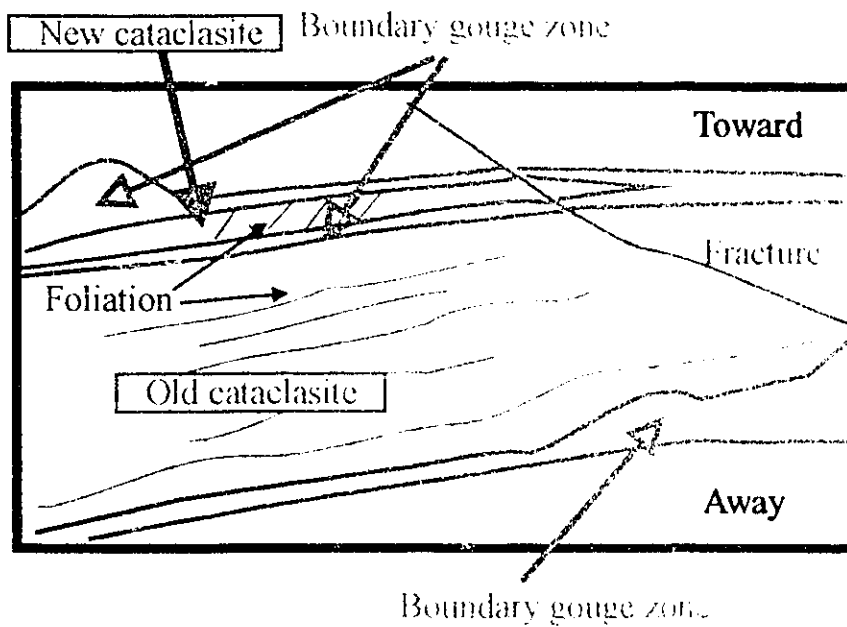


Figure 5.26. An example of Type I mode of fault rock zone.

For Type III mode, only the last movement can be determined by the ESR plateau dating method. Single fault strands are as wide as a few meters, and vary internally in apparent degree of reworking, but nevertheless exhibit uniform ESR age. This shows that any given strain event is capable of thorough resetting of ESR signals throughout a large volume of fault rock for Type III faulting mode. Some examples were described in the former section and others will be described in the next chapter (Chapter 6).

#### **5-4. Summary**

Two major fault zones (San Gabriel and Santa Susana-Sierra Madre) and folds are developed in the Little Tujunga region. The trace of thrust faults and folds of the Santa Susana-Sierra Madre fault zone are roughly parallel to the San Gabriel fault zone, indicating that the maximum horizontal stress was nearly perpendicular to the San Gabriel fault zone. Bends in the main strands of the San Gabriel fault zone yielded local transpressive regimes and changed the direction of maximum horizontal stress to a lower angle to the main strands, resulting in the development of subsidiary faults and folds oblique to the main trend of the fault. These structural features can be explained by the process of low drag-decoupled shear combined with transpression.

The fault zones with fault rocks in the Little Tujunga region were formed about 12-5 Ma ago and reactivated with Type I, II, and III mode by strain softening and strain hardening processes since then. For Type I and II fault zones, ESR plateau dating method

can determine the age of each stage of evolution of fault rock zones; on the other hand, for Type III fault zone, only the age of last movement can be determined by ESR method. The activity of distinct fault rock units of the fault zones were separated in time up to several hundred thousand years, but may also be so close in time to be irresolvable by ESR dating method.

## **Chapter 6**

### **Chronology of movement on the San Gabriel fault zone**

#### **6-1. Fault movement history analysis using ESR plateau method**

Tectonic deformation events commonly show a cyclic variation of the strain rate. An orogenic event or an extensional basin evolution can be considered a long term cyclic deformation typically on a time scale > 20 Ma. Cyclicality on a smaller time scale can be seen in activity of fault zones (Knipe, 1989). Some studies of fault zones have tried to unravel cyclic fault movement history using the microstructure of the fault rocks (White et al., 1986; Blenkinsop and Drury, 1988), but cannot provide absolute ages. Geologic assessment of the periodicity of fault movement has been attempted using stratigraphic and structural evidence (Mckee et al., 1984; Bell and Katzer, 1990).

Each segment of a fault zone has its own movement history. Some active strands of a fault zone may be abandoned as other faults take over the strain accommodation (Knipe, 1989). However, we can determine only the last movement of a fault segment using ESR dating method. Let us assume that 3 faults developed in a fault zone, and were reactivated several times (Fig. 6.1). Although ESR signals in each fault were reset

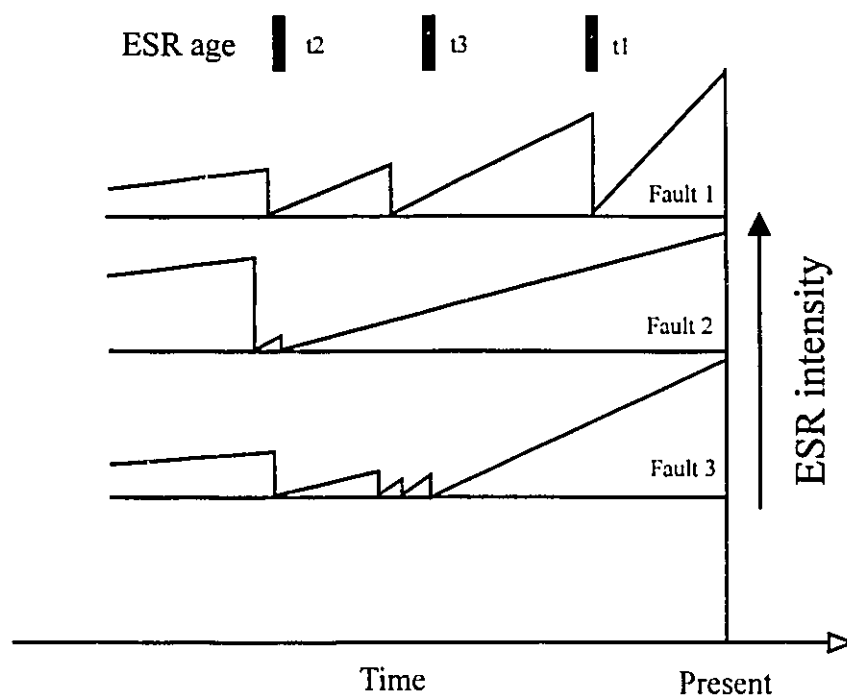


Figure 6.1. Temporal variation of ESR intensity. ESR signals can be reset by a series of fault movements during active periods. Each individual break in a fault zone has its own movement history. However, we can determine only the last movement of each fault using ESR plateau dating method ( $t_1$ ,  $t_2$ ,  $t_3$ ; ESR age estimates for fault F1, F2, F3). Steeper rise in ESR intensity after faulting is due to creation of new precursor ESR centers by shearing.

several times due to successive faulting events. We can observe only the ages of last movements of fault 1 ( $t_1$ ), fault 2 ( $t_2$ ) and fault 3 ( $t_3$ ). This failure to detect overprinted events somewhat degrades the richness of the ESR dating record. However, historic earthquake faulting events show that some subsidiary faults or parts of the main fault rock zone did not reactivate during successive faulting events but preserve records of older faulting events (Type I and II mode).

In this study I have investigated temporal and spatial patterns of the Quaternary fault activity of the San Gabriel fault zone, to test for spatial clustering of fault activity in restraining bends, such as is known from modern seismic activity on other fault systems. I investigated whether the relationships between structural features and fault activity could be used to analyze the dynamics and kinematics of paleoearthquake movements. I have also attempted to estimate the temporal distribution of paleoseismic activity on a  $10^5 - 10^6$  y time scale. Such knowledge of the long term pattern of fault movement would provide a better context to the evaluation of potential hazards from earthquakes.



## 6-2. Fault movement history of the San Gabriel fault zone

Crowell (1952, 1986a) has suggested that major strike slip occurred along the San Gabriel fault zone from 12 Ma to about 5 Ma years ago. During this period, the San Gabriel fault zone was possibly the main trace of the San Andreas fault system. The fault is considered to have become inactive about 5 Ma years ago and the major strike slip movement transferred to the present San Andreas fault zone. The reactivation along the San Gabriel fault zone was less active than before with dip slip after 5 Ma ago. Weber (1985, 1986, 1988) suggested however that the fault has much smaller right lateral displacement that proposed by Crowell (1952, 1986a), and argued that activity along the San Gabriel fault zone continued into the Quaternary. He showed a series of the evidences of Quaternary movements along the fault zone (Weber, 1985). In the Little Tujunga region he observed: (1) older alluvium and ancient landslide deposits displaced downward on the north side of the fault; (2) igneous-metamorphic rocks are displaced upward relative to older alluvium along the north side of a fault in the Dillon Divide area; (3) a low scarp across the surface of terrace deposits slightly west of Little Tujunga Canyon Road; (4) the entire drainage area of Little Tujunga Canyon is left-deflected about 0.5 Km.

### 6-2-1. Results of ESR dating of fault rocks

Samples were collected from the San Gabriel fault zone as shown on figure 6.2. Some of the results of ESR plateau dating of fault rocks collected in the Little Tujunga region were given in the previous chapters (Chapters 4 and 5). In this section, I will describe the results of ESR analysis of some additional samples (Table 6.1). Average ESR plateau age estimates in each locality and local geological features are summarized in Table 6.2. For a detailed discussion of the sensitivity and dose-response of the various ESR signals used here, see Chapter 4.

Wherever we could independently determine the sequence of fault movements by intersection relationships, the sequence of ages obtained by ESR analysis agrees with the sequence indicated by geological relationships.

For example, where the main strand of the San Gabriel fault crosses the Big Tujunga Canyon road, a major 70 m thick fault zone is developed in heterogeneous granitic gneiss and leucogranite (Fig 6.2; locality 9). Minor anastomosing shear bands had been developed in the greenish grey fault gouge (SG25), while purple gouge (SG26) cuts these minor shear bands. The width of the purple gouge ranges from 5 to 10 cm. Dark grey fault gouge (SG27) is developed within a fracture zone about 4 m away from the purple gouge zone. As expected, the reactivated younger gouge (SG26) shows a lower age ( $236\pm 11$  ka) than that of the older host gouge (SG25;  $557\pm 19$  ka). The age of the nearby dark grey gouge (SG27;  $236\pm 12$  ka) is identical in age to the purple one. Although they

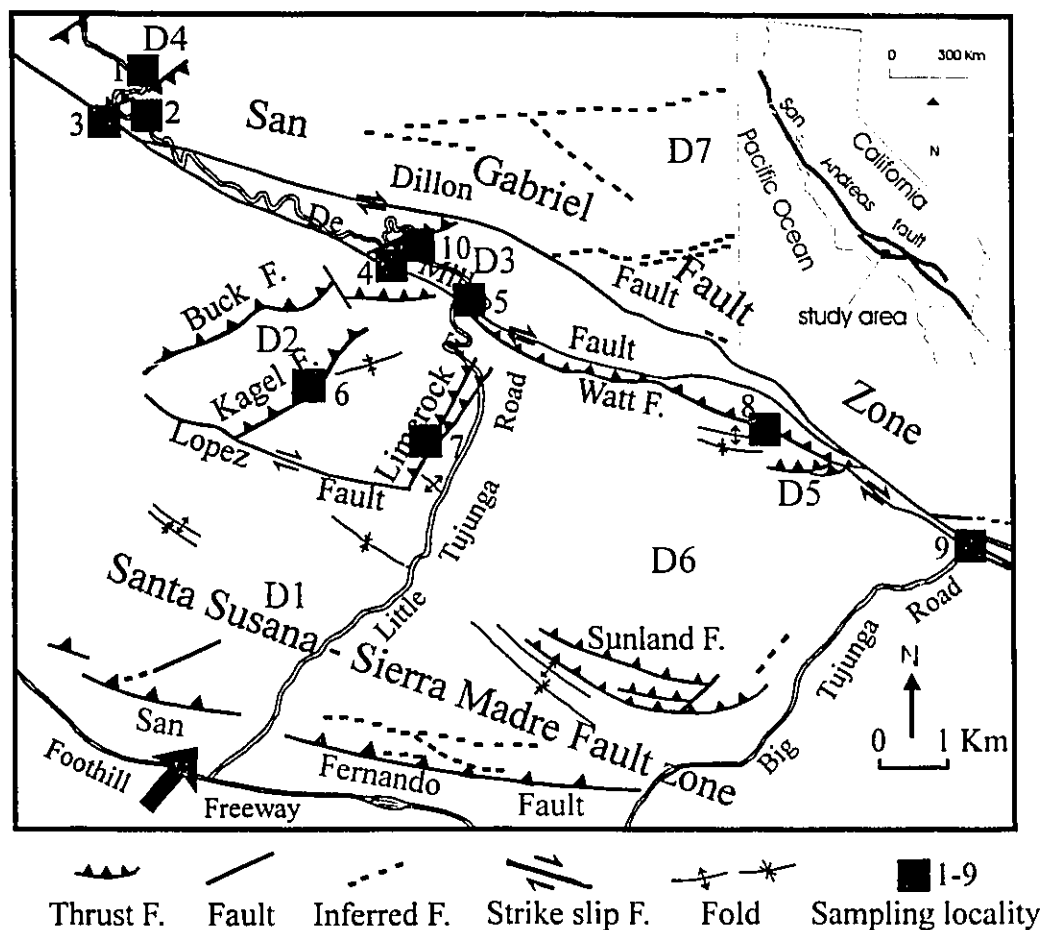


Figure 6.2. Structural map of the Little Tujunga region, showing locations of sample sites; locality 1, Santa Clara Divide fault; locality 2, Bear Divide fault; locality 3, San Gabriel fault at Bear Divide; locality 4, De Mille fault southwest of Dillon Divide; locality 5, Barrel Spring fault; locality 6, Kagel fault; locality 7, Limerock fault; locality 8, Watt fault; locality 9, San Gabriel fault at Big Tujunga Road; locality 10, Dillon Divide fault.

Table 6.1\*. ESR analytical data and results for fault rocks from the San Gabriel fault zone.

Fault	Sample	Grain size ( $\mu\text{m}$ )	Center	$D_E$ (Gy)	U (ppm)	Th (ppm)	K (%)	Dose rate ( $\mu\text{Gy/a}$ )	ESR age (ka)	Locality
De Mille	91039B	250-350	E'	8595 $\pm$ 469	4.76	9.53 $\pm$ 0.17	0.73 $\pm$ 0.04	2597 $\pm$ 105	3309 $\pm$ 225	4
De Mille	91039C	150-250	E'	2474 $\pm$ 196	4.76	9.53 $\pm$ 0.17	0.73 $\pm$ 0.04	2767 $\pm$ 123	894 $\pm$ 81	4
De Mille	91039D	100-150	E'	1300 $\pm$ 134	4.76	9.53 $\pm$ 0.17	0.73 $\pm$ 0.04	2929 $\pm$ 144	444 $\pm$ 51	4
De Mille	91039E	75-100	E'	1131 $\pm$ 84	4.76	9.53 $\pm$ 0.17	0.73 $\pm$ 0.04	3149 $\pm$ 179	359 $\pm$ 34	4
De Mille	91039F	<45	E'	1225 $\pm$ 51	4.76	9.53 $\pm$ 0.17	0.73 $\pm$ 0.04	3560 $\pm$ 251	334 $\pm$ 28	4
Kagel	91043C	150-250	OHC	4377 $\pm$ 281	4.16	13.46 $\pm$ 0.24	2.84 $\pm$ 0.14	4902 $\pm$ 224	893 $\pm$ 70	6
Kagel	91043D	100-150	E'	3964 $\pm$ 379	4.16	13.46 $\pm$ 0.24	2.84 $\pm$ 0.14	5096 $\pm$ 241	778 $\pm$ 83	6
Kagel	91043E	75-100	OHC	3960 $\pm$ 402	4.16	13.46 $\pm$ 0.24	2.84 $\pm$ 0.14	5348 $\pm$ 270	741 $\pm$ 84	6
Kagel	91043E	75-100	E'	4377 $\pm$ 281	4.16	13.46 $\pm$ 0.24	2.84 $\pm$ 0.14	5348 $\pm$ 270	738 $\pm$ 72	6
Kagel	91043F	<45	OHC	4155 $\pm$ 317	4.16	13.46 $\pm$ 0.24	2.84 $\pm$ 0.14	5801 $\pm$ 334	716 $\pm$ 68	6
Kagel	91043F	<45	E'	4032 $\pm$ 194	4.16	13.46 $\pm$ 0.24	2.84 $\pm$ 0.14	5801 $\pm$ 334	695 $\pm$ 52	6
Watt	91044B	150-250	AI	3751 $\pm$ 318	3.65	8.94 $\pm$ 0.17	2.58 $\pm$ 0.13	3968 $\pm$ 182	945 $\pm$ 91	8
Watt	91044C	100-150	E'	2994 $\pm$ 237	3.65	8.94 $\pm$ 0.17	2.58 $\pm$ 0.13	4146 $\pm$ 194	722 $\pm$ 67	8
Watt	91044C	100-150	AI	2360 $\pm$ 265	3.65	8.94 $\pm$ 0.17	2.58 $\pm$ 0.13	4146 $\pm$ 194	569 $\pm$ 69	8
Watt	91044D	75-100	E'	2134 $\pm$ 97	3.65	8.94 $\pm$ 0.17	2.58 $\pm$ 0.13	4300 $\pm$ 207	496 $\pm$ 33	8
Watt	91044D	75-100	AI	2039 $\pm$ 172	3.65	8.94 $\pm$ 0.17	2.58 $\pm$ 0.13	4300 $\pm$ 207	474 $\pm$ 46	8
Watt	91044E	45- 75	E'	997 $\pm$ 74	3.65	8.94 $\pm$ 0.17	2.58 $\pm$ 0.13	4497 $\pm$ 227	222 $\pm$ 20	8
Watt	91044E	45- 75	AI	2091 $\pm$ 297	3.65	8.94 $\pm$ 0.17	2.58 $\pm$ 0.13	4497 $\pm$ 227	465 $\pm$ 70	8
Watt	91044F	<45	E'	1096 $\pm$ 56	3.65	8.94 $\pm$ 0.17	2.58 $\pm$ 0.13	4849 $\pm$ 274	226 $\pm$ 17	8
Watt	91044F	<45	AI	1063 $\pm$ 49	3.65	8.94 $\pm$ 0.17	2.58 $\pm$ 0.13	4849 $\pm$ 274	219 $\pm$ 16	8
San Gabriel	SG21C	100-150	OHC	629 $\pm$ 70	1.63	16.45 $\pm$ 0.3	2.2 $\pm$ 0.11	3877 $\pm$ 178	162 $\pm$ 20	9

San Gabriel	SG21D	75-100	OHC	656±74	1.63	16.45±0.3	2.2±0.11	4032±192	163±20	9
San Gabriel	SG21E	45- 75	OHC	635±100	1.63	16.45±0.3	2.2±0.11	4233±216	150±25	9
San Gabriel	SG21E	45- 75	E'	729±67	1.63	16.45±0.3	2.2±0.11	4233±216	172±18	9
San Gabriel	SG21F	<45	OHC	584±38	1.63	16.45±0.3	2.2±0.11	4589±266	127±11	9
San Gabriel	SG21F	<45	E'	648±72	1.63	16.45±0.3	2.2±0.11	4589±266	141±18	9
San Gabriel	SG25D	75-100	OHC	1268± 64	1.08	3.36±0.13	1.74±0.09	2269±118	559± 41	9
San Gabriel	SG25D	75-100	E'	1308± 104	1.08	3.36±0.13	1.74±0.09	2269±118	577± 55	9
San Gabriel	SG25E	45-75	OHC	1257± 75	1.08	3.36±0.13	1.74±0.09	2338±123	537± 43	9
San Gabriel	SG25E	45-75	E'	1334± 88	1.08	3.36±0.13	1.74±0.09	2338±123	571± 48	9
San Gabriel	SG25F	<45	OHC	1365± 52	1.08	3.36±0.13	1.74±0.09	2457±135	556± 37	9
San Gabriel	SG25F	<45	E'	1355± 137	1.08	3.36±0.13	1.74±0.09	2457±135	552± 75	9
San Gabriel	SG26C	100-150	OHC	1009± 64	1.08	3.36±0.13	1.74±0.09	2211±114	456± 37	9
San Gabriel	SG26D	75-100	OHC	528± 49	1.08	3.36±0.13	1.74±0.09	2269±118	233± 25	9
San Gabriel	SG26E	45- 75	OHC	565± 43	1.08	3.36±0.13	1.74±0.09	2338±123	242± 23	9
San Gabriel	SG26E	45- 75	E'	596± 36	1.08	3.36±0.13	1.74±0.09	2338±123	255± 20	9
San Gabriel	SG26F	<45	OHC	590± 46	1.08	3.36±0.13	1.74±0.09	2457±135	221± 28	9
San Gabriel	SG26F	<45	E'	544± 61	1.08	3.36±0.13	1.74±0.09	2457±135	241± 16	9
San Gabriel	SG27C	100-150	OHC	1360±59	0.8	1.47±0.12	1.28±0.06	1549± 78	878± 58	9
San Gabriel	SG27D	75-100	OHC	789± 11	0.8	1.47±0.12	1.28±0.06	1585± 80	498± 26	9
San Gabriel	SG27D	75-100	E'	430± 18	0.8	1.47±0.12	1.28±0.06	1585± 80	271± 18	9
San Gabriel	SG27E	45- 75	OHC	820± 50	0.8	1.47±0.12	1.28±0.06	1627± 83	504± 40	9
San Gabriel	SG27E	45- 75	E'	386 ± 20	0.8	1.47±0.12	1.28±0.06	1627± 83	237± 17	9
San Gabriel	SG27F	<45	OHC	721± 39	0.8	1.47±0.12	1.28±0.06	1698± 90	425± 32	9
San Gabriel	SG27F	<45	E'	400± 18	0.8	1.47±0.12	1.28±0.06	1698± 90	236± 16	9

---

\* The remainder of ESR analytical data can be found in chapters 4 and 5.

Table 6.2. Results of ESR age estimates.

Locality	Fault	Sample	ESR age (ka)	<sup>1</sup> Main/Subsidiary	<sup>2</sup> Domain
1	Santa Clara Divide	91071	354±45	subsidiary	4
2	Bear Divide	SG44	1173±130	subsidiary	4
2	Bear Divide	SG40	824±70	subsidiary	4
2	Bear Divide	SG41	357±19	subsidiary	4
3	San Gabriel (Bear Divide)	91077	342±32	main	
3	San Gabriel (Bear Divide)	91075	169±8	main	
3	San Gabriel (Bear Divide)	91076	158±10	main	
4	De Mille	91039	350±22	main	
5	Barrel Spring	91030/91031	238±8	subsidiary	3
6	Kagel	91043	716±33	subsidiary	2
7	Limerock	91004	346±23	subsidiary	2
8	Watt	91044	222±10	main	
9	San Gabriel (Big Tujunga road)	SG25	557±19	main	
9	San Gabriel (Big Tujunga road)	SG26	236±11	main	
9	San Gabriel (Big Tujunga road)	SG27	236±12	subsidiary	5
9	San Gabriel (Big Tujunga road)	SG21	133±9	subsidiary	5
10	Dillon Divide	91091	773±53	subsidiary	3
10	Dillon Divide	91092	1034±81	subsidiary	3

1. Main specifies the main strands of the San Gabriel Fault zone (San Gabriel, Dillon, De Mille, and Watt faults). Subsidiary fault specifies the faults developed both in the restraining bends and nearby main strands of the San Gabriel fault zone.

2. Domain is determined by the characteristics of structural features, which is related with the process of low drag-decoupled shear combined with transpression (see Fig. 5.1).

have different ESR intensities, grain size distribution, host rocks, radiation sensitivity, and dose rate, these two samples give similar ESR plateau ages. The larger grains, on the other hand, give different ages (not systematic) due to the different degrees of partial resetting of ESR signals at the time of fault movement. Such similar ESR plateau ages would be quite fortuitous if ESR signals of grains smaller than critical size had not been all zeroed at the time of fault movement. This fact indicates that these two faults were reactivated at approximately the same time. Many minor faults had been developed in the fractured zone. Sample SG21 was collected from one of minor thrust faults with gouge 1-2 cm wide. The OHC signal yields a plateau of constant ages for grains smaller than 75  $\mu\text{m}$ . The ages from E' signal decrease and converge to the plateau value. The weighted mean of this sample is  $133 \pm 9$  ka.

The De Mille fault is the middle strand of three main branches of the San Gabriel fault zone in the Little Tujunga region. I collected gouge sample from this fault southwest of Dillon Divide (Fig. 6.2; locality 5). In this locality, a flower structure is developed on a scale of a few meters (see Fig. 5.3); the fault plane is convex-upward flattening to horizontal at the surface (N56°W/45°NE) and steepen downward (N56°W/ 80°NE). Drag fold developed in the southwest side block indicate that this block has moved down. The sharp fault plane is developed in the footwall block and fault gouge 20-30 cm wide is bounded by cataclasite 40-180 cm wide, which is developed in the hanging wall block. This fault has a combination of reverse and strike-slip displacement. These observations indicate that the central block (Domain 3) between the Dillon and De Mille fault was

uplifted by the transpression. Sample 91039 collected from white gouge shows a plateau for grains smaller than 75  $\mu\text{m}$ . The weighted mean of ESR ages lying on the plateau is  $350\pm 22$  ka.

The Kagel fault, a subsidiary thrust fault developed in Domain 2 by transpression, which thrusts basement rocks over Saugus formation (Fig. 6.2; locality 6), gives an E' age of  $716\pm 33$  ka.

The Watt fault thrusts Martinez (Palaeocene) conglomerates over Saugus (lower Pleistocene) very coarse sandstone (Fig. 6.2; locality 8). The narrow wedges of Paleocene Martinez formation between the De Mille and Watt faults have been brought into their present positions by dextral strike slip movement. Sample 91044 from the 15~20 cm wide reddish brown fault gouge zone shows an E' plateau for particles of  $<75$   $\mu\text{m}$  grain size and the Al signal in the smallest grains yields the same age as the plateau age of the E' signal. The weighted mean of the ages in the plateau range is  $222\pm 10$  ka.

### **6-3-2. Temporal and spatial pattern of fault activity in the Little Tujunga region in the Pleistocene.**

ESR ages of fault movements help to elucidate the structural relationship between each domain and to establish the structural evolution of this region in late Pleistocene time. A plot of the distribution of dates (Fig. 6.3) shows that, between 400 and 100 ka, ESR ages of movements are clustered. That is, the fault movements appear to occur in



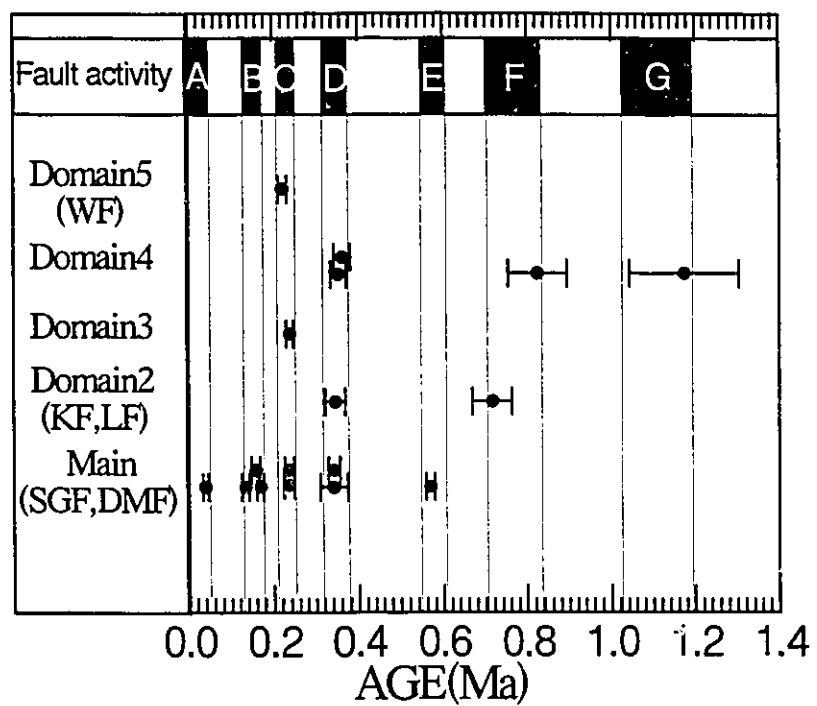


Figure 6.3. The temporal pattern of fault activity of the San Gabriel fault zone in the Little Tujunga region.

active periods, averaging 24 ka in length, separated by rest (dormant) periods of about 64 ka average length. Within active periods, the apparent interval between earthquake movements is about 7.9 ka (Table 6.3). This interval is less than the resolution limit of ESR dating. However, the maximum separation between events within one active period is larger than this resolution limit and shows that events within an active period were dispersed in time to an extent which cannot yet be fully resolved. Activity within each period is seen both on subsidiary faults and on the main strand of the San Gabriel fault. Earlier than 400 ka, the record of alternating active and dormant periods is not evident, probably because of obliteration of older events by younger ones. It is likely, however, that a clustered pattern of activity was present throughout the past.

The spatial pattern of fault activity in the Little Tujunga region (Fig. 6.4) shows that the curved geometry of the San Gabriel fault controlled the distribution of fault activities. The earliest record of activity is from near Bear Divide where a fault breccia zone was active at 1200 ka. This was cut later (824 ka) by fault gouge (Bear Divide fault). A cataclasite zone about 1 m wide has been formed in Dillon Divide fault (1030 ka). It is probable that other faults were formed or reactivated at about the same time, but our data do not show other movements from this time, presumably because the faults involved were reactivated in later active periods. A portion of the Bear Divide breccia zone was reactivated later along one of its bounding fault planes, but without affecting the ESR signals within the remainder of the breccia. Likewise, all the ESR age estimates discussed below represent the last fault movements at a given sampling location; in

Table 6.3. Recurrence intervals for the fault activity of the San Gabriel fault zone in the Little Tujunga region.

Active period	ESR age (ka)	<sup>#</sup> Interval within active period (ka)	Average interval (ka)	Average ESR age (ka)	<sup>\$</sup> Interval (ka)
A	39				
	133				
B	158	25	18	153	114
	169	11			
C	222				
	236	14			
	236	0	5.3	233	80
	238	2			
D	342				
	346	4			
	350	4			
	354	4	4.8	351	118
	363	7			
Average		7.9			

# Interval within active period = later ESR age - former ESR age within active period.

\$ Interval between active period = average ESR age of the next active period - average ESR age of the former active period.

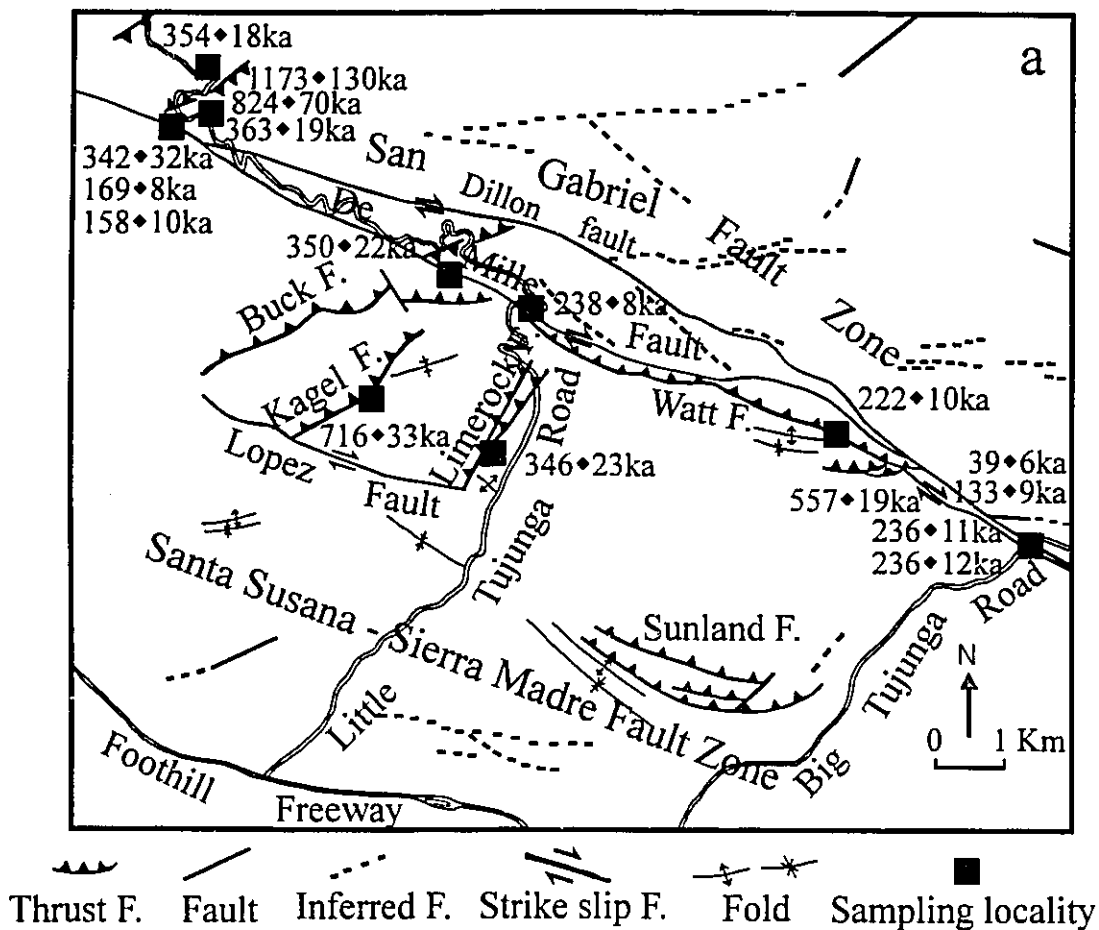


Figure 6.4. The spatial pattern of fault activity of the San Gabriel fault zone in the Little Tujunga region (a): during active period B (b); during active period C (c); during active period D (d).

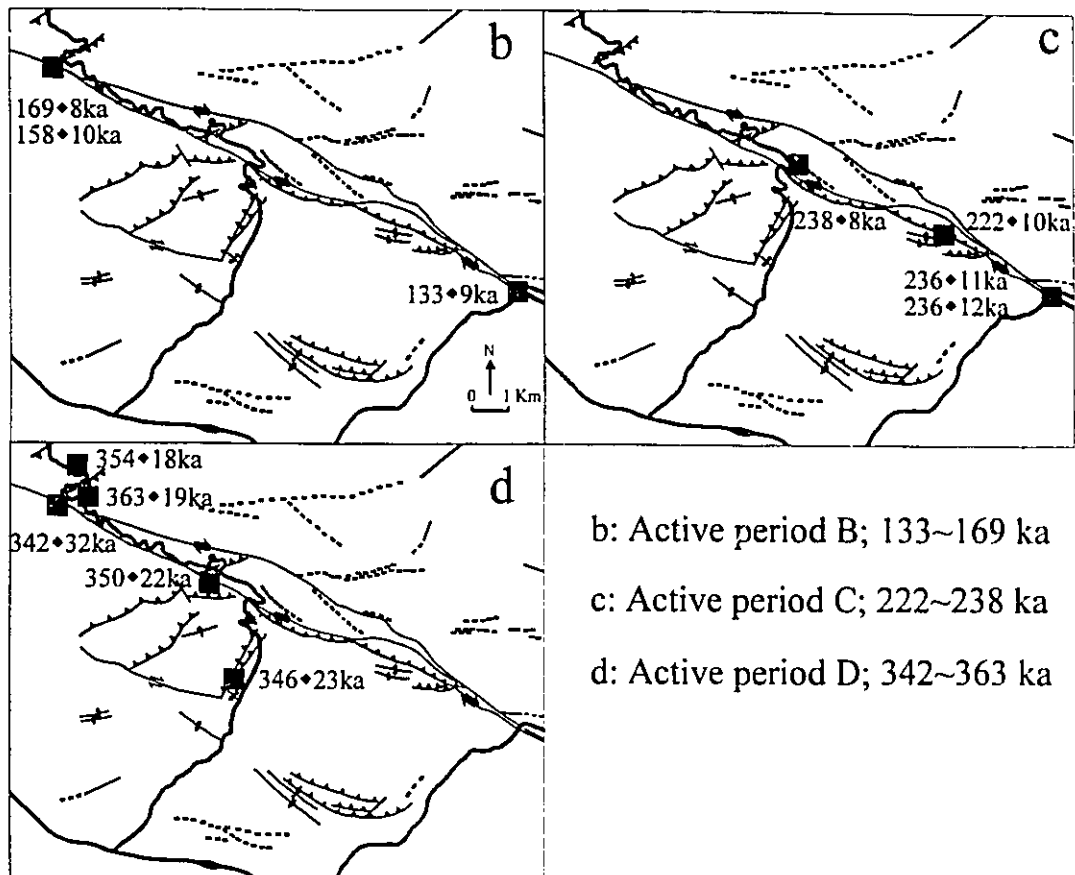


Figure 6.4. (continued)

general ESR signals do not appear to have been affected by later faulting events in adjacent fault rock units.

The Kagel fault in Domain 2, the Dillon Divide fault in Domain 3 and the Bear Divide fault in Domain 4 were all active around 0.8-0.7 Ma; they may represent an active period (F on Fig. 6.3), although no other events from this period have been observed. All represent fault movements associated with transpression around the restraining bend of the Dillon fault. Likewise a single date of 0.56 Ma obtained from a 70 m-wide gouge zone on the main San Gabriel fault at Big Tujunga road may represent another active period (E on Fig. 6.3), but further dates from this period are lacking. Later movements on reactivated gouge zones are also observed here in periods C and A.

During period D, fault movements occurred on the main strand of the San Gabriel fault at Bear Divide, the De Mille, Limerock faults in Domain 2, the Santa Clara Divide and Bear Divide faults in Domain 4. Such a spatial distribution is consistent with the pattern of aftershock and surface ruptures in a restraining bend (Kahle et al., 1988; Sibson, 1986). Sibson (1986) pointed out that aftershock epicenters tend to lie along the primary rupture or its extensions, with distinctive rhomboidal clusters associated with the jog at a releasing bend or offset (dilatational jog), and that aftershocks are distributed over a broad area at a restraining bend (antidilatational jog). The spatial distribution of ESR ages for period D (Fig. 6.4d) suggests that rapid (aftershock and surface rupture in an earthquake event) and long-term (at about 20 ka intervals) fault activities in the restraining bend show a consistent pattern, suggestive of inhibited slip transfer through

the bend causing deformation to spread out over a broad area. A wave of fault activity may have swept from northwest to southeast along the San Gabriel fault zone, further propagation of fault activity being prohibited by the restraining bend of the Dillon fault (here, Domain 2 and 4). This suggests that ESR dating method can be used to test for segmentation of prehistoric earthquake faults as proposed by Schwartz and Coppersmith (1984). Activity on the Dillon fault predominated over the other main strands (Watt and De Mille faults) in this period (Fig. 6.4).

During period C, renewed activity is observed in the main strand of San Gabriel fault where it crosses Big Tujunga road. The Watt thrust and the Barrel Spring oblique-slip faults became active, consistent with the restraining bend model. The De Mille fault was also activated and fault activity was shifted to Domain 3 and 5 due to the bend of the De Mille fault (see Fig. 6.3 and 6.4c).

During active period B, the main strand of the San Gabriel fault in Bear Divide, and a minor thrust near the San Gabriel fault in Big Tujunga road were reactivated. These localities span the whole study area and possibly the entire San Gabriel fault was active in this period. The three dates from this period suggest that activity wave moves from northwest to southeast (Fig. 6.4b), but further data would be required to confirm this trend.

A single ESR date of  $41 \pm 7$  ka was obtained in an earlier study by Buhay (1987). This date marks renewed activity on the main strand of the San Gabriel fault in Big Tujunga road, and may be the only indication of an active period ("A") at about this time.

Later events are not recorded in outcrop samples, due to the uplift of the San Gabriel Mountains and consequent lowering of normal stress on fault planes.

### 6-3-3. Discussion

Several interesting patterns of fault activity emerge from the above data. As noted earlier, the dates appear to be clustered into active and rest periods, although resetting of older ESR signals ( $> 0.4$  Ma) obscures this pattern. A similar pattern can be seen in  $^{14}\text{C}$ -dated Holocene fault movements (Sieh et al., 1989; see Fig. 6.5). Rest periods in their data ranged from 150 to 330 a, while, within the active periods, recurrence intervals between earthquakes were generally  $<100$  a. Similarly, the fault movement history recorded in sedimentary rocks in the Ridge basin northwest of study area appears to also show a long term (probably Ma) cyclic fault activity pattern. Crowell (1982) suggested a conveyor-belt mechanism to account for the distribution of the sedimentary units in the Ridge basin, which consist of alternating sandstone and shale members. During the rest period, the sediments were deposited in the depocenter near the source area. During each active period, the depocenter was both depressed and moved right-laterally to the southeast with respect to the source area; at the same time, the source area was elevated and erosionally rejuvenated. In a later chapter, I will discuss the self-similar rest-active-rest activity pattern and the fractal clustering of the fault activity.

The ESR data also suggest the presence of synchronous regional activity over two



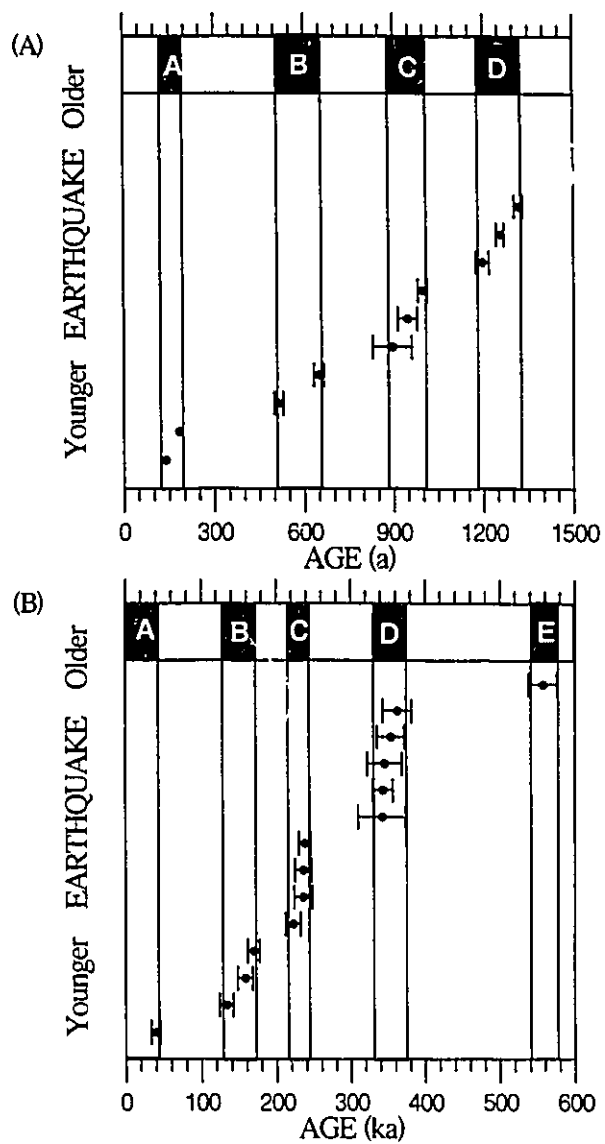


Figure 6.5. Comparison of the fault activity pattern of the San Andreas fault at Pallett Creek (Sieh et al., 1989; A) and the San Gabriel fault in the Little Tujunga region (B).

or more domains: Domains 2 and 4 for the Dillon fault (period D) and Domains 3 and 5 for the De Mille fault (period C). This is consistent with local transpression regimes being generated by bends of the San Gabriel fault leading to development of thrust or reverse faults and oblique strike slip faults near the restraining bend. The bend prohibits the propagation of strain along the fault, and fault activities are therefore spread out around this locus (Fig. 6.4 c and d).

Temporal resolution of the ESR dates is sufficient to define shifts in the spatial distribution of fault activity. Propagation of fault activity may have been inhibited in each period by bends in faults (Dillon and De Mille, respectively). Some historic earthquakes show a similar pattern, although on a shorter time scale. For example, the 1968 Borrego Mountain earthquake was initiated on the center of the Coyote Creek fault and mainly propagated to southeast; the 1979 Imperial Valley earthquake initiated just south of the U.S.-Mexico border and mainly propagated to the northwest; the 1987 Superstition Hills earthquake initiated on the northwest end of the Superstition Hills fault and propagated to the southeast (Fig 6.6). In addition, the epicenter also migrated from northwest to southeast and back to northwest in turn.

We also see a record of fault activity being transferred from one fault to another in the same structural domain. For example, the Kagel fault was active in period F, and then abandoned as the Limerock fault took over the strain accommodation in active period D. The displacement direction of both of these faults is southeast, roughly parallel to the trace of the San Gabriel fault. Thus the ESR dates show foreland-wards transfer of fault

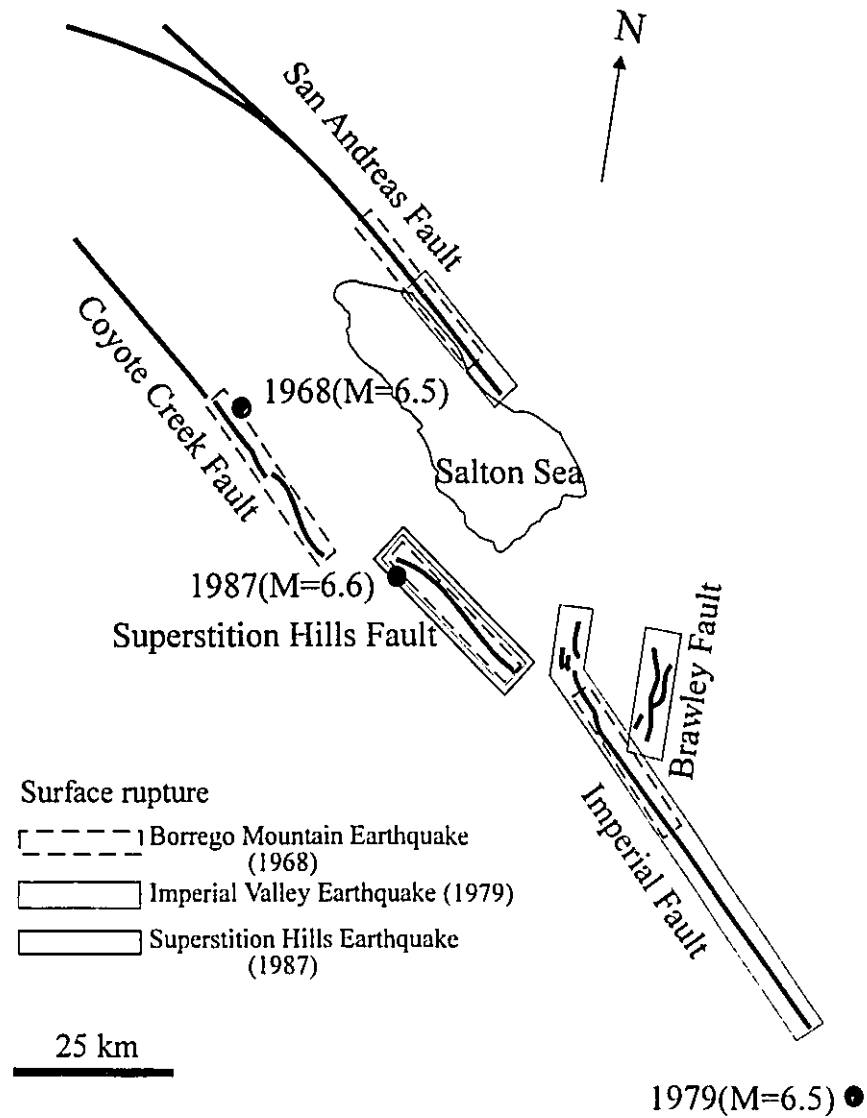


Figure 6.6. Examples of historic earthquake fault movement pattern.

activity in this imbricate thrust tectonic regime (Fig 6.4a). A similar transfer of activity is seen in fault activity associated with historic earthquakes (Fig. 6.6). During the 1968 Borrego Mountain earthquake, portions of the Coyote Creek and Imperial faults, Superstition Hills fault and part of the San Andreas fault were reactivated; during the 1979 Imperial Vally earthquake, the Imperial fault, Superstition Hills fault and part of the San Andreas fault took over the fault activity and the Brawley fault zone formed or reactivated, but the Coyote Creek fault was not activated; during the 1987 Superstition Hills earthquake, only the Superstition Hills fault was activated and movement did not occur on the other faults. Thus, only the Superstition Hills fault was reactivated during earthquakes in 1968, 1979, and 1987.

### **6-3. San Fernando Earthquake, California, 1971, $M_L = 6.4$**

The San Fernando earthquake occurred on the southern margin of the San Gabriel Mountains and broke the surface along a discontinuous, 15 km long zone from the western side of San Fernando to Big Tujunga Canyon (Fig. 6.2). Displacement was the result of reverse slip of as much as 2.1 m along a range-front thrust fault (San Fernando fault), which dips north about  $55^\circ$ . The San Fernando fault zone consists of 3 major surface ruptured segments: Mission Wells, Sylmar, and Tujunga segments. Many smaller segments developed north of the Sylmar and Tujunga segments. Fault gouge developed in a fault scarp 1 m high formed in the bedrock in Lopez Canyon (U. S. Geological

survey staff, 1971). The bedrock here consists of sandstone, conglomerate, and shale (Pico formation). Kamb et al. (1971) pointed out that the amount of fault gouge exposed in the fault scarp indicates that previous movements have occurred at an unknown time and that one of the faults bounding the fault gouge zone was reactivated during the San Fernando earthquake. The strikes and dips of the sedimentary rocks and the fault segment (about 50 m) in this site are the same (N80° W/ 65-70°), which indicate that this fault initiated as a bedding plane fault. The faults of the San Gabriel fault zone were not active during this earthquake (Crowell, 1986b). The San Fernando fault belongs to the Santa Susana-Sierra Madre fault zone and was activated by compression nearly perpendicular to the San Gabriel fault zone. These fault activity patterns are consistent with the low drag-decoupled + transpression pattern explained above (Fig. 5.5). That is, the San Fernando fault was formed by regional stress nearly perpendicular to the main fault, but this stress did not activate any faults in the strike-slip and local transpressive regime during this earthquake (Fig. 5.5C).

#### 6-4. Conclusions

ESR plateau ages for the San Gabriel fault zone range from 1170 to 40 ka. After 0.4 Ma they appear to cluster into active and dormant periods. Similar temporal clustering of fault activity is also seen in historic earthquake records, and Holocene earthquake fault activity, suggesting a scale-independent pattern of cyclity in fault activity.

Resetting of ESR signals by younger faulting events obscures this pattern in the record of the older events.

Bends of the San Gabriel fault yielded local transpressive regimes in the Little Tujunga region and result in the development of subsidiary faults. Within a given active period, the activity of faults show spatial clustering at a restraining bend in the San Gabriel fault. The restraining bend prohibits the propagation of fault activity and thus fault strain spreads out and results in the reactivation of subsidiary faults. Even though earlier events tend to be obliterated by younger ones, some of these subsidiary faults reserve the record of the faulting events older than those of the main strand, and allow us to recognize spatio-temporal pattern of fault activity in the post-0.4 Ma period.

Although the San Gabriel fault zone has been active for ~12 Ma, ESR dating only shows ages younger than 1.2 Ma. The ESR dating method has intrinsic maximum age limit of about 2-4 Ma, but we do not see events as old as that. Events older than 1.2 Ma have presumably been obliterated by later faulting events. I suppose that much of the fault gouge which I studied was actually formed over a long time (12-5 Ma), and periodically reactivated, extending into late Pleistocene time.

## **Chapter 7**

### **Structural evolution of the Little Tujunga region**

#### **7-1. Introduction**

Two of the major fault zones, the San Gabriel and Santa Susana-Sierra Madre fault zones of the San Andreas fault system are developed in the Little Tujunga region. The Little Tujunga region lies on the northern edge of the Los Angeles basin, which was filled through most of the Tertiary. Some folds, the Little Tujunga anticline and syncline and the Verdugo mountain folds, developed in Tertiary sedimentary rocks and are roughly parallel to the main fault trend in this area. Some thrust faults and folds southwest of the San Gabriel fault zone are oblique to the trend of the main fault zone.

In early studies of this region (Hill, 1930), both the San Gabriel and Santa Susana-Sierra Madre fault zones were considered to be reverse fault systems developed by compression in a NNE-SSW direction. Any other subsidiary faults and folds were also considered to be the results of this compression.

Since, Howell (1949) noted the probability of strike slip movement of the San Gabriel fault in the Little Tujunga region, Crowell (1952, 1982, 1986a) suggested that large right lateral movement (about 60 km) had occurred along the San Gabriel fault zone.

Other researchers advocated much smaller right lateral movement than that proposed by Crowell along the San Gabriel fault zone (Paschall and Theodore, 1961; Weber, 1986, 1988).

In recent years, the orientation of stress fields in the vicinity of the San Andreas fault system as determined by several researchers has shown that the maximum horizontal stress direction is oriented at a high angle ( $70^{\circ}$ - $90^{\circ}$ ) to the main trend of fault zone (Mount and Suppe, 1987, 1992; Zoback et al., 1987). This stress field was responsible for several historic earthquakes (Kern County, 1952; San Fernando earthquake, 1971), and including the Northridge earthquake in January, 1994. The thrust faults developed in the Santa Susanna-Sierra Madre fault zone in the Little Tujunga region were considered as being developed by this compression (Chapter 5). This stress direction, together with an absence of a heat flow anomaly (Lachenbruch and McGarr, 1990) indicates that the San Andreas fault is weak both in a relative and absolute sense (Chester et al., 1993). The degree of strain partition between compression and shear movement is not known well yet.

In this chapter, structural evolution in the Little Tujunga region is investigated based on the extrapolation of fault activity in the Quaternary period described in the previous chapters (Chapter 5 and 6). The geological structures were evolved by the process of low drag-decoupled shear combined with transpression (Chapter 5). The kinematics and dynamics of the faulting process of the San Gabriel fault zone in the late Quaternary was studied by the ESR age distribution in the Little Tujunga region (Chapter

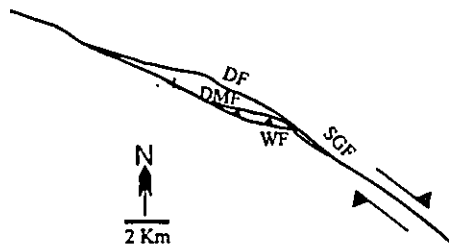


6). The relationship between Quaternary or recent fault activities and the geometry of the fault zone is certainly a key to understanding many of the deformations of the past. By extrapolation of this analysis, I investigate the structural evolution in the Little Tujunga region since the formation of the San Gabriel fault zone.

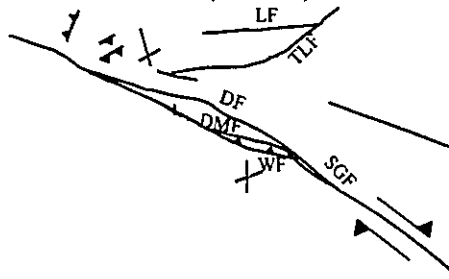
Furthermore, I tried to study the relationship between the local structures in the Little Tujunga region and the evolution of the structures of the San Gabriel Mountains using grouping of different types of fault activities. This model includes the transtension in the Ridge basin area, simple strike-slip fault in the central segment of the fault zone and transpression in the southeast front of the San Gabriel Mountains along the San Gabriel fault zone. This interpretation of structural evolution is based on the stratigraphic and structural data from the Ridge basin (May et al., 1993; Crowell, 1982; Link, 1982), paleomagnetic data (Levi and Yeats, 1993, Terres and Luyendyk, 1985) and structural data from the Little Tujunga region and southeast front of the San Gabriel Mountains.

## **7-2. Structural evolution of the Little Tujunga region**

Figure 7.1 shows the structural evolution in the Little Tujunga region since the Miocene. There are no pre-Quaternary sedimentary rocks exposed in the fault zone area except for wedges of the Paleocene Martinez formation cut by the San Gabriel fault in the Little Tujunga region. Therefore, I deduced the structural evolution based on the data from the Ridge basin northwest of the study area (May et al.; 1993; Link; 1982; Crowell;



B. Pliocene- Pleistocene (5 - 2 Ma)



C. Pleistocene - Present (2 - 0 Ma)

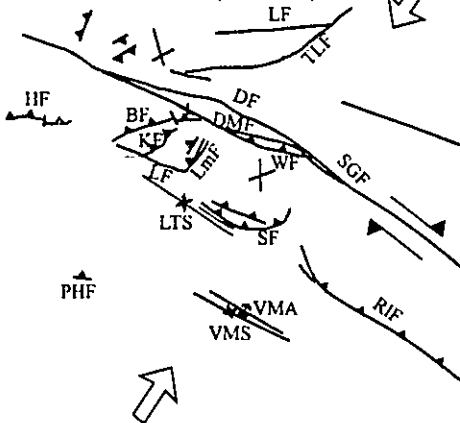


Figure 7.1. Structural evolution of the Little Tujunga region. Symbols; DF, Dillon Fault; DMF, De Mille fault; SGF, San Gabriel fault; WF, Watt fault; LF, Lonetree fault; TLF, Transmission Line fault; HF, Hospital fault; BF, Buck fault; KF, Kagel fault; LmF, Limerock fault; LF, Lopez fault; SF, Sunland fault; RIF, Rowley fault; PHF, Pacoima Hills fault; LTS, Little Tujunga syncline; VMA, Verdugo Mountain anticline; VMS, Verdugo Mountain syncline.

1982, 1986a).

Miocene-Pliocene (12-5 Ma): Structural evolution in the Little Tujunga region presumably began in the middle Miocene when the San Gabriel fault zone became active. Major slip along the main San Gabriel fault occurred between approximately 12 Ma and 5 Ma in the Ridge basin (May et al.; 1993; Link; 1982; Crowell; 1982, 1986a). This suggest that the fault activity occurred along the whole length (about 150 km) of the San Gabriel fault in that period. The Watt fault was formed in the Little Tujunga region at first.

The narrow wedges of Paleocene Martinez formation along the De Mille and Watt faults can be explained by a strike-slip duplex process. Woodcock and Fisher (1986) pointed out that strike-slip fault systems often contain zones of imbricate faults geometrically similar to imbricate fans or duplexes in thrust fault systems. They suggested that a contractional duplex can develop in a restraining bend while extensional duplexes develop in releasing bends. The wedges of the Martinez formation have been brought into their present positions by dextral strike slip movement. The nearest outcrops of Martinez to those in the Little Tujunga region are at St. Francis reservoir about 26 km to the northwest, and in Aliso Canyon, a distance of about 30 km to the southwest (Howell, 1949). When the Watt fault was activated, Paleocene Martinez formation along with basement rock was displaced about 26 km to the southeast (Fig. 7.2A). A local transpression regime developed in Domains 3 and 5 at the bend of the fault trace of the

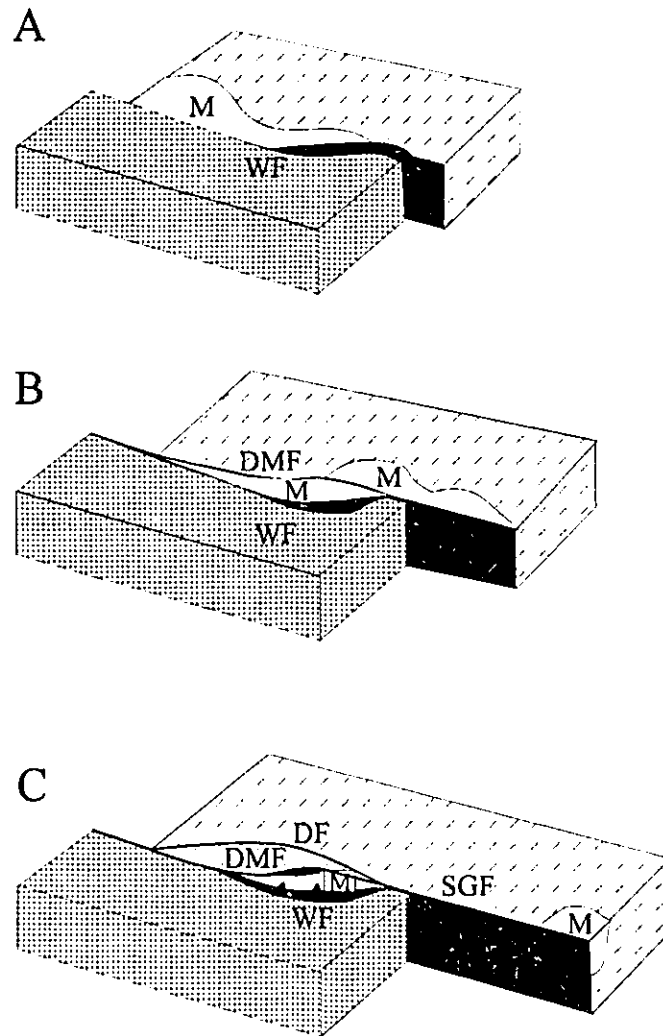


Figure 7.2. Sequence of the development of the San Gabriel fault zone in the Little Tujunga region by the strike-slip duplex process. A: Paleocene Martinez formation has been displaced with the basements rocks by the Watt fault. B: The De Mille fault was formed by the strike-slip duplex process and the Watt fault was deactivated. Basement rocks have been brought into its position by dextral strike-slip of the De Mille fault. C: The Dillon fault was formed by the strike-slip duplex process. The reverse slip component of the Watt fault became predominant over strike-slip component. Symbols: SGF; San Gabriel Fault; DF; Dillon Fault; WF; Watt fault; DMF; De Mille Fault; M; Martinez formation.

Watt-San Gabriel faults system. The De Mille and Dillon faults were formed in turn in this restraining bend by the contractional duplex process (Fig 7.2B,C). Displacement ceased on the Watt fault and was taken up by the De Mille fault leading to further displacement of basement rocks from the northwest (Fig. 7.2B). When both the Dillon and De Mille faults were reactivated, the central block (Domain 3) was uplifted and the reverse slip component of the Watt fault became predominant over strike slip so that a flower structure was developed and the Martinez formation that had existed northeast of the main fault zone was displaced about 34 km to the southeast (Fig, 7.2C). Today, there are no outcrops of the Martinez formation in the central San Gabriel Mountains due to increased uplift and erosion during late Pleistocene. Therefore, Paleocene Martinez formation wedges along the San Gabriel fault zone were isolated from its original structural context. Such a wedge shaped, isolated block of a once-continuous mass is known as an exotic duplex (Woodcock and Fisher, 1986) similar to 'far-travelled horses' in thrust systems.

The right-lateral slip rate between 8 and 4 Ma ago, about 12.5 mm/a, was calculated from the displacement of the Violin Breccia in the Ridge basin (Crowell, 1979). This slip rate is similar to the estimated average slip rate (12 mm/a) of the present active San Jacinto fault zone (Rockwell et al., 1990) but is lower than those of the various segments of the San Andreas fault zone (20-35 mm/a; Powell and Weldon, 1992). Southwest of the San Gabriel fault zone, marine Modelo formation was deposited at the northern edge of the Los Angeles basin during the Miocene.

Pliocene-Pleistocene (5-2 Ma): Because the main fault activity of the San Gabriel fault zone was transferred to the San Andreas fault zone, the activity of the San Gabriel fault zone was much less active than before. The curvature of the San Gabriel-Dillon fault system yielded the local transpressive regime (restraining bend, antidualational jog); intense thrusting and oblique slip faults had been developed in Domains 2 and 4. It is noteworthy that oblique-slip (strike-slip + reverse-slip) faults predominate over strike-slip faults which are well developed in a wrench tectonic environment. To the southwest of the San Gabriel fault zone, the marine Pico formation was deposited in the northern edge of the Los Angeles basin in the Pliocene. In the late Pliocene, compression across the main fault zone developed thrust faults subparallel to the San Gabriel fault and uplifted the Little Tujunga region. The terrestrial Saugus formation was deposited unconformably over the Pico formation in lower Pleistocene.

Pleistocene-Recent (2-0 Ma): In the late Pliocene or early Pleistocene, the Verdugo Mountain syncline and anticline were formed and syndepositional reverse faults and asymmetrical load structures developed in the Saugus formations, while later, the Little Tujunga syncline and Sunland thrust fault were formed in Domain 1 by maximum horizontal stress directed perpendicular to the main San Gabriel fault. Buck, Kagel and Limerock thrust faults and folds in the Saugus formation developed obliquely (30-40°) to the San Gabriel fault in Domain 2 were reactivated by the transpression process. The relative age relationships between folding and faulting are however not so clear in this domain. In these thrust faults, crystalline rocks are thrust over Saugus formation,

indicating that these faults were reactivated or formed in the Pleistocene. The Lopez fault and North Fork fault cut the Buck thrust fault, were developed as tear faults in the transpressive regime (Domain 2). These tear faults were formed mainly because of the impossibility of translating a huge rock mass as a single unit.

To maintain plain strain, the block between the Dillon and De Mille faults (Domain 3) was uplifted, severely fractured and faulted by the transpression process. Northeast striking dextral strike slip faults were developed by the contractional duplex process and northeast striking thrust faults and northwest trending Riedel strike-slip faults were well developed in Domain 3. The reverse slip component of the Watt fault became stronger after deposition of Saugus formation and open folds and thrust faults were developed in Domain 5 by the transpression due to the curvature of the De Mille fault.

The recent deformation activity of the Little Tujunga region can be summarised as follows: When the Dillon fault and San Gabriel fault system was activated, (Fig. 7.3A) thrust and oblique strike slip faults developed or reactivated mainly in Domains 2, 3 and 4. During the period when both the Dillon and the De Mille faults were active, the strain was accommodated by uplifting, fracturing and faulting mainly in Domain 3 by a transpression process (Fig. 7.3B). When the Dillon fault was deactivated but the De Mille fault remained active, thrust faults and folds developed in Domains 3 and 5 (Fig. 7.3C). These deformation patterns have repeated by cyclic variation of strain rate, and structural features were overprinted continuously. Meanwhile, fold development and fault activity have continued in Domains 1, 6 and 7 due to the regional stress perpendicular to the main

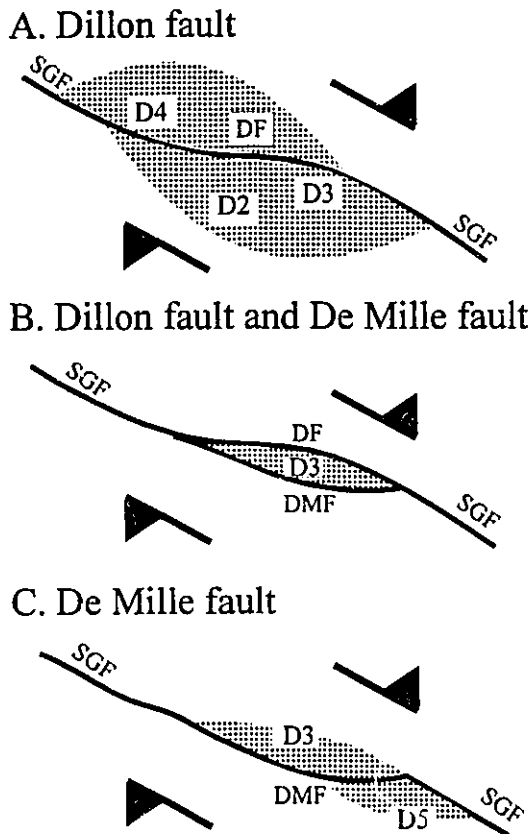


Figure 7.3. The distribution of deformation. A: When the Dillon fault became active, the fault activity was distributed in domain 2,3 and 4 due to the bend of fault trace. B: When both the Dillon and De Mille faults became activated, the central block (Domain 3) was uplifted, fractured and faulted. C: When The De Mille fault alone was active, the deformation was distributed mainly in Domains 3 and 5. Symbols; SGF, San Gabriel fault; DF, Dillon fault; DMF, De Mille fault; D1, Domain 1; D2, Domain 2; D3, Domain 3; D4, Domain 4.



strand of the San Gabriel fault.

### **7-3. Relation to regional tectonics**

The arcuate geometry of the San Gabriel fault in this region yielded transpression/transension and simple-strike slip fault regimes. In its northwest segment, extensional structures were developed in the transtension environment, while simple strike slip movement was dominant in the central segment, and then compensated by shortening in the southeast segment. This interlinkage of movement in the zones is similar with that observed in extensional ridge systems, transform faults and subduction (abduction) zones in the plate tectonics, respectively. Characteristic structural development has occurred in each regime. In the previous section, I explained the evolution of structures in the simple strike-slip regime even though local transpressive regimes were observed in the Little Tujunga region. In this section, I develop a possible interpretation of the evolution of the linked fault structures in the San Gabriel Mountains since the formation of the San Gabriel fault zone. Most of the discussions below were based on the paleogeology and paleogeography suggested by Powell (1993) and Matti and Morton (1993), however I mainly focused on the structural development in each regime in the linked fault system. For details of the balanced palinspastic reconstruction of the geology and geography in southern California, refer to "The San Andreas fault system" edited by Powell et al. (1993).

Miocene-Pliocene (12-5 Ma): The San Gabriel fault zone became the active strand in the San Andreas fault system in southern California. In the late Miocene, right lateral movement occurred along the Hitchbrook-Cajon Valley-San Gabriel (southern strand)-Stoddard Canyon-Banning segments (Matti and Morton, 1993). The geometry of this linked fault system showed asymmetric arcuate shape (Fig. 7.4A) resulting in the transtensive regime in the northwest segment, simple strike slip fault regime in the central segment and transpression regime in the southeast segment of the San Gabriel fault zone. The activity of this fault system was abandoned at about 7.5 Ma, and has been transferred to the San Gabriel (northern strand) segment. This transfer of fault activity appear to have occurred by a contractional strike slip duplex process due to the curvature of the southeast segment of the San Gabriel fault zone.

In area of the northwest segment of the San Gabriel fault zone, May et al. (1993) observed that the principal San Gabriel fault appears to become subhorizontal (listric fault) at a present-day subsurface depth of about 4 km and proposed that the Ridge basin was formed by the northwest-southeast extension (strike-slip basin). During continued right lateral slip of the San Gabriel fault zone, oblique normal slip occurred along the listric fault bounding the Ridge basin and sedimentary strata were continuously tilted and moved southeastward. This pattern of deposition allowed 14 km of sediments to accumulate without deep burial (Crowell, 1982). On the other hand, Weldon et al. (1993) proposed that the Ridge basin have been originated in a compressional setting by shortening and flexural downwarping of the crust between the Squaw Peak-Liebre

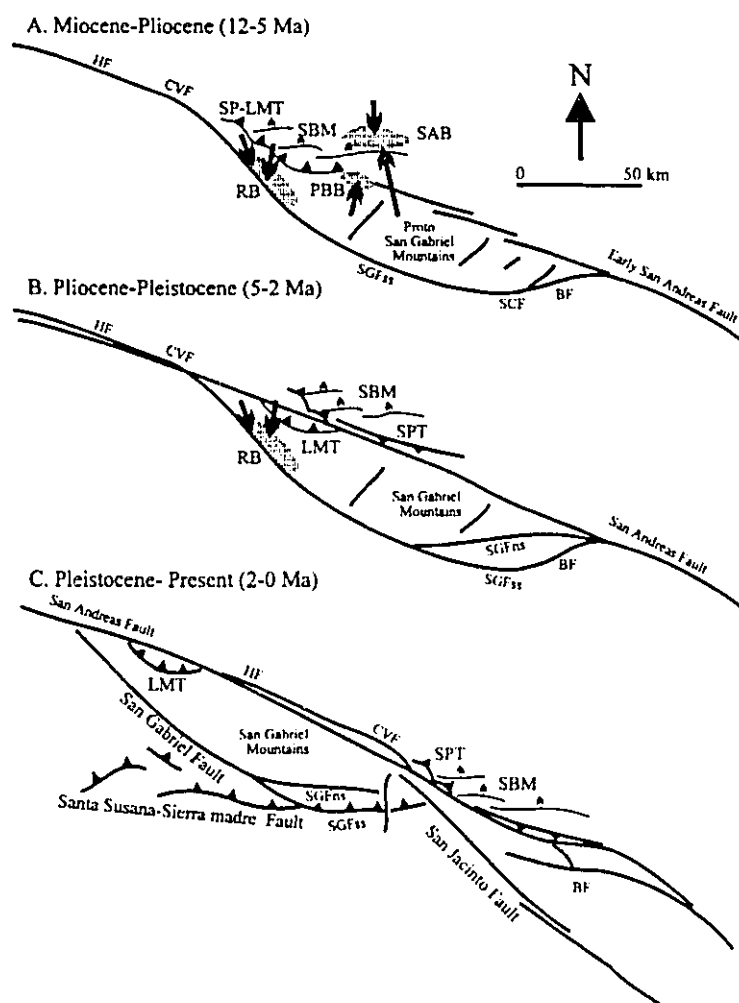


Figure 7.4. Tectonic evolution of the San Gabriel Mountain area. Symbols; HF, Hitchcock fault; CVF, Cajon Valley fault, SGFss, San Gabriel fault (southern strand); SGFns, San Gabriel fault (northern strand); SCF, Stoddard Canyon fault; BF, Banning fault; SP-LMT, Squaw Peak-Liebre Mountain thrust; SPT, Squaw Peak thrust; LMT, Liebre Mountain thrust; RB, Ridge basin, SAB, Santa Ana basin; PBB, Punchbowl basin; SBM, San Bernardino Mountains. (Modified from Powell and Weldon, 1992).

Mountain thrust system and the San Gabriel fault. They characterized the San Gabriel fault zone as a strike-slip fault with compression on secondary thrusts producing downwarped basins (Weldon et al., 1993).

The western San Bernardino Mountains region began to uplift and the Squaw Peak and Liebre Mountain thrust system was developed in that region (Matti and Morton, 1993; Weldon et al., 1993). The Punchbowl basin was receiving the sediments from the western San Gabriel Mountains (Matti and Morton, 1993).

Terres and Luyendyk (1985) estimated the paleomagnetic directions in the Vasquez (late Oligocene to early Miocene) and Mint Canyon (middle to late Miocene) formations between the San Gabriel and San Andreas fault zones and suggested that the San Gabriel region first was rotated clockwise in the early Miocene due to dextral shear within the Pacific-North American plate shear zone and later was rotated counterclockwise in Pliocene to recent time.

The tectonic activity of the northwest segment of the San Gabriel fault zone is summarised as (1) uplift on the western San Bernadino Mountains and development of the Squaw Peak and Liebre Mountain thrust systems; (2) development of Ridge basin as a strike slip basin; (3) filling the Punchbowl basin; (4) uplift of the western San Gabriel Mountains becoming the source of sediments of Ridge and Punchbowl basins; (5) clockwise rotation of the San Gabriel block in the early Miocene and counterclockwise rotation in Pliocene.

The spatial distribution of diverse observations discussed above can be explained

by a general "transrotation" model describing the deformation of blocks bounded faults. A transpression model (Sanderson and Marchini, 1984) has been used to explain the structural features formed by transcurrent movement accompanied by extension or compression. Here, I consider rotation of a block bounded by steep faults (Fig. 7.5). Two pairs of local transpressive and transtensive regimes are developed by transcurrent movement combined with rotation of central block. Transpressive regimes are created in the area where the edge of the rotated block meets the bounding blocks and transtensive regimes are created in the behind area of the block by divergency between bounding and rotated central blocks. I termed this type of deformation as "transrotation", meaning a combination of transcurrent and rotation. Transrotation can occur in any scale from micro- to regional tectonic regimes. For examples, winged porphyroclasts system shows transrotational deformation; foliations around the porphyroclasts are curved in the transpressive regimes and triangular volumes of matrix are entrained into the transtensive regimes between the wings and porphyroclast. For a regional scale example, Ridge and Punchbowl basins were generated in the transtensive regimes and development of Squaw Peak, Liebre Mountain thrusts and uplift of western San Gabriel Mountains had occurred in the transpressive regimes in the region near the northwest segment of San Gabriel fault zone.

Major deformation has occurred by simple strike slip movement in the central segment of the San Gabriel fault zone. However, local curvature of the trace of the San Gabriel fault yielded several local transpressive and transtensive regimes during simple

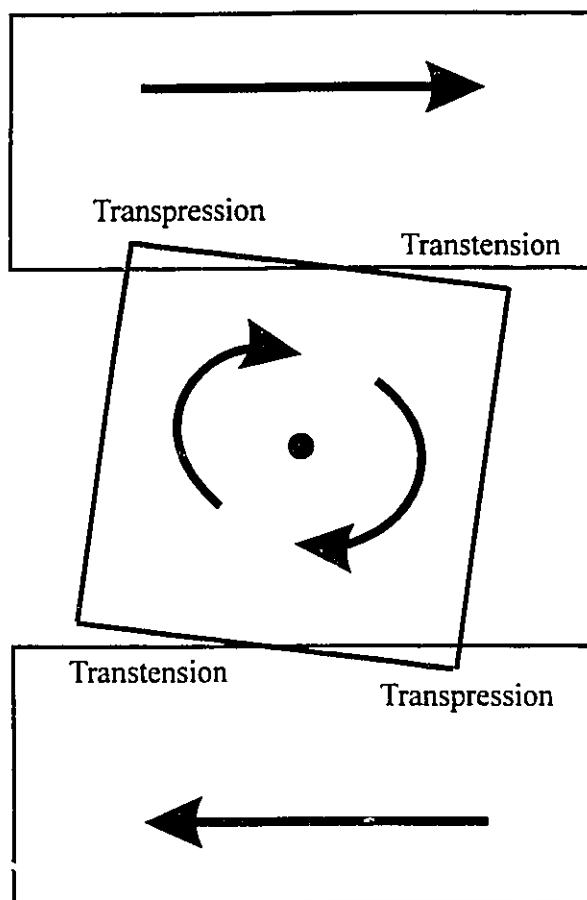


Figure 7.5. Transrotational Model.

strike-slip movement. For example, southeast of the Sierra Highway, a 150 m wide sliver of the lower Pico beds has been uplifted between two main strands of San Gabriel fault zone by the local transpressive process (Oakeshott, 1958). As described in the previous section, the central block between the De Mille and Dillon fault has been uplifted in the Little Tujunga region.

The San Gabriel Mountains was uplifted due to the curvature of the trace of the San Gabriel (southern strand)-Stoddard Canyon-Banning segments (Fig 7.4A). These mountains then became the main source of sediments of the Santa Ana and Punchbowl basins (Weldon et al., 1993).

The main fault activity was transferred from the San Gabriel fault zone to the San Andreas fault zone in about 5 Ma ago (Crowell, 1982). Weldon et al. (1993) suggested that depositional record of the Phelan Peak formation exposed at the northwestern end of Cajon Valley represent the dextral strike slip movement history of the San Andreas fault zone with a slip rate of 3 to 4 cm/yr.

During the Pleistocene-Recent (2-0 Ma), a slip rate of about 3.5 cm/yr for the San Andreas fault zone in the Transverse Ranges was estimated by dating, offsets, clasts assemblage and flow directions data observed in the sediments on the floor of the western Mojave Desert. Most of these sediments were shed off the central San Gabriel Mountains across the San Andreas fault zone (Weldon et al., 1993). Paleomagnetic data obtained in the Ventura basin near the central segment of the San Gabriel fault zone suggest that (1) the uplift of the Santa Susana Mountains by the thrust fault system occurred at about 0.7-

0.6 Ma; (2) the hangingwall block of the Santa Susana fault has rotated 30° clockwise since 2.3 Ma, while the footwall block of the Santa Susana fault shows no rotation during this time interval (Levi and Yeats, 1993). The southern strand of the San Gabriel fault was reactivated in the Peistocene as a reverse or thrust fault called the Sierra Madre fault zone.

#### **7-4. Conclusions**

The arcuate geometry of the San Gabriel fault yielded characteristic deformation regimes along the fault zone. The Ridge basin has been formed by northwest-southeast extension in the transtensive regime associated with dextral strike-slip movement of the San Gabriel fault zone.

The structural evolution of the Little Tujunga region (a central segment of the San Gabriel fault zone) was governed by mainly dextral strike slip movement, however, local curvature of the trace of the fault has caused development of major branches (De Mille and Dillon faults) by strike slip duplex process.

The long term pattern of temporal partition between compressional deformation and strike-slip deformation in the Little Tujunga region can be summarized as follows: During Miocene-Pliocene (12-5 Ma), strike-slip deformation was dominate (Crowell, 1979). The relation between Modelo (Miocene) and Pico (Pliocene) is conformity (Hill, 1930) or slight unconformity (Oakeshott, 1958). The Saugus (Quaternary) formation was



deposited over Modelo (Miocene) with a slight angular unconformity. These depositional relationships indicate that there was no strong compressional deformation in the Little Tujunga region. Compressional deformation became stronger after the Pleistocene. Folds and thrust faults subparallel to the San Gabriel fault zone developed after deposition of the Saugus formation.

The short term pattern of partition between compressional deformation and strike-slip deformation is not clear yet. Results of this study (Chapter 6) show that the activity of the San Gabriel fault zone (strike-slip deformation) has periodic nature, although much less than earlier (12-5 Ma). Compressional deformation is active at present (San Fernando (1972) and Northridge (1994) earthquakes) in the San Fernando Valley. To study the short term temporal relations between strike-slip and compressional deformation, we need to date the faults in the Santa Susana-Sierra Madre fault zone.

The eastern San Gabriel Mountains were uplifted in the transpressive regime due to the curvature of the San Gabriel fault.

## **Chapter 8**

### **Fractal clustering of fault activity in California**

#### **8-1. Introduction**

The dating of past earthquakes is of great importance to the understanding of the mechanism of earthquake generation, as well as future seismic risk. A variety of paleoseismic dating methods exist (Pierce, 1986) on the basis of which records of past activity can be obtained on various time scales. We can now consider the extent to which such records exhibit regular temporal patterns such as clustering or oscillations. Most paleoseismic records preserve only records of occurrence of events and not magnitude, whereas historic records, available in some areas for more than 100 a, also provide data on shock intensity. Here I will consider whether the temporal distribution of earthquakes displays fractal behavior. Spatial or temporal data are said to form a fractal set if, when inspected at successively larger scales, they exhibit self-similarity (Turcotte, 1992). That is, the set exhibits some pattern which is repeated on both larger and smaller scales. The degree of clustering of events is expressed by the fractal dimension  $D$  ( $0 < D < 1$ ). In the time domain, higher  $-D$  sets exhibit a lower degree of clustering of events in time.

Smalley et al. (1987) studied the temporal variation of seismicity in several regions near Efate Island in the New Hebrides island arc for the period 1978 to 1984. They suggest that the seismicity shows fractal clustering, that is, that clustering of fault activity in time is a scale-invariant process.

Here I will consider three sources of data on the temporal distribution of earthquakes in southern and central California: ESR dates on fault gouge (Lee and Schwarcz, 1994a, b, c);  $^{14}\text{C}$  dating of organic sediments in fault zones (Sieh et al., 1989); and historic records of earthquakes (Fig. 8.1).

## **8-2. Paleoseismicity and historic earthquake data**

### **8-2-1. ESR dating of the San Gabriel fault zone in the Little Tujunga region**

ESR ages from the main strands and subsidiary faults in the Little Tujunga region range from 1170 to 40 ka. ESR ages estimates for this region appear to cluster into active periods separated by rest periods (Fig. 6.5). Active periods were taken to be the intervals between the oldest event and the youngest event within a given clusters of dates. The average length of an active period is estimated to about 24 ka and the average length of rest period is about 64 ka in the Little Tujunga region.

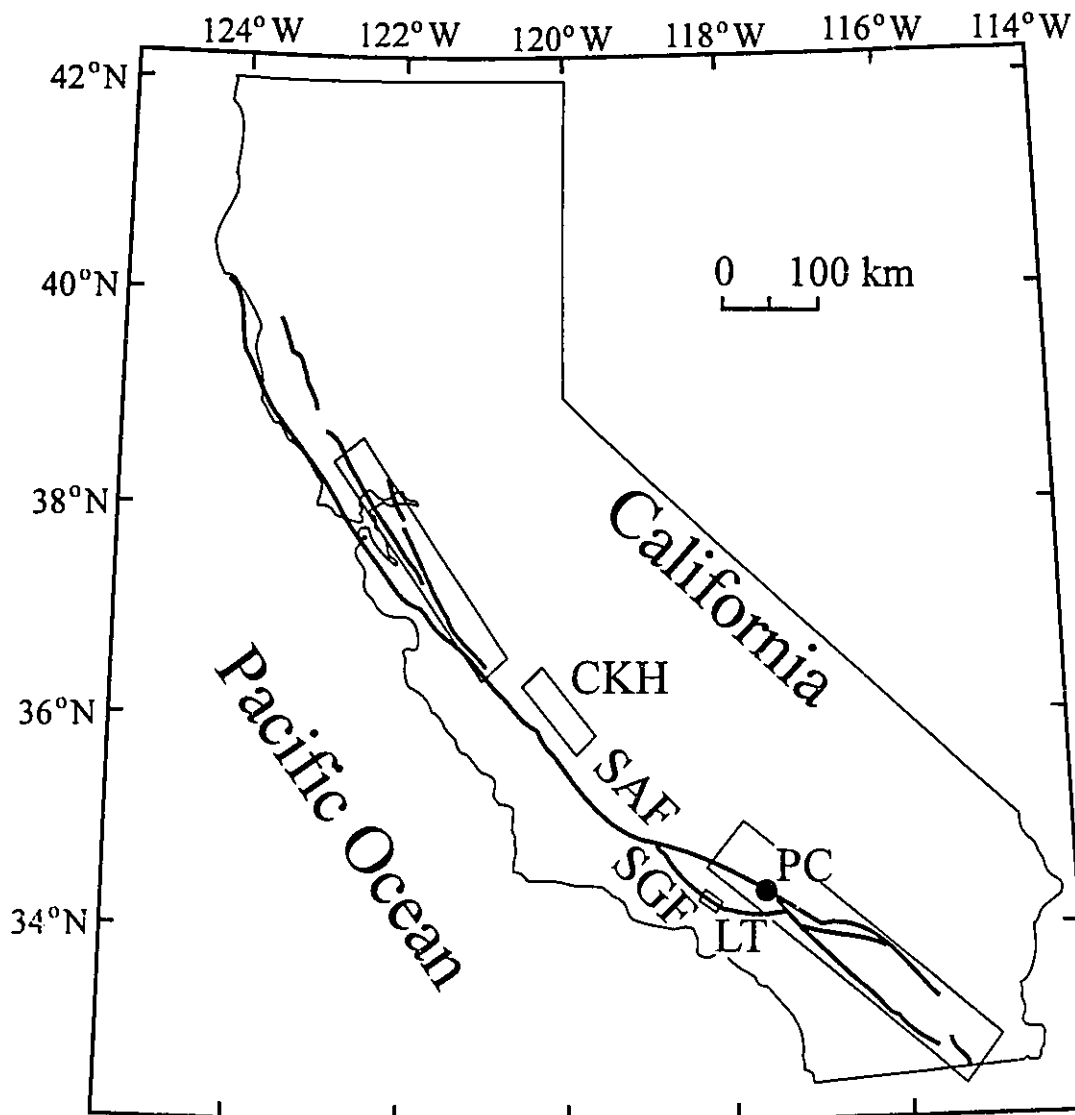


Figure 8.1. Fault map of California showing the study area. SAF, San Andreas Fault; SGF, San Gabriel Fault; CKH, Coalinga-Kettleman Hills; PC, Pallett Creek; LT, Little Tujunga.

### **8-2-2. $^{14}\text{C}$ dating of paleoearthquakes at Pallett creek, San Andreas fault zone**

The records of paleoearthquakes during the last two millennia is revealed by geological structures such as faults, folds, and liquefaction features within the marsh and stream deposits at Pallett Creek (Sieh, 1978, 1984; Sieh et al., 1989). Sieh et al. (1989) dated the 10 most recent events by radiocarbon analysis of organic matter from beds overlying and underlying beds of earthquake horizons. The estimated average length of dormancy between A.D. 671 and A.D. 1857 is 132 a, assuming 9 intervals. However, five of the nine intervals are less than 100 a whereas three intervals are between about 200 and 330 a (Sieh et al., 1989). This suggests that the fault activity on this time scale is clustered into active periods separated by dormant (rest) periods as shown in figure 6.5. The average lengths of the active and rest periods are about 99 a and 261 a, respectively as observed at Pallett Creek.

### **8-2-3. Historic record of earthquakes in California**

The historical record of major earthquakes ( $M \geq 3$ ) within the San Andreas fault system was obtained from the catalog of earthquake history of Hill et al. (1990). They selected earthquakes recorded in California from 1933 through 1988 to study focal mechanisms and transform-boundary kinematics. I used their data (Fig. 5.11, Table 5.2 and 5.3 of their paper) to analyze the fractal clustering of historic major earthquakes.

#### 8-2-4. Seismic records in southern California

A continuous seismic record for southern California between Jan. 1 and Dec. 31, 1981 was obtained from the Cal Tech on-line data base. In 1981, 1664 seismic events larger than magnitude 2 occurred in this region. Using the spacing population technique (see below), I tested the fractal properties of the temporal variation in seismicity in southern California at a scale of seconds.

#### 8-3. Fractal clustering of fault activity

Two methods, interval counting and spacing population, have been used to study the spatial distribution of fractures and seismicity (Gillespie et al., 1993; Velde et al., 1991; Smalley et al., 1987). Gillespie et al. (1993) suggest that the spacing population technique (Harris et al., 1991) should be used wherever possible, because the fractal characteristic pattern is more easily distinguished by this method. I used a spacing population method to study the degree of temporal clustering of fault activity.

This simple technique, suggested by Harris et al. (1991), was used for analysis of spatial distribution of fractures (Gillespie et al., 1993). Spacings between events  $t_i$ , which in our case are recurrence intervals, are represented on log-log plots of  $t_i$  vs. cumulative number,  $\sum N_i$ , where  $\sum N_i$  is the number of events with recurrence interval  $\geq t_i$ . If faulting events population follow a fractal size distribution of dimension  $D$ , then we expect that

$$\sum N_i = t_i^{-D} \quad (8.1)$$

If a plot of  $\log \sum N_i$  vs.  $\log t_i$  yields a straight line, then the fractal dimension (D) is given by its slope. Analysis of synthetic data sets with known characteristics (Gillespie et al., 1993) showed that random and Kolmogorov distributions of intervals form convex upwards curves; whereas fractal distributions of intervals give straight lines.

For the  $^{14}\text{C}$  data set, Sieh et al. (1989) argued that all the paleoearthquakes at Pallett Creek had been recognized. Although, the data represent activity at only one site on the San Andreas fault zone, they are believed to be an unbiased sample of earthquake recurrences on the San Andreas fault. The ESR data set is less complete because older events tend to be lost due to resetting, because not all faults in the region have been sampled, but this should also be an unbiased sample of earthquakes in the interval from 50 ka to 400 ka.

I have applied the spacing population method to the data sets obtained from the  $^{14}\text{C}$  and ESR dating methods. Spacings between individual ESR and  $^{14}\text{C}$  dates are taken to represent average recurrence intervals, although both methods would have lost much of the data for different reasons in each area. A fractal clustering is observed which gives fractal dimensions of 0.67 and 0.46 for both fault zones, respectively (Fig. 8.2). Clustering of fault activity on the San Gabriel fault zone ( $D = 0.46$ ) is stronger than that on the San Andreas fault zone ( $D = 0.67$ ).

Recurrence intervals ( $t_i$ ) were also obtained from spacings of historic earthquakes in central and southern California, on time scales of days. Both data sets give straight

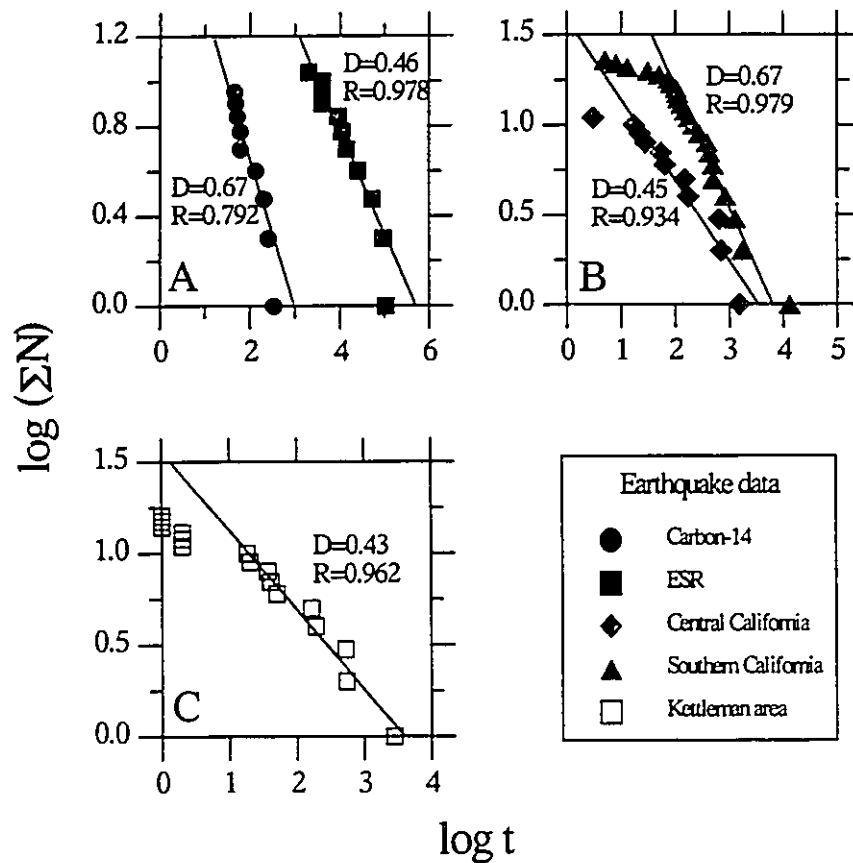


Figure 8.2. Population curves for intervals of fault activities determined by the ESR and  $^{14}\text{C}$  dating methods (A), of historic earthquakes in Southern and central California (B) and of historic earthquake in Coalinga-Kettleman Hills region (C).  $t$ ; in years for fig. A; in days for fig. B and C; R; correlation coefficient; D; fractal dimension.



lines with fractal dimension of 0.45 and 0.67, respectively (Fig. 8.2). Interestingly, the fractal dimension obtained from historic earthquakes in southern California is consistent with that determined by the  $^{14}\text{C}$  dating method in Pallett Creek, while the fractal dimension of the earthquake spacings in central California is similar to that in the San Gabriel fault zone as determined by the ESR dating method. The fractal dimension in the Kettleman Hills area of central California is about 0.43 which is similar to the fractal dimension obtained from the San Gabriel fault zone (Fig. 8.2). A similar analysis of a one-year long seismic record for 1981 gives a curve with upward convex shape indicating random distribution (Fig. 8.3).

#### 8-4. Discussion

These results show that dates of earthquakes occurring on both the San Gabriel and San Andreas faults exhibit clustering, but the degree of clustering varies significantly between these faults in southern California (Fig 8.4). If we can assume that the fractal dimension of temporal clustering can be used as a "fingerprint" for the affinity of a set of data to a particular tectonic regime, then it appears that ancient earthquakes along the San Gabriel fault zone were driven by the same mechanism that drives historic earthquakes in central California, with an approximate  $D$  value of 0.45; whereas both historic and  $^{14}\text{C}$ -dated earthquakes on the San Andreas fault zone in southern California are more weakly clustered, as shown by their higher fractal dimension of 0.67.

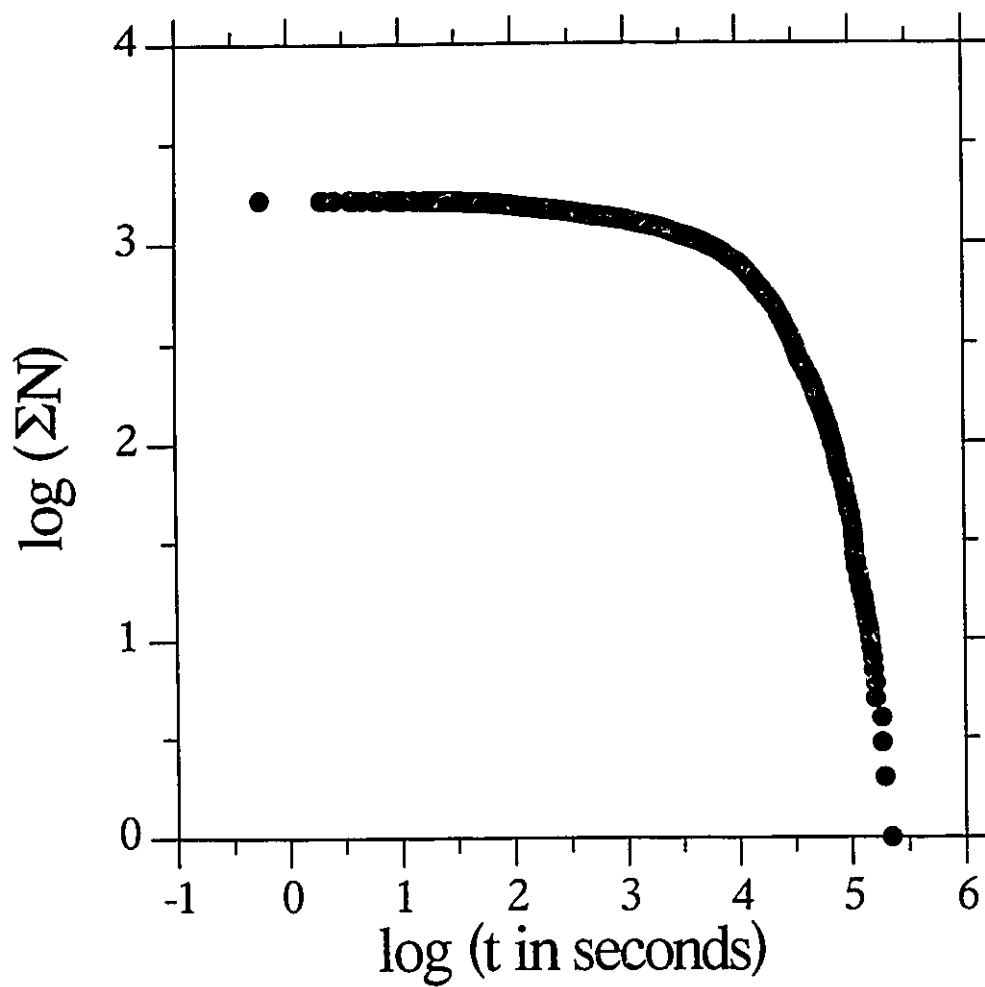


Figure 8.3. Population curve for intervals of seismic events in southern California in 1981.

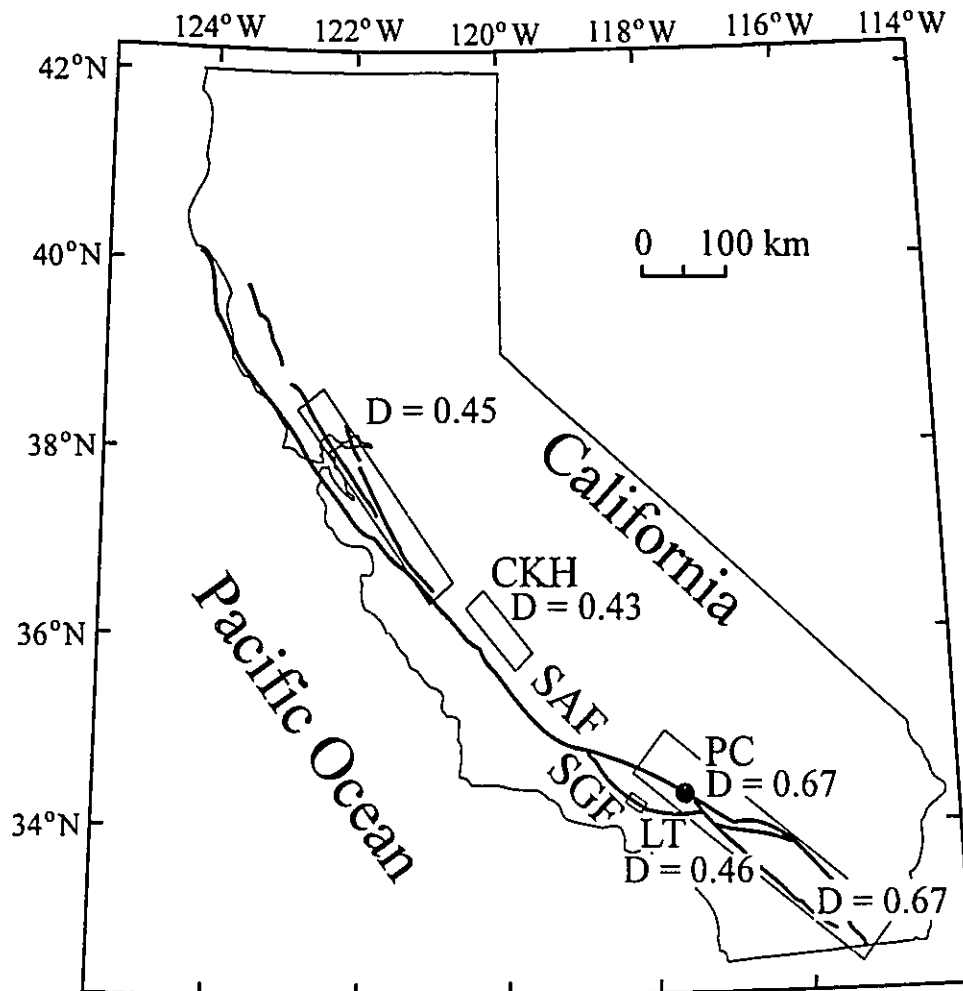


Figure 8.4. Fractal dimensions of fault activity in California. The fractal dimensions of the paleoearthquakes in the Little Tujunga region and Pallet Creek were determined by the dates of ESR and C methods. the others were determined by the historic earthquakes. SAF, San Andreas Fault; SGF, San Gabriel Fault; CKH, Coalinga-Kettleman Hills; PC, Pallett Creek; LT, Little Tujunga.

This is especially interesting in the light of evidence that activity on the San Gabriel fault switched to the San Andreas fault about 5 Ma ago (Crowell, 1986a). The preservation to the present day of the  $D=0.45$  value in central California may show the spatial link between this older strand of the main strike-slip fault region (San Gabriel fault zone) to its parent region to the north. Another possibility, which is less clear, is that the two data sets (ESR and  $^{14}\text{C}$ ) represent isolated phases of a series of self-affine fractals (Mandelbrot, 1985); the remainder of the data ( $0.45 < D < 0.67$ ) might be revealed if an appropriate dating method existed for the intermediate time range.

On the other hand, a sample of the seismic record from 1981 shows a random, non-fractal distribution of intervals between events. There was no big ( $M>5$ ) earthquake event in this period except for April 26 ( $M=5.7$ ). There occurred many pre- and post-seismic events for this earthquake event; seismic events were clustered around this time. The remainder are distributed randomly which we infer to be typical of the background fault activity in southern California. Apparently fractal clustering of events only occurs in a longer seismic catalog ( $t > 5$  years) or/and smaller spatial scale.

Because each dating method has a limited time range, there is so far no method for comparing ESR dating results for fault rocks with other independent dating method. The present study shows however that the ESR dates exhibit fractal clustering of similar dimension to other earthquake data for this region. This is indirect confirmation of the accuracy of the actual ages which I have obtained by the ESR plateau-dating method (Chapter 4), and that this method can be used to evaluate the pattern of fault activity at

a time scale beyond the limits of  $^{14}\text{C}$  dating method (~50 ka).

### 8-5. Conclusions

I have shown that there is a clustering of fault activity in California with well-defined fractal dimensions varying from 0.43 to 0.67. This common behavior is observable along both the San Gabriel and San Andreas fault zone with different degree of clustering, over a time scale spanning 5 orders of magnitude, from historic to several hundreds of thousands of years. Furthermore, it is interesting that, by their very nature, the various clustering intervals must be nested within one another, although they appear to have different fractal dimension for different spatial and time scale (Kagan and Jackson, 1991). That is, the 250-year cycles of alternating active and rest periods, analysed using  $^{14}\text{C}$  dating would lie within one of the 100,000-year cycles such as those whose periodicity was determined by ESR dating method. An even higher order of temporal clustering is suggested by the sedimentation record from the Ridge basin (Crowell, 1982). There, fault-triggered breccias alternate with low-energy detrital sediments (shales and sands) on a time scale of millions of years (Ensley and Verosub, 1982). Periods of breccia deposition would correspond to periods of increased strike-slip activity on the San Gabriel fault that bounds the Ridge basin. The fact that the clustering pattern of movements on the San Andreas fault zone in central California falls on the same trend of cumulative frequency vs. interval with the San Gabriel fault (the older

strand of the San Andreas fault zone in southern California) suggest that both the northern part of the San Andreas and the San Gabriel fault zones participate in the same dynamic system that controlled rest/active period distributions. The different pattern of clustering of fault movements in the San Andreas fault zone in southern California maybe a result of local variation in the physical properties and structural features of that region.

These observations naturally lead one to wonder what are the characteristics of the earthquake-generating dynamic system that are responsible for a regular pattern of activity ranging over  $10^5$  years and over much of California. While it is beyond the scope of this thesis to account for the origin of this common pattern, it must be related to the temporal and spatial scaling of the dynamic processes associated with motion along the combined San Gabriel/ San Andreas fault system. We can analogize the distribution of cluster sizes to frequency distributions generated in a resonant system, where the lowest-frequency component is associated with the driving force in the system. The fractal dimension through the population of clustering patterns is controlled by their common linkage to that driving force and its temporally fractal behavior. If we further assume that the fundamental cause of stress release through earthquakes (as opposed to continuous creep) is due to some stick-slip mechanisms acting along the faults, then perhaps the progressively shorter-term clusterings of these events (rest/active spacings) may be controlled by movements at progressively shallower crustal depths and lower ductility, leading to response on shorter time scales. This is a problem beyond the scope of this study, but it would seem to be a fruitful direction of future study, partly through more

detailed conformation of the temporal fractal behavior of earthquakes. In this regard, it is interesting that, at the highest frequency end of the temporal distribution ( $t < 1$  y) the fractal pattern appears to break down (Fig. 8.3). This may, however, be partly an effect of the mixing of signals from many sources each of which separately would reflect certain fractal dimension ( $D= 0.43-0.67$ ), but which collectively present an apparently random pattern.

## **Chapter 9**

### **Underground Research Laboratory, Pinawa, Manitoba, Canada**

#### **9-1. Introduction**

Several countries including Canada are investigating the potential for disposal of highly radioactive nuclear waste in deep underground repositories. Atomic Energy of Canada Limited (AECL) is doing various researches related to nuclear waste disposal deep in a plutonic rock mass in the Underground Research Laboratory (URL), near Pinawa, Manitoba (Gascoyne, 1986; Gascoyne and Schwarcz, 1986; McNutt et al., 1987; Brown et al., 1989; Martin, 1990; Haimson et al., 1993). The URL has been excavated in the large Lac du Bonnet granite batholith, which shows largely two types of granite; (1) pink porphyritic, gneissic and/or xenolithic granite and; (2) grey homogeneous and equigranular granite (Brown et al., 1989).

A series of samples of fault rocks were collected at the URL site. These were obtained from drill cores in storage at the site, and which penetrated a series of gently dipping fault zones that intersect the URL site at depths of about 200-300 m (Fig. 9.1). Samples of the drill core were removed and brought to McMaster for analysis.



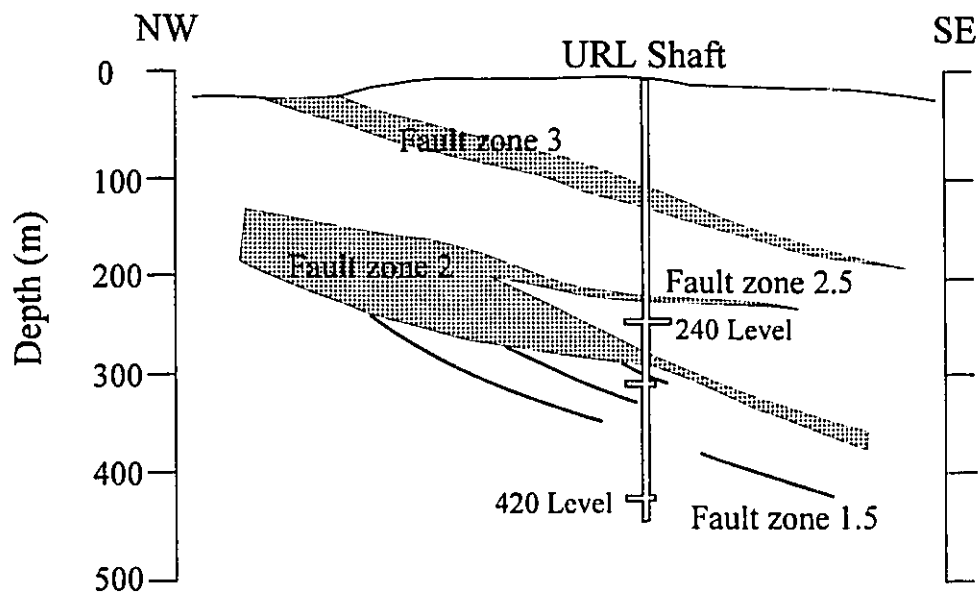


Figure 9.1. Generalized northwest-southeast section of the URL site, showing the two main fault zones and the main shaft (after Martin, 1990).

The list of samples is given in Table 9.1. The goal of these studies is to test whether ESR dating method can be used in general as a validation procedure in the construction of radwaste disposal sites.

### **9-2. Analytical techniques**

The procedure of ESR plateau dating of fault rocks was described in Chapter 3. For some samples smaller than 45  $\mu\text{m}$ , I omitted the last stage (etching in nitric and fluoboric acid) of treatment. These samples, basically, consist of quartz, feldspar and other material in gouge matrix.

For samples which are in saturation, we cannot obtain an age of last resetting, since their ESR intensities ceased to grow some time in the past. The best that we can do is to estimate the minimum age of last resetting, based on an estimate of the maximum  $D_E$  that could be detected (i.e., the dose beyond which the DRC flattens out). For the quartz samples which I have studied here, this appears to occur at a dose of between 8,000 and 10,000 Gy (grays).

### **9-3. Results of ESR plateau dating**

Of the ten samples which I studied, seven were found to be in ESR saturation. The saturated samples show constant ESR intensities or fluctuations in intensities with added

Table 9.1. Samples of fault rocks collected from drill cores in URL site.

Sample	Type	Location	Borehole	Depth in core (m)	Vertical depth from surface (m)	Thickness of fault rock (cm)
AECL1	gouge	FZ 2	HC 2	34	260	3
AECL2	gouge	FZ 2	HC 3	41.2	260	0.4
AECL3	gouge	FZ 2	HC 4	38.3	260	1
AECL4	breccia	FZ 2	HC 13	41.1	260	2
AECL5	gouge	FZ 2	HC 15	17.1-17.2	260	0.5-1
AECL6	gouge	FZ 2	HC 15	19.9-19.97	260	0.5
AECL7	gouge		WA 1	340.6		4
AECL9	gouge		WA 1	344.82		2
AECL10	gouge		WD 1	109.7		>10
AECL12	gouge		URL8.2	82.21		0.3

artificial dose. Examples of saturated E' signals from the various size fractions of a single sample are shown in figure 9.2. Both normally separated quartz aliquots and whole gouge matrix of sample AECL1 show constant ESR intensities with added dose. Dose rates for each samples are determined by concentrations of radioactive elements within gouge. A lower ESR age limit can be estimated by dividing saturation dose by dose rate. For example, the estimated dose rate is 11800  $\mu\text{Gy/a}$  for AECL2. For this dose rate and a saturation dose of 9 kGy, the minimum age of fault movements of AECL2 is 765 ka. The other minimum ages of fault movements for saturated samples are estimated by above method and are listed in Table 9.2. The minimum age of fault activities range between 0.8 and 2 Ma. However two samples (AECL9 and 12) show abnormally high dose rates resulting in smaller (0.3-0.4 Ma) minimum age of fault activity (Table 9.2).

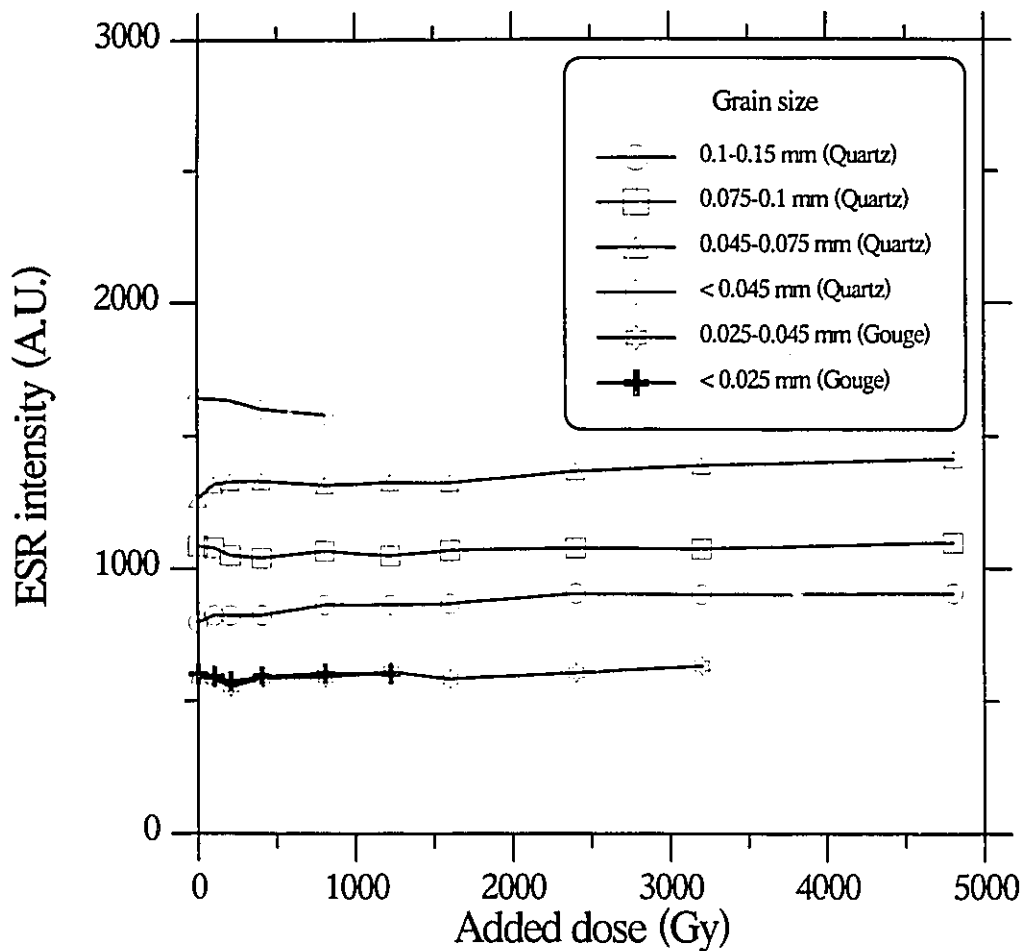


Figure 9.2. An example of dose response curves of a saturated sample. The intensities for E' signals of both quartz and whole gouge matrix from AECL1 are constant with added dose due to the saturation.

Table 9.2. ESR analytical data and the minimum ages of fault movements for saturated samples.

Sample	Grain size ( $\mu\text{m}$ )	Center	*D <sub>e</sub> (Gy)	U (ppm)	Th (ppm)	K (%)	Dose rate ( $\mu\text{Gy/a}$ )	Minimum ESR age (Ma)
AECL1C	100-150	E'	9000±900	11.72	38.7±0.7	0.697±0.035	6443±307	1.4±0.2
AECL1D	75-100	E'	9000±900	11.72	38.7±0.7	0.697±0.035	6922±381	1.3±0.2
AECL1E	45-75	E'	9000±900	11.72	38.7±0.7	0.697±0.035	7585±495	1.2±0.1
AECL1F	<45	E'	9000±900	11.72	38.7±0.7	0.697±0.035	8830±726	1±0.1
AECL2C	100-150	E'	9000±900	10.31	65.6±1.1	0.486±0.024	8695±407	1±0.1
AECL2D	75-100	E'	9000±900	10.31	65.6±1.1	0.486±0.024	9316±500	1±0.1
AECL2E	45-75	E'	9000±900	10.31	65.6±1.1	0.486±0.024	10171±64	0.9±0.1
AECL2F	<45	E'	9000±900	10.31	65.6±1.1	0.486±0.024	11762±93	0.8±0.1
AECL5C	100-150	E'	9000±900	4.28	45.8±0.8	0.707±0.035	5639±260	1.6±0.2
AECL5D	75-100	E'	9000±900	4.28	45.8±0.8	0.707±0.035	6015±315	1.5±0.2
AECL5E	45-75	E'	9000±900	4.28	45.8±0.8	0.707±0.035	6531±401	1.4±0.2
AECL5F	<45	E'	9000±900	4.28	45.8±0.8	0.707±0.035	7482±574	1.2±0.2
AECL6C	100-150	E'	9000±900	9.62	52.6±0.9	0.374±0.019	7323±343	1.3±0.1
AECL6D	75-100	E'	9000±900	9.62	52.6±0.9	0.374±0.019	7848±423	1.2±0.1
AECL6E	45-75	E'	9000±900	9.62	52.6±0.9	0.374±0.019	8572±546	1.1±0.1
AECL6F	<45	E'	9000±900	9.62	52.6±0.9	0.374±0.019	9921±795	0.9±0.1
AECL7C	100-150	E'	9000±900	3.41	20.59±0.37	0.801±0.04	3393±151	2.6±0.3
AECL7D	75-100	E'	9000±900	3.41	20.59±0.37	0.801±0.04	3597±179	2.5±0.3
AECL7E	45-75	E'	9000±900	3.41	20.59±0.37	0.801±0.04	3873±223	2.3±0.3
AECL7F	<45	E'	9000±900	3.41	20.59±0.37	0.801±0.04	4383±314	2.1±0.3
AECL9C	100-150	E'	9000±900	67.19	19.34±0.35	0.9±0.04	20445±941	0.4±0.05
AECL9D	75-100	E'	9000±900	67.19	19.34±0.35	0.9±0.04	21948±1169	0.4±0.05

AECL9E	45-75	E'	9000±900	67.19	19.34±0.35	0.9±0.04	24034±1525	0.4±0.04
AECL9F	<45	E'	9000±900	67.19	19.34±0.35	0.9±0.04	28034±2266	0.3±0.04
AECL12C	100-150	E'	9000±900	51.4	24.3±0.4	0.365±0.018	16135±749	0.6±0.06
AECL12D	75-100	E'	9000±900	51.4	24.3±0.4	0.365±0.018	17340±934	0.5±0.06
AECL12E	45-75	E'	9000±900	51.4	24.3±0.4	0.365±0.018	19014±1222	0.5±0.06
AECL12F	<45	E'	9000±900	51.4	24.3±0.4	0.365±0.018	22219±1817	0.4±0.05

\* Saturation dose was estimated from growth curves of unsaturated samples (AECL3, 4 and 10).

The ESR intensities for unsaturated samples generally are growing along a single saturating exponential function which can be expressed by:

$$I = I_{\max} (1 - \exp(-a(D_{\text{add}} + D_E))) \quad (9-1)$$

where  $I$  = ESR intensity,  $I_{\max}$  = maximum ESR intensity when all traps are filled,  $a$  = fraction of unfilled defects that trap electrons per dose unit,  $D_{\text{add}}$  = added dose in the laboratory and  $D_E$  = equivalent dose determined in the laboratory with absorbed dose in natural environment. An example of growth curves of E' signals is shown in figure 9.3 for AECL10. When the intensities are close to the saturation level, the errors are relatively high (about 20 %) in the estimation of equivalent dose.

The ESR data and ages for the three unsaturated samples which I studied are shown in Table 9.3.

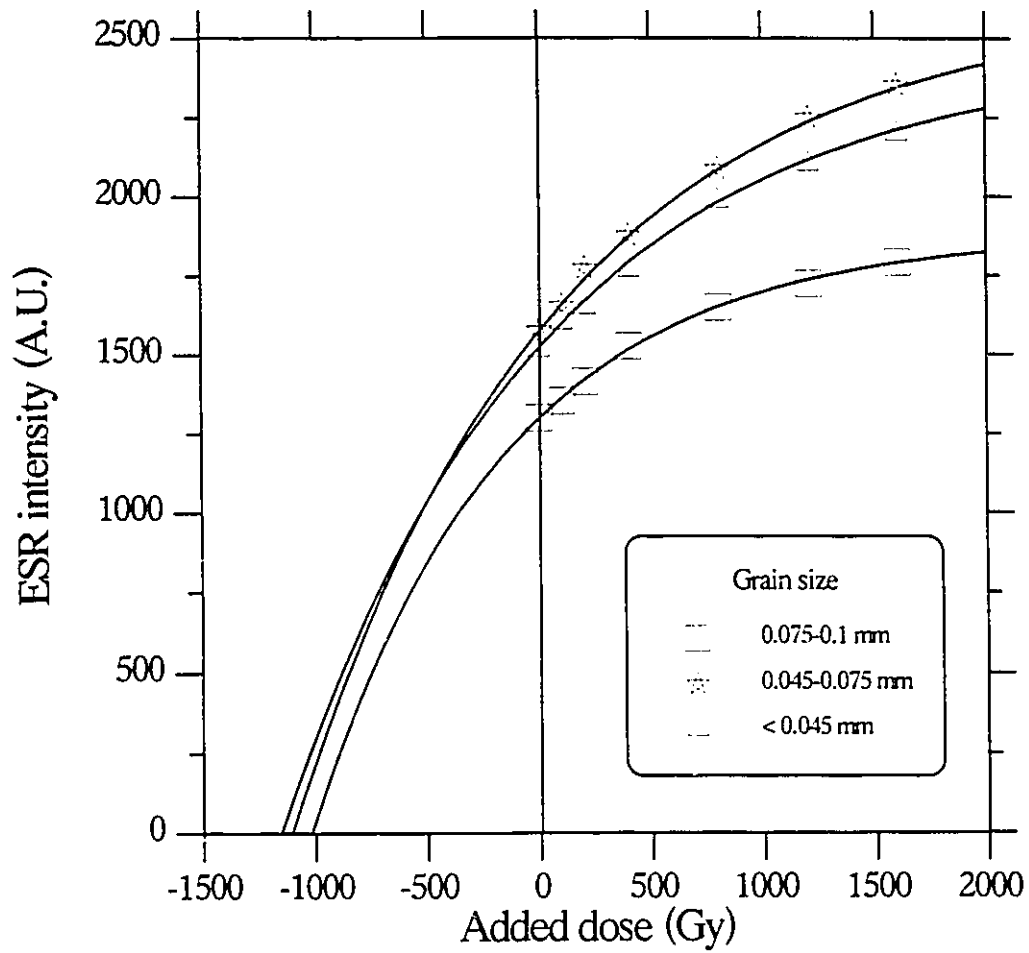


Figure 9.3. An example of growth curves for unsaturated sample. The ESR intensities are growing along single saturating exponential curves with added dose.

Table 9.3. ESR analytical data and results for unsaturated samples from URL site.

Sample	Grain size ( $\mu\text{m}$ )	Center	$D_E$ (Gy)	U (ppm)	Th (ppm)	K (%)	Dose rate ( $\mu\text{Gy/a}$ )	ESR age (ka)
AECL3C	100-150	E'	3879 $\pm$ 558	10.53	54.2 $\pm$ 0.9	0.545 $\pm$ 0.027	7859 $\pm$ 364	494 $\pm$ 75
AECL3D	75-100	E'	3956 $\pm$ 806	10.53	54.2 $\pm$ 0.9	0.545 $\pm$ 0.027	8415 $\pm$ 448	470 $\pm$ 99
AECL3E	45-75	E'	4339 $\pm$ 488	10.53	54.2 $\pm$ 0.9	0.545 $\pm$ 0.027	9179 $\pm$ 578	473 $\pm$ 61
AECL3F	<45	E'	4973 $\pm$ 931	10.53	54.2 $\pm$ 0.9	0.545 $\pm$ 0.027	10604 $\pm$ 840	469 $\pm$ 95
AECL3G	25-45	E'	4933 $\pm$ 674	10.53	54.2 $\pm$ 0.9	0.545 $\pm$ 0.027	10604 $\pm$ 840	465 $\pm$ 74
AECL3H	<25	E'	5646 $\pm$ 785	10.53	54.2 $\pm$ 0.9	0.545 $\pm$ 0.027	12417 $\pm$ 1182	455 $\pm$ 77
AECL4C	100-150	E'	3756 $\pm$ 528	6.52	32.3 $\pm$ 0.5	0.699 $\pm$ 0.035	5106 $\pm$ 231	736 $\pm$ 109
AECL4D	75-100	E'	3805 $\pm$ 471	6.52	32.3 $\pm$ 0.5	0.699 $\pm$ 0.035	5445 $\pm$ 280	699 $\pm$ 94
AECL4E	45-75	E'	2428 $\pm$ 460	6.52	32.3 $\pm$ 0.5	0.699 $\pm$ 0.035	5909 $\pm$ 357	411 $\pm$ 82
AECL4F	<45	E'	2670 $\pm$ 659	6.52	32.3 $\pm$ 0.5	0.699 $\pm$ 0.035	6772 $\pm$ 515	394 $\pm$ 102
AECL10C	100-150	E'	1547 $\pm$ 79	10.45	8.34 $\pm$ 0.2	0.76 $\pm$ 0.04	4219 $\pm$ 187	367 $\pm$ 25
AECL10D	75-100	E'	995 $\pm$ 80	10.45	8.34 $\pm$ 0.2	0.76 $\pm$ 0.04	4490 $\pm$ 226	222 $\pm$ 21
AECL10E	45-75	E'	1093 $\pm$ 102	10.45	8.34 $\pm$ 0.2	0.76 $\pm$ 0.04	4863 $\pm$ 287	225 $\pm$ 25
AECL10F	<45	E'	1171 $\pm$ 110	10.45	8.34 $\pm$ 0.2	0.76 $\pm$ 0.04	5568 $\pm$ 414	210 $\pm$ 2



Some of the data are based on ESR spectra of unseparated gouge matrix. I have discovered that these are similar to those of quartz separated from the same fault gouge. An example is shown in figure 9.4. The ESR spectra of gouge matrix do not show any interference signals in the OHC and E' signals range. However, the intensity of E' signals of whole gouge matrix is much smaller than that of quartz due to dilution of quartz by ESR-inertive feldspar. The two growth curves for quartz and gouge matrix from AECL3 converge to the same  $D_E$  indicating gouge matrix can be used ESR plateau dating (Fig. 9.5). For saturated samples, the ESR intensity of both gouge matrix and quartz show constant value with added dose as shown in figure 9.2. If we cannot obtain enough quartz samples from fault gouge in drill core such as figure 9.6, I suggest that gouge matrix itself can be used for ESR plateau dating. This will also simplify the processing of material for dating.

The ages calculated from the E' signal of each size fraction are shown in figure 9.7. AECL3 shows no variation in age with grain size, showing that the age plateau extends to the largest size fraction (100-150  $\mu\text{m}$ ) of quartz separated from fault gouge. For this sample, I infer that  $r_c > 125 \mu\text{m}$ . ESR ages estimated from gouge matrix (< 45  $\mu\text{m}$ ) also lie on the plateau, indicating complete resetting of E' signal at the time of fault movements. For AECL4 and AECL10, the ESR ages decrease with decreasing grain size, down to the minimum plateau. The longer length of plateau of AECL3 suggests that deformation of AECL3 (fault gouge) was stronger than that of AECL4 (fault breccia) and AECL10 (thicker gouge zone). Gouge sample, AECL3, was collected from a thin film

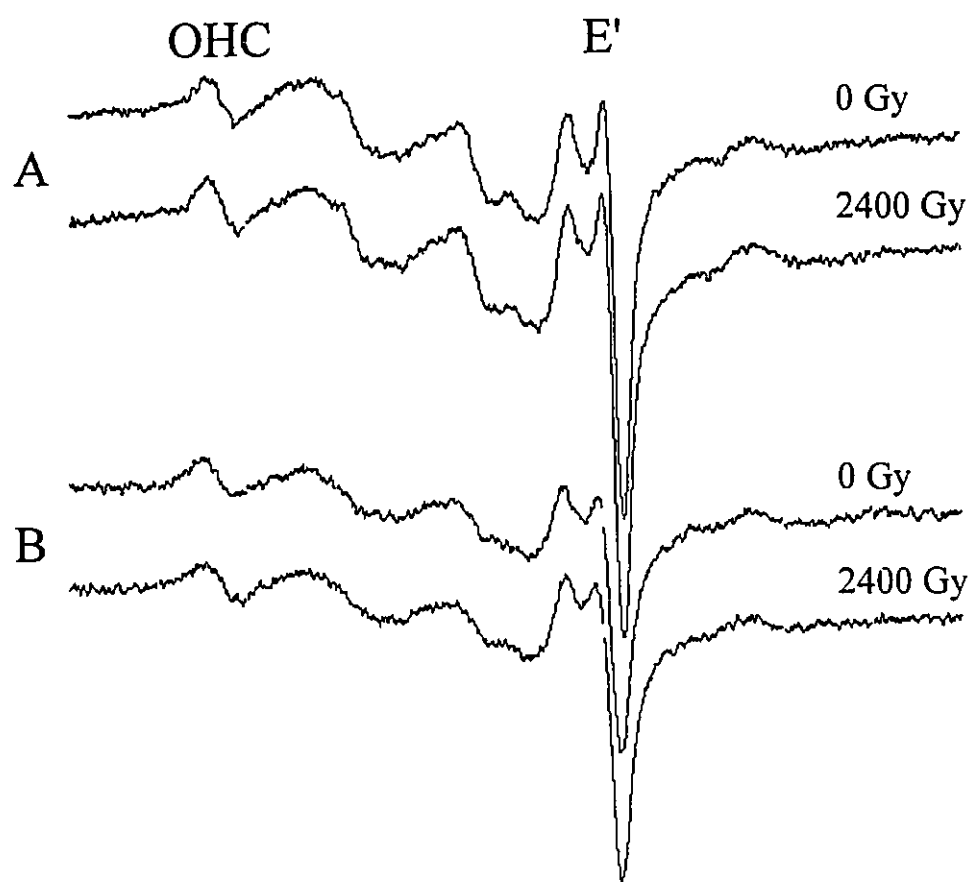


Figure 9.4. ESR spectra of quartz and gouge matrix from AECL3.

A. Natural and irradiated (2400 Gy) quartz.

B. Natural and irradiated (2400 Gy) gouge matrix.

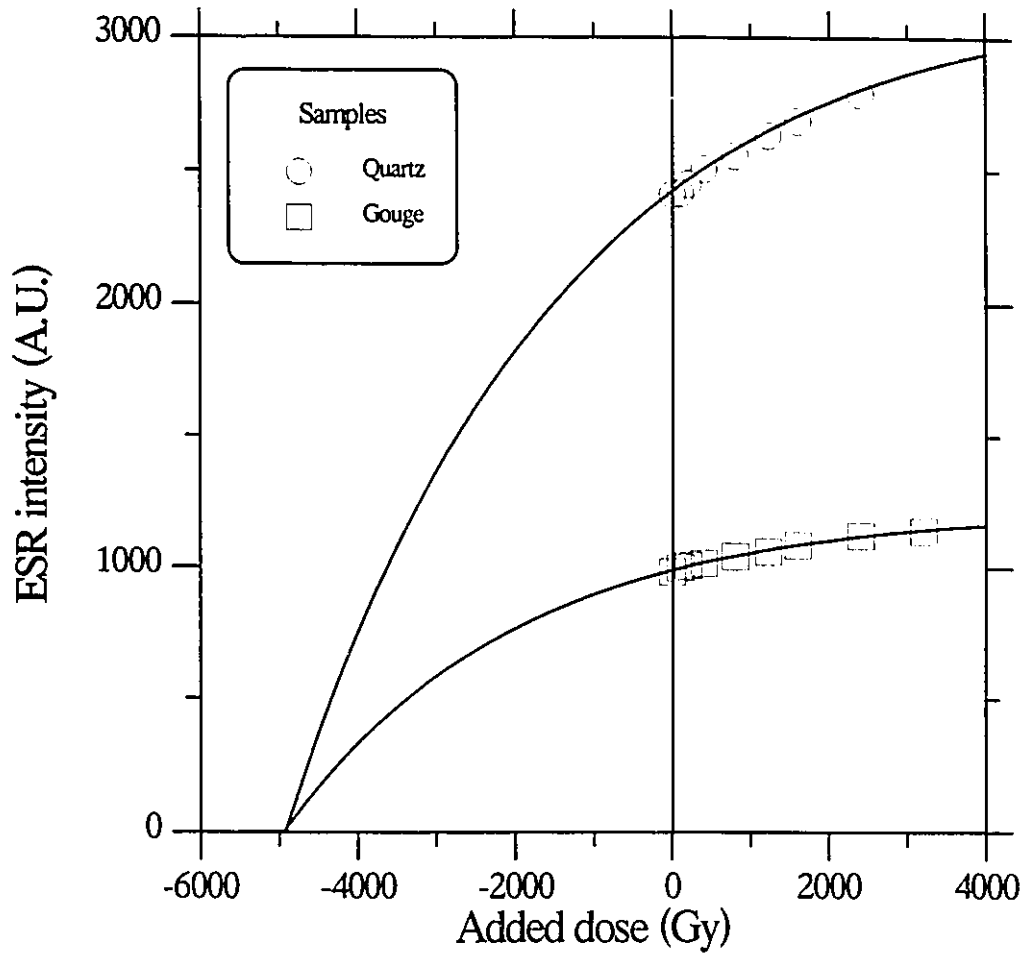


Figure 9.5. Growth curves for quartz and gouge matrix of AECL3 (Grain size; quartz; 0.045-0.075 mm; gouge matrix ; 0.025-0.045 mm). Regression curves are determined by Grün's Fit-Sim program.

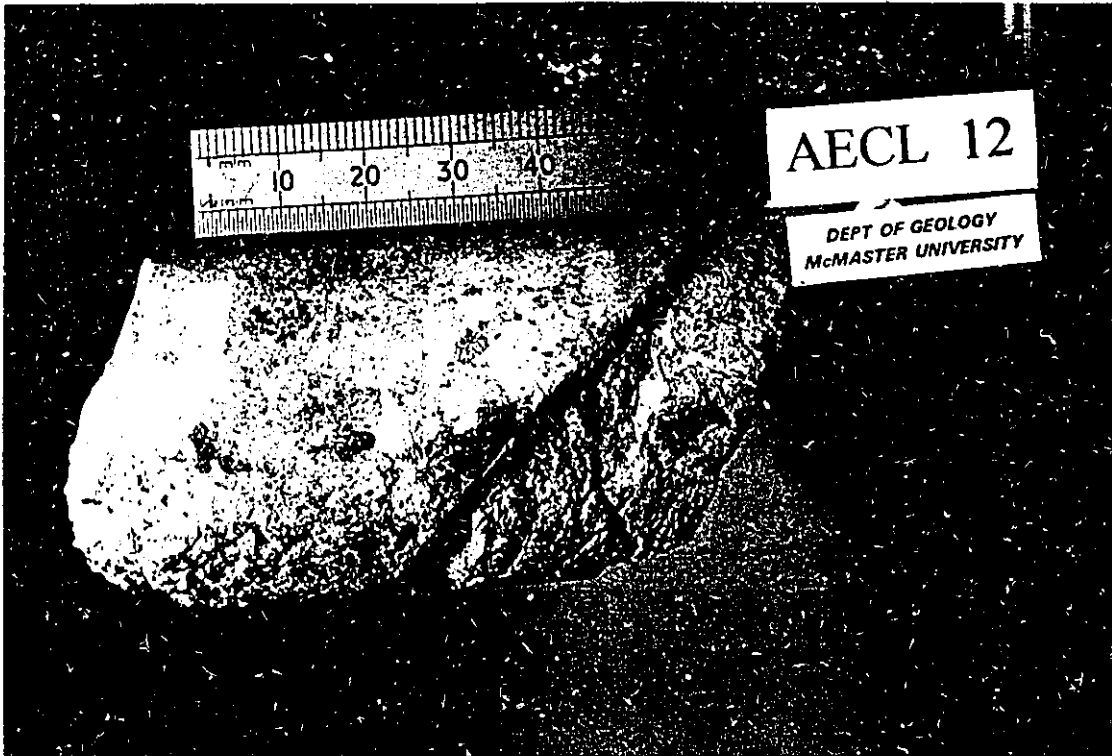


Figure 9.6. Photograph of AECL12. Fault gouge zone is too thin to do ESR plateau dating using quartz grains.

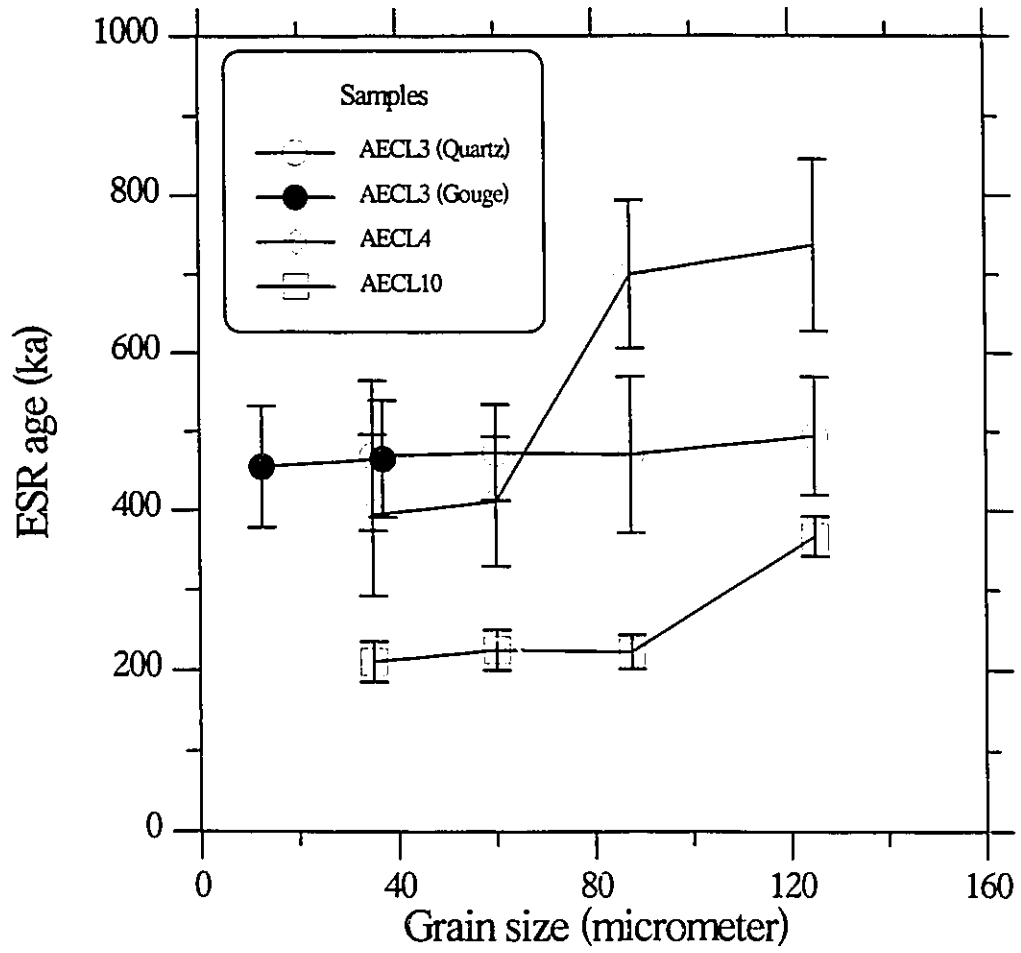


Figure 9.7. ESR age vs. grain sizes for unsaturated samples.

in the only left-hand fragment in photograph of this drill core (Fig. 9.8a), so that the width of gouge zone is not certain. However, the gouge was strongly comminuted and well foliated, indicating strong cataclastic deformation. AECL4 (Fig. 9.8b) collected from a fault breccia; the deformation was considered to be the weakest of the three samples. AECL10 (Fig. 9.8c) was collected from thicker fault gouge zone (at least 10 cm in width). The plateau ages represent the last resetting of E' signal during fault movements. The appearance of saturated samples is similar with unsaturated fault gouge in the drill core.

The weighted means of ESR ages lying on the plateaus are  $475 \pm 33$  ka for AECL3,  $404 \pm 64$  ka for AECL4 and  $219 \pm 14$  ka for AECL10 (Fig. 9.9). Although the displacement of each fault movement is difficult to estimate, the depth of the fault rocks was about 260 m. The normal stress condition appears to be sufficient for complete resetting of ESR signals (Lee and Schwarcz, 1994b).

#### **9.4. Possible mechanism of fault movement in URL site**

The present samples were all collected from or near fault zone 2 (Fig. 9.1). My data show that three reactivation events occurred in this fault zone. All were during past interglacial stages, namely isotope stages 13 (AECL3), 11 (AECL4), and 7 (AECL10) (Fig. 9.9). The remaining samples are already saturated for all the ESR centers; they are too old to date the last fault movement using the ESR dating method.

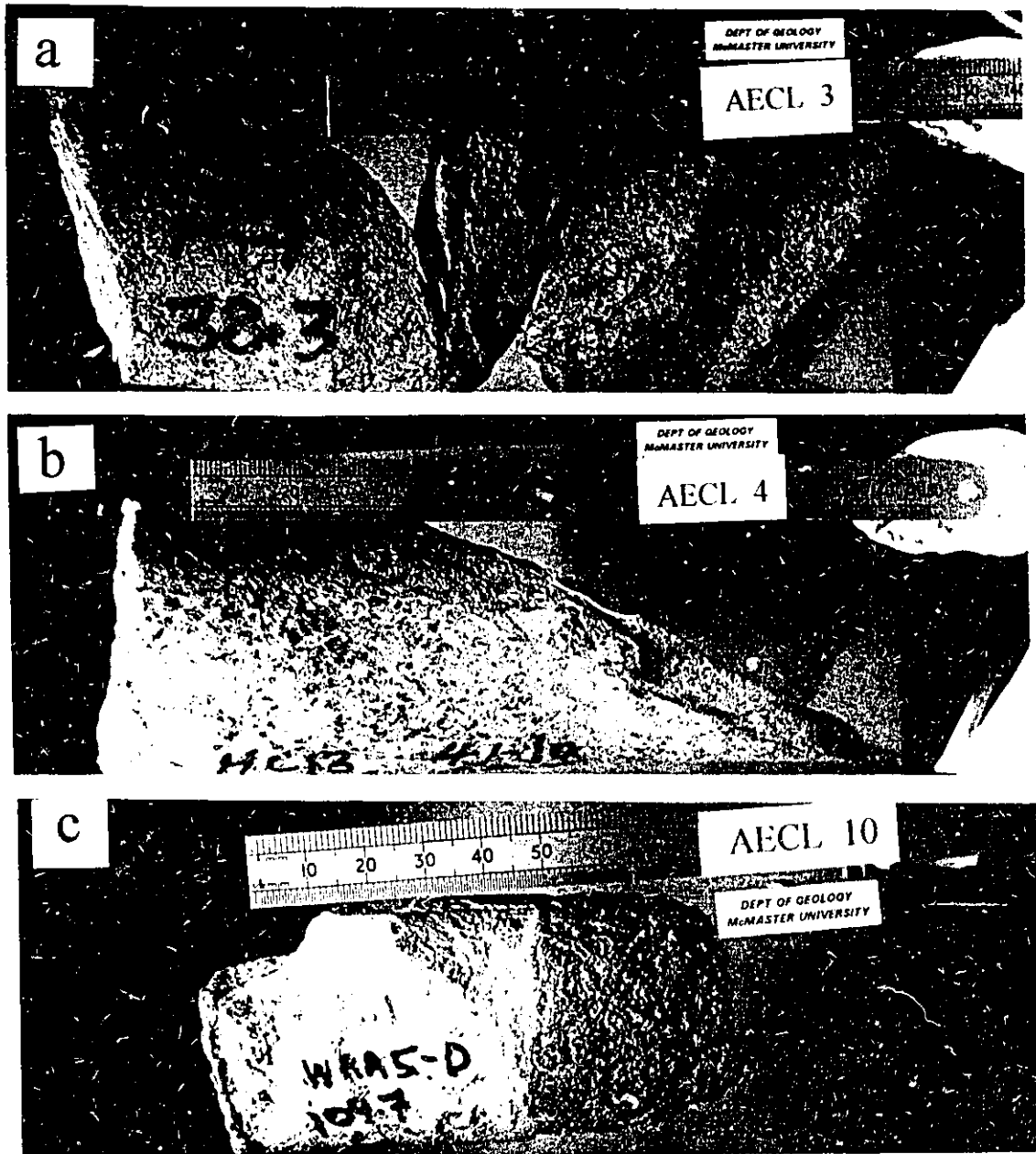


Figure 9.8. (a) A drill core sample of AECL3. Fault gouge was collected from a thin film in the only the left-hand fragment of this photograph. (b) A drill core sample including fault breccia. The matrix of breccia was used for ESR dating. (c) A fraction of thick fault gouge.

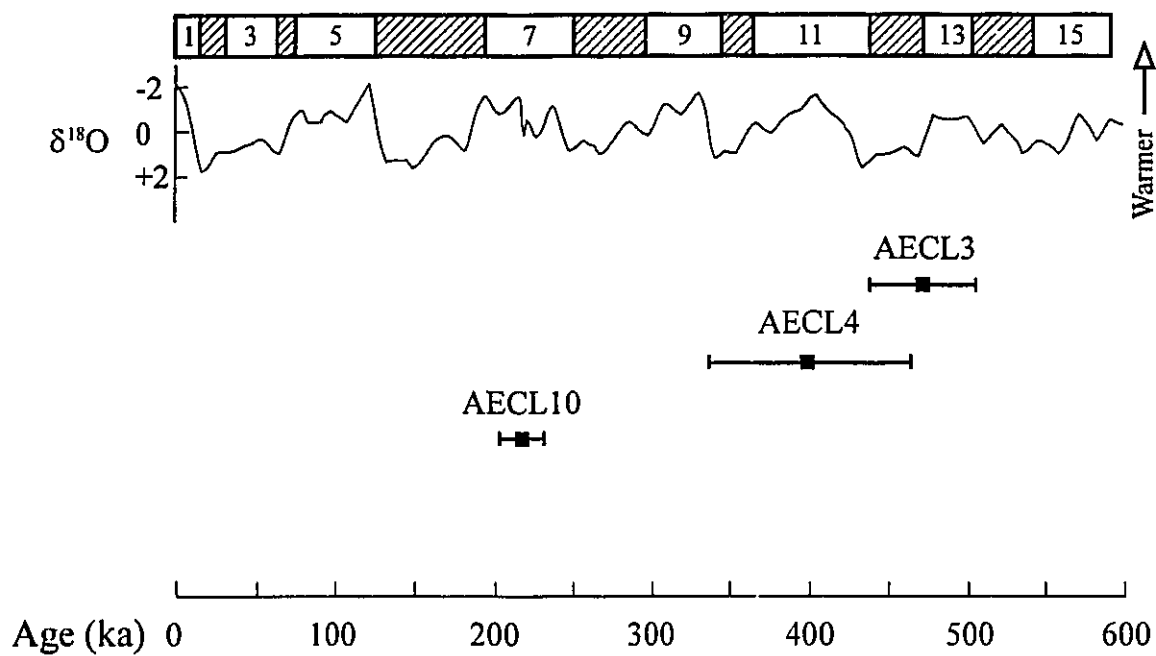


Figure 9.9. Stable isotope stages and ESR plateau ages of fault rocks collected from the thrust fault zones in URL site.



Recently, Johnston (1989) suggested that the weight of an ice sheet suppresses low angle fault activities in the underlying crust by reducing the deviatoric stress while increasing the normal stress on potentially seismogenic faults. Wood (1989) showed some examples of thrust fault activities triggered by unloading from melting of ice sheet in Northern Fennoscandia around 9000 years BP.

Although the approximate vertical depth of fault rocks collected from the drill-core samples is about 260 m, there is a possibility that the movement of thrust faults was triggered at depth and propagated upward. The measured stress field in the URL site indicates that the direction of maximum horizontal stress is rotated from SE (depth > fault zone 2) to NE (depth < fault zone 2) bounded by the fault zone 2 (Martin, 1990; Haimson, 1993). The estimated stresses at a depth of 445-515 m below the surface are  $S_v=12-14$  Mpa;  $S_h=36$  Mpa;  $S_H=54$  Mpa where  $S_v$  is the vertical stress,  $S_h$  is the minimum horizontal stress and  $S_H$  is the maximum horizontal stress (Haimson, 1993). I presume that this stress field was consistent during the Holocene and the late Pleistocene (up to ~ 2 Ma). The dip of fault zone 2 (thrust fault) is about 25-30° southeast. During the period of glaciation, an imposed ice sheet overburden stress ( $\rho_i g z$ ; where  $\rho_i$  is the density of ice sheet,  $g$  is the acceleration due to gravity, and  $z$  is the thickness of ice sheet) was added to the vertical stress ( $S_v$ ). This ice sheet overburden stress ( $S_i$ ) will cause the normal stress to the fault plane ( $\sigma_n$ ) to increase and the shear stress on the fault plane ( $\tau$ ) to decrease. These two effects increased the stability of the fault blocks. On the contrary, unloading due to melting of an ice sheet during interglacials would have caused  $\sigma_n$  to decrease and

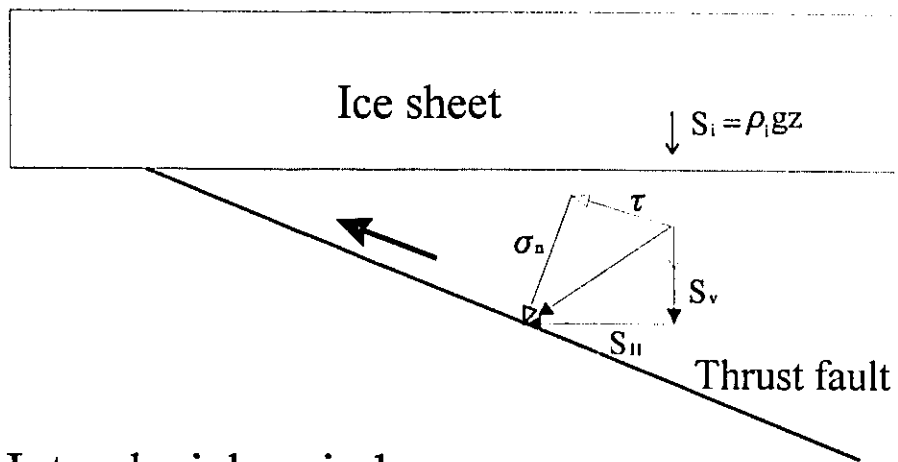
$\tau$  to increase resulting in reactivation of the fault (Fig. 9.10).

### 9.5. Conclusions and recommendations for further research

I have carried out ESR analyses of quartz from ten samples of fault gouge at the URL site. Seven of the samples were in saturation and therefore I can only estimate the minimum time that has elapsed since last resetting of their ESR signals by faulting. These minimum ages range from 0.3 to 2.5 Ma. Three of the samples contained quartz that was not yet in saturation and exhibited plateaus of age vs grain size. The three plateau ages,  $475 \pm 33$  ka,  $404 \pm 64$  ka and  $219 \pm 14$  ka, all appear to lie within interglacials (Fig. 9.9). Although the precision of the two older gouge samples do not allow us to define their age with adequate precision, these data are consistent with a model in which movement on the faults is triggered by unloading of ice from the overlying bedrock surface at the end of a glacial stage. During the glacial periods, the faults are immobilized because ice loading increases normal stress on the gently dipping thrust planes. This raises the interesting possibility that a more complete survey of ESR ages on such fault gouge samples will allow us to reconstruct the history of ice sheet advances across the Canadian Shield.

I have not detected any evidence of recent (Holocene) tectonic activity in the samples analysed so far. Most of the fault gouge zones (7 out of 10) appear to have been immobile for long times, and the only detectible movements appear to be associated with

Glacial period



Interglacial period

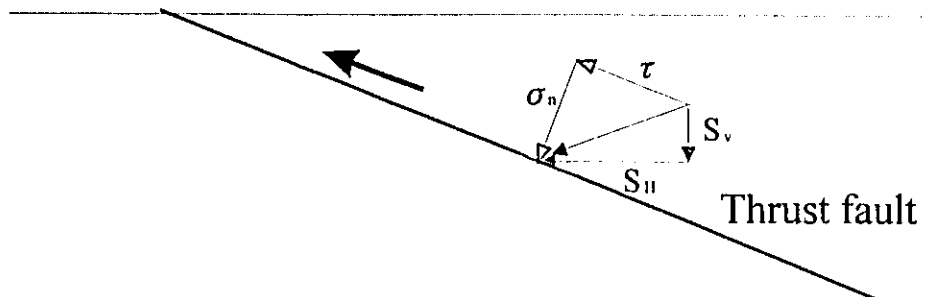


Figure 9.10. Variation of stress field between glacial and interglacial period.

interglacial unloading. This is of some concern when we consider the risk of future seismic activity at this site. We are now in an interglacial period which began about 9,000 y ago with the retreat of the Laurentide Ice Sheet from the region of the URL. Therefore, we are now in a period typical of those in which some seismicity occurred in the past. This would appear therefore to be a period of increased risk. We should therefore consider what is the probability of experiencing additional seismic events. Although we know that in general the Canadian Shield is an area of extremely low seismic activity, this fact is based on observations over a time range of a few hundred years at most, whereas we are now concerned with stability of the site on a much longer time frame (some thousands of years).

Unfortunately the limited number of analyses carried out in this preliminary study do not give us an adequate basis on which to estimate the long-term probability of seismic activity. For example, none of the three events detected by us are within the last interglacial (Isotope Stage 5). I would therefore recommend that this research be continued in order to accumulate enough data to give a more precise estimate of the age distribution of past seismic events. The present research has shown that this can be done more economically than in past ESR analyses of fault activity, by using whole gouge samples which have only been stripped of paramagnetic (Fe-bearing) minerals. This work should be extended to faults encountered at greater depths in the site, in order to evaluate the variation of seismicity with depth; stress release events may be more common at shallower depths.

## Chapter 10

### Conclusions

The results of analyses of fault rocks collected from the San Gabriel fault zone give us much information about ESR plateau dating method, the evolution of fault zones with fault rocks, the pattern of paleo-fault activity, and the evolution of structural features. These different kinds of information were developed on different spatial scales ranging from the lattice structure of quartz (ESR centers), grain scale (ESR plateau method), outcrop scale (cross-cutting relationship, the evolution of fault zone with equivalent fault rocks), local tectonics (tempo-spatial clustering of fault activity in the Little Tujunga region), and regional tectonics (fractal clustering of fault activity in California, comparing the tectonic activity between active (California) and inactive (Canadian shield) area).

In most application of ESR dating to fault movement, it is essential to demonstrate that the ESR signal was fully zeroed at the time of faulting events. The result of analysis of experimentally sheared quartz and fault rocks collected in the Little Tujunga region suggest that the ESR plateau dating method can be used as an adequate criterion for determination of total resetting of ESR signals. Two or more ESR signals with different zeroing sensitivities that show the same ESR age plateau enhance the likelihood that zeroing of ESR signals occurred at the time of fault movement. Subsamples collected

along/across a fault rock zone showed concordant ESR plateau ages, which explain the complete resetting of ESR signals at the time of faulting events.

In outcrop scale, the sequence of ESR plateau ages agrees with the sequence indicated by geological relationships. For Type I and II faulting modes, the ESR plateau dating method can determine each stage of the evolution of fault zones with equivalent fault rocks; on the other hand, for Type III mode, only the age of last movement can be determined.

Two major fault zones, the San Gabriel and Santa Susana-Sierra Madre fault zones are developed in the Little Tujunga region, southern California. The trace of thrust faults and folds of the Santa Susana-Sierra Madre fault zone roughly parallel to the San Gabriel fault zone, indicate that maximum horizontal stress was nearly perpendicular to the San Gabriel fault zone. Subsidiary faults and folds were developed obliquely to the main trend of the San Gabriel fault zone in the local transpressive regimes generated by the curvature of the trace of the main fault zone. These structural features can be explained by a process of low drag-decoupled shear combined with transpression.

ESR plateau ages for the San Gabriel fault zone range from 1170 to 40 ka. After 0.4 Ma they appear to cluster into active and dormant periods. Similar temporal clustering of fault activity is also seen in historic earthquake records, and Holocene earthquake fault activity, suggesting a scale-independent pattern of cyclicity in fault activity. Resetting of ESR signals by younger faulting events obscures this pattern in the record of the older events.

Within a given active period, the activity of faults show spatial clustering at a restraining bend in the San Gabriel fault. The restraining bend prohibits the propagation of fault activity and thus fault strain spreads out and results in the reactivation of subsidiary faults. Even though earlier events tend to be obliterated by younger ones, some of these subsidiary faults reserve the record of the faulting events older than those of the main strand, and allow us to recognize spatio-temporal pattern of fault activity in the post-0.4 Ma period.

Although the San Gabriel fault zone has been active for  $\geq 12$  Ma, ESR dating only shows ages younger than 1.2 Ma. The ESR dating method has an intrinsic maximum age limit of about 2-4 Ma, but we do not see events as old as that. Events older than 1.2 Ma have presumably been obliterated by later faulting events. I suppose that much of the fault gouge which I studied was actually formed over a long time (12-5 Ma), and periodically reactivated, extending into late Pleistocene time.

The arcuate geometry of the San Gabriel fault zone had yielded the characteristic deformation regimes along the fault zone. In its northwest segment, the Ridge basin has been formed by transtensive process. The structural evolution of the central segment (Little Tujunga region) was mainly governed by dextral strike slip movements. The eastern San Gabriel mountain continued uplifting in the transpressive regime in the southeast segment of the fault zone.

The temporal clustering behavior of fault activity is observable in California over a time scale spanning 5 orders of magnitude, from historic to several hundreds of

thousands of years. The fractal dimension ranging 0.43-0.46 of historical record of earthquakes in central California is similar with that (0.45) of the paleoseismic record of the San Gabriel fault zone. The fractal dimension of the San Andreas fault zone in southern California both in historic and paleoseismic time scales is 0.67 indicating more evenly distributed fault movements than that of the central California. On time scales  $< 1$  y, the distribution is largely random.

I have also carried out ESR analyses of quartz from ten samples of fault gouge collected at URL site, Pinawa, Manitoba. Seven of the samples were in saturation. The three ESR plateau ages appear to lie within interglacials, which is consistent with a model in which movement on the faults is triggered by unloading of ice from the overlying bedrock surface at the end of a glacial stage.

Comparing the results of ESR analyses of an active area with that of inactive areas, all the faults (100 %) analyzed so far in the San Gabriel fault zone were reactivated within 1.2 Ma. On the other hand, only 30 % of the faults studied in the Canadian shield (Pinawa, Manitoba) showed evidence of reactivation, probably triggered by unloading from melting of ice in interglacial periods. These results show that ESR plateau dating method can be used to evaluate fault activity patterns and crustal stability with a temporal resolution of 5-15 %.



## References

- Aitken, M. J. (1990). *Science-based dating in archaeology*. Longman, London and New York.
- Aitken, M.J., and Smith, B.W. (1988). Optical dating: recuperation after bleaching. *Quat. Sci. Rev.*, 7, 387-393.
- Anderson, J.L., Osborne, R.H., and Palmer, D.F. (1980). Petrogenesis of cataclastic rocks within the San Andreas fault zone of southern California, U.S.A. *Tectonophysics*, 67, 221-249.
- Anderson, J.L., Osborne, R.H., and Palmer, D.F. (1983). Cataclastic rocks of the San Gabriel fault: expression of deformation at deeper crustal levels in the San Andreas fault zone. *Tectonophysics*, 98, 209-251.
- Anderson, J.H., Feigl, F.J., and Schlesinger, M. (1974). The effects of heating on color centers in germanium-doped quartz. *J. phys. Chem. Solids*, 35, 1425-1428.
- Arends, J., Dekker, A.J., and Perdok, W.G. (1963). Color centers in quartz produced by crushing. *Phy. Stat. Sol.*, 3, 2275-2279.
- Ariyama, T. (1985). Conditions of resetting the ESR clock during faulting. In: Ikeya, M. and Miki, T. (eds.), *ESR Dating and Dosimetry*, Ionics, Tokyo, 249-256.

Bakun, W.H., and McEvilly, T.V. (1984). Recurrence models and Parkfield, California, earthquakes. *J. Geophys. Res.*, 89, 3051-3058.

Bar, M., Kolodny, Y., and Bentor, U.K. (1974). Dating of faults by fission track dating of epidotes - An attempt. *Earth and Planet. Sci. Lett.*, 22, 157-166.

Bartsch-Winkler, S., and Schmoll, H.R. (1992). Utility of radiocarbon-dated stratigraphy in determining late Holocene earthquake recurrence intervals, upper Cook Inlet region, Alaska. *Geol. Soc. Am. Bull.*, 104, 684-694.

Bell, W.T. (1980). Alpha dose attenuation in quartz grains for thermoluminescence dating. *Ancient TL*, 12, 4-8.

Bell, J.W., and Katzer, T. (1990). Timing of late quaternary faulting in the 1954 Dixie valley earthquake area, central Nevada. *Geology*, 18, 622-625.

Berthe, D., Choukroune, P., and Jegouzo, P. (1979). Orthogneiss, mylonite and non-coaxial deformation of granites: The example of the South Armorican shear zone. *J. Struct. Geol.*, 1, 31-42.

Biegel, R.L., Sammis, C.G., and Dietrich, J.H. (1989). The frictional properties of a simulated gouge having a fractal particle distribution. *J. Struct. Geol.*, 11, 827-846.

Blenkinsop, T.G., and Rutter, E.H. (1986). Cataclastic deformation of quartzite in the Moine Thrust Zone. *J. Struct. Geol.*, 8, 669-682.

Blenkinsop, T.G., and Drury, M.R. (1988). Stress estimates and fault history from quartz microstructures. *J. Struct. Geol.*, 10, 673-684.

Brown, A., Soonawala, N.M., Everitt, R.A., and Kamineni, D.C. (1989). Geology and geophysics of the Underground Research Laboratory site, Lac du Bonnet Batholith, Manitoba. *Can. J. Earth Sci.*, 26, 404-425.

Buhay, W. (1987). A theoretical study on ESR dating of geological faults in southern California. Unpublished M. Sc. thesis, McMaster university, Hamilton, Canada.

Buhay, W.M., Schwarcz, H.P., and Grün, R. (1988). ESR dating of fault gouge: the effect of grain size. *Quat. Sci. Rev.*, 7, 515-522.

Buhay, W.M. (1991) Comment on "Increase of radiation sensitivity of ESR centers by faulting and criteria of fault dates". *Earth and Planet. Sci. Lett.*, 105, 574-577.

Buhay, W.M., Clifford, P.M., and Schwarcz, H.P. (1992) ESR dating of the Rotoiti breccia, New Zealand. *Quat. Sci. Rev.*, 11, 267-271.

Byerlee, J.D.(1978). Friction of rocks. *Pure & Appl. Geophys.*, 116, 615-626.

Chester, F.M., and Logan, J.M. (1986). Implication for mechanical properties of brittle faults from observations of the Punchbowl fault zone, California. *Pure & Appl. Geophys.*, 124, 79-106.

Chester, F.M., and Logan, J.M. (1987). Composite planar fabric of gouge from the Punchbowl fault, California. *J. Struc. Geol.*, 9, 621-634.

Chester, R.M., Evans, J.P., and Biegel, R.L. (1993). Internal structure and weakening mechanisms of the San Andreas fault. *J. Geophy. Res.*, 98, 771-786.

Colman, S.M., and Pierce, K.L. (1981). Weathering rinds on andesitic and basaltic stones as a Quaternary age indicator, western United States. U.S. Geol. Surv. Prof. Pap., 1210, 56 pp.

Crowell, J.C. (1952). Probable large lateral displacement on the San Gabriel fault, southern California. AAPG Bulletin, 36, 2026-2035.

Crowell, J.C. (1962). Displacement along the San Andreas fault, California. Geol. Soc. Am. Spec. Pap., 71, 61 p.

Crowell, J.C. (1979). The San Andreas fault system through time. J. Geol. Soc. London, 136, 293-302.

Crowell, J.C. (1982). The tectonics of Ridge basin, southern California, In: Crowell, J. C., and Link, M. H. (eds.) Geologic history of Ridge basin: Los Angeles, Pacific Section, Society of Economic Paleontologists and Mineralogists, 25-42.

Crowell, J.C. (1986a). Geologic history of the San Gabriel fault, central Transverse Ranges, Kern, Los Angeles, and Ventura counties, California. California Geology, 39, 276-281.

Crowell, J.C. (1986b). Active tectonics along the western continental margin of the conterminous United States: Active Tectonics, National Academy Press, Washington, D.C., 20-29.

Engelder, J.T. (1974). Cataclasis and the generation of fault gouge. Geol. Soc. Am. Bull., 85, 1515-1522.

Engelder, J.T. (1978). Aspects of asperity-surface interaction and surface damage of rocks during experimental frictional sliding. *Pure & Appl. Geophy.*, 116, 705-716.

Ensley, R.A., and Verosub, K.L. (1982) Biostratigraphy and magnetostratigraphy of southern Ridge basin, central Transverse Ranges, California. In: Crowell, J. C., and Link, M. H. (eds.), *Geologic history of Ridge basin: Los Angeles*, Pacific Section, Society of Economic Paleontologists and Mineralogists, 13-14.

Evans, J.P. (1988). Deformation mechanisms in granitic rocks at shallow crustal levels. *J. Struct. Geol.*, 10, 437-443.

Eyal, Y., Kaufman, A., and Matthews, M.B. (1992). Use of  $^{230}\text{Th}/\text{U}$  ages of striated carnotites for dating fault displacements. *Geology*, 20, 829-832.

Flinn, D. (1977). Transcurrent faults and associated cataclasis in Shetland. *J. Geol. Soc. Lond.*, 133, 231- 248.

Forman, S.L., Machette, M.N., Jackson, M.E., and Maat, P. (1989) An evaluation of thermoluminescence dating of paleoearthquakes on the American Fork Segment, Wasatch fault zone, Utah. *J. Geophy. Res.*, 94, 1622-1630.

Fleuty, M.J. (1975). Slickensides and slickenlines. *Geol. Mag.*, 112, 319-322.

Fukuchi, T., Imai, N., and Shimokawa, K. (1986). ESR dating of fault movement using various defect centres in quartz; the case in the western South Fossa Magna, Japan. *Earth and Planet. Sci. Lett.*, 78, 121-128.

Fukuchi, T. (1988). Applicability of ESR dating using multiple centres to fault movement - The case of the Itoigawa-Shizuoka Tectonic Line, a major fault in Japan. *Quat. Sci. Rev.*, 7, 509-514.

Fukuchi, T. (1989). Increase of radiation sensitivity of ESR centres by faulting and criteria of fault dates. *Earth Planet. Sci. Lett.*, 94, 109-122.

Fukuchi, T. (1992a). A reply to comments by W.M. Buhay on "Increase of radiation sensitivity of ESR centers by faulting and criteria of fault dates". *Earth and Planet. Sci. Lett.*, 114, 211-213.

Fukuchi, T. (1992b). ESR studies for absolute dating of fault movements. *J. Geol. Soc. London*, 149, 265-272.

Fukuchi, T. (1993). Vacancy-associated type ESR centers observed in natural silica and their application to geology. *Appl. Radiat. Isot.*, 44, 179-184.

Garrison, E.G., Rowlett, R.M., Cpwan, D.L., and Holroyd, L.V. (1981). ESR dating of ancient flints. *Nature*, 290, 44-45.

Gascoyne, M. (1986). Evidence for the stability of the potential nuclear waste host, sphene, over geological time, from uranium-lead ages and uranium-series measurements. *Appl. Geochem.*, 1, 199-210.

Gascoyne, M., and Schwarcz, H.P. (1986). Radionuclide migration over recent geologic time in a granitic pluton. *Chem. Geol.*, 59, 75-85.

Gibbs, R.E. (1926). Structure of alpha quartz: Proceedings of the Royal Society of London, A: Mathematical and Physical Sciences, 110, 443-455.

Gillespie, P.A., Howard, C.B., Walsh, J.J., and Watterson, J. (1993). Measurement and characterisation of spatial distributions of fractures. *Tectonophysics*, 226, 113-141.

Godfrey-Smith, D.I., Huntley, D.J., and Chen, W.H. (1988). Optical dating studies of quartz and feldspar sediment extracts. *Quat. Sci. Rev.*, 7, 373-380.

Griffith, A.A. (1920). The phenomena of rupture and flow in solids. *Phil. Trans. Roy. Soc., A* 221, 163-198.

Griffith, A.A. (1924). The theory of rupture. In *Proc. 1st Int. Congr. Appl. Mech.*, (eds) C.B. Biezeno and J.M. Burgers. Delft: Tech. Boekhandel en Drukkerij J. Walter Jr., 54-63.

Grün, R. (1989) Electron spin resonance (ESR) dating. *Quaternary International*, 1, 65-109.

Grün, R. (1992). Remarks on ESR dating of fault movements. *J. Geol. Soc. London*, 149, 261-264.

Grün, R., Schwarcz, H.P., and Zymela, S. (1987). Electron spin resonance dating of tooth enamel. *Can. J. Earth Sci.*, 24, 1022-1037.

Hailwood, E.A., Maddock, R.H., Fung, T., and Rutter, E.H. (1992). Palaeomagnetic analysis of fault gouge and dating fault movement, Anglesey, North Wales. *J. Geol. Soc. London*, 149, 273-284.

Haimson, B., Lee, M., Chandler, N., and Martin, D. (1993). Estimating the state of stress from subhorizontal hydraulic fractures at the underground research laboratory, Manitoba. *Int. J. Rock Mech. Min. Sci. & Geotech. abstr.*, 30, 959-964.

Halliburton, L.E. (1985). Defect models and radiation damage mechanisms in alpha-quartz, *Crystal Lattice Defects and Amorphous Materials*, 12, 163-190.

Hanmer, S. and Passchier, C. (1991). Shear-sense indicators: a review. Geological survey of Canada paper 90-17.

Harris, C., Franssen, R., and Loosveld, R. (1991). Fractal analysis of fractures in rocks: the Cantor's Dust method-comment. *Tectonophysics*, 139, 255-273.

Hickman, S.H., Zoback, M.D., and Healy, J.H. (1988). Continuation of a deep borehole stress measurement profile near the San Andreas fault. 1. Hydraulic fracturing stress measurements at Hi Vista, Mojave desert, California. *J. Geophys. Res.*, 93, 15183-15195.

Hill, M.L. (1930). Structure of the San Gabriel Mountains, north of Los Angeles, California. *Univ. California Dept. Geol. Sci. Bull.*, 19, 137-170.

Hill, D.P., Eaton, J.P., and Jones L. M. (1990). Seismicity, 1980-86, in *The San Andreas Fault System, California*. U.S. Geol. Surv. Prof. Pap., 1515, 115-151.

Hitt, K.B., and Martin, J.J. (1983). Radiation-induced mobility of lithium and sodium in alpha-quartz. *J. Appl. Phys.*, 54, 5030-5031.

Hochstrasser, G., and Antonini, J.F. (1972). Surface states of pristine silica surfaces. *Surface Science*, 32, 644- 664.



House, W.M., and Gray, D.R. (1982). Cataclasites along the Salville thrust, U.S.A. and their implications for thrust-sheet emplacement. *J. Struc. Geol.*, 4, 257-269.

Howell, B.F. Jr., (1949). Structural geology of the region between Pacoima and Little Tujunga Canyons, San Gabriel Mountains, California. Unpublished Ph.D. thesis, pp.110, California Institute of Technology, Pasadena, California.

Howell, B.F., Jr., (1954). Geology of the Little Tujunga area, Los Angeles County. In: R.H. Jahns (eds) *Geology of southern California: California Div. Mines Bull. 170, Map Sheet 10.*

Huntley, D.J., Godfrey-Smith, D.I., and Thewalt, M.L.W. (1985). Optical dating of sediments, *Nature*, 313, 105-107.

Ikeya, M. Miki, T., and Tanaka, K. (1982). Dating of a fault by Electron Spin Resonance on intrafault materials, *Science*, 215, 1392-1393.

Ikeya, M. (1993). *New Applications of Electron Spin Resonance: Dating, Dosimetry, and Microscopy.* Singapore, World Scientific, 500 pp.

Imai, N. and Shimokawa, K. (1989). ESR dating of the tephra "Crystal ash" distributed in Shinshu, central Japan. *Appl. Radiat. Isot.*, 40, 1177-1180.

Isoya, J., Weil, J.A., and Halliburton, L.E. (1981). EPR and *ab initio* SCF-MO studies of the Si H-Si system in the  $E'_4$  center of alpha- quartz. *J. Chem. Phys.*, 74, 5436-5448.

Isoya, J., and Weil, J.A. (1979). Uncompensated titanium (3+) center in alpha-quartz. *Phys. Status. Solidi A*, 52, K193.

Ito, T., and Sawada, S. (1985). Reliable criteria for the selection of sampling points for ESR fault dating. In: Ikeya, M. and Miki, T. (eds.), ESR dating and Dosimetry, Ionics, Tokyo, 229-237.

Jani, M.G., Bossoli, R.B., and Halliburton, L.E. (1983). Further characterization of the  $E_1'$  center in crystalline  $\text{SiO}_2$ . Phys. Rev. B: Condensed Matter, 27, 2285-2293.

Johnston, A.C. (1989). The effect of large ice sheets on earthquake genesis. In: Gregersen S. and Basham, P.W. (eds.), Earthquakes at North-Atlantic passive margins: neotectonics and postglacial rebound, 581-599. Kluwer Academic Publishers, Dordrecht, Boston and London.

Kagan, Y.Y. and Jacson, D.D. (1991) Long-term earthquake clustering. Geophy. J. Inter., 104, 117-133.

Kahle, J.E., Wills, C.J., Hart, E.W., Treiman, J. A., Greenwood, R.B., and Kaumeyer, R.S., (1988). Surface rupture Superstition Hills earthquakes of November 23 and 24, 1987, California Geology, 41, 75-84.

Kamb, B., Silver, L.T., Abrams, M.J., Carter, B.A., Jordan, T.H., and Minster, J.B. (1971). Pattern of faulting and nature of fault movement in the San Fernando earthquake. In: The San Fernando, California, Earthquake of February 9, 1971, U.S. Geol. Surv. Prof. Pap., 733, 41-54.

Kanaori, Y., Miyakoshi, K., Kakuta, T., and Gatake, Y. (1980). Dating fault activity by surface textures of quartz grains from fault gouges. Eng. Geol., 16, 243-262.

Kanaori, Y., Tanaka, K. and Miyakoshi, K. (1985). Further studies on the use of quartz grains from fault gouges to establish the age of faulting. *Eng. geol.*, 21, 175-194.

Knipe, R.J. (1989). Deformation mechanisms-recognition from natural tectonites. *J. Struc. Geol.*, 11, 127-146.

Kosaka, K., and Sawada, S. (1985). Fault gouge analysis and ESR dating of the Tsurukawa fault, west of Tokyo: significance of minute sampling. In: Ikeya, M. and Miki, T. (eds.), *ESR dating and Dosimetry*, Ionics, Tokyo, 257-266.

Kralik, M., Klima, K., and Riedmuller, G. (1987). Dating fault gouges. *Nature*, 327, 315-317.

Kralik, M., Clauer, N., Holnsteiner, R., Huemer, H., and Kappel, F. (1992). Recurrent fault activity in the Grimsel Test Site (GTS, Switzerland): revealed by Rb-Sr, K-Ar and tritium isotope techniques. *J. Geol. Soc. London*, 149, 293-301.

Kranz, R.L. (1983). Microcracks in rocks: a review. *Tectonophysics*, 100, 449-480.

Lachenbruch, A.H., and McGarr, A. (1990). Stress and heat flow. *U.S. Geol. Surv. Prof. Pap.*, 1515, 261-277.

Lee, H.K., and Schwarcz, H.P. (1993). An experimental study of shear-induced zeroing of ESR signals in quartz: *Appl. Radiat. Isot.*, 44, 191-195.

Lee, H.K., and Schwarcz, H.P. (1994a). Dating of fault gouge: Further tests of the plateau method. *Quat. Sci. Rev.*, 13, 629-634.

Lee, H.K., and Schwarcz, H.P. (1994b). Criteria for complete zeroing of ESR signals during faulting of the San Gabriel fault zone, Southern California. *Tectonophysics*, 235, 317-337.

Lee, H.K., and Schwarcz, H.P. (1994c). ESR plateau dating of periodicity of activity on the San Gabriel fault zone, Southern California. submitted to *Geol. Soc. Am. Bull.*

Lee, H.K., and Schwarcz, H.P. (1994d). A fractal clustering of fault activity in California. Submitted to *Geology*.

Levi, S., and Yeats, R.S. (1993). Paleomagnetic constraints on the initiation of uplift on the Santa Susana fault, Western Transverse Range, California. *Tectonics*, 12, 688-702.

Link, M.H. (1982). Provenance, paleocurrents, and paleogeography of Ridge basin, southern California. In: Crowell, J.C. and Link, M.H. (eds.), *Geologic history of Ridge basin, southern California: Los Angeles, Pacific Section, Society of Economic Paleontologists and Mineralogists*, 265-276.

Lloyd, G.E., and Knipe, R.J. (1992). Deformation mechanisms accommodating faulting of quartzite under upper crustal conditions. *J. Struct. Geol.*, 14, 127-143.

Logan, J. M., Friedman, M., Higgs, N. Dengo, C., and Shimamoto, T. (1979). Experimental studies of simulated fault gouge and their application to studies of natural fault zones. *Proc. Conf. VIII- analysis of Actual Fault zones in Bedrock. U.S. Geol. Surv. Open-file Rept. 79-1239*, 305-343.

Lyons, R.G., Bowmaker, G.A., and O'Connor, C.J. (1988). Dependence of accumulated dose in ESR dating on microwave power: a contra-indication to the routine use of low power levels. *Nucl. Tracks Radiat. Meas.*, 14, 243-251.

Lyons, R.G. (1989). Contribution to electron spin resonance dating with special reference to speleothems. Unpublished Ph. D. thesis. University of Auckland, New Zealand.

Mandelbrot, B.B. (1985). Self-affine fractals and fractal dimension, *Physica Scripta*, 32, 257-260.

Marone, C., and Scholz, C.H. (1989). Particle-size distribution and microstructures within simulated fault gouge. *J. Struc. Geol.*, 11, 799-814.

Martin, C.D. (1990). Characterizing in situ stress domains at the AECL Underground Research Laboratory. *Can. Geotech. J.*, 27, 631-646.

Maschmeyer, D., and Lehmann, G. (1984). New electron centers in neutron- irradiated natural quartz. *Sol. Stat. Comm.*, 50, 1015-1018.

Matti, J.C., and Morton, D.M. (1993). Paleogeographic evolution of the San Andreas fault in southern California; a reconstruction based on a new cross fault correlation. In: Powell, R.E., Weldon II, R.J. and Matti. J.C. (eds.), *The San Andreas fault system; Displacement, palinspastic reconstruction, and geological evolution. Geol. Soc. Am. Mem.*, 178, 107-159.

May, S.R., Ehman, K.D., Gray, G.G., and Crowell, J.C. (1993). A new angle on the tectonic evolution of the Ridge basin, a "strike-slip" basin in Southern California. *Geol. Soc. Am. Bull.*, 105, 1357-1372.

McCalpin, J. P., Forman, S.L., and Lowe, M. (1994). Reevaluation of Holocene faulting at the Kaysville site, Weber segment of the Wasatch fault zone, Utah. *Tectonics*, 13, 1-16.

McGarr, A., Zoback, M.D., and Hanks, T.C. (1982). Implications of an elastic analysis of in situ stress measurements near the San Andreas fault. *J. Geophys. Res.*, 87, 7797-7806.

Mckee, J.W., Jones, N.W., and Long, L.E. (1984). History of recurrent activity along a major fault in northeastern Mexico. *Geology*, 12, 103-107.

McKenzie, D., and Brune, J.N. (1972). Melting on fault planes during large earthquakes. *Geophys. J. R. Astron. Soc.*, 29, 65-78.

McNutt, R.H., Gascoyne, M., and Kamineni, D.C. (1987).  $^{87}\text{Sr}/^{86}\text{Sr}$  values in groundwaters of the East Bull Lake pluton, Superior Province, Ontario, Canada. *Appl. Geochem.*, 2, 93-101.

Means, W.D. (1987). A newly recognized type of slickenside striation. *J. Struct. Geol.*, 9, 585-590.

Means, W.D. (1984). Shear zones of Type I and II and their significance for reconstruction of rock history. *Geol. Soc. Am. Abs.*, 16, 50.

Menges, C.M., McFadden, L.D., and Bull, W.B. (1979). Terrace development in a thrust-faulted terrane, San Fernando area, Southern California [abs]. *Geol. Soc. Am. Abs.*, 17, 370.

Miki, T., and Ikeya, M. (1982). Physical basis of fault dating with ESR. *Naturwissenschaften*, 69, 90-91.

Mitra, G. (1984). Brittle to ductile transition due to large strains along the White Rock Thrust, Wind River Mountains, Wyoming. *J. Struct. Geol.*, 6, 51-61.

Mitra, G. (1992). Deformation of granitic basement rocks along fault zones at shallow to intermediate crustal levels. In: Mitra, S., and Fisher G.W. (eds.), *Structural Geology of Fold and Thrust Belts*, The Johns Hopkins university Press.

Moiseyev, B.M., and Rakov, L.T. (1976). Paleodosimetric properties of the  $E_1'$  centers in quartz. *Doklady Akademii Nauk. SSSR.*, 233, 142-144.

Morse, P.D. II, (1987). Data acquisition and manipulation on the IBM PC for ESR spectroscopy. *Biophys. J.*, 51, 440a.

Mount, V.S., and Suppe, J. (1987). State of stress near the San Andreas fault: Implications for wrench tectonics. *Geology*, 15, 1143-1146.

Mount, V.S., and Suppe, J. (1992). Present-day stress orientation adjacent to active strike-slip faults: California and Sumatra. *J. Geophys. Res.*, 97, 11995-12013.

Nambi, K.S.V., and Aitken, M.J. (1986). Annual dose conversion factors for TL and ESR dating. *Archaeometry*, 28, 202-205.

Oakeshott, G.B. (1954). Geology of the western San Gabriel Mountains, Los Angeles County. In: Jahns, R.H. (ed.), *Geology of southern California: California Div. Mines Bull.* 170, Map Sheet 9.

Odom, A.L., and Rink, W.J. (1988). Natural accumulation of Schottky-Frenkel defects: Implications for a quartz geochronometer. *Geology*, 17, 55-58.

Orowan, E. (1949). Fracture and strength of solids. *Rep. Prog. Phys.*, 12, 48-74.

Petit, J.P. (1987). Criteria for the sense of movement on fault surfaces in brittle rocks. *J. Struct. Geol.*, 9, 597-608.

Pierce, K.L. (1986). *Dating methods: Active Tectonics*, National Academy Press, Washington, D. C., 195-214.

Porat N., and Schwarcz, H.P. (1991). Use of signal subtraction methods in ESR dating of burned flint. *Nucl. Tracks Radiat. Meas.*, 18, 203-212.

Powell, R.E., and Weldon II, R.J. (1992). Evolution of the San Andreas fault. *Ann. Rev. Earth Planet. Sci.*, 20, 431-468.

Powell, R.E. (1993). Balanced palinspastic reconstruction of pre-late Cenozoic paleogeology, southern California; Geologic and kinematic evolution of the San Andreas fault system. In: Powell, R.E., Weldon II, R.J., and Matti, J.C. (eds.), *The San Andreas fault system; Displacement, palinspastic reconstruction, and geological evolution*. *Geol. Soc. Am. Mem.* 178, 1-106.

Powell, R.E., Weldon II, R.J., and Matti, J.C. (1993). The San andreas fault system; Displacement, palinspastic reconstruction, and geological evolution. *Geol. Soc. Am. Mem.*, 178, 332 p..

Putnis, A. (1992). *Introduction to mineral science*. Cambridge, New York.



Rakov, L.T., Milovidova, N.D., Kuvshinova, K.A., and Moiseyev, B.M. (1986). An ESR study of Ge centers in natural polycrystalline quartz. *Geokhimiya*, 9, 1339-1344. Translated in *Geochemistry International* (1986), 23, 61-66.

Ramsay, J.G., and Graham, R.H. (1970). Strain variation in shear belts. *Can. J. Earth Sci.*, 7, 786-813.

Ramsay, J.G., and Huber, M.I. (1983). *The techniques of modern structural geology*, Vol. 1, Strain Analysis, Academic Press, London.

Ramsay, J.G., and Huber, M.I. (1987). *The techniques of modern structural geology*, Vol. 2, Folds and fractures, Academic Press, London.

Renyou, L., Zicheng, P., Sizhao, J., and Peihua, H. (1989). Estimation of the Influence of experimental conditions on ESR dating results. *Appl. Radiat. Isot.*, 40, 1071-1075.

Rhodes, E.J. (1988). Methodological considerations in the optical dating of quartz. *Quat. Sci. Rev.*, 7, 395-400.

Rhodes, E.J. (1990). Optical dating of sediment. Unpublished D. Phil thesis, Oxford University.

Rink, W.J. (1990). Experimental and theoretical investigation of radiation-induced, electron paramagnetic resonance-detected point defects in quartz: implications for geochronometry. Unpublished Ph. D. thesis, The Florida State University, Florida, USA.

Rink, W.J., and Odom, A.L. (1991). Natural alpha recoil particle radiation and ionizing radiation sensitivities in quartz detected with EPR: implications for geochronometry. *Nucl. Tracks Radiat. Meas.*, 18, 163-173.

Rink, W.J., Rendell, H. Marseglia, E.A., Luff, B.J., and Townsend, P.D. (1993). Thermoluminescence spectra of Igneous quartz and Hydrothermal vein quartz. *Phys. Chem. Minerals*, 20, 353-361.

Rockwell, T., Loughman, C., and Merifield, P. (1990). Late Quaternary rate of slip along the San Jacinto fault zone, near Anza, southern California. *J. Geophys. Res.*, 95, 8593-8605.

Rudra, J.K., Fowler, W.B., Yip, K.L., and Fiegl, F.L. (1985). Model for the  $E_2'$  center in alpha quartz. *Phys. Rev. Lett.*, 55, 2614-2617.

Rutter, E.H., Maddock, R.H., Hall, S.H., and White, S.H. (1986). Comparative microstructures of natural and experimentally produced clay-bearing fault gouges. *Pure & Appl. Geophys.*, 124, 3-30.

Sammis, C.G., Osborne, R.H., Anderson, J.L., Banerdt, M., and White, P. (1986). Self-similar cataclasis in the formation of fault gouge. *Pure & Appl. Geophys.*, 124, 53-78.

Sammis, C., King, G., and Biegel, R. (1987). The kinematics of gouge deformation. *Pure & Appl. Geophys.*, 125, 777-812.

Sanderson, D.J., and Marchini, W.R.D. (1984). Transpression, *J. Struct. Geol.*, 6, 449-458.

Scholz, C.H. (1990). *The mechanics of earthquakes and faulting*. Cambridge University Press, New York.

Scholz, C.H., Beavan, J., and Hanks, T.C. (1979). Frictional metamorphism, argon depletion, and tectonic stress on the Alpine fault, New Zealand. *J. Geophys. Res.*, 84, 6770-6782.

Schwarcz, H.P., Buhay, W.M., and Grun, R. (1987). ESR dating of fault gouge. U.S.G.S. Open File Rept. of 87-673 in *Directions in paleoseismology* (edited by Crone, A.J. and Olmdahl, E.), 50-64.

Schwarcz, H.P., and Grün, R. (1992). ESR dating and the origin of modern man. *Phil. Trans. Roy. Soc. Lon.*, B 337, 145-148.

Schwartz, D.P., and Coppersmith, K.J. (1984). Fault behavior and characteristic earthquakes: Examples from the Wasatch and San Andreas fault zones. *J. Geophys. Res.*, 89, 5681-5698.

Sedlock, R.L., and Hamilton, D.H. (1991). Late Cenozoic tectonic evolution of Southwestern California. *J. Geophys. Res.*, 96, 2325-2351.

Shimokawa, K., and Imai, N. (1986). Simultaneous determination of alteration and eruption ages of volcanic rocks by electron spin resonance. *Geochimica et Cosmochimica Acta*, 51, 115-119.

Shimokawa, K., Imai, N., and Moriyama, A. (1988). ESR dating of volcanic and baked rocks. *Quat. Sci. Rev.*, 7, 529-532.

- Sibson, R.H. (1977). Fault rocks and fault mechanisms. *J. Geol. Soc. Lond.*, 133, 191-213.
- Sibson, R.H. (1986a). Brecciation processes in fault zones: Inferences from earthquake rupturing. *Pure and Appl. Geophy.*, 124, 159-175.
- Sibson, R.H. (1986b). Earthquakes and lineament infrastructure: *Phil. Tras. Roy. Soc. Lon.*, A317, 63-79.
- Sibson, R.H. (1989). Earthquake faulting as a structural process. *J. Struc. Geol.*, 11, 1-14.
- Sibson, R.H. (1992). Fault-valve behavior and the hydrostatic-lithostatic fluid pressure interface. *Earth Sci. Rev.*, 32; 141-144.
- Sieh, K.E. (1978). Prehistoric large earthquakes produced by slip on the San Andreas fault at Pallett Creek, California. *J. Geophy. Res*, 83, 3907-3939.
- Sieh, K.E. (1984). Lateral offsets and revised dates of large prehistoric earthquakes at Pallet Creek, southern California. *J. Geophys. Res.*, 89, 7641-7670.
- Sieh, K.E., Stuiver, M., and Brillinger, D. (1989). A more precise chronology of Earthquakes produced by the San Andreas fault in Southern California. *J. Geophy. Res.*, 94, 603-623.
- Simpson, C., and Schmid, S.M. (1983). An evaluation of criteria to deduce the sense of movement in sheared rocks. *Geol. Soc. Am. Bull.*, 94, 1281-1288.

Singhvi, A.K., Banerjee, D., Pande, K., Gogte, V., and Valdiya, K.S. (1994). Luminescence studies on neotectonic events in south-central Kumaun Himalaya. *Quat. Sci. Rev.*, in press.

Smalley, R. F., Chatelain, J. L., Turcotte, D. L., and Prevot, R. (1987). A fractal approach to the clustering of earthquakes: applications to the seismicity of the New Hebrides. *Bull. Seis. Soc. Am.*, 77, 1368-1381.

Smith, B.W., Aitken, M.J., Rhodes, E.J., Robinson, P.D., and Geldard, D.M. (1986). Optical dating: methodological aspects. *Radiation Protection Dosimetry*, 17, 229-233.

Smith, B.W., Rhodes, E.J., Stokes, S., Spooner, N.A., and Aitken, M.J. (1990). Optical dating of sediments: initial quartz results from Oxford. *Archaeometry*, 32, 19-31.

Solntsev V.P., Mashkovtsev, R.J., and Shcherbakova, M.Ya. (1977). Electron paramagnetic resonance of the radiation centers in quartz. *J. Struct. Chem.*, 18, 578-583 (Engl Transl)

Stock, J.M., and Healy, J.H. (1988). Continuation of a deep borehole stress measurement profile near the San Andreas fault. 2. Hydraulic fracturing stress measurements at Black Butte, Mojave desert, California. *J. Geophys. Res.*, 93, 15196-15206.

Stokes, S. (1991). Quartz-based optical dating of Weichselian coversands from the eastern Netherlands. *Geologie en Mijnbouw*, 70, 327-337.

Suppe, J. (1985). *Principles of structural geology*. Prentice-Hall, New Jersey.

Sylvester, A.G. (1988). Strike-slip faults. *Geol. Soc. Am. Bull.*, 100, 1666-1703.

Tagami, T., Lal, N., Sorkhabi, R.B., and Nishimura, S. (1988). Fission track thermochronologic analysis of the Ryoke belt and the Median Tectonic Line, Southwest Japan. *J. Geophys. Res.*, 93, 13705-13715.

Tanaka, K., and Shidahara, T. (1985). Fracturing, Crushing and grinding effects on ESR signal of quartz. In: Ikeya, M. and Miki, T.(eds), *ESR dating and Dosimetry*, Ionics, Tokyo, 239-247.

Tanaka, T., Sawada, S., and Ito, T. (1985). ESR dating of late Pleistocene near-shore and terrace sands in southern Kanto, Japan. In: Ikeya, M. and Miki, T. (eds.), *ESR dating and Dosimetry*, Ionics, Tokyo, 275-280.

Tanaka, K. (1990). Dating of fault movement by the ESR method; basis and application: Unpublished Ph D. thesis, University of Kyushu, Japan.

Terres, R.R., and Luyendyk, B.P. (1985). Neogene tectonic rotation of the San Gabriel region, California, suggested by Paleomagnetic vectors. *J. Geophys. Res.*, 90, 12467-12484.

Tjia, H.D. (1967). Sense of fault displacements. *Geologie Mijnb.*, 46, 392-396.

Toyoda, S., and Ikeya, M. (1991) Thermal stabilities of paramagnetic defect and impurity centers in quartz: basis for ESR dating of thermal history. *Geochem. J.*, 25, 437-445.

Toyoda, S. (1992). Production and Decay characteristics of paramagnetic defects in quartz: applications to ESR dating. Unpublished Ph. D. thesis. Osaka University, Toyonaka, Osaka, Japan.

Turcotte, D.L. (1992) *Fractals and Chaos in Geology and Geophysics*, Cambridge University Press, Cambridge.

Twiss, R.J., and Gefell, M.J. (1990). Curved slickenfibers: a new brittle shear sense indicator with application to a sheared serpentinite. *J. Struct. Geol.*, 12, 471-481.

U.S. Geological Survey Staff, (1971). Surface faulting, In: *The San Fernando, California, earthquake of February 9, 1971*. U. S. Geol. Surv. Prof. Pap., 733, 55-76.

Van Dissen, R.J., Berryman, K.R., Pettinga, J.R., and Hill, N.L. (1992). Paleoseismicity of the Wellington-Hutt Valley Segment of the Wellington Fault, North Island, New Zealand. *New Zealand J. Geol. Geophys.*, 35, 165-176.

Velde, B., Dubois, J., Moore, D., and Touchard, G. (1991). Fractal patterns of fractures in granites. *Earth and Planet. Sci. Lett.*, 104, 25-35.

Vita-Finzi, C. (1992). Radiocarbon dating of late Quaternary fault segments and systems. *J. Geol. Soc. London*, 149, 257-260.

Wallace, R.E., and Morris, H.T. (1986). Characteristics of faults and shear zones in deep mines. *Pure & Appl. Geophys.*, 124, 107-125.

Walters, G.K., and Estle, T.L. (1961). Paramagnetic Resonance of defects introduced near the surface of solids by mechanical damage. *J. Appl. Phys.*, 32, 1854-1850.

Weber, F.H., Jr., (1985). Geology of selected areas along the San Gabriel fault zone between Saugus and the San Andreas fault, and reinterpretation of structural elements and displacement history, Kern, Los Angeles, and Ventura counties, California. Division of Mines and Geology Open-File Report (OFR) 85-15 LA.

Weber, F.H., Jr., (1986). Geologic relationships between the San Gabriel and San Andreas faults, Kern, Los Angeles, and Ventura counties, California - a new interpretation. *California Geology*, 39, 5-14.

Weber, F.H., Jr., (1988). Geologic relationships along the San Gabriel fault between Hardluck canyon and Castaic, Los Angeles and Ventura counties. *California Geology*, 41, 229-238.

Weeks, R.A. (1956). Paramagnetic resonance of lattice defects in irradiated quartz. *J. Appl. Phys.*, 27, 1376-1381.

Weeks, R.A. (1963). Paramagnetic spectra of  $E_2^+$  centers in crystalline quartz. *Phys. Rev.*, 130, 570-576.

Weeks, R.A., and Abraham, M. (1965), Electron spin resonance of irradiated quartz: atomic hydrogen. *J. Chem. Phys.*, 42, 68-71.

Weil, J.A. (1984). A review of electron spin spectroscopy and its application to the study of paramagnetic defects in crystalline quartz. *Phy. and Chem. Minerals*, 10, 149-165.



Weldon, R.J., Meisling, K.E., and Alexander, J. (1993). A speculative history of the San Andreas fault system in the central Transverse ranges. In: Powell, R.E., Weldon II, R.J. and Matti, J.C. (eds.), *The San Andreas fault system; Displacement, palinspastic reconstruction, and geological evolution*. Geol. Soc. Am. Mem., 178, 161-198.

Wesson, R.L., Page, R.A., Boore, D.M., and Yerkes, R.F. (1974). Expectable earthquakes and their ground motions in the Van Norman reservoirs area, in *The Van Norman reservoirs area, northern San Fernando Valley, California*: U.S. Geol. Sur. Circular, 691(B), 1-9.

White, S.H., Bretan, P.G., and Rutter, E.H. (1986). Fault zone reactivation: kinematics and mechanisms. *Phil. Trans. R. Soc. Lond.* A317, 81-97.

Wieser, A., and Regulla, D.F. (1989). ESR dosimetry in the "Giga-rad" range. *Appl. Radiat. Isot.*, 40, 911-913.

Wilcox, R.E., Harding, T.P., and Seely, D.R. (1973). Basic wrench tectonics. *AAPG Bulletin*, 57, 74-96.

Wintle, A.G., Lancaster, N., and Edwards, S.R. (1994). Infrared stimulated luminescence (IRSL) dating of late-Holocene aeolian sands in the Mojave Desert, California, USA. *The Holocene*, 4, 74-78.

Wills, C.J., and Borchardt, G. (1993). Holocene slip rate and earthquake recurrence on the Honey Lake fault zone, northeastern California. *Geology*, 21, 853-856.

Wojtal, S., and Mitra, G. (1986). Strain hardening and strain softening in fault zones from foreland thrusts. *Geol. Soc. Am. Bull.*, 97, 674-687.

Wojtal, S., and Mitra, G. (1988). Nature of deformation in some fault rocks from Appalachian thrusts. In: Mitra, G., and Wojtal, S. (eds.), Geometries and mechanics of thrusting, with special reference to the Appalachians. Geol. Soc. Am. Spec. Pap., 222, 17-33.

Wood, R.M. (1989). Extraordinary deglaciation reverse faulting in Northern Fennoscandia. In: Gregersen S. and Basham, P.W. (eds), Earthquakes at North-Atlantic passive margins: neotectonics and postglacial rebound, 141-173. Kluwer Academic.

Woodcock, N.J., and Fischer, M. (1986). Strike-slip duplexes. J. Struct. Geol., 8, 725-735.

Yip, K.L., and Fowler, W.B. (1975). Electronic structure of  $E'_1$  centers in  $\text{SiO}_2$ . Phys. Rev. B: Solid State, 11, 2327-2338.

Yokoyama, Y., Falgueres, C. and Quaegebeur, J.P., 1985. ESR dating of quartz from Quaternary sediments: a first attempt. Nucl. Tracks Radiat. Meas., 10, 921-928.

Zimmerman, D.W. (1971). Thermoluminescence dating using fine grains from pottery. Archaeometry, 13, 29-52.

Zimmerman, D.W. (1972). Relative thermoluminescence effects of alpha- and beta-radiation. Radiation Effects, 14, 81-92.

Zoback, M.D., Zoback, M.L., Mount, V.S., Suppe, J., Eaton, J.P., Healy, J.H., Pooenheimer, D., Reasenber, P., Jones, L., Raleigh, C.B., Wong, I.G., Scotti, O., and Wentworth, C. (1987). New evidence on the state of stress of the San Andreas fault system. Science, 238, 1105-1111.